RUHR-UNIVERSITÄT BOCHUM

SFB 837
Interaction Modeling in Mechanized Tunneling

Veselin Zarev

Model Identication for the Adaption of Numerical Simulation Models - Application to Mechanized Shield Tunneling

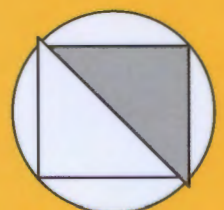Bochum 2016

Heft 55

Schriftenreihe Grundbau, Boden- und Felsmechanik

Heft 55

Model Identification for the Adaption of Numerical Simulation Models – Application to Mechanized Shield Tunneling

Dissertation

as a requirement of the degree of
Doktor-Ingenieur (Dr.-Ing.)

at the Faculty of
Civil and Environmental Engineering
Ruhr-Universität Bochum

submitted by
Veselin Zarev
from Kyustendil / Bulgaria

Reviewers
Prof. Dr.-Ing. habil. Tom Schanz
Prof. Dr. Maria Datcheva
Prof. Dr.Sc. Ivan Dimov
Prof. Dr. Akbar Javadi

Bochum, Germany, August 2016

Vorwort des Herausgebers

Die Arbeit von Herrn Dipl.-Ing. Veselin Zarev entstand im Rahmen unserer Forschung im TP C2 des hiesigen Sonderforschungsbereichs „Interaktionsmodelle im maschinellen Tunnelbau". Generell beschäftigt sich die Arbeit mit der Modellvalidierung bei der Verwendung von numerischen Simulationen. Ziel ist es, mittels der Modellidentifikation das numerische Modell zu adaptieren und zwar im Fortgang des jeweiligen Projektes z.B. während der Bauphase und beim Eingang von baubegleitenden Messergebnissen. Dieses Konzept kann allgemein auf die unterschiedlichsten Fragestellungen des Bauingenieurwesens angewandt werden.

Die Arbeit umfasst neben den eigentlichen geotechnischen Inhalten maßgebliche Komponenten aus dem Gebiet „Computational-Geotechnics" und der angewandten Mathematik, wie etwa der Statistik. Endgültiges Ziel der Untersuchungen von Herrn Zarev ist es, zunächst an Hand von synthetischen Messungen, da konkrete Messergebnisse realer und geeignete Projekte noch nicht zur Verfügung standen (Ausnahme Westerschelde Tunnel, NL), die anfänglich unbekannten bzw. unscharf bekannten Materialparameter des Baugrundes zu identifizieren. Für derartige Untersuchungen ist zunächst ein sog. Vorwärtsmodell notwendig, welches eine adäquate und realistische im Sinne von physikalisch realistische, numerische Modellierung des maschinellen Tunnelvortriebs erlaubt. Neben dem Stoffgesetz kommen besonders die für den maschinellen Tunnelvortrieb typischen Subsysteme zum Tragen. Dies sind die Abbildung der eigentlichen Tunnelbohrmaschine, die Tunnelauskleidung, die Ortsbruststützung und der sequenzielle Baufortschritt, die Interaktion zwischen dem Tunnel und dem Baugrund, die sog. Ringspaltverpressung und die Berücksichtigung von geometrischen Randbedingungen wie etwa dem Steuerspalt, die Konizität der Tunnelbohrmaschine. Daneben gilt es, die Untergrundverhältnisse im Sinne der konstitutiven Eigenschaften der beteiligten Bodenschichten zu quantifizieren. Dies geschieht dadurch, dass ausgehend von z.B. Ergebnissen vorweg eilender Baugrunduntersuchungen und dem Baugrundgutachten die inverse Analyse (Parameterberechnung) baubegleitend erfolgt und dadurch eine Aktualisierung dieser Material-Bodenkennwerte möglich wird.

Ein wesentlicher Aspekt der Submodellbeschreibung ist die Modellierung der sog. Ringspaltverpressung. Diese Aufgabe ist aus verschiedener Hinsicht sehr schwierig. Spielt sich doch der eigentliche Vorgang der Ringspaltverpressung geometrisch gesehen in einem sehr kleinen Bereich ab, was besondere Herausforderungen an die Diskretisierung mit sich bringt. Daneben ist die Ringspaltverspressung im starken Sinne eigentlich ein Konsolidationsproblem, d.h. eine hydraulisch-mechanisch gekoppelte Berechnung wird notwendig. Die genauen Vorgänge auf der Mikroebene beim Einpressen des Ringspaltmörtels in den umgebenden Boden sind sehr komplex und konnten in Zusammenarbeit mit dem Lehrstuhl Kontinuumsmechanik (Prof. Steeb) gelöst werden. Es zeigt sich, dass die mikromechanisch korrekte Modellierung in unmittelbarer Ringspaltnähe wohl einen Einfluss hat, jedoch dieser Einfluss, wenn man etwa die Oberflächensetzung im Auge hat, vernachlässigbar scheint.

Numerische Simulationsmodelle, und hierbei handelt es sich um dreidimensionale Netze, beinhalten eine Vielzahl von Parametern. Zur Reduktion dieses Parametersatzes auf die für die Berechnung relevanten Ergebnisse, schlägt Herr Zarev den Einsatz einer Sensitivitätsanalyse vor. Damit gelingt es, Parameter die keine Bedeutung für die im Vordergrund stehenden Modellantworten zu haben, bei der Identifikation im folgenden Schritt herauszunehmen und sie mit realistischen Schätzwerten zu belegen. Nach erfolgreichem Abschluss der Sensitivitätsanalyse liegen damit Ergebnisse vor, die die unterschiedlichen Modellparameter über den zeitlichen Verlauf der Simulation unterschiedlichen Einfluss auf die gewünschten Berechnungsgrößen haben. Mit der reduzierten Anzahl von Modellparametern führt Herr Zarev im nächsten Schritt die sog. Parameterrückrechnung durch. Dazu verwendet er einen am Lehrstuhl in vorhergehenden Promotionen erarbeiteten genetischen Algorithmus, den sog. PSO Algorithmus.

Die Arbeit endet mit der Behandlung eines tatsächlich ausgeführten Tunnels in den Niederlanden. An diesem Tunnel in weichem Boden ist es Herrn Zarev möglich, sein bisher qualitatives Konzept an einer realen Bauaufgabe zu verifizieren. Schlussendlich gelingt es Herrn Zarev den Fehler zwischen den beobachteten Messergebnissen und den von ihm prognostizierten Berechnungsergebnissen sehr gering zu halten. Es ergibt sich eine deutliche Verbesserung gegenüber den nur auf den Daten des Baugrundgutachtens beruhenden Berechnungen.

Wir Danken der DFG herzlich für die nachhaltige Unterstützung unserer wissenschaftlichen Arbeiten.

Bochum, Oktober 2015   Tom Schanz

Danksagung

Bochum, August 2016   Veselin Zarev
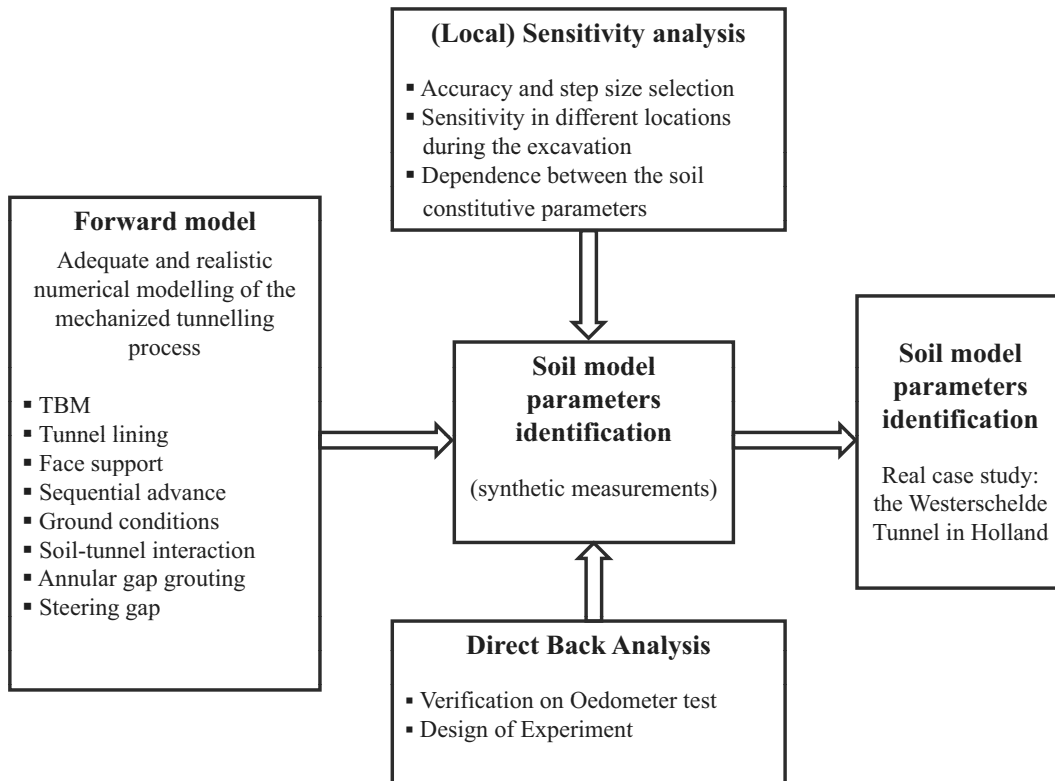
Abstract

The primary purpose of the research presented in this thesis is to define an adequate numerical model to simulate the mechanized tunnelling process in the most realistic way. The main concern is to make the model as robust and realistic in detail as possible, whilst keeping the calculation time reasonably low. An adequate numerical model is understood to include all relevant components of the mechanized tunnelling process, including the tunnel boring machine (TBM), face support, grouting the annular gap, tunnel lining, and sequential advance, as well as having the correct model boundary (mechanical and hydraulic) and initial soil and groundwater conditions. The defined model is used as a forward model in back calculating the model input parameters of the adopted advanced elastoplastic soil constitutive model. To do this, first, a derivative-based local sensitivity analysis (LSA) is performed on the main input parameters of the soil model. The purpose is to increase understanding of the parameters which are subject of the calibration (identification). The applicability and the accuracy of the LSA are investigated and discussed. An appropriate step size is selected for calculating the partial derivatives involved in the LSA. Next, for calibration of the input soil parameters, a direct back analysis is carried out, using the Particle Swarm Optimizer (PSO) to minimize the discrepancies between the numerical predictions and the measurements. Initially, synthetic measurements are used in order to verify the optimization procedure. Further, eight synthetic identification variants are defined and studied, with respect to the number of observation points used, available records, and measurement noise. It is shown how the amount and the accuracy of the measurement data (observations) influence the performance of the model parameter identification procedure. Finally, the proposed back analysis strategy is applied to a real shallow tunnel project in soft ground.

The proposed model identification procedure is summarized in the chart below:

(Local) Sensitivity analysis

- Accuracy and step size selection
- Sensitivity in different locations during the excavation
- Dependence between the soil constitutive parameters

Forward model

Adequate and realistic numerical modelling of the mechanized tunnelling process

- TBM
- Tunnel lining
- Face support
- Sequential advance
- Ground conditions
- Soil-tunnel interaction
- Annular gap grouting
- Steering gap

Soil model parameters identification

(synthetic measurements)

Soil model parameters identification

Real case study: the Westerschelde Tunnel in Holland

Direct Back Analysis

- Verification on Oedometer test
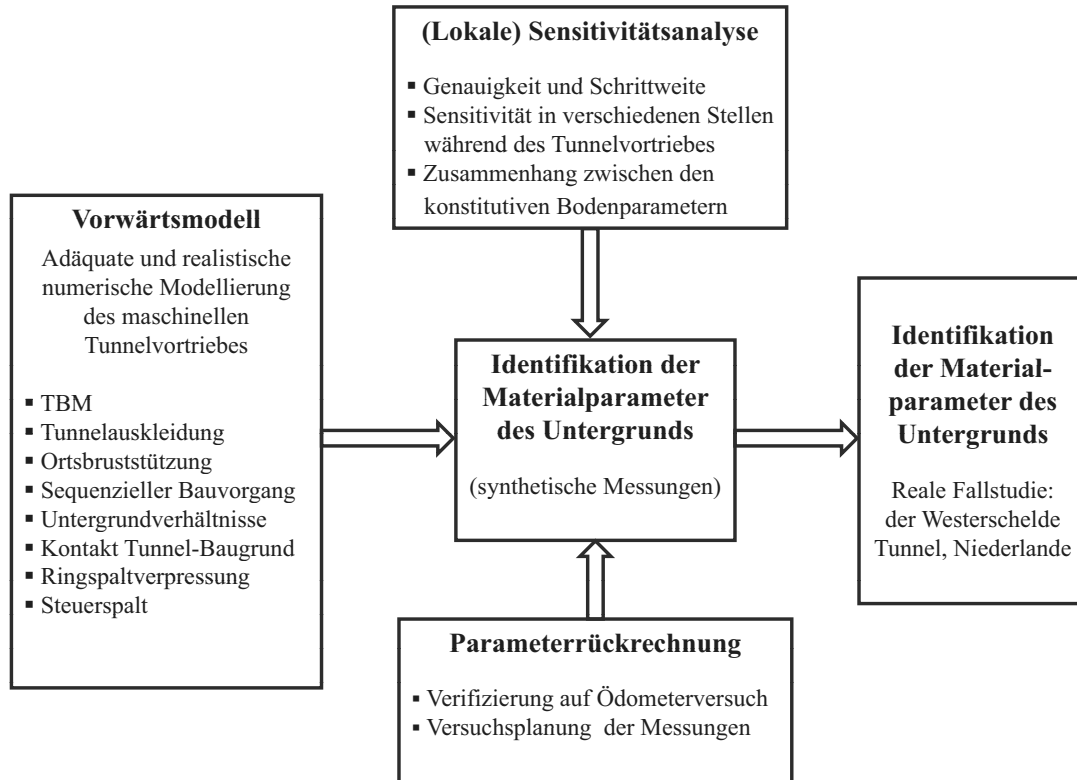- Design of Experiment

Zusammenfassung

Hauptziel der vorliegenden Doktorarbeit ist die Identifikation der Modellparameter des Untergrundes für die Adaption numerischer Simulationsmodelle für den schildgestützten maschinellen Tunnelvortrieb. Die Identifikation der Modellparameter des Untergrundes versteht sich als die Identifikation der konstitutiven Bodenparameter des verwendeten Stoffgesetzes.

Am Anfang fokussiert sich die Doktorarbeit auf die Entwicklung eines adäquaten numerischen Modells für die realistische Abbildung des maschinellen Tunnelvortriebes. Eine adäquate Modellbildung muss alle wesentlichen am Vortriebsgeschehen beteiligten Komponenten, wie Tunnelbohrmaschine (TBM), Ortsbruststützung, Ringspaltverpressung, Tunnelauskleidung (Tübbingsausbau) sowie sequenzieller Vortrieb berücksichtigen. Außerdem müssen zum Modell entsprechende mechanische und hydraulische Randbedingungen vorgegeben werden.

Ziel ist die Entwicklung eines robusten und numerisch effizienten Simulationsmodells, im Sinne einer Vorwärtsrechnung, welches später für die Parameteridentifikation der konstitutiven Eingabeparameter des verwendeten Bodenmodells mittels einer iterativen direkten Rückrechnung (engl.: *direct back analysis*) benutzt wird. Um das zu unterstützen, ist eine lokale Sensitivitätsanalyse durchgeführt worden, um die Auswirkung der Modellparameter hinsichtlich der Modellantwort zu analysieren. Zusätzlich ist die Genauigkeit der verwendeten lokalen Sensitivitätsanalyse überprüft und eine zutreffende Schrittweite für die Berechnung der partiellen Ableitungen bestimmt worden. Für die Minimierung der Abweichungen zwischen den real gemessenen (bzw. zunächst synthetisch gewonnenen) und den simulierten Modellantworten wurde als nächstes eine direkte Rückrechnung mittels der Partikle Swarm Optimization (PSO) durchgeführt. Verschiedene Identifikationsvarianten hinsichtlich des Ortes und der Anzahl der Messungen, im Sinne einer Versuchsplanung (engl.: *design of experiment*), wurden untersucht. Am Ende ist eine reale Fallstudie gerechnet worden, in welcher die Rückrechnung bei einem seichten Tunnel im Lockergestein eingesetzt wurde.

Die Vorgehensweise in der vorliegenden Doktorarbeit ist unten schematisch dargestellt:

(Lokale) Sensitivitätsanalyse

- Genauigkeit und Schrittweite
- Sensitivität in verschiedenen Stellen während des Tunnelvortriebes
- Zusammenhang zwischen den konstitutiven Bodenparametern

Vorwärtsmodell

Adäquate und realistische numerische Modellierung des maschinellen Tunnelvortriebes

- TBM
- Tunnelauskleidung
- Ortsbruststützung
- Sequenzieller Bauvorgang
- Untergrundverhältnisse
- Kontakt Tunnel-Baugrund
- Ringspaltverpressung
- Steuerspalt

Identifikation der Materialparameter des Untergrunds

(synthetische Messungen)

Identifikation der Material-parameter des Untergrunds

Reale Fallstudie: der Westerschelde Tunnel, Niederlande

Parameterrückrechnung

- Verifizierung auf Ödometerversuch
- Versuchsplanung der Messungen

Contents

1. Introduction and Overview

1.1. Motivation and Objectives

Complex underground geotechnical design projects situated in urban areas close to the ground surface – e.g. tunnels, (deep) excavation pits, caverns, etc. – incorporate risks such as possible damage to existing sensitive buildings and structures on the ground surface (Nagel *et al.* 2012), and also to existing cavities, e.g. spray concrete lined caverns in the underground (Thurlow & Knitsch 2011). Various geotechnical site investigation methods of the subsoil are employed before the construction of the project in order to evaluate the existence of such risks. The investigation is commonly performed using a selection of geophysical, boring, sampling, in-situ testing, and laboratory methods. The interpretation of the obtained data involves a certain degree of uncertainty, because of the different origins, variability, and complexities associated with the real soil behaviour (Mayne *et al.* 2001). Usually, test borings are the primary means for collecting the required subsurface information and soil samples for further laboratory testing. However, the number of the test borings is often restricted (due to cost-effectiveness and technical feasibility) and this leads to an incomplete evaluation of the subsurface conditions. Furthermore, the estimated soil parameters needed for a reliable geotechnical design derived from such investigations deviate, to a certain extent, from the actual subsoil conditions because of the soil samples being disturbed upon removal and the difference in scale between the sample and subsoil layer, as stated in Nagel *et al.* (2012).

Besides economic viability, major objective of tunnelling in urban areas is to keep the ground deformations, especially the surface settlements, as small as possible. For this reason, closed face shield tunnelling has become a well-established tunnel construction method in soft ground, especially in urban areas, because of its relatively higher excavation speed, and relatively low – 0.5 % or less – average amount of the ground losses. Needed values of soil model parameters can be obtained by performing field measurements and/or from laboratory tests. However, in tunnelling, it is often technically difficult to collect sufficient data for reliable numerical simulations. Frequently, there are significant

disagreement between the calculations and the real measurements during tunnelling, due to e.g. variation of the soil layers or different type of obstacles in front of the tunnel face (see Meier *et al.* 2009a, Miro *et al.* 2013, Kuszyk & Sieminska-Lewandowska 2013). In such cases, the direct back analysis can be used as a helpful tool for minimizing the disagreement and calibrating the numerical simulation. Thus, interlinking the observations (measurements) during the tunnel construction with the numerical predictions can be purposively applied to improve the still inaccurate recording of the subsoil situation. This new information can be used for improvement of the tunnel design in order of minimizing risks such as possible damage to sensitive structures and buildings at the ground surface. This is the motivation for the work in this thesis.

Shield supported tunneling is basically a three dimensional process. Furthermore, the given problem is non-linear, due to the highly non-linear and heterogeneous material behaviour of the subsoil, the flow of the fluids through the pore volume (soil consolidation in time and space around the tunnel) and the frictional contact between the TBM skin and soil. Additionally, the mechanized tunnelling is complex process, because numerous components are involved – the TBM, the face support, the concrete tunnel lining, the grouting mortar, and the (layered/heterogeneous) ground. Considering these features, analytical solutions can only be used for a simplified description of certain aspects of the advancement process, whereas, in contrast, numerical methods such as the Finite Element Method (FEM) are capable of solving complex problems and to deliver more reliable predictions of the soil-process interactions that take various process and soil parameters into account (Nagel 2009, Gioda & Swoboda 1999, Potts 2003, Schweiger 2008). Currently, FEM has developed from a research tool into a widespread engineering tool, that occupies a position next to conventional (analytical) design methods (Brinkgreve & Engin 2013).

1.2. Organization of the Thesis

Chapter 2:   This chapter starts with the current state of the art of numerical modelling of shield supported mechanized tunnelling. Further, it is presented the state of the art of model parameters identification and sensitivity analysis. Finally, the monitoring during tunnelling is briefly presented and discussed.

Chapter 3:   This chapter deals with the finite element modelling of closed face shield supported mechanized tunnelling. A three-dimensional numerical model is created with the finite element software PLAXIS 3D (version 2011) to analyze the mechanized tunnelling in assumed soft ground conditions. Such ground conditions are most typical in

urban areas where the tunnels are constructed with low overburden (cover depth) – typically one to only a few times the tunnel diameter. The numerical model represents the typical characteristics of the tunnelling performed by a slurry shield tunnel boring machine (TBM). The numerical simulation is performed according to the motto: "As simple as possible, as complex as necessary"; i.e. the goal is to create an adequate numerical model including an appropriate soil constitutive model, as well as correct model boundary and initial conditions. The elaborated model provides an appropriate representation of the real tunneling project components such as tunnel advance, face support, grouting the annular gap, etc. The next feature of the adequate numerical model is that the calculation takes a reasonably long time. The numerical model created in this way serves as a forward model in a back analysis procedure. For this, the mapping of the most relevant components of the tunnelling process in the model is investigated. Special attention is given to tunnelling in water-saturated ground conditions, applying an elastoplastic consolidation analysis. It is shown that the TBM advance speed and the soil hydraulic conductivity influence the surface settlements to a great extent. Furthermore, the influence of incorporating the evolution of the soil hydraulic conductivity on the predicted numerical response has been investigated. Hydraulic conductivity changes in the surrounding subsoil around the tunnel are caused by the infiltration process from the injected back-filled grout.

Chapter 4: This chapter consists of two main parts – the first one is the *Sensitivity Analysis (SA)* and the second one is the *Back Analysis*. A local SA is applied to the main input soil constitutive parameters of the advanced elastoplastic model that is employed. This is done prior the back analysis, in order to asses the FE-model performance and to increase understanding about the identified parameters. The applicability of the local SA for this particular geotechnical problem is investigated and discussed. An appropriate step size is selected for calculating the partial derivatives via a first-order finite difference scheme. Next, the results provided by the performed local SA, by the variation of the identified parameters (probability density function, PDF), and by the global SA performed in Miro *et al.* (2012a) are compared to each other. For the identification of the chosen main input parameters of the employed elastoplastic soil constitutive model, a direct back analysis was carried out using the Particle Swarm Optimizer (PSO) to minimize the discrepancy between the (synthetic) observations/measurements and the numerical simulation of the mechanized tunnelling. For performing the direct back analysis, the 3D FE-code Plaxis has been coupled with PSO toolbox using the MATLAB software. Several identification variants are studied in which different amount of information/measurements obtained during tunnelling is considered. The effect of noise in the measurements is also investigated.

Chapter 5:   In this chapter the performed numerical simulation of the mechanized tunnelling is verified on a real project – the Eeast Line of the Westerschelde Tunnel in the Netherlands. Finally, the results of the performed back analysis are presented, evaluated and discussed.

The thesis concludes with a summary and outlook.

2. State of the Art

2.1. Numerical Modelling of Shield Supported Mechanized Tunnelling

During the past decade, increased use of numerical simulations for the prediction of the ground behaviour, the surface settlements and the loading and deformation of the lining of shield-driven tunnels in *soft ground* has occurred. In the tunnel engineering literature the terms *hard rock* and *soft ground* are often adopted. Hard rock is understood as a stiff and strong ground that is able to carry itself without support from a tunnel lining. Tunnelling through such hard rock often involves blasting (drilling and blasting methods), or alternatively, open face hard rock TBMs that have no shield, leaving the area behind the cutter head open for rock support. On the other hand, tunnelling in soft ground (e.g. clay, silt, sand, gravel, or mud) is understood to involve more or less immediate tunnel support, as it is by the mechanized tunnelling via (soft ground) TBMs.

Generally, 3D analyses have to be performed when facing complex geologies and/or geometries, e.g. tunnel joints or connections to underground stations. The three-dimensionality is encountered first by the load transfer (arching effect; see Section 3.1) in both directions – transversely and longitudinally to the tunnel axis. Second, soil deformations occur along the tunnel circumference, in the ground ahead of the tunnel, and in the tunnel face. For tunnel heading stability, a 3D analysis is required because of the arching effect at the tunnel face that is activated in both longitudinal and transversal directions (Vermeer *et al.* 2003, Möller 2006).

The ever-increasing power and efficiency of modern computer technology and the considerable progress in computational mechanics have stimulated the development of more complex numerical models involving more features. As a consequence, the numerical simulations are nowadays widely employed in the tunneling design (see e.g. Nagel 2009). Compared to the relatively large number of models developed in the context of NATM

tunnelling (see e.g. Beer 2003), only small number of fully 3D numerical models for mechanized shield tunnelling exist, due to its considerably more complex nature, demanding modelling, and longer calculation time. More or less severe idealizations are often made in the numerical simulation of mechanized shield supported tunnelling, e.g. by assuming the surrounding underground to have a fully drained or undrained behaviour, by modelling its stress-strain behaviour using a linear elastic or linear elastic-perfectly plastic constitutive laws, or by neglecting individual components of the construction process (Nagel 2009). In the following paragraphs, seven scientific, state-of-the-art simulation models for the analysis of the closed face shield supported mechanized tunnelling in soft ground conditions that use a variety of assumptions and modelling techniques to describe the tunnel construction, the soil behaviour and the soil-structure-interactions between TBM/tunnel lining and subsoil are presented briefly. These models have in common that the tunnelling is simulated in three dimensions (3D) by applying a step-by-step simulation procedure of the construction process. Five of these simulations are performed using the Finite Element (FE) Method and two of them are performed using the Finite Difference (FD) Method.

In his Doctoral thesis, Franzius (2003) performed a finite element analysis of 3D tunnel construction of the westbound Jubilee Line Extension tunnel beneath St. James's Park in London. The analysis was performed using the Imperial College Finite Element Program (ICFEP) (Potts & Zdravkovic 1999, 2001), which uses a modified Newton-Raphson non-linear solver with an error-controlled sub-stepping stress-point algorithm (Zdravkovic & Potts 2010; Potts 2012). An open-face shield tunnelling machine was used. The tunnelling process is modelled using a step-by-step approach, in which the finite elements in front of the tunnel are successively removed/deactivated, while successively installing/activated lining elements behind the tunnel face. The excavation length is selected to 2.50 m. The entire ground profile is assumed to be homogeneous, represented by London Clay with a lateral earth pressure coefficient at rest $K_0 = 1.5$. A hydrostatic pore water pressure distribution is applied with a groundwater table 2 m below the ground surface. Pore water suction is applied in the partially saturated zone above the water table. The hydraulic behaviour of the soil is modelled as undrained. The tunnel diameter is set to 4.75 m and the cover depth to 30.5 m. Interface elements with zero thickness are used for modelling the soil-structure interaction between the soil and the lining elements. The soil is modelled using two models: a) an isotropic non-linear elastoplastic soil model with a yield surface described by Mohr-Coulomb model and b) a cross anisotropic material model, based on the formulation of Graham & Houlsby (1983) and combined with a small-strain stiffness formulation (based on Jardine *et al.* 1986). The concrete tunnel lining is modelled using linear elastic plate (shell) elements. Finally, the numerical predictions are compared

with the real measurements. None of the two used soil models could match the surface settlements profiles well at this high K_0-regime.

Schmitt *et al.* (2005) developed a 3D numerical model to simulate the tunnel driving process with an EPB (Earth Pressure Balance) machine. This model was subsequently used to perform probabilistic studies. The TBM is considered via modelling of its shield skin with volume elements (solid elements). These volume elements are directly connected to the volume elements of the surrounding soil without using any interface elements in between. Furthermore, the tunnel lining and the grouting mortar are taken into account as separate model components, whereas hydration of the mortar over time is considered by changing its modulus of elasticity. For a description of the mechanical behaviour of the assumed no water saturated subsoil (i.e. no groundwater table), a linear elastic-perfectly plastic material law with Drucker-Prager yield surface and a non-associated flow rule is used. The TBM advance and the tunnel construction are simulated by deactivating soil elements in front of the TBM or by changing their material properties to the material properties of the TBM, the grouting mortar, and the lining tube. A constantly distributed surface load is applied directly to the nodes of the soil volume elements at the heading face, to simulate support by means of an earth slurry. The same numerical model was later extended to partially saturated soil conditions by Schmitt *et al.* (2008) using the FD Method (FLAC^{3D} software, Itasca 2009). Effects such as permeable or impermeable tunnel heading face and variation of the groundwater level have been studied.

Do *et al.* (2013) developed a 3D numerical model of a railway tunnel that is excavated and constructed via a closed face slurry shield TBM. The main goal of their study was to create a simulation that is able to demonstrate the influence of the used soil constitutive model by observing the tunnel lining behaviour and ground displacements around the tunnel perimeter. The model has been developed in FLAC^{3D} software (Itasca 2009), which uses the finite difference method. The tunnel is constructed using a step-by-step approach with an excavation length of 1.50 m, which is equal to the width of one lining ring. Several important components of the tunnelling process are involved in the simulation, including the TBM shield conicity, the face and the grouting support pressures, the pressure around the shield due to the flow of both support media into the steering gap, the hardening of the grout over the time, the hydraulic jack forces, and the segmentation of the tunnel lining. The lining consists of precast reinforced concrete tubbings (segments) that are modelled via linear elastic embedded liner elements. The segment joints (longitudinal joints) are modelled with double node connections. This connection is represented by a set containing rotational, axial, and radial springs. The ring joints

(circumferential joints; see Fig. 3.5 for further clarification) are also modelled with double connections. The supports are modelled by applying distributed loads directly onto the surrounding elements. The TBM shield is not modelled with volume or plate elements. Instead prescribed displacements of the soil nodes around the TBM perimeter are used. Two soil constitutive models are used – the simple linear elastic-perfectly plastic Mohr-Coulomb (MC) model and the advanced elastoplastic Cap-Yield (Cysoil) model (Itasca 2009). The Cysoil model is a double hardening (shear/deviatoric and cap/volumetric) model. The model is characterized by a frictional Mohr-Coulomb shear envelope (zero cohesion), and an elliptic volumetric cap. It is similar to the Plaxis Hardening Soil model (Schanz 1999); however, differences exist e.g. in the hardening and dilatancy laws (Itasca 2009). Both soil models (i.e. their input parameters) are calibrated first on a simulation of a standard drained triaxial test. The numerical predictions of the tunnel excavation have demonstrated that the simple MC model does not realistically represent the ground behavior during tunnelling. Moreover, using this simple model results in lower structural forces in the tunnel lining, which, in turn, means that the entire tunnel design will be unsafe (Do *et al.* 2013).

In his Doctoral thesis, Möller (2006) developed a 3D simulation of the mechanized tunnelling via Slurry Shield TBM. Used is the FE-software Plaxis. Special attention in the analysis is paid to the study of the tunnel lining forces – bending moments and normal forces. The subsoil is assumed to be no water saturated (i.e. no groundwater table). To model its mechanical behaviour, two soil constitutive models are employed – a linear elastic-perfectly plastic model with Mohr-Coulomb yield surface (MC model), and the advanced elastoplastic Hardening Soil model (HS model). The tunnel lining is modelled via plate elements (shell elements) with linear elastic deformational behaviour. Between the elements of the soil and the tunnel lining, interface elements with Mohr-Coulomb frictional contact are applied. Interactions between the tunnelling process and the soil are considered using the so-called grout pressure method (see also Maidl 2008): at the heading face, a high pressure is applied to simulate the heading face support by means of a bentonite suspension. To the soil around the excavated volume, a radial, lower pressure is applied that represents the contact pressure between the TBM and soil, or the presence of a pressurised fluid film within the steering gap. Both of these pressures increase linearly from the tunnel crown to the tunnel invert. Behind the TBM, the elements representing the lining tube are activated, whereas the annular gap is first modelled as free space. Radial pressure is applied to the soil elements in the area of the annular gap, representing the grouting pressure, whereas the soil is allowed to deform until it comes into contact with the newly activated lining elements. At a certain distance from the TBM tail, where

the grouting mortar is assumed to be hydrated, the radial pressure is unassigned and grouting mortar elements filling the gap are activated (Möller & Vermeer 2008). Finally, the numerical model is validated on the Second Heinenoord Tunnel (started in 1996 in the Netherlands), using only the HS model. The results shown that the transverse settlements profile is slightly too flat, when compared to the steepness of the measured settlements profile. According to the author's opinion (Veselin Zarev), one explanation for this could be that the HS model does not consider the higher soil stiffness at small strains.

In order to model the tunnel construction process and the soil volume disturbed by the excavation, Komiya *et al.* (1999), modify the material parameters of the soil volume elements in front of the cutter wheel of the TBM. The TBM itself is modelled with volume elements of high stiffness. The TBM advance is simulated by applying external forces at the back of the shield, which represent the mechanical jack forces. The TBM is pressed into the soil elements with changed material parameters and interface elements are defined between the TBM and the surrounding soil over the shield skin. After each time step, the soil around the TBM is remesh to the current position of the TBM. The underground is assumed to be fully water saturated with an anisotropic soil hydraulic conductivity. The mechanical behaviour is modelled employing the Sekiguchi-Ohta model, which represents a Cam-Clay type model with consideration of K_0 (stress-induced) anisotropy by means of rotation of the yield surface. Grouting of the tail void is modelled by applying radial pressure directly to the soil elements, where, after the grouting mortar has hydrated, this pressure is deactivated and the displacements of the soil nodes are fixed. From a comparison of the numerical predictions with the measurements (in a tunnelling project in Tokyo) Komiya *et al.* (1999) concluded that the soil displacements 1 m above the tunnel crown and the surface settlements are modelled with reasonable accuracy. This model was later used to study a real tunnel excavation in a fully water saturated subsoil with a triple-face TBM in Tokyo, where the numerical predictions (surface settlements and subsoil displacements) were also compared with the field measurements (Komiya 2009). The results agreed with the field observations (Komiya 2009).

The next numerical simulation is the one presented by Kasper (2004a) in his doctoral thesis. The numerical model is built in the FE-software MSC.Marc. Within this FE-model, the TBM, the hydraulic jacks, the tunnel lining, the face support, and the grouting mortar are considered as separate components. The subsoil is assumed to be fully water saturated, where excess pore water pressures are generated and analysed by applying an elastoplastic coupled consolidation analysis. The mechanical behaviour of the subsoil is described employing the modified Cam-Clay model. The contact between the TBM and

the subsoil is considered by applying an area force to the tunnel heading face, by interface frictional contact between the TBM shield skin and subsoil, and by the application of a two-phase formulation for the grouting mortar. The hydration (cementing) process of the grouting mortar is modelled using a constitutive law with time variable stiffness properties. The numerical simulation is used to study the effect of various parameters such as the tunnel overburden, the support pressures (face and grout pressure), the length and the weight of the TBM, the shield conicity, the flexural rigidity of the hydraulic jacks, the soil stiffness for primary loading and un-/reloading, the soil angle of internal friction, the soil hydraulic conductivity, the hydration characteristics of the grouting mortar with respect to the ground displacements, the excess pore water pressures and the lining forces (Kasper & Meschke 2005, 2006a,b). The model is validated on various measurement data found in the literature.

The last model reviewed here is the presented by Nagel (2009) in his doctoral thesis. The model is built in the object-oriented parallelised FE-code KRATOS (Dadvand *et al.* 2008), and it is based conceptually on the previously described model of Kasper (2004a). Both simulations originate in the same research group at the Ruhr-Universität Bochum, Germany, whose head is Prof. Dr. techn. G. Meschke. However, in Nagel (2009), several additional features are included, such as partly saturated soil conditions as a three-phase material consisting of an elastoplastic soil skeleton, pore water, and pore air. The stress-strain behaviour of the subsoil is modelled using the Clay And Sand model (CAS-model), according to Yu (1998). Additionally, the flow of the support mediums along the shield of the TBM within the steering gap is considered. This becomes possible through modification of the original contact formulation soil-TBM elements (Mohr-Coulomb frictional contact) considering a pressurised fluid film within the steering gap.

According to Nagel (2010), to create an adequate and realistic numerical simulation of the mechanized tunnelling process, all relevant components such as TBM, soil and groundwater conditions, lining, tail void (annular gap) grouting, face support, and the tunnel driving process have to be considered. In the present numerical simulation, all of these components are considered (see Section 3.1).

The methodology to model shield supported mechanized tunnelling used in the current doctoral thesis has been presented in a series of publications: Zarev *et al.* (2011a), Zarev *et al.* (2011b), Schanz *et al.* (2012), Zarev *et al.* (2013).

2.2. Model Parameter Identification and Sensitivity Analysis

If the discrepancy between measurements (observations) and computed data is too large, an optimization problem for minimizing this difference can be formulated. Optimization problems for calibration of the model input parameters of numerical simulations are often also called identification problems (Will 2006). Through the availability of parameter optimization algorithms, the iterative parameter identification can be automated (applying a direct back analysis) and more complex problems can be treated. Such automated identification procedures have become important for a wide range of geotechnical engineering problems including mechanized tunnelling in urban areas. Only if the adequate numerical model is calibrated by successfully fitting the real measurements, is it possible to deliver reliable predictions. Subsequently, it is possible to use the numerical model to simulate various modifications in the construction plan if large unexpected deformations occurred.

Over the past decades a number of optimization algorithms have been used extensively for solving various engineering optimization problems, e.g. optimizing of geometries/shape optimization (see e.g. Puttke *et al.* 2013), parameter identification (see e.g. Meier 2008, Meier *et al.* 2009a, 2009b), etc. To discuss and describe all algorithms in detail is beyond the scope of this thesis. A review and detailed description is given e.g. in Meier (2008) where several optimization algorithms, particularly for geotechnical problems are investigated. In Meier *at al.* (2009b) the sensitivity analysis methods are introduced as follows:

"*Stochastic methods:* The stochastic methods use mainly combinatorial and/or random number based paradigms. Examples are Monte-Carlo sampling, Latin-Hypercube sampling, Metropolis Algorithm, Gibbs Sampler, and Simulated Annealing. Clear advantages of these approaches are their robustness and invariance towards rough objective function. Furthermore, many of these algorithms show global characteristics. Among their disadvantages is the relatively poor performance with respect to problems with a larger number of unknown variables.

Gradient-based methods: Gradient-based methods calculate the first derivative of the objective function and explore the search space step by step in the direction opposite to the steepest slope (for minimization of the objective function value). Examples are the Newton-Raphson method, the Quasi-Newton method after Davidon and the Maximum-Likelihood method. This class of algorithms performs best on convex, well-posed problems.

Simplex and complex methods: Simplex and complex based methods also attempt to minimize the objective function. In contrast to the gradient-based methods, this approach avoids calculation of the derivatives and the related disadvantages concerning the accuracy of their calculation (see e.g. Section 4.1.1.1). However, the local characteristic of this method predominates. One example of this class is the Nelder-Mead algorithm (downhill simplex method).

Population-based methods: Methods in this category use a set of individuals – each representing a parameter value assignment – and employ paradigms known from the nature with regard to the interaction of those individuals. Examples are Genetic algorithms (GA), Evolutionary methods (EA), Ant Colony Optimization (ACO), and the Particle Swarm Optimizer (PSO). Advantages are the high robustness and a relative high efficiency, even for problems with many unknown parameters.

Approximation methods: The basic idea of the approximation methods is a local or global approximation of the objective function (see e.g. Section 4.2.1.1). The extreme value search can then be temporarily performed on this replacement. Examples are adaptive response surface methods, Kriging, Moving Least Squares, and Artificial Neural Networks (ANN). These methods benefit from the fact that the optimization is very fast because of the short time span necessary to compute the (approximate) objective function value. Clearly, as a nontrivial task, the way in which the substitute topology is determined has to be considered.

Hybrid methods: The category of hybrid methods comprises methods using a mix of the paradigms described above. Examples are the Shuffled Complex Evolution method (SCE) and the Evolutionary Annealing-Simplex algorithm (EAS), amongst others. With an appropriate combination of known strategies these methods are usually robust and exhibit a high efficiency."

Another example is given in Javadi *at al.* (2005), where a hybrid optimization algorithm is presented that is based on a combination of the neural network and the genetic algorithm. In the proposed algorithm, a back-propagation neural network is used to improve the convergence of the genetic algorithm in the search for a global optimum.

Solving numerically, e.g. via finite element method (FEM), of nonlinear elastoplastic 3D problems related to mechanized tunnelling simulations is often expensive with regard to computational resources and time. This leads to difficulties in applying back analysis to identify model parameters. A helpful tool to asses the model performance is the sensitivity analysis (SA) performed prior the back analysis. SA can be used for:

- increasing understanding or quantification of the numerical model,

- evaluating the importance of each input parameter (ranking of the parameters),

- finding the most sensitive parameters for which one can decide to invest additional effort in reducing the uncertainties,

- reducing the number of the model parameters to be identified via back analysis by excluding the least sensitive ones, and

- evaluating the confidence level of the identified input parameters.

Not least, by knowing the most sensitive (i.e. most important) model input parameters, more efforts may be invested in an estimation of the search space of these parameters. Also, more suitable initial values of the parameters can be selected for starting the iterative identification procedure.

The SA is often referred to be either local or global (Dimov & Georgieva 2010, Sobol 1993, Homma & Saltelli 1996, Saltelli *et al.* 2008); each of them has its advantages and disadvantages. In the present thesis a local (derivative-based) SA, which is discussed in detail in Section 4.1.1, is used.

2.3. Monitoring During Tunnelling – Observational Method

2.3.1. Monitoring of Ground Deformations During Tunnelling

According to Kavvadas (2003), the goals of measuring the ground deformation are different in mountain and urban tunnel projects. Because of the large overburden height (up to several hundred meters), the main goal of monitoring the deformations during the construction of mountain tunnels is to ensure that the surrounding ground pressures are sufficiently controlled, i.e., an acceptable margin of safety against collapse of the super-structure exists. By contrast, in urban tunnels, the main goal of monitoring the ground deformations is to restrict the ground displacements (e.g. the surface settlements) to values sufficiently low to prevent damage to sensitive buildings at the ground surface. As a consequence, the basic difference in deformation monitoring comes from the fact that, in mountain tunnels, the goal is to protect against an ultimate limit state (i.e. collapse), whilst, in urban tunnels, the goal is to protect against serviceability limit states (i.e.

crack initiation) for the buildings at ground surface. Because of the differences in these two design philosophies, the types and the necessary accuracy of measuring the ground deformations vary significantly between the two classes of tunnels, as follows (Kavvadas 2003, p. 373):

- "In mountain tunnels, considerable ground deformations are deliberately permitted (and often provoked) in order to reduce the initially very large "geostatic" loads on the temporary support by increasing ground de-confinement. The de-confinement is achieved by controlled inward ground deformation at the excavation face, controlled delay in the completion of the temporary support measures (by increasing the distance from the face where the tunnel invert is closed), a relatively flexible temporary support system (e.g. long passive rock-bolts and thin sprayed concrete liners) and, finally, by installing the permanent lining at a later time when evolution of the long-term (creep) ground deformations has practically stopped. The control of ground deformations depends strongly on efficient and timely deformation measurements. However, due to the large ground deformations (several centimeters and even several tens of centimeters), the required level of precision of these measurements needs not be excessive; typically, accuracy of the order of one centimeter is sufficient in mountain tunnel applications."

- "In urban tunnels, the main objective is limiting ground deformations around the tunnel and thus causing the minimum possible movement and disturbance at ground surface and the structures founded there. This is achieved nowadays by means of TBMs by which the final (concrete) lining is installed as quickly as possible."

In both classes of tunnelling projects – mountain or urban – the measurements (ground displacements, stresses, pore water pressures, etc.) can be successfully used for verification of the tunnel design. If the measurements indicate notable deviations from the design values, the iterative direct back analysis can be applied as an efficient tool for assessing the real soil response (i.e. the real soil parameters) without the need for additional (often expensive and time consuming) sub-surface soil investigations.

Generally, two main possibilities for measuring the subsoil deformations exist – either the measuring instruments are installed from the ground surface before excavation, or they are installed from the tunnel during the construction. The main disadvantage when the monitoring is performed with instruments installed from the tunnel is that the total ground deformations cannot be recorded, because some of them have been already occurred before installing the instruments. Hence, measurement instruments installed on the tunnel lining (e.g. optical reflector targets) or installed in the surrounding ground

around the tunnel lining (e.g. borehole rod extensometers) have to be placed as early as possible (Kavvadas 2003). A third possibility for monitoring is to use a pilot tunnel, which can employ the advantages of the previous two possibilities. The pilot tunnel has smaller diameter and is excavated prior to the main tunnel. The pilot tunnel can be used not only as instrumentation, but also for compensation grouting between the main tunnel and the ground surface where sensitive buildings are located (see e.g. Naterop 2001, Bosshard *et al.* 2001, Thut *et al.* 2002).

The deformation monitoring in tunnelling projects typically includes some of the following measurements (Kavvadas 2003, Thurlow & Knitsch 2011): a) convergence of the tunnel walls, and settlement of the tunnel crest (measured from inside the tunnel), b) deformations at the ground surface, which includes settlements and tilts of surface buildings (performed with geodetic surveying instruments and/or with geotechnical instruments such as liquid level gauges, tilt sensors, surface clinometers/tiltmeters, precise taping, and crack-meters), and c) deformations of the subsoil, around the tunnel and below the ground surface (performed with geotechnical instruments such as extensometers, inclinometers, sliding curvometers, deep settlement plates, borehole rod extensometers, and sliding micrometers).

Whilst measuring the ground and lining deformations are the most used methods of monitoring the tunnel response, the following measurements are also sometimes done (Kavvadas 2003, Thurlow & Knitsch 2011): groundwater pressure (performed with different types of hydraulic piezometers), and ground pressures acting on the tunnel lining that are influenced by the grout pressures and the properties of the fresh grout (see e.g. Bezuijen & Talmon 2006). Further, it is possible to be used strain gauges on the TBM shield to measure shield strains. The shield strains can be correlated with the actual ground and tunnelling conditions, and this way understanding about the interaction between the shield, the subsoil, and the support mediums (grout mortar and bentonite suspension) can be gained (see e.g. Murray *et al.* 2008).

Finally, the back analysis is an important method for verifying or re-determining the necessary design parameters of the geotechnical project. The back analyses have to be performed instantly after receiving the recorded measurements so that the project design and construction methods can be evaluated and modified, if needed, without any considerable delay during the construction/excavation period (Sakurai 1997). The procedure of the observational method is shown as a flow chart in Figure 2.1.
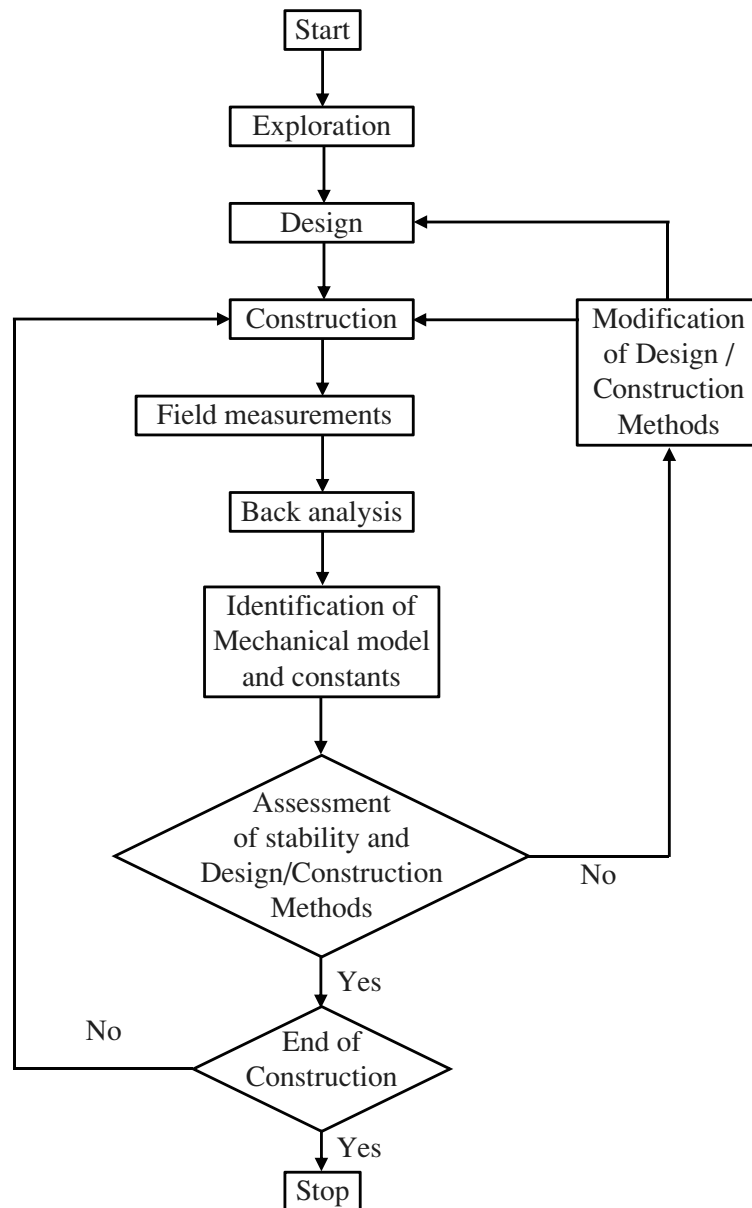
Figure 2.1.: Procedure of assessing the design and construction methods (after Sakurai 1997).

2.3.2. Monitoring of the Operational Parameters of the TBM

In addition to the ground deformations, monitoring of the operational parameters of the TBM has to be performed at the same time, because these also influence the soil response (e.g. settlements, water levels, pore pressures, etc.). For mechanized tunnel excavation via TBM, the following operational parameters can be measured (Boubou *et al.* 2008): TBM advance (excavation speed), face support pressure, grouting pressure in the annular gap

(backfilling pressure), grouted volume of mortar in the annular gap, torque on the cutting wheel, total thrust force, power excavating 1 m^3, time for installing one segmental ring of the lining, changes in the vertical angle of the TBM, and changes in horizontal angle of the TBM. These measurements have to be compared simultaneously with the recorded ground measurements (displacements, pore water pressures, etc.), so that the reason for e.g. the increased settlements can be evaluated – is it due to e.g. inefficient grouting and/or delay in the excavation speed, or is it due to soil layer changes, or is it because of both soil parameter and TBM operational parameter changes. Only considering all these measurements simultaneously – of the ground response and the TBM data – guarantee a plausible back analysis (see e.g. Cao *et al.* 2013).

2.4. Metamodelling Strategies

Because each run of the forward model (the FE-model of the mechanized tunnelling) is time-consuming, it is very helpful to replace this FE-model with a metamodel (surrogate model). The metamodelling is also known es a response surface analysis.

Various possibilities for approximation the response/output of the 3D FE-model of the mechanized tunnel excavation (i.e. using a surrogate model in the form of an analytical functions) are investigated in Khaledi (2012) and Khaledi *et al.* (2012). There, the performance and the accuracy of five metamodeling approaches are investigated – namely, Response Surface Methodology (RSM), Moving Least Squares (MLS), Proper Orthogonal Decomposition with Radial Basis Functions (POD-RBF), Proper Orthogonal Decomposition with Extended Radial Basis Functions (POD-ERBF), and Neighbourhood Approximation (NA). The considered FE-model is to the one used in this thesis. The effect of the sample size and the sampling method on the accuracy of the metamodels, is also investigated. Finally, it has been demonstrated that the POD-RBF metamodeling approach (see Buljak 2010 and 2012) is the most efficient and robust method, because it generates very accurate metamodels, even for small sample sizes, and its performance is not influenced by the sampling method.

Another example is presented in Ninić *et al.* (2011b). Trained Artificial Neural Networks (ANN), developed by means of a comprehensive, process-oriented FE-simulation model for mechanized tunnelling are used as a metamodel to provide the tunnelling-induced settlements. Javadi *et al.* (2002, 2003) have successfully implemented an ANN in a finite element program as a substitute for conventional constitutive models.

Additionally, specific parallelization techniques using shared or distributed memory systems are used to reduce the computational time of the complex numerical model (Meschke *et al.* 2013, Stascheit *et al.* 2011, Bui *et al.* 2013, Meschke *et al.* 2011).

3. Numerical Modelling of Shield Supported Mechanized Tunnelling

It is created a three-dimensional (3D) numerical model in the finite element software PLAXIS 3D (version 2011) for analyzing the mechanized tunnelling in urban areas in an assumed homogeneous soft ground. The numerical model is meant to represent the typical characteristics of the tunnelling process by means of slurry shield tunnel boring machine (TBM) as presented in Figure 3.1. The numerical simulation is elaborated according to the motto: "As simple as possible, as complex as necessary". For doing this the mapping of the most relevant components in the simulation is investigated in the next Section 3.1.

3.1. Components of the Mechanized Tunnelling Process

The main components of the mechanized tunnel excavation process (see the last paragraph in Section 2.1) are investigated, in order to understand which are more influencing the numerical predictions (see here also Schanz *et al.* 2012).

The numerical model is meant to represent the typical characteristics of the tunnelling process by means of slurry shield TBM in an assumed homogeneous and dry subsoil. The case where the ground is fully water saturated will be investigated separately later in Section 3.5. Because the geometry (assumed cylindrical shape of the tunnels), material properties, initial and excavation conditions are all symmetric about a vertical plane containing the longitudinal axis (i.e. the X-axis), only one-half of the model needs to be analyzed. In Figure 3.2 there are given the main dimensions of the created FE-model. The whole model is 250 m long (in the X-axis direction), 100 m wide (in the Y-axis direction) and 77 m deep (in the Z-axis direction). The model combines a shallow and a deep tunnel. The shallow tunnel have an overburden $1D$ (D is the tunnel diameter) and the deep tunnel have an overburden $5D$. The excavation of the shallow and the deep tunnel will be simulated separately. However, in this way using one single finite element
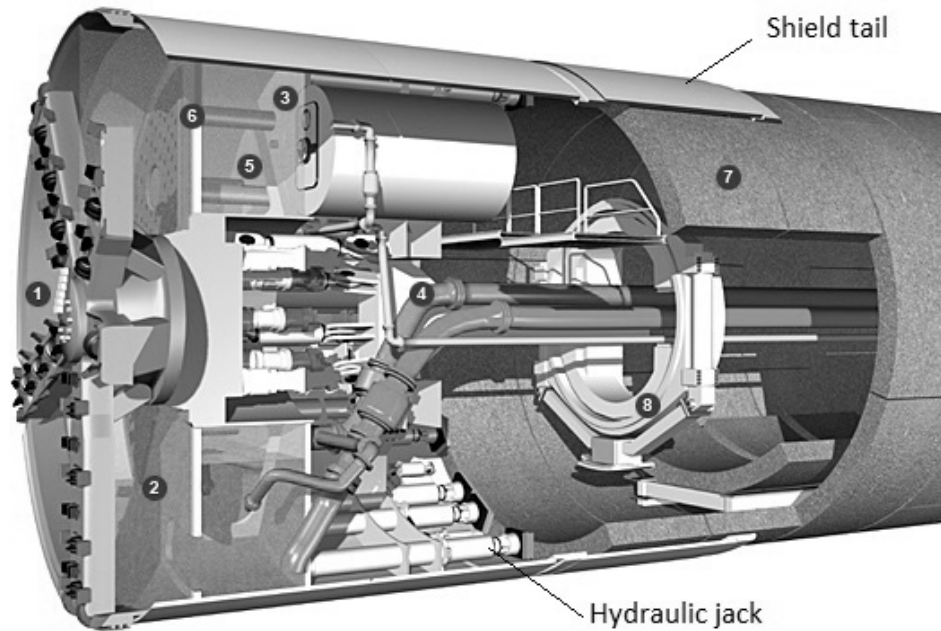
Figure 3.1.: Typical overview of a closed face slurry shield TBM: (1) cutterhead, (2) excavation chamber, (3) bulkhead, (4) slurry feed line, (5) air cushion, (6) diving wall, (7) segmental tunnel lining, (8) segmental erector.   Source: Herrenknecht AG.

model (FE-model) for the both tunnels (instead of two FE-models like in previous work of the author, see Schanz *et al.* 2012) the possible influence on the results coming from the different FE-discretization will be avoided. The chosen slurry shield TBM is 9.0 m long, simulated with cylindrical plate elements, and an area with a total length of 100.5 m for the shallow, and 199.5 m for the deep tunnel in the X-direction has been investigated. The tunnel diameter is D=8.5 m. The chosen FE-discretization (mesh) adopted for the simulation is shown in Figure 3.3. The space occupied by the soil material is discretized using 10-node tetrahedral elements. The number of these soil elements in the model is about 130000.

As explained above, there are modelled shallow ($1D$ overburden; D tunnel diameter) and deep tunnel ($5D$ overburden) and the excavation of each one is simulated separately. The stress state for the both type of tunnels is different. The main difference in the stress state for deep and shallow tunnels is that by a shallow tunnel the arching effect (or shortly arching) at the tunnel face – in both longitudinal and transversal direction – is not fully activated. While, by deep tunnels the arching can be fully mobilized. Arching can be defined as the stress redistribution which results in many cases in a decrease in loading over a structure. Terzaghi (1943) explained how stress transfer from yielding parts of a soil mass to adjacent non-yielding parts leads to the formation of an arching zone.
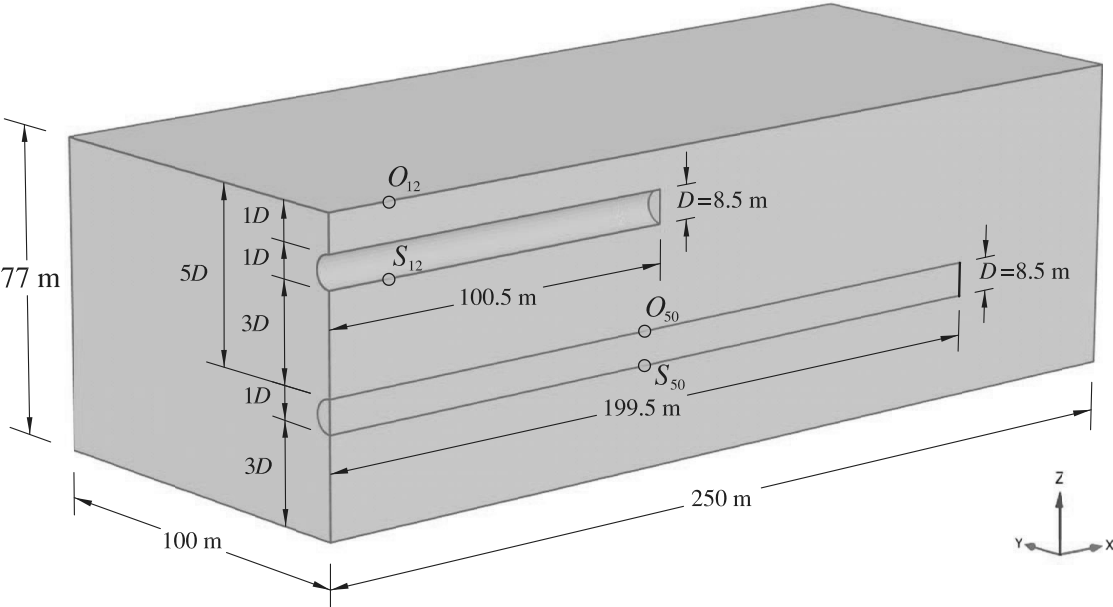
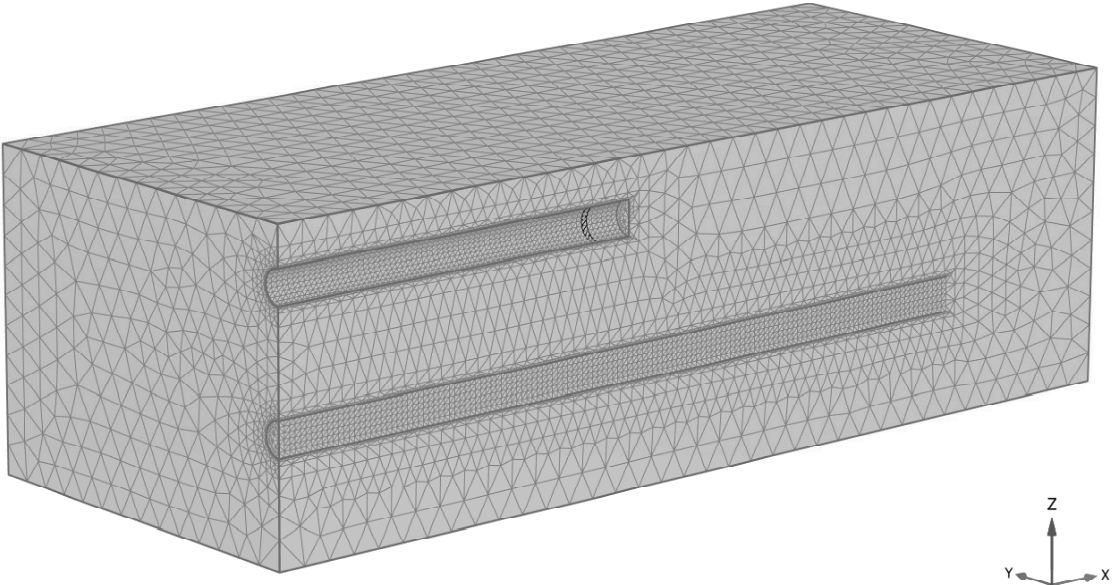Figure 3.2.: Main dimensions of the numerical model.

Figure 3.3.: Finite element discretization (mesh) of the numerical model.

3.1.1. Face Support

In a closed face shield supported tunnelling the heading face is supported by a pressurised substance in the excavation chamber in order to ensure the stability of the soil in front of the face and hold back the ground water if such is available. Two types of support media can be used (Maidl *et al.* 1996): 1) a bentonite suspension (hydroshields), or 2) an earth slurry consisting of the excavated material (Earth Pressure Balance shields (EPB shields)). These are commonly used for permanent support of the tunnel face, while temporary support of the face can be ensured using 3) compressed air. Temporary support is necessary if the excavation chamber of the TBM has to be entered by the working staff for repair of the cutting tools or for removal of boulders. The choice of the support depends on the geological conditions. Coarse soils with relatively high permeability, like sands and fine gravels are most suitable to be excavated with hydroshields, whereas for finer grained cohesive soils with relatively low permeability ($< 10^{-5}$ m/s) EPB shields are mostly preferred. Although, typical application range for EPB shields are plastic to soft clays and silts, due to their good applicability to serve as the basis of the support slurry. By the use of additives like foam, polymers or bentonite for conditioning of the soil the application range of EPB shields can be extended (Nagel 2009). During the tunnelling sometimes it is also used a pure 4) mechanical support for permanently supporting of the tunnel face.

3.1.1.1. Hydroshields (Bentonite Suspension Support)

In case of hydroshield tunnelling a suspension of bentonite and water (bentonite slurry) is applied for the heading face support. The pressure within the suspension is given by the total pressure, which is controlled by a compressed air reservoir (see (5) in Fig. 3.1) behind diving wall ((6) in Fig. 3.1), and pressure gradient within the suspension due to its unit weight. As the bentonite suspension behaves like a *Newton*ian fluid the pressure distribution at the heading face is linear with a minimum value at the tunnel crown and maximum value at the tunnel invert. By measurements Bakker *et al.* (2003) have proven that the assumption of a linear support pressure distribution is strictly valid and the pressure is not affected by the rotation of the cutting wheel. A filter cake can form if the pores of the soil are clogged by bentonite particles. The other extreme case is if the pores of the soil are too coarse and the suspension penetrates into the pore space. Thus, the positive heading effect of the applied face support may decrease at that moments. According to Anagnostou & Kovári (1996a) the deeper infiltration of slurry into the ground represents

a safety risk that cannot be compensated by raising the fluid pressure. In extremely coarse and poorly-graded soils the control of the slurry pressure for stabilizing the heading face becomes ineffective. Anagnostou & Kovári (1994) have investigated the effect of the TBM advance rate (excavation speed) on the slurry infiltration. They found, the higher the excavation speed, the less the slurry penetrates into the ground, and, consequently the higher the safety against active failure of the tunnel face.

3.1.1.2. EPB Shields (Earth Slurry Support)

When the tunnel is excavated using an EPB shield the support substance is derived directly from the excavated material. By measurements of the earth slurry pressure within the excavation chamber of EPB shield Bazuijen *et al.* (2005) showed a significant difference in comparison to the linear support pressure distribution within a hydroshield. The pressure distribution in the excavation chamber is influenced above all by the shear strength of the earth slurry. The shear strength of the slurry depends on its composition, which is characterized by the excavated material and by additives like foam and polymers (Bazuijen *et al.* 2005). Additionally, an influence of the rotation direction of the cutting wheel into the pressure gradient was found that causes a non-symmetric distribution of the support pressure at the heading face. The gradient decreases if the cutter head moves in direction of the gravitation and increases vice versa. As a consequence, the pressure distribution in front of the cutting wheel is not really known and further research is needed (Bazuijen 2013).

Moreover, as the working chamber is filled with excavated soil under pressure, a distinction must be drown between the total and effective stresses acting upon the heading face. Only the effective normal stresses can be denoted as actual support pressure on the excavation face (Anagnostou & Kovári 1996b). By further measurements Bazuijen *et al.* (2005) found that the total pressure and the pore pressure both were identical, i.e. no effective stresses developed within the earth slurry. However, the tunnel construction studied was an excavation in a sandy subsoil and it can be expected that for the advance in a ground that is more typical for an EPB shield (i.e. a subsoil with relatively low permeability), the stress state in the earth slurry will consist of effective stresses and pore water pressures as independent pressure component (Anagnostou & Kovári 1996a, Bazuijen *et al.* 2005).

3.1.1.3. Support by Means of Compressed Air

In a case the working chamber has to be entered by working staff the support substance used for the permanent support is temporally replaced by compressed air. In addition to the compressed air a mechanical support can be applied through the cutting wheel. Due to the negligible unit weight of the air the applied pressure is constant over the heading face. To prevent the groundwater from inflow into the excavation chamber the air pressure is matched to the water pressure at the tunnel invert, so that an excess of air pressure over water pressure occurs at the tunnel crown (Maidl *et al.* 1996).

3.1.1.4. Mechanical Support

Sometimes it is also used a pure mechanical support by which the face pressure is provided to the face by the cutting wheel itself. Additionally to the cutting wheel, steel plates may be installed in between the free spaces of the cutting arms, to slide along the tunnel face while rotating the boring machine. However, this method is only suitable for predominantly stable cohesive grounds above the groundwater table.

3.1.1.5. Mapping in the Numerical Simulation

For the numerical simulation in this thesis a hydroshield was chosen. The support pressure at the tunnel face needed to prevent active failure at the tunnel face is simulated as a non-uniformly linearly distributed pressure load acting on the FE-nodes at the tunnel face – see. Fig. 3.4. In that case it is assumed that a perfect membrane/filter cake develops at the face. For the shallow tunnel in the considered homogeneous and dry subsoil the pressure is set from 115 kN/m^2 (675 kN/m^2 for the deep tunnel) at the tunnel crown to 200 kN/m^2 (760 kN/m^2 for the deep tunnel) at the tunnel invert at each excavation stage. Later in the investigated shallow tunnelling in fully water saturated ground (see Section 3.5) because of the additional unit weight of the acting groundwater the face pressure is increased as follows: 245 kN/m^2 at the crown to 330 kN/m^2 at the invert. The face support should be larger than the resulting horizontal total earth pressure in order to maintain stable face conditions at TBM face. To avoid bentonite flow backwards into the annular gap, the face pressure should be smaller than the grouting pressure.

3.1.2. Sequential Advance

The closed face shield supported tunnelling is characterized by a relatively complex construction process and complex interactions between the ground, the supporting measures at the face (face support), the tail void (annular gap), and the TBM.

3.1.2.1. Tunnel Driving Process

The sequential tunnelling process is characterized by a sequence of thrust and standstill stages. The permanent support of the subsoil is realized by a construction process that consists of the following steps which are described below. In front of the TBM the soil is being excavated using a rotating steel cutting wheel ((1) in Fig. 3.1). Simultaneously, the whole TBM is pushed forward by elongation of the hydraulic jacks that counteract on the end of the lining tube. The excavation is processed until the length of one lining ring (normally about 1.5 to 2.0 m) has been advanced. Subsequently, the TBM stops and the next lining ring (tubing) is erected. After the ring building has finished, the excavation starts again. As explained in the previous Section 3.1.1, different support measures are applied in course of this step-by-step tunnel construction to stabilize the soil and to prevent the groundwater (if present) from flowing into the already excavated tunnel. The soil in front of the TBM is supported by a pressurized medium – a bentonite suspension, an earth slurry or a compressed air that fills the excavation chamber and transfers the support pressure onto the heading face. The subsoil surrounding the excavated area is borne at first by the TBM and its steel shield skin and afterwords by the lining tube that is erected under the support of the shield tail. In order to prevent the soil to move into the annular gap that arises between the tunnel lining and the surrounding subsoil when the TBM is pushed forward, this gap is grouted simultaneously with the TBM advancing using a pressurized mortar (will be described later in details in Section 3.1.7).

The described construction process leads to short and long term deformations of the surrounding subsoil in front, above and behind the TBM. In front of the TBM the short term deformations are caused by volume losses at the heading face due to disturbance of the primary stress state of the surrounding soil and relaxation of the soil into the excavation chamber. Above the TBM the deformations occur due to deformation of the shield tail and deformations of the soil into the steering gap due to overcutting and tapering (i.e. conical shape) of the TBM (see further Section 3.1.6). Behind the TBM the soil deformations are induced by the grouting of the annular gap and by deformations of the erected tunnel lining – ovalisation of the lining. Also, long term settlements result from the consolidation

of the soil and eventually from creep effects. Safe and cost- and time-efficient mechanized tunnelling – especially in urban areas, demands for the reliable determination of the expected time-dependent settlements, stresses and deformations of the lining, prognoses of possible critical subsoil conditions, and other design-relevant parameters.

3.1.2.2. Mapping in the Numerical Simulation

The excavation process is modelled by means of a quasistatic formulation of the corresponding FE-model. It results in modelling the excavation process via step-by-step procedure and consequently the advancement of the shield tunnelling is simulated (see Fig. 3.4). In the first step, i.e. first calculation phase, the initial ground conditions are applied. First, the vertical stresses in the soil are generated that are in equilibrium with the self-weight of the soil. Horizontal stresses, however, are calculated from the value of K_0 – coefficient of lateral earth pressure at rest. For the chosen normally consolidated soil (over-consolidation ratio $OCR = 1$ and pre-overburden pressure $POP = 0$) K_0 is calculated according to the well-known Jaky's semi-empirical formula (see Jaky 1948): $K_0^{nc} = 1 - \sin \varphi$. This relationship is the most widely-used formula to estimate the at-rest pressure in geotechnical engineering practice, and according also to Michalowski (2005) in the last sentence of his paper: "...the theoretical formula $K_0^{nc} = 1 - \sin \varphi$ is a good representation of the true
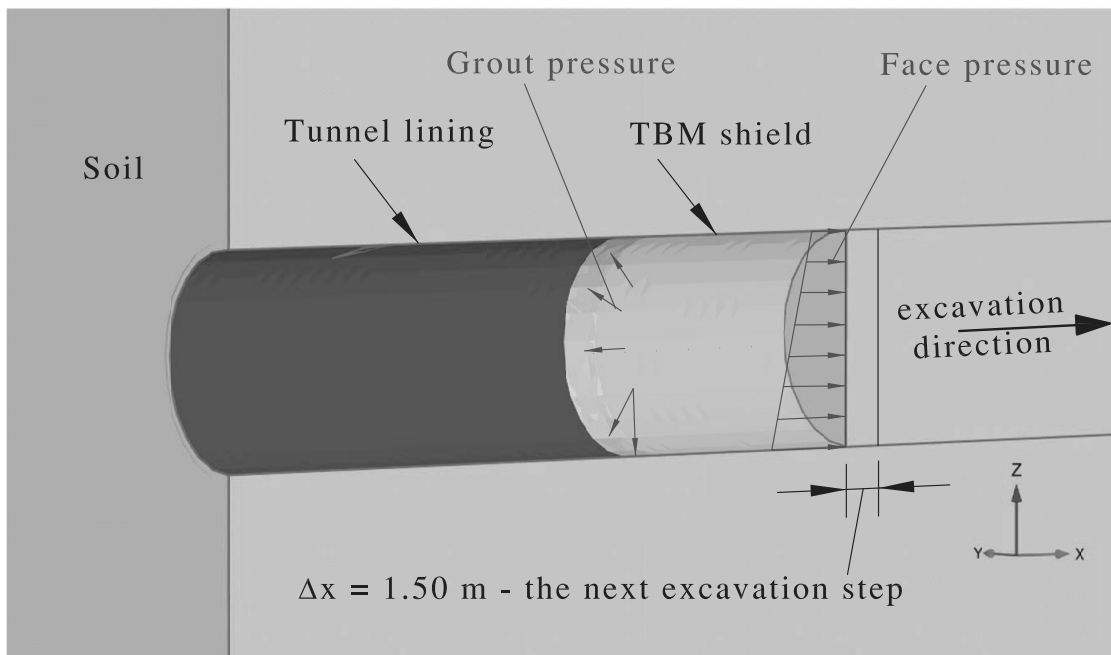
Figure 3.4.: Step-by-step excavation of the tunnel, and representation of the main relevant components in the mechanized tunnelling.
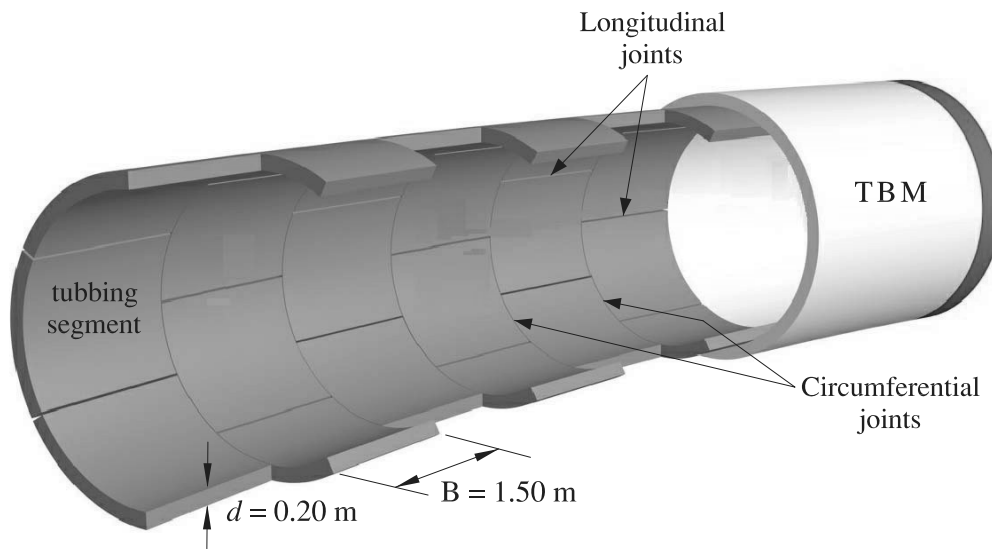
Figure 3.5.: Schematic view of the segmental tunnel lining tube (Source: VMT GmbH).

stress ratio in soils at rest". Schanz *et al.* (1999) also stated the same fact that the above Jaky's formula is a "highly realistic correlation". Later, in Section 3.1.3.2 by the description of the Hardening Soil model K_0^{nc} will be discussed again. All of the next calculation phases (i.e. excavation stages) are meant to simulate an advance of 1.50 m (1.50 m is the assumed tubing length in longitudinal direction; see in Fig. 3.5). The steps which are modelled in a single excavation stage are the following:

- excavation of the soil at tunnel heading (deactivation of the finite elements at that place with 1.50 m tunnel advance);

- applying a face support pressure at the tunnel face;

- activation of the TBM shield, i.e. of the plate elements (the next 1.50 m);

- applying the back-fill grouting pressure at the back of the TBM;

- installing (activation) a new concrete lining ring with width of 1.50 m.

The slurry shield TBM is 9.0 m long, simulated via plate elements. Plate elements are also used for the concrete tunnel lining. However, the segmentation (see in Fig. 3.5 the longitudinal and circumferential joints between the tubing segments) of the tunnel lining is not considered in the model. In reality, the segmentation introduces quite a complex structural behaviour of the lining resulting in local stresses which can be reproduced only by very detailed modelling procedures (see e.g. Blom 2012, Blom *et al.* 1999) not feasible within the framework of the proposed FE-model. The concrete tunnel lining is therefore modelled in a simplified way as a continuous tube (like assumed in many other tunnel

Table 3.1.: Parameters of the employed linear elastic model for the structural elements.

Parameter	Lining	TBM	Unit
d	0.20	0.35	[m]
E	30 000	210 000	[MPa]
γ	24	38	[kN/m³]
ν	0.10	0.30	[-]

simulations like e.g. in Kasper & Meschke 2006a). However, neglecting the segmentation and thus neglecting the interactions between the tunnel rings may underestimate the structural capacity of the tunnel linning (Galvan & Pena 2013). The parameters of the isotropic, linear elastic model assigned to the plate elements are given in Table 3.1. For seek of simplicity the action of the hydraulic jacks on the newly erected tunnel lining (see in Fig. 3.1) was not considered, and therefor it is assumed that hydraulic jacks do not influence the ground deformation.

3.1.3. Ground

The mechanical behaviour of the ground may be modelled at various degree of accuracy. Hereafter, it is investigated the influence of three soil constitutive models which have different complexity and accuracy for representing the soil response:

- a simple linear elastic perfectly-plastic model, with a Mohr-Coulomb yield surface – the Mohr-Coulomb model (MC model) (see Brinkgreve *et al.* 2011a);

- an advanced elastoplastic model with isotropic double hardening – shear (deviatoric or frictional) and cap (volumetric) hardening – the Hardening Soil model (HS model). It distinguishes between primary loading and unloading/reloading stress paths (see Brinkgreve *et al.* 2011a, Schanz 1998, and Schanz 1999);

- HS model extended to account for the higher stiffness of the soil at very small strains – the Hardening Soil model with small-strain stiffness (HSsmall model) (see Brinkgreve *et al.* 2011a, Benz 2007, Benz 2009).

Next, the three soil constitutive models are described separately. The HS model is described in detail, because it will be used later in the in the performed sensitivity and back analyses. While the MC and the HSsmall model are described shortly.

3.1.3.1. The Mohr-Coulomb Model

The simple linear elastic perfectly-plastic Mohr-Coulomb model is a combination of Hooke's law and the generalised form of Coulomb's failure criterion. The model involves five input parameters. These are the two elastic parameters from Hooke's law – the Young's modulus E' and the Poisson's ratio ν, the two plastic parameters from Coulomb's failure criterion – the angle of internal friction φ and the cohesion c, and additionally the dilatancy angle ψ. The latter parameter comes from the employment of a non-associated flow rule, which is used to model realistically the plastic (irreversible) volume changes due to shearing.

This model includes only a limited number of features that soil behaviour shows in reality. Failure behaviour is generally quite well captured – at least for drained conditions (see e.g. Brinkgreve 2005). However, stiffness behaviour below the failure contour is assumed to be purely linear elastic according to the Hooke's law. Also, major limitations of the MC model are that it does neither include stress-dependency nor stress-path dependency nor strain dependency of stiffness. Hence, the model has limited capabilities to accurately model deformation behaviour before failure, especially in situations where the stress level is changing significantly and/or in a case that multiple different stress paths are followed, as it is the case by tunnel excavation.

In Figure 3.6 it is represented graphically the basic idea of the MC model. There are shown the stress-strain behaviour for primary loading, yielding at some failure stress σ'_f (i.e. the horizontal part in the left graph) and unloading, and the representation of the failure surface for general stress state in principal stress space.

3.1.3.2. The Hardening Soil Model

The used Hardening Soil model is an advanced elasto-plastic soil constitutive model for simulating the behaviour of different types of soil, Schanz *et al.* (1999), Schanz (1998b). It is formulated in the framework of classical theory of plasticity. In the model the total strains (elastic plus plastic part) are calculated using a stress-dependent stiffnesses with a power law according to the approach of Ohde (1951) and Janby (1963), which are different for primary loading and un-/reloading. The plastic strains are calculated by introducing a multi-surface yield criterion. Hardening is assumed to be isotropic depending on both plastic shear and plastic volumetric strains. Shear hardening is used to model irreversible strains due to primary deviatoric loading, while cap (or compression) hardening is used to model irreversible plastic strains due to primary compression in oedometer loading and
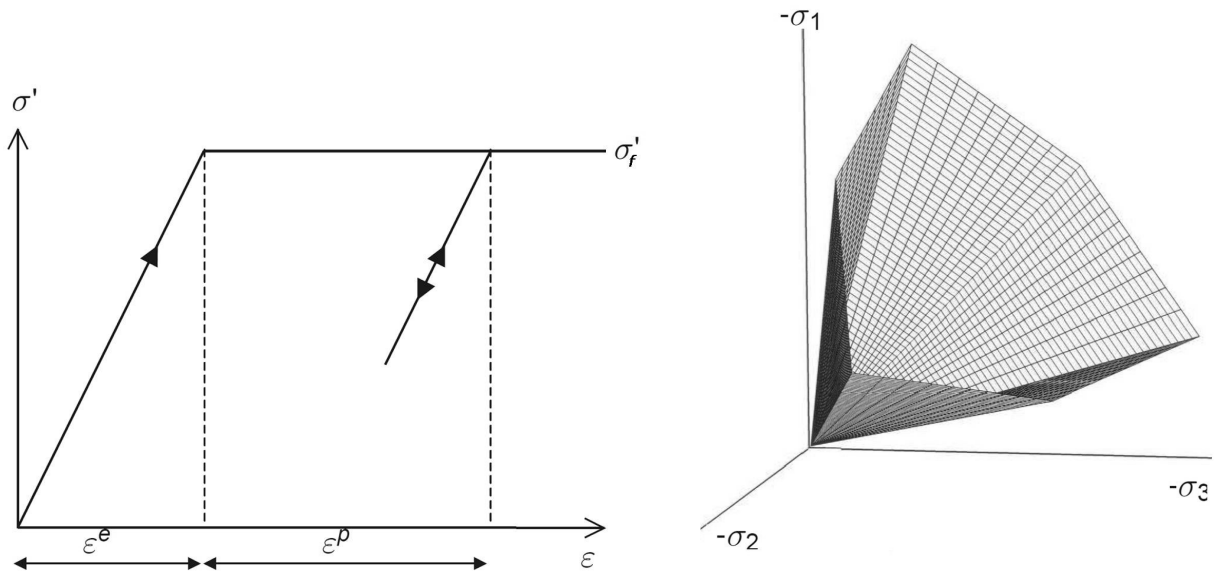
Figure 3.6.: Basic idea of the MC model. *Left*: linear elastic perfectly-plastic material behaviour; *Right*: yield surface in principal stress space for cohesionless soil ($c = 0$); compressive stresses are considered negative (Brinkgreve 2011a).

isotropic loading. For the shear hardening a non-associated and for the cap hardening an associated flow rule are assumed. The compressive stress and strain are considered to be negative.

Although, the HS model can be regarded as an advanced soil constitutive model, there are a number of features of real soil behaviour the model does not include. It is a hardening model that does not reproduce the strain-softening behaviour due to soil dilatancy. Anisotropy, destructuration (de-bonding), or creep effects are also not included. Moreover, the model does not distinguish between higher stiffness at small strains, i.e. shear strains lower than 0.00001 (1×10^{-5}), and reduced stiffness at engineering strain levels.

3.1.3.2.1. Constitutive Equations for Standard Drained Triaxial Test

When the soil is subjected to primary deviatoric loading a decrease in stiffness is observed and irreversible plastic strains develop. Here a basic idea for the formulation of the Hardening Soil model is that the stress-strain curve, i.e. the relationship between the vertical (elasto-plastic) strain ε_1, and the deviatoric stress q ($q = \sigma_1 - \sigma_3$), in a primary triaxial ($\sigma_2 = \sigma_3$ – minor principal stress, i.e. cell pressure) loading, can be well approximated by a hyperbola. Kondner (1963) and Kondner & Zelasko (1963) first have formulated such a hyperbolic relationship. Standard drained triaxial tests tend to yield nonlinear

stress-strain curves that can be described by:

$$-\varepsilon_1 = \frac{q_a}{E_i} \frac{(\sigma'_1 - \sigma'_3)}{q_a - (\sigma'_1 - \sigma'_3)} = \frac{1}{E_i} \frac{q}{1 - q/q_a} \qquad \text{for} \qquad q < q_f \qquad (3.1)$$

where E_i is the initial tangent stiffness modulus for small strain or initial slope of the stress-strain curve and q_a is the asymptotic value of the shear strength, which has no physical meaning itself, but mathematical. E_i is related to E_{50} (which will be described later) by:

$$E_i = \frac{2E_{50}}{2 - R_f} \qquad (3.2)$$

In Equation 3.1 the (Mohr-Coulomb) failure stress q_f, and the quantity q_a are defined as:

$$q_f = (c \cot \varphi - \sigma'_3) \frac{2 \sin \varphi}{1 - \sin \varphi} \qquad \text{and} \qquad q_a = \frac{q_f}{R_f} \qquad (3.3)$$

The above relationship for q_f is derived from the Mohr-Coulomb failure criterion (Mohr 1900), which involves the strength parameters φ and c. This deviatoric measure q_f was used also by Duncan & Chang (1970) in their famous hypo-elastic (nonlinear elastic) constitutive model based on the above hyperbolic formulation by Konder & Zelasko. The conceptional difference in the formulation by Konder & Zelasko, and that by Duncan & Chang is illustrated in Figure 3.7. As soon as $q = q_f$, the failure criterion is satisfied and perfectly plastic yielding occurs. The ratio between q_f and q_a is given by the failure ratio R_f. Because q_f is always smaller than q_a, the value of R_f is always smaller than unity, and varies from 0.5 to 0.9 for most soils (Duncan *et al.* 1980). However, in the present thesis for all calculations a value of $R_f = 0.9$ is used because it has been found as suitable for many soils (Brinkgreve *et al.* 2011a). The hyperbolic stress-strain relationship is plotted in Figure 3.7.

3.1.3.2.1.1. Stiffness for Primary Loading

The parameter E_{50} is the confining stress (σ'_3 in a triaxial test) dependent stiffness modulus for primary loading. E_{50} is scaled for it's stress dependency with a power law (Ohde 1951, Janbu 1963)

$$E_{50} = E_{50}^{ref} \left(\frac{c \cos \varphi - \sigma'_3 \sin \varphi}{c \cos \varphi + p^{ref} \sin \varphi} \right)^m \qquad (3.4)$$

where E_{50}^{ref} is the material reference stiffness modulus corresponding to the reference confining stress p^{ref} ($p^{ref} = -\sigma'_3$, a reference minor principal stress), and m is the exponent of the power law. The power varies in the range $0.5 < m < 1.0$ (von Soos 1990). In order to
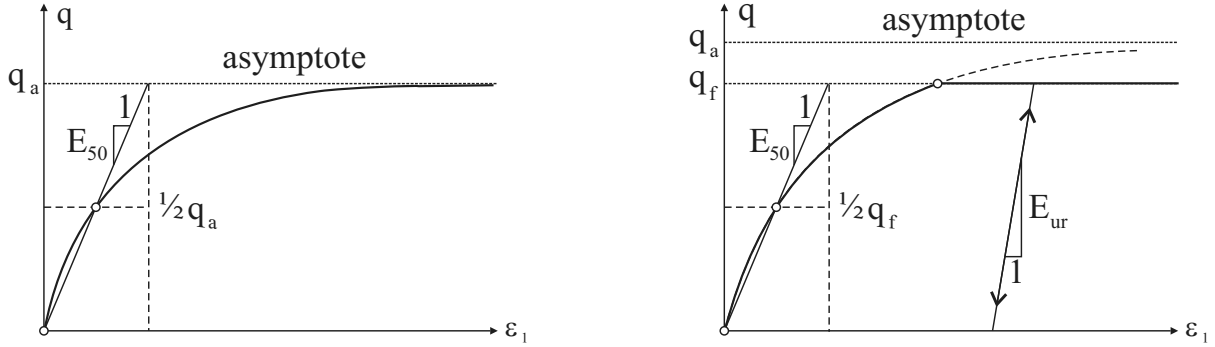
Figure 3.7.: Hyperbolic stress-strain relationship by Konder & Zelasko (1963) (*left*) and its modification by Duncan & Chang (1970) (*right*).

simulate a logarithmic compression behavior, as observed for soft clays, the power should be taken equal to 1.0 (Brinkgreve *et al.* 2011a). For example for Norwegian sands and silts, Janbu (1963) reports values of m around 0.5. In the present study it was used a value of $m = 0.7$ for the considered homogeneous ground. In the HS model E_{50} is used instead of the initial modulus E_i for small strains (see Eq. 3.1). The reason for this is that E_i as a tangent modulus is much more difficult to be determined experimentally. However, E_i is an internal model parameter which is recalculated from Equation 3.2. The secant modulus E_{50}^{ref} is determined from triaxial stress-strain curve for a mobilization of the maximum shear strength q_f as shown in Figure 3.7, right.

3.1.3.2.1.2. Stiffness for Un- / Reloading

In contrast to E_{50}, explaining the magnitude of both the elastic and the plastic strains, E_{ur} is a true elasticity modulus for unloading and reloading paths. It is also stress-level dependent and it is defined as:

$$E_{ur} = E_{ur}^{ref} \left(\frac{c \, \cos \varphi - \sigma_3' \sin \varphi}{c \, \cos \varphi + p^{ref} \sin \varphi} \right)^m \tag{3.5}$$

where E_{ur}^{ref} is the reference Young's modulus for unloading and reloading, corresponding to the reference pressure $p^{ref}(p^{ref} = -\sigma_3'$, a reference minor principal effective stress). In this way the un-/reloading stress path is modelled as purely (nonlinear) elastic relation by combining Equations 3.5 and 3.6, and a constant value for un-/reloading Poisson's ratio ν_{ur}.

$$G_{ur}^{ref} = \frac{1}{2(1 + \nu_{ur})} \, E_{ur}^{ref} \tag{3.6}$$

For drained triaxial test stress paths with $\sigma_2' = \sigma_3' = const$, the elastic Young's modulus E_{ur} remains constant and the elastic strains are given by the equations:

$$-\varepsilon_1^e = \frac{q}{E_{ur}}, \qquad -\varepsilon_2^e = -\varepsilon_3^e = -\nu_{ur}\frac{q}{E_{ur}} \tag{3.7}$$

Here it should be realized that restriction is made to strains that develop during deviatoric loading, whilst the strains that develop during the very first stage (i.e. isotropic compression with $\sigma_1' = \sigma_2' = \sigma_3'$) of the test are not considered. For the first stage of isotropic compression (with consolidation), the HS model predicts fully elastic volume changes according to Hooke's law.

3.1.3.2.1.3. Shear Yield Surface, Failure Condition, Hardening Law

The extension of the nonlinear elastic Duncan-Chang soil model (Duncan & Chang 1970) to an elasto-plastic formulation was proposed by Schanz (1998), respectively Schanz *et al.* (1999) with an introduction of the following shear hardening yield function for the standard drained triaxial case:

$$f_s = \bar{f} - \gamma^p \tag{3.8}$$

where $\bar{f}$ is a function of stress:

$$\bar{f} = \frac{2}{E_i}\frac{q}{1 - \frac{q}{q_a}} - \frac{2q}{E_{ur}} \tag{3.9}$$

and γ^p is an internal material variable (strain-hardening parameter) and is a function of plastic strains:

$$\gamma^p = -\varepsilon_1^p - (-\varepsilon_2^p - \varepsilon_3^p) = -(2\varepsilon_1^p - \varepsilon_v^p) \approx -2\varepsilon_1^p \tag{3.10}$$

Of course in a case of triaxial compression or triaxial extension states of stress there are two yield functions (and two plastic potential functions, as will be described latter), so that from Equations 3.8 and 3.9 it follows:

$$f_{s,12} = \frac{2}{E_i}\frac{(\sigma_1' - \sigma_2')}{1 - \frac{(\sigma_1'-\sigma_2')}{q_a}} - \frac{2(\sigma_1' - \sigma_2')}{E_{ur}} \tag{3.11}$$

$$f_{s,13} = \frac{2}{E_i}\frac{(\sigma_1' - \sigma_3')}{1 - \frac{(\sigma_1'-\sigma_3')}{q_a}} - \frac{2(\sigma_1' - \sigma_3')}{E_{ur}} \tag{3.12}$$

In reality, plastic volumetric strains ε_v^p will never be precisely equal to zero, but for hard soils plastic volume changes tend to be small when compared with the axial strain, so that the approximation ($\varepsilon_v^p \approx 0$) in Equation 3.10 is generally acceptable.

An essential feature of the above definition for $\bar{f}$ (i.e. Eq. 3.9) is that it matches the hyperbolic law according to Equation 3.1. When considering primary loading, as this implies the yield condition $f_s = 0$ it follows $\gamma^p = \bar{f}$ and further the plastic strains are:

$$-\varepsilon_1^p \approx \frac{1}{2}\bar{f} = \frac{1}{E_i}\frac{q}{1-\frac{q}{q_a}} - \frac{q}{E_{ur}} \tag{3.13}$$

For the deviatoric loading stage of the triaxial test, the total axial strains are the sum of the elastic component (Eq. 3.7) and the plastic component (Eq. 3.13):

$$-\varepsilon_1 = (-\varepsilon_1^e) + (-\varepsilon_1^p) \approx \underbrace{\frac{1}{E_i}\frac{q}{1-\frac{q}{q_a}}}_{\text{Eq. 3.1}} \tag{3.14}$$

For a given constant value of the hardening parameter γ^p, the yield condition $f_s = 0$ can be visualized in $p' - q$-plane by means of yield locus. When plotting such yield loci, one has to use Equations 3.9 and 3.10, as well as Equations 3.4 and 3.5 for E_{50} and E_{ur} respectively. Because of the later expressions, the shape of these yield loci depends on the exponent m. For values of $m = 1$ straight lines are obtained, however slightly curved yield loci corresponds to lower values of the exponent. Figure 3.8 shows the shape of successive yield loci for increasing values of γ^p considering $m = 0.5$, being typical for hard soils (e.g. dense sand).
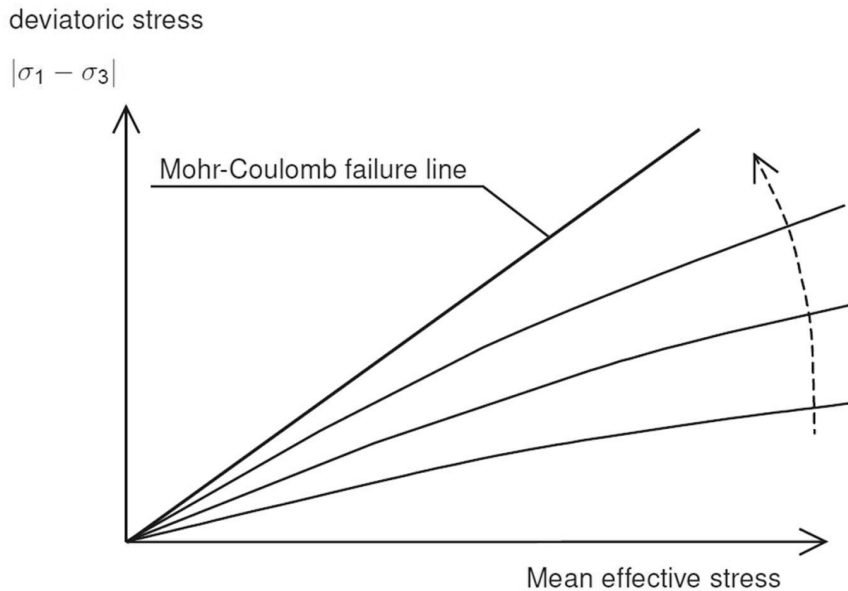
Figure 3.8.: Successive yield loci for various constant values of the shear-hardening parameter γ^p and considering the exponent of the power low $m = 0.5$ (Brinkgreve 2011a).

3.1.3.2.1.4. Flow Rule, Plastic Potential Functions

The HS model also involves a relationship between rates of plastic strain, i.e. relationship between the plastic volumetric strain $\dot{\varepsilon}_v^p$ and the plastic shear strain $\dot{\gamma}^p$. This shear hardening flow rule has the linear form:

$$\dot{\varepsilon}_v^p = \sin \psi_m \, \dot{\gamma}^p \qquad (3.15)$$

The angle of mobilized dilatancy ψ_m in Equation 3.15 can for example be calculated according to the well-known Rowe's stress dilatancy theory (Rowe 1962, Rowe 1971). A main drawback of Rowe's approach, is the highly contractive behavior at low mobilized friction angles φ_m. Therefore, the mobilized dilatancy angle (i.e $\sin \psi_m$) is set to be greater or equal to zero (see Eq. 3.16) overriding Rowe's original equation. With some additional considerations ψ_m in the HS model is defined as follows:

$$\begin{array}{llll}
\text{For} & \sin \varphi_m < \frac{3}{4} \sin \varphi : & & \psi_m = 0 \\[4pt]
\text{For} & \sin \varphi_m \geq \frac{3}{4} \sin \varphi & \text{and} \quad \psi > 0 : & \sin \psi_m = \max \left(\frac{\sin \varphi_m - \sin \varphi_{cv}}{1 - \sin \varphi_m \sin \varphi_{cv}} \right) \\[4pt]
\text{For} & \sin \varphi_m \geq \frac{3}{4} \sin \varphi & \text{and} \quad \psi \leq 0 : & \psi_m = \psi \\[4pt]
\text{If} & \psi = 0 : & & \psi_m = 0
\end{array} \qquad (3.16)$$

where φ_{cv} is the critical state friction angle (or ultimate friction angle; represents a condition of shearing at constant volume), being a material constant independent of the soil density (Schanz & Vermeer 1996), and the mobilized friction angle is:

$$\sin \varphi_m = \frac{\sigma_1' - \sigma_3'}{\sigma_1' + \sigma_3' - 2c \, \cot \varphi} \qquad (3.17)$$

The above equations are a small enhancement of the Rowe's theory, as explained by Schanz & Vermeer (1996). The mobilized dilatancy angle ψ_m, follows the Rowe's theory, for larger values of the mobilized friction angle φ_m, as long as this results in a positive value of ψ_m. For small mobilized friction angles and for negative values of ψ_m, as computed by Rowe's formula (as long as the dilatancy angle ψ is positive), ψ_m is taken zero. In all cases when $\varphi = 0$, ψ_m is set equal to zero.

The essential property of the stress-dilatincy theory is that the material (i.e. the soil) contracts for small stress ratios $\varphi_m < \varphi_{cv}$, whilst dilatancy occurs for high stress ratios $\varphi_m > \varphi_{cv}$. At failure, when the mobilized friction angle equals the failure angle φ (or peak friction angle), it is found from Rowe's formula (Eq. 3.16) that:

$$\sin \psi = \frac{\sin \varphi - \sin \varphi_{cv}}{1 - \sin \varphi \, \sin \varphi_{cv}} \qquad (3.18)$$

or equivalently:

$$\sin \varphi_{cv} = \frac{\sin \varphi - \sin \psi}{1 - \sin \varphi \, \sin \psi} \tag{3.19}$$

Hence, the critical state angle φ_{cv} can be computed from the failure angles φ and ψ according to

$$\varphi_{cv} = \varphi - \psi. \tag{3.20}$$

In Plaxis this computation (of Eq. 3.20) is performed automatically, needed are only the direct input parameters φ (peak friction angle) and ψ (ultimate dilatancy angle).

The above definition of the flow rule (Eq. 3.15) is equivalent to the definition of the plastic potential functions $g_{s,12}$ and $g_{s,13}$ according to:

$$g_{s,12} = \frac{(\sigma_1' - \sigma_2')}{2} - \frac{(\sigma_1' + \sigma_2')}{2} \sin \psi_m \tag{3.21}$$

$$g_{s,13} = \frac{(\sigma_1' - \sigma_3')}{2} - \frac{(\sigma_1' + \sigma_3')}{2} \sin \psi_m \tag{3.22}$$

These type of plastic potentials for the shear yield surfaces are non-associated, i.e. $g_s \neq f_s$. Using the *Koiter-rule* (Koiter 1960) for yielding depending on two yield surfaces (*Multi-surface plasticity*) one finds:

$$\dot{\varepsilon}^p = \lambda_{12} \frac{\partial g_s, 12}{\partial \sigma} + \lambda_{13} \frac{\partial g_s, 13}{\partial \sigma} = \lambda_{12} \begin{bmatrix} 1/2 - 1/2 \, \sin \psi \\ -1/2 - 1/2 \, \sin \psi \\ 0 \end{bmatrix} + \lambda_{13} \begin{bmatrix} 1/2 - 1/2 \, \sin \psi \\ 0 \\ -1/2 - 1/2 \, \sin \psi \end{bmatrix} \tag{3.23}$$

with λ_{12} and λ_{13} nonnegative plastic multipliers. Calculating the different plastic strain rates by the above equation, Equation 3.15 directly follows.

3.1.3.2.2. Cap Yield Surface

Shear yield surfaces as indicated in Figure 3.8 do not describe the plastic volumetric strain that is measured in isotropic compression. Therefore a second type of yield surface – the cap yield surface – is introduced to close the elastic region in the direction of the horizontal p'-axis (p' – mean effective stress, Eq. 3.26). For this it is defined a second modulus for primary loading – the oedometer modulus E_{oed} defined by the equation:

$$E_{oed} = E_{oed}^{ref} \left(\frac{c \, \cos \varphi - \frac{\sigma_3'}{K_0^{nc}} \, \sin \varphi}{c \, \cos \varphi + p^{ref} \, \sin \varphi} \right)^m. \tag{3.24}$$

Hence, E_{oed}^{ref} is a tangent stiffness at a vertical stress in the Oedometer of $-\sigma_1' = \frac{-\sigma_3'}{K_0^{nc}} = p^{ref}$.

The triaxial modulus E_{50} largely controls the shear yield surface, while the oedometer modulus E_{oed} controls the cap yield surface. In fact, E_{50} largely controls the magnitude of the plastic strains γ_s that are associated with the shear yield surface. Similarly, E_{oed} is used the control the magnitude of the plastic volumetric strains ε_v^{pc} that originate from the yield cap (plastic volumetric cap strains). The cap-type yield function (ellipse) has the formulation:

$$f_c = \frac{\widetilde{q}^2}{\alpha^2} + p'^2 - p_p^2,$$ (3.25)

where α is an auxiliary model parameter that relates to K_0^{nc} as will be discussed later. Additionally

$$p' = \frac{\sigma_1' + \sigma_2' + \sigma_3'}{3},$$ (3.26)

and

$$\widetilde{q} = \sigma_1' + (\delta - 1)\sigma_2' - \delta\sigma_3',$$ (3.27)

with

$$\delta = \frac{3 + \sin\varphi}{3 - \sin\varphi}.$$ (3.28)

The parameter $\widetilde{q}$ is a special stress measure for deviatoric stresses. In the case of triaxial compression $(-\sigma_1' > -\sigma_2' = -\sigma_3')$ it yields to $\widetilde{q} = -(\sigma_1' - \sigma_3')$ and for triaxial extension $(-\sigma_1' = -\sigma_2' > -\sigma_3')$ it reduces to $\widetilde{q} = -\delta(\sigma_1' - \sigma_3')$. For yielding on the cap surface it is used an associated flow rule $(g_c = f_c)$.

The magnitude of the yield cap (see Fig. 3.9) is determined by the isotropic preconsolidation stress p_p, which is the maximum equivalent isotropic stress level p_{eq} that a stress point has experienced up to the current moment, i.e. load step.
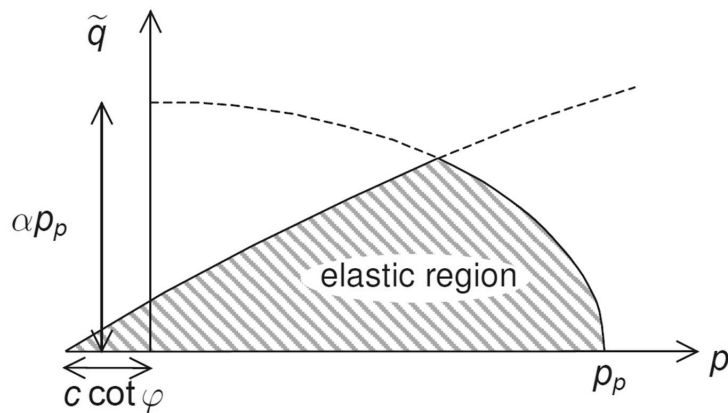
Figure 3.9.: Yield surfaces of the HS model in $p - \widetilde{q}$-plane (Brinkgreve 2011a).

This equivalent isotropic stress p_{eq} is defined as the intersection point between the stress contour (with similar shape as the yield contour) through the current stress point and the isotropic stress p-axis and is given by the equation:

$$p_{eq} = \sqrt{p^2 + \frac{\widetilde{q}^2}{\alpha^2}}, \tag{3.29}$$

with p mean total stress.

The hardening law relating p_p to volumetric cap strain ε_v^{pc} is:

$$\varepsilon_v^{pc} = \frac{\beta}{1-m} \left(\frac{p_p}{p^{ref}} \right)^{1-m}. \tag{3.30}$$

The volumetric cap strain is the plastic volumetric strain in isotropic compression. The additional model parameters α and β in Equations 3.29 and 3.30 are internal cap parameters, and there is a relationship of the form:

$$\alpha \leftrightarrow K_0^{nc}$$
$$\beta \leftrightarrow E_{oed}^{ref}$$

such that K_0^{nc} and E_{oed}^{ref} are used as direct input parameters that determine the magnitude of α and β respectively. The shape of the yield cap is given by an ellipse in $p - \widetilde{q}$-plane, as indicated in Figure 3.9. The main difference with the cam-clay type soil constitutive models, as implemented in Plaxis, is that for HS model, the ellipse is around the origin of the axes (Fig. 3.9). The ellipse has length p_p on the p-axis and $\alpha\, p_p$ on the $\widetilde{q}$-axis. Hence p_p determines its magnitude and α its aspect ratio. High values of α lead to steep caps underneath the Mohr-Coulomb failure line, whereas small α-values define caps that are much more pointed around the p-axis. The ellipse is used both as a yield surface and as a plastic potential, so that:

$$\varepsilon^{\dot{p}c} = \lambda \frac{\partial f_c}{\partial \sigma} \quad \text{with:} \quad \lambda = \frac{\beta}{2p'} \left(\frac{p_p}{p^{ref}} \right)^m. \tag{3.31}$$

Input data on initial p_p-values is provided by means of the procedure for initial stress generation by the FE-code (see the used K_0-procedure described in Section 3.1.2.2).

The total yield contours of the HS model in principal stress space for cohesionless soil are represented in Figure 3.10.
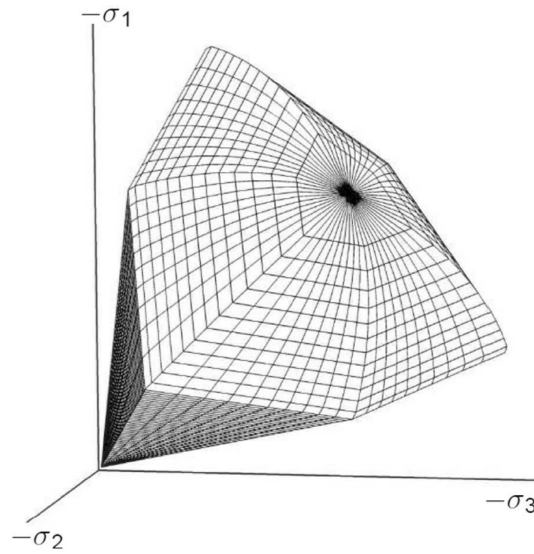
Figure 3.10.: Representation of total yield contours of the HS model in principal stress space for cohesionless soil (Brinkgreve 2011a).

3.1.3.2.3. Parameters of the HS model

In the initial calculation phase for generating the initial soil conditions there are used the unit weight of the soil $\gamma_{unsat/sat}$, and also the value of K_0^{nc} (see Section 3.1.2.2) regardless of what type of soil constitutive model it will be used after that in the subsequent calculations. If the soil is overconsolidated additionally it is needed the value of the overconsolidation ratio (OCR) or equivalent the value of the preoverburden pressure (POP) (see Brinkgreve *et al.* 2011b, Chapter 2.8 The Initial Pre-Consolidation Stress in Advanced Models).

Finally the direct user input parameters of the HS model are:

ν_{ur}	Poisson's ratio for unloading-reloading	[-]
φ	Peak angle of internal friction (effective; for brevity $\varphi = \varphi'$)	[°]
ψ	Angle of dilatancy	[°]
c	Cohesion (effective; for brevity $c = c'$)	[kN/m²]
E_{50}^{ref}	Secant stiffness in standard drained triaxial test	[kN/m²]
E_{oed}^{ref}	Tangent stiffness for primary oedometer loading	[kN/m²]
E_{ur}^{ref}	Unloading / reloading stiffness	[kN/m²]

K_0^{nc}	Coefficient of lateral earth pressure at rest for nor-mally consolidated soil	[-]
m	Power for stress-level dependency of stiffness	[-]
p^{ref}	Reference stress for stiffnesses	[kN/m²]
R_f	Failure ratio q_f/q_a	[-]

In Plaxis E_{ur}^{ref} is not used directly in the calculations, it is first recalculated to G_{ur}^{ref} according to Equation 3.6 by using the value of ν_{ur}. Furthermore E_{50}^{ref} is also not used directly and it is recalculated to E_i^{ref} by using the relationship of Equation 3.2 with the value of R_f. In the HS model there exist also another internal parameters which are not quantified as results of standard triaxial and oedometer test directly and hence, are not expected to be entered by the user. Such additional internal model parameters are α and β as already introduced. In double hardening situation, i.e both yield loci are hardened simultaneously, analytical back calculation of internal model parameters generally is not possible. Therefore, these internal parameters are solved for an iterative scheme so that the HS model simulates the user input E_{50}^{ref} in a triaxial element test and both, E_{oed}^{ref} and K_0^{nc} in an oedometer element test, to within a tolerated error (Benz *et al.* (2008); Personal communication with Dr. Paul Bonnier from Plaxis B.V.).

3.1.3.3. The Hardening Soil Model with Small-Strain Stiffness

The HSsmall model is an extension of the HS model. In fact, all the model features described for the HS model are also included in the HSsmall model (see Brinkgreve *et al.* 2011a, Benz 2007, Benz *et al.* 2009). Additionally to the HS model, the HSsmall model incorporates a formulation of the small-strain stiffness. Many authors have investigated the bahaviour of soils using high precision laboratory tests, e.g. for granular materials Viggiani & Atkinson (1995); for clays Burland (1989), Houlsby & Wroth (1991), Atkinson & Sallfors (1991). They obtained a reversible elastic behaviour and higher stiffness for strains less then 1×10^{-5} and showed that the shear modulus was nearly constant under very small-strains (see additionally Clayton 2011). This effect is called a small-strain stiffness, and it is believed to be a fundamental property of all types of geotechnical materials including clays, silts, sands, gravels, and rocks (Tatsuoka *et al.* 2001) under static and dynamic loading (Burland 1989) and for drained and undrained loading conditions (Lo Presti *et al.* 1996).
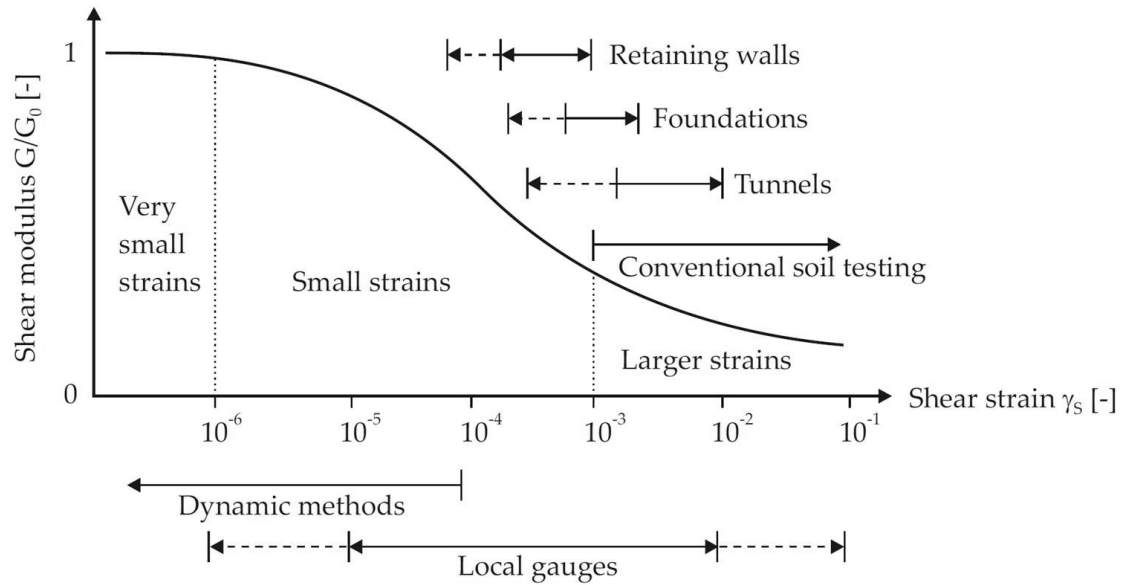
Figure 3.11.: Characteristic strain-stiffness behaviour of soil with typical strain ranges for laboratory tests and structures (after Atkinson & Sallfors 1991, and Mair 1993).

As shown in Figure 3.11, for strain levels larger than 1×10^{-5} a rapid drop of small-strain stiffness is measured, i.e. degradation of the shear modulus of the soil G. Therefore, considering a constant modulus at higher strain levels would not be an appropriate approximation for detailed analyses of the shape and magnitude of settlements due to an excavation process like tunnelling. Also the soil stiffness that should be used in the analysis of geotechnical structures – including also tunnels – is not the one that relates to the strain range at the end of construction according to Figure 3.11. Instead, very small-strain soil stiffness and its nonlinear dependency on strain amplitude have to be properly taken into account. To do this, using the ideas proposed by Hardin & Drnevich (1972) the HS model is extended with the relatively simple expression for the small strain stiffness decay of the shear modulus, similar to the one suggested by Santos & Correia (2001):

$$\frac{G_s}{G_0} = \frac{1}{1 + a \left| \dfrac{\gamma}{\gamma_{0.7}} \right|} \qquad \text{with} \qquad a = 0.385 \qquad (3.32)$$

where G_s is the actual shear modulus (secant shear modulus) at shear strain γ, G_0 is the initial shear modulus (or sometimes written as $G_{\max}$ or G_{dyn}, the subscript staying for maximum, respectively for dynamic modulus), $\gamma_{0.7}$ is the shear strain at which the secant shear modulus G_s is reduced to about 70 % of its initial value G_0. In fact, using $a = 0.385$ and $\gamma = \gamma_{0.7}$ gives $G_s/G_0 = 0.722$. Hence, the formulation "about 70 %" should be interpreted more accurately as 72.2 %.

Concluding, only two additional input parameters, to these needed for the HS model, are required to control the stress and strain history dependent stiffness of the HSsmall model. These are the initial shear modulus G_0^{ref} defined for the reference pressure p^{ref} and the shear strain $\gamma_{0.7}$. Like the stress dependent moduli of the HS model the actual shear modulus G_0 is calculated from:

$$G_0 = G_0^{ref} \left(\frac{c \cos \varphi - \sigma_3' \sin \varphi}{c \cos \varphi + p^{ref} \sin \varphi} \right)^m ,$$ (3.33)

where m was the power law exponent that scales also the other stiffness parameters of the HS model. The threshold shear strain $\gamma_{0.7}$ is taken independent of mean stress.

Figure 3.11 shows the stiffness degradation curve, reaching far into the plastic material behaviour at large engineering strains. In the HS and the HSsmall model, stiffness degradation due to plastic straining is simulated with strain hardening. Therefore, before reaching plastic material behaviour, the small-strain stiffness reduction curve in the HSsmall model is cut-off at shear strain $\gamma_{cut-off}$ (see in Fig. 3.12) where the tangent stiffness modulus G_t is reduced to the unloading/reloading stiffness G_{ur}. The unloading/reloading stiffness G_{ur} relates to the HS model parameter E_{ur} as follows:

$$G_{ur} = \left(\frac{E_{ur}}{2 \left(1 + \nu_{ur} \right)} \right) .$$ (3.34)
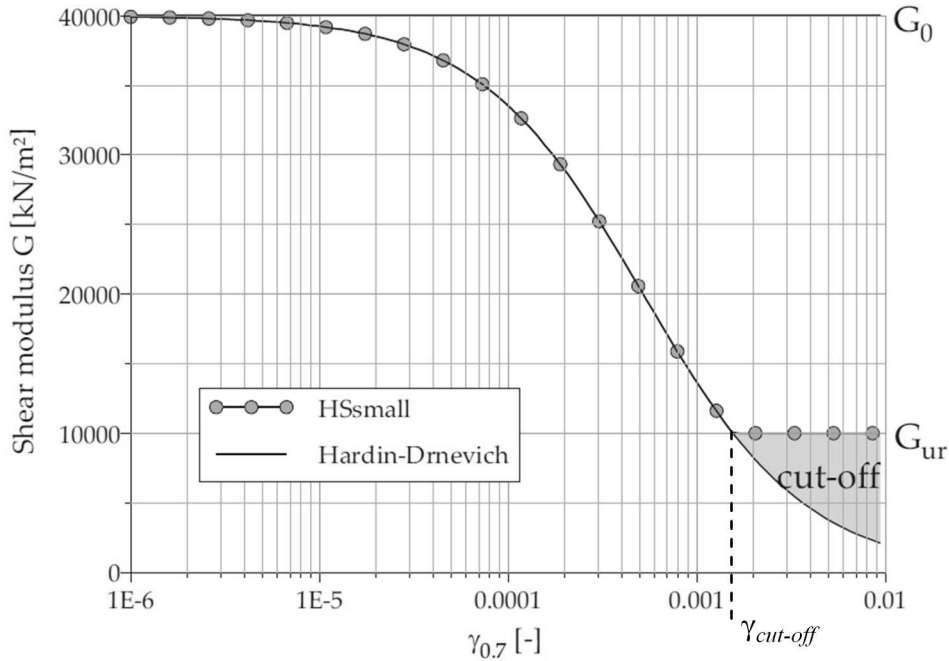
Figure 3.12.: Cut-off of the small-strain degradation curve as used in the HSsmall model (acc. to Benz 2007).
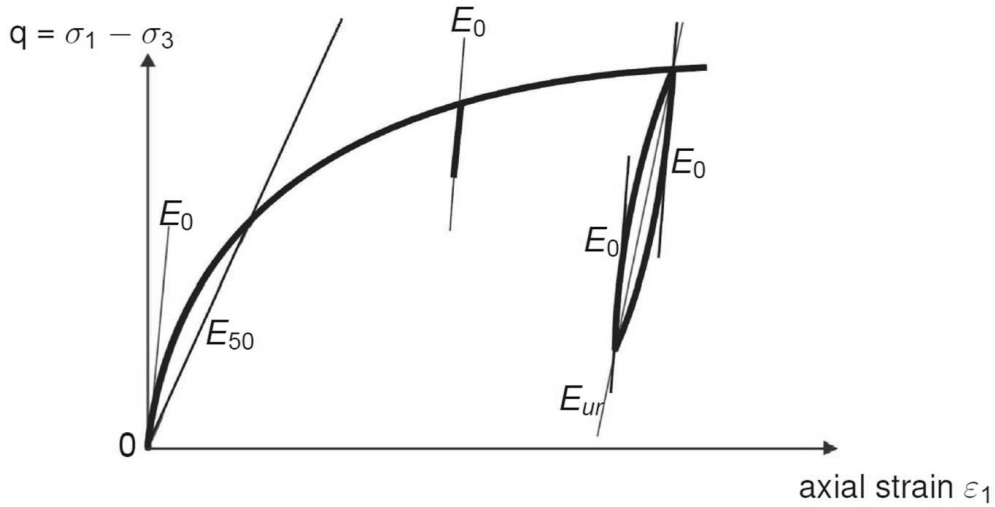
Figure 3.13.: Stiffness parameters E_{50}, E_{ur}, and $E_0 = 2G_0(1 + \nu_{ur})$ of the HSsmall model in a triaxial test (Brinkgreve 2011a).

The elastic constants E_{ur} and ν_{ur} have already been introduced above in the description of the HS model. The shear strain $\gamma_{cut-off}$ can be calculated as:

$$\gamma_{cut-off} = \frac{1}{0.385} \left(\sqrt{\frac{G_0}{G_{ur}}} - 1 \right) \gamma_{0.7}. \tag{3.35}$$

Figure 3.13 illustrates the model's stiffness parameters E_{50}, E_{ur}, and $E_0 = 2G_0(1 + \nu_{ur})$ in a triaxial test.

The same limitations as for the HS model are also valid for the HSsmall model – no softening due to soil dilatancy, nor destructuration (de-bonding), nor creep are taken into account.

3.1.3.4. Calibration of the Models in Simulation of Standard Laboratory Tests

In Table 3.2 there are given the input parameters for the used three soil constitutive models: the Mohr-Coulomb model (MC), the Hardening Soil model (HS), and the Hardening Soil model with small-strain stiffness (HSsmall), for simulation of dense soil material (see Section 3.1.4). In the next Table 3.3 there are given additionally the input parameters of the HS model used for simulation of loose soil material – Material 2 (see Section 3.1.4).

At the beginning, the three soil models, i.e. their stiffness modules are calibrated in a simulation of Oedometer and standard Triaxial test (consolidated drained), as shown in Figure 3.14, respectively in Figure 3.15. The question by the simple MC model is which

Table 3.2.: Parameters of the used three soil constitutive models: the Mohr-Coulomb model (MC), the Hardening Soil model (HS), and the Hardening Soil model with small-strain stiffness (HSsmall) (for simulation of dense soil material; see Section 3.1.4).

Parameters	MC	HS	HS-small	
φ	35.0	35.0	35.0	[°]
ψ	5.0	5.0	5.0	[°]
c	10.0	10.0	10.0	[kN/m^2]
E'	100 000	–	–	[kN/m^2]
E_{50}^{ref}	–	35 000	35 000	[kN/m^2]
E_{oed}^{ref}	–	35 000	35 000	[kN/m^2]
E_{ur}^{ref}	–	100 000	100 000	[kN/m^2]
G_0^{ref}	–	–	130 000	[kN/m^2]
$\gamma_{0.7}$	–	–	0.00015	[-]
p^{ref}	–	100	100	[kN/m^2]
m	–	0.7	0.7	[-]
R_f	–	0.90	0.90	[-]
ν	0.30	–	–	[-]
ν_{ur}	–	0.20	0.20	[-]
$\gamma_{\texttt{unsat}}$	17.0	17.0	17.0	[kN/m^3]
$\gamma_{\texttt{sat}}$	20.0	20.0	20.0	[kN/m^3]
$K_0^{nc} = 1 - \sin\varphi$	0.426	0.426	0.426	[-]
OCR	1.0	1.0	1.0	[-]
$R_{\texttt{inter}}$	0.60	0.60	0.60	[-]

stress path has to follow – the primary loading or the unloading, as shown in Figure 3.14, because the MC model doesn't distinguish between loading and unloading stress paths. Thereafter, it was decided for the MC model to use further in the calculations an E-modulus equal to the $E_{ur}^{ref} = 100\,000$ kN/m^2, because the tunnelling is an excavation problem which is dominated by unloading due to the removing of the soil from the tunnel. In both Figures 3.14 and 3.15 it is shown at the very beginning of the primary loading the effect of the higher small-strain stiffness; this effect is also present at the unloading/reloading stress paths.

Table 3.3.: Input parameters of the HS model used for simulation of loose soil material – Material 2 (see Section 3.1.4).

Parameter	Value	Unit
φ	30.0	[°]
ψ	0	[°]
c	1.0	[kN/m²]
E_{50}^{ref}	15 000	[kN/m²]
E_{oed}^{ref}	15 000	[kN/m²]
E_{ur}^{ref}	50 000	[kN/m²]
p^{ref}	100	[kN/m²]
m	0.70	[-]
R_f	0.90	[-]
ν_{ur}	0.20	[-]
γ_{unsat}	17.0	[kN/m³]
γ_{sat}	20.0	[kN/m³]
$K_0^{nc} = 1 - \sin\varphi$	0.500	[-]
OCR	1.0	[-]
R_{inter}	0.60	[-]

3.1.4. Dense / Loose Subsoil Conditions

It is investigated the influence of tunnelling in a dense (good subsoil conditions; see Table 3.2), and in a loose (poor subsoil conditions; see Table 3.3) subsoil material. For this calculations it is used the HS model.

3.1.5. Soil-Tunnel Interaction

3.1.5.1. Interaction Between the Soil and the Tunnel (TBM and Tunnel Lining)

The contact between the steel shield skin of the TBM and the surrounding subsoil is determined by the load-deformation behaviour of the soil and the TBM (Nagel 2010), and also by the geometry of the TBM – overcuting and tapering (see further Section 3.1.6). The overcuting and the conical shape of the TBM results geometrically in an initial gap between the undeformed subsoil and the shield, which is called the steering gap. Thus, the soil surrounding the TBM can deform until it gets, at least partly, into frictional contact with the TBM steel skin. The deformation of soil into the steering gap may be influenced
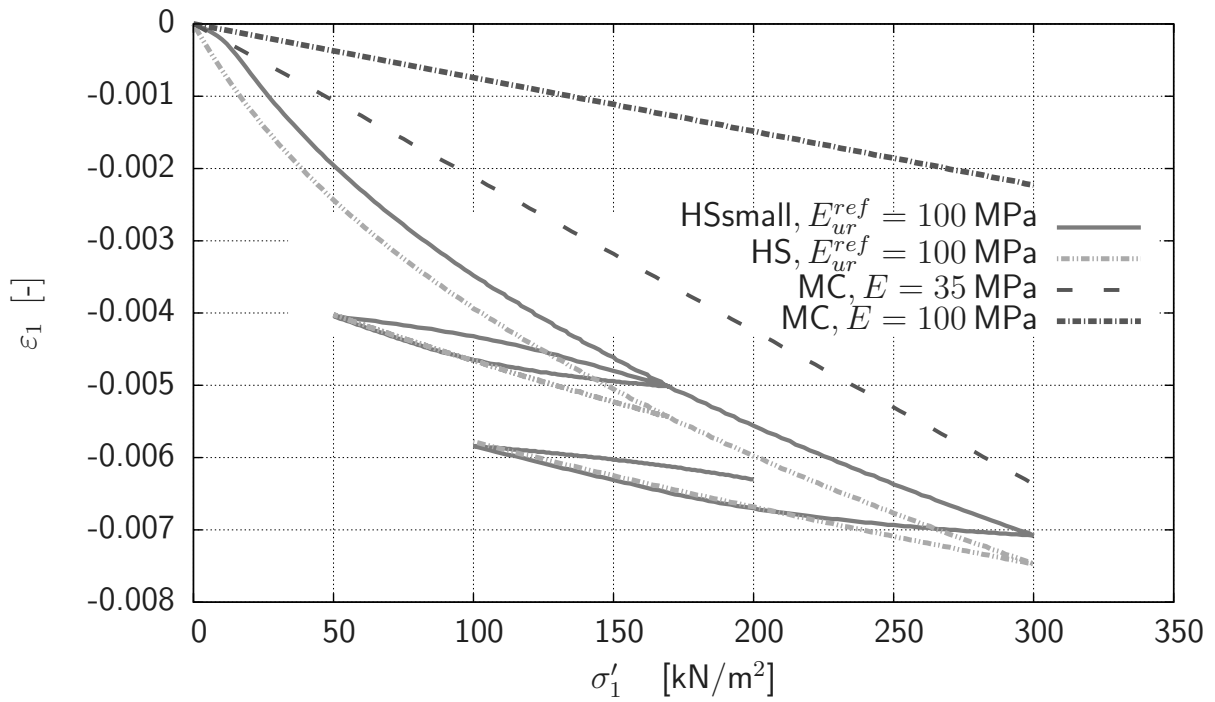
Figure 3.14.: Calibration of MC to HS to HSsmall model in a simulation of Oedometer test
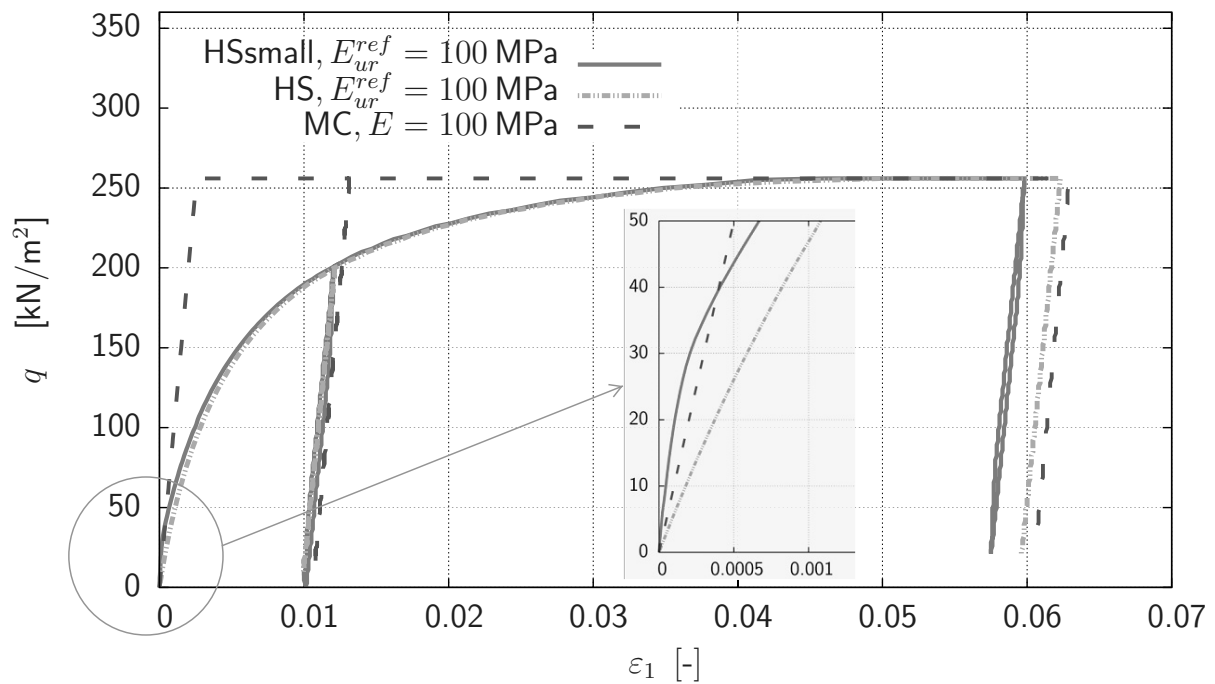
Figure 3.15.: Calibration MC to HS to HSsmall model in a Drained Triaxial test (cell pressure $\sigma'_3 = 80$ kN/m²)

by the presence of pressurised fluids (e.g. coming from the face support and/or fresh grout mortar) filling the space between TBM and soil (Bezuijen 2007, Bezuijen 2009). The pressure of such fluid film in-between may reduce additionally the frictional contact at that place.

3.1.5.2. Mapping in the Numerical Simulation

The contact between the shield skin (plate elements in the FE-model) with the surrounding ground (soil volume elements), and between the tunnel lining (plate elements in the FE-model) and the ground is simulated via reducing with 40 % the shear strength of the soil at this contact zone. This value is assumed as realistically for a pure contact between steel (i.e. the TBM shield skin) and soil in that case. To simulate the soil-structure interaction special joint elements called in PLAXIS interfaces are applied to the plate elements on their side in contact with the soil. The frictional contact is based on Mohr-Coulomb friction, by which the relative displacements between the shield skin and the soil, and the resulting shear stresses in the soil are taken into account. By this the roughness of the interaction is modelled by chosing a suitable value for the strength reduction factor $R_{\mathtt{inter}}$. This factor relates the interface strength (i.e. steel skin friction and adhesion) to the soil strength (friction angle φ and cohesion c). It is assumed $R_{\mathtt{inter}} = 0.6$ which corresponds to 40 % reduction of the shear strength as explained above (see also in Table 3.2 and 3.3).

Additionally, it is investigated the influence of the contact properties by their variation. Particularly, it is investigated the reduction of the stiffness and the strength in the interfaces. For doing this it is assigned a linear elastic perfectly-plastic model, with a Mohr-Coulomb yield surface (the MC model as already described before in Section 3.1.3.1) to these interfaces with parameters for interface stiffness $E' = 100\,000$ kN/m^2 and $\nu = 0.3$, and for interface strength $\varphi = 35.0°$, $\psi = 5.0°$ and $c = 10$ kN/m^2; $R_{\mathtt{inter}}$ is set to 1.0, i.e. no additional strength reduction in that case. Further, there are reduced subsequently one after another the E-modulus and the value of the angle of internal friction φ.

3.1.6. Steering Gap

Due to engineering restrictions, the diameter of the cutterhead (see (1) in Fig. 3.1) has to be few cm larger (usual value of 6-8 cm, or even smaller) than the shield at front of the TBM. This is called overcutting and it is necessary to prevent the boring machine to get stuck during the excavation. Additionally, the shield of the TBM is slightly tapered

(conical), i.e. the shield diameter at the front is larger than at the shield tail. This difference is relatively small, normally around 0.4 % of the TBM diameter (Bezuijen 2007), as also assumed in the present study. In this way geometrically between the TBM and the subsoil the steering gap originates. This is necessary to allow the TBM to maneuver in the subsoil, to reduce the hydraulic jack forces and to minimize the wear of the shield skin.

3.1.6.1. Bentonite and Grout Flow Around the TBM

According to Bezuijen (2007) not only the annular gap (will be described later in Section 3.1.7), but also the steering gap between the shield and surrounding subsoil may is filled with grouting mortar (flowing from the tail of the TBM), and bentonite suspension (flowing from the front of the TBM). Additionally, the direct injection of a bentonite suspension into the steering gap through nozzles within the shield skin is an effective method to reduce the settlements and to minimize the friction between shield skin and subsoil. In particular if the steering gap becomes wider due to curvature of the alignment such an inflow of the process fluids is very likely to occur (see Sugimoto *et al.* 2006). Finite element calculations (Hoefsloot & Verweij 2005, Kasper & Meschke 2006) have shown that the calculated settlement trough is too deep when it is assumed that the TBM shield is in direct contact with the soil all over the TBM, i.e. when the soil is completely free to move into the steering gap up to the shield skin, because there is no pressurized fluid inbetween. Therefore, it is of main importance to quantifies the amount of contact between the soil and the TBM in order to indicates what volume loss can be expected depending on the face pressure and the grout pressure around the TBM.

3.1.6.2. Mapping in the Numerical Simulation

Within the 3D numerical simulation of a closed face shield supported tunnelling the interaction between the TBM and the surrounding subsoil in the area of the steering gap are commonly modelled via distributed loads on the subsoil (see Möller & Vermeer 2008), or by modelling the TBM as a deformable body connected in a continuous manner to the soil elements (see Komiya *et al.* 1999). However, such model assumptions are relative simple, a more complex contact algorithm is presented in Kasper & Meschke (2004).

Bezuijen (2007) has investigated analytically the flow and the pressure distribution of the support mediums – grout and bentonite – between the shield and the subsoil. As it is there shown the actual size of the steering gap is a function of the flow of the grout and

bentonite around the TBM shield. In the present research there have been investigated only two extreme possible situations – ones the steering gap is assumed to be completely filled with the support mediums – bentonite and grout, i.e. no steering gap or no possibility of the surrounding soil to move into this gap (called here for simplicity "TBM without conicity"), ones it is not filled and the soil is free to move into the gap up to the TBM shield (called "TBM with conicity").

For the variant "TBM with conicity" there are applied surface contractions to the plate elements of the TBM. The applied contraction decrease linearly from 0.05 % at the front of the TBM to 0.50 % at the tail of the TBM over the 9.0 m of the TBM. This corresponds to 0.55 % volume losses at that place.

For the variant "TBM without conicity" no surface contractions are applied, i.e. no volume losses around the TBM are considered, because it is assumed that the steering gap is completely filed with process fluids. This variant is used in all other calculations in the present thesis.

3.1.7. Grouting the Annular Gap

3.1.7.1. Description of the Process

The difference between the external diameter of the TBM and the newly installed tunnel lining causes an annular gap (or tail void) between the soil and the lining at the tail end of the TBM (see Fig. 3.1 and 3.16). This annular gap is larger than the steering gap and is in order of 8 to 20 cm. To prevent a movement of the subsoil into the annular gap, and thus surface settlements, it is filled simultaneously with pressurized grout mortar through nozzles in the shield skin of the TBM (Babendererde 1999), as shown in Figure 3.16. Also the aim of the backfilling of the annular gap is to achieve a stable bedding as also to recover the primary stress state, i.e. the stress state in the surrounding soil before the tunnel excavation. The grouting of the annular gap has not only an effect on the stresses and deformations of the soil but also on the groundwater pressures (Brassinga 2005). The annular gap is backfilled with mortar, which is injected from a reservoir, acting as a buffer, to ensure a constant grouting pressure, independent from the excavation velocity of the TBM.

Additionally, after the grouting mortar takes places in the annular gap there are processes involved like a) bleeding of the grout (i.e. grout consolidation), and b) shrinkage by the hardening of the grout. The grout consolidation is water outflow from the fresh pressurized

grout into the surrounding subsoil, by which the injected fresh grout is hardened and in the same time it looses a volume up to 10 % (see Bezuijen 2002, Bezuijen & Talmon 2003, Bezuijen & Talmon 2004, Bezuijen & van der Zon 2007). Grout consolidation is the dominant mechanism when the tunnel is constructed in a relatively permeable soil (like sand). When the surrounding subsoil is relatively impermeable (like rock or clay) there is no consolidation of the grout, but there are also volume losses of the grout (up to 3 % found by Bezuijen & van der Zon 2007) only due to the hardening process. Usually 30 % more grout than the volume of the annular gap has to be applied (Bezuijen & Talmon 2004) and after applying the grout its volume can be reduced with 5 to 10 % due to bleeding caused by consolidation and shrinkage by the hardening process. Subsequently, to achieve this larger grout volume the grout pressure by the injection must be higher then the sum of the total vertical earth and ground water pressure at the tunnel crown. Bezuijen (2002) has found by performing element tests that there is no penetration of grout material when the surrounding soil is relatively permeable e.g. sand. He has showed that no solid particles from the grout penetrate into the sand, but the pore water and solvable parts of the grout do penetrate. Next, only the grouting itself is modelled in the FE-model without investigations on the volume changes which may occur after the grout is placed, as it will be explained.

3.1.7.2. Mapping in the Numerical Simulation

Three possible variants for modelling the grouting – I, II, III, and one additional IV for comparison reason (presented in Fig. 3.16) – are considered and investigated on the shallow tunnel. In variant I it is applied a non-uniformly distributed load directly to the soil elements by deactivating the plate elements in the same place (see Fig. 3.4 and 3.16) for a length of 1.50 m, after the last plate of the TBM. In variant II there is considered additionally a thin layer of fresh grout (0.15 m thick, for filling the annular gap at that place) modelled as a linear-elastic material ($E = 10$ kN/m^2, $\nu = 0.3$, $\gamma = 17$ kN/m^3) for a length of 1.50 m; in that case the plate (i.e. the tunnel lining) is activated on that place, and a user defined hydrostatic pore pressure is applied to this grout volume. Because the fresh pressurized grout mortar behaves like a liquid the modulus of elasticity E is close to zero, therefore it is assumed a value of 10 kN/m^2 for the simulation. Variant III is the same like variant II, but instead of an user defined pore pressure, there are applied uniformly distributed loads, which acts not only on the soil elements like in variant I, but also on the plate elements at that place. For a comparison it is considered also a IV^{-th} variant, where the grouting pressure, i.e. the annular gap is not modelled – see the last
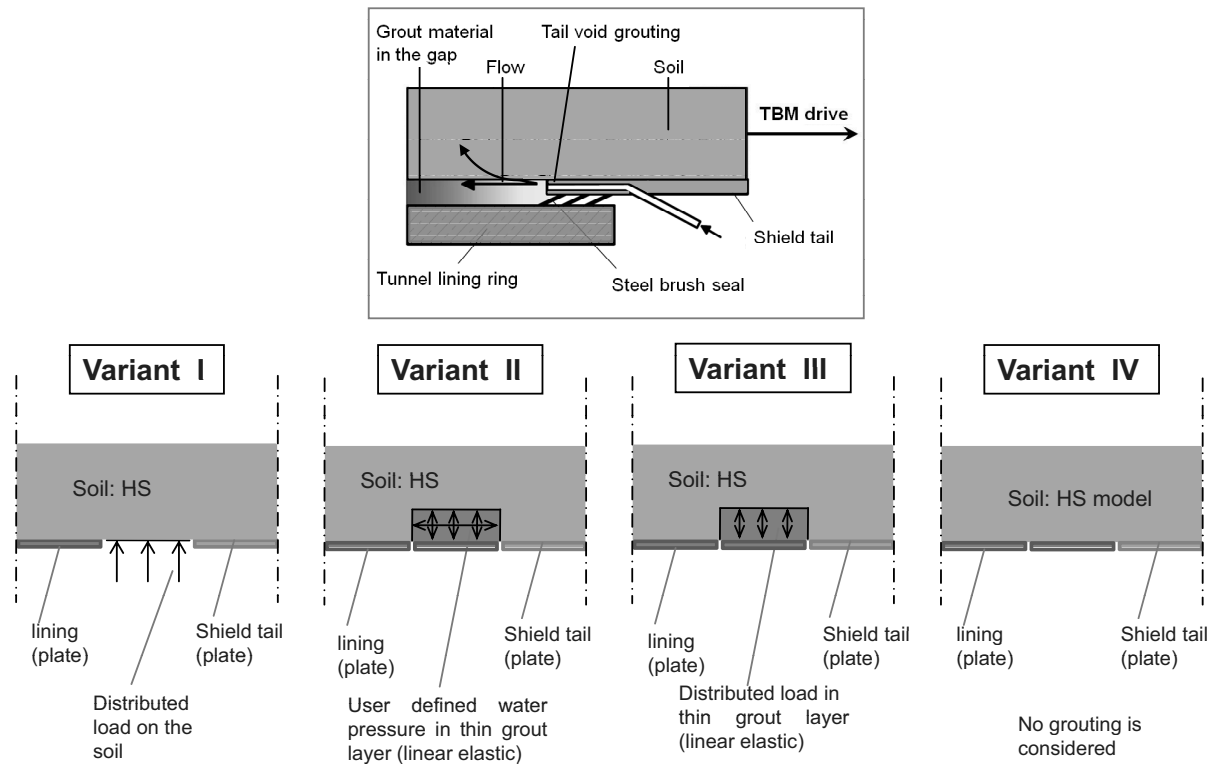
Figure 3.16.: Investigated variants of modelling the grouting of the annular gap in the three-dimensional FE-model.

variant IV in Figure 3.16. In all of the three variants I, II and III the used input values of the applied loads are the same: from 145 kN/m² at the tunnel crown to 230 kN/m² at the tunnel invert in a case of dry subsoil. For all calculations with the deep tunnel it is used only grouting variant I with values of the grouting pressure from 705 kN/m² at the tunnel crown to 790 kN/m² at the tunnel invert in a case of dry subsoil. For the later case of water-saturated subsoil (assumed groundwater table on the surface; see Section 3.5) the grouting pressure is increased to values of 275 kN/m² at the crown to 360 kN/m² at the invert of the shallow tunnel. These values of the grouting pressure are chosen so that there will be a higher (or at least equal) to the sum of the total vertical earth and ground water pressure at the tunnel crown.

3.2. Boundary Conditions of the Numerical Model

3.2.1. Mechanical Boundary Conditions

In the case of a static deformation analysis, prescribed boundary displacements are introduced at the boundaries of the FE-model. Particularly, the vertical and the bottom horizontal boundaries are non-physical (synthetic) boundaries that have been chosen so that they do not actually influence the deformation behaviour of the construction to be modelled. In other words: the boundaries have to be placed enough far away.

The mechanical boundary conditions (boundary displacements conditions) as adopted for the numerical simulation in the present study are illustrated in Figure 3.17. The two vertical model boundaries at the nodes with their normal in X-direction (i.e. the normal coinciding with the excavation X-direction and parallel to the YZ-plane) are fixed in X-direction ($u_x = 0$) and free to displace in Y- and Z-direction. The another two vertical boundaries with their normal in Y-direction (i.e. parallel to the XZ-plane) are fixed in Y-direction ($u_y = 0$) and free to displace in Y- and Z-direction. At all of these four vertical boundaries there are allowed only normal stresses σ' and no shear stresses τ. The model bottom horizontal boundary is fixed in all directions ($u_x = u_y = u_z = 0$). However, normal stresses as well shear stresses may occur on this boundary. The upper horizontal boundary (the ground surface) has no fixities at all and it is free in all directions.

The plate elements of the TBM and the tunnel lining that extend to the two vertical boundaries in the model have two fixed rotations in the nodes at the boundary. At the vertical model boundary (the plane of symmetry) with a normal in Y-direction the rotational fixities are $\phi_x = \phi_z = 0$ ($\phi_y = $ free). This allows bending moments to take place. At the second vertical boundary with a normal in X-direction the rotational fixities are $\phi_y = \phi_z = 0$ ($\phi_x = $ free). At the vertical model edge, where these two boundaries are crossing, the rotation is allowed in all directions with $\phi_x = \phi_y = \phi_z = 0$.

Internal boundaries that arise in the model from the removal (deactivation) of elements – soil volume elements and/or plate elements, are automatically taken in Plaxis to be free (Brinkgreve *et al.* 2011b). However, on such boundary at each excavation stage it is activated either a plate element or a distributed load on the nodes representing the support pressures as a loading conditions.

3.2.2. Hydraulic Boundary Conditions

A consolidation analysis requires additional boundary conditions on excess pore water pressures in the model. Here one may distinguishes between two conditions in the FE-code: *open* – a boundary which is free draining (zero excess pore water pressure), i.e. which is dictated by no change from the generated initial hydrostatic pore water pressure conditions and *closed* – a no flow boundary, i.e the pore water pressures are permitted to change accordingly. The boundary conditions are defined also in Figure 3.17. In the model only the vertical plane of symmetry is closed, while the remaining boundaries are defined as open.

In order to simulate the whole excavated tunnel perimeter as completely impermeable, additionally attention is paid to the internal model hydraulic boundaries that arise from the excavation (deactivation) of the soil volume elements. In order to make them a no flow boundaries, interface elements (which are used as a fully impermeable screen) around the excavated tunnel perimeter have been defined, including also the front of the tunnel where the face support is acting.

3.3. Observation Cross-Sections

For the shallow tunnel it is defined an observation cross-section situated at the 26^{-th} excavation stage, i.e. 39.00 m from the tunnel beginning. This distance is chosen in order that there is no influence from the left vertical model boundary (perpendicular to the excavation direction in X-axis) at the tunnel beginning. Additionally, at that boundary
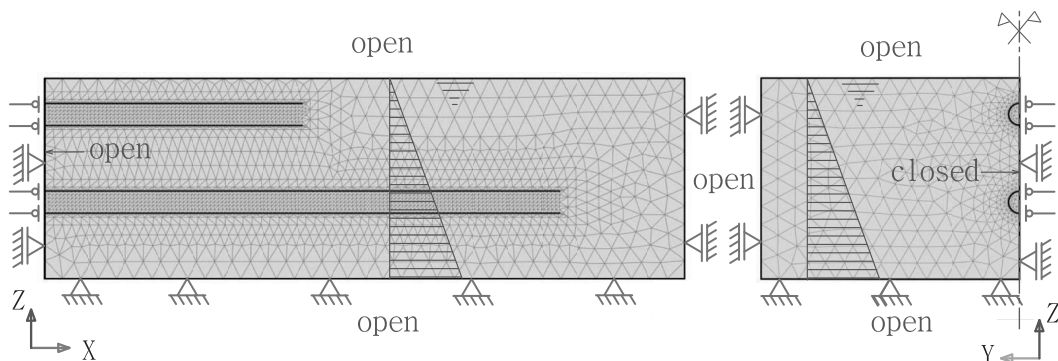
Figure 3.17.: Mechanical and hydraulic boundary conditions adopted to the FE-model. *Left*: longitudinal cross-section trough the model, i.e. longitudinal view of the model; *Right*: vertical cross-section.

due to the prescribed boundary conditions the shear stresses τ are equal to zero (as already explained in Section 3.2.1). As a result the phase displacements (and also the final displacements alongside this vertical boundary) are anomalous larger, and this is due to this boundary condition which is incompatible with the deformational state of the ground (s. also e.g. Anagnostou 2007). Based on the same considerations for the deep tunnel it is defined an observation cross-section situated at the $50^{\text{-th}}$ excavation stage, i.e. 75.00 m from the tunnel beginning. At that cross-sections there are measured displacements in chosen FE-nodes (e.g. on the ground surface (point O), at the tunnel crown (point F), at the tunnel side wall (point U), and at the tunnel invert (point S) as shown in Figure 3.18 for the shallow tunnel where the subscript 26 means that it is situated at the $26^{\text{-th}}$ excavation stage), and pore water pressures in stress points at different locations around the tunnel perimeter (see further Section 3.5) during the excavation. Particularly, there are measured the vertical displacements u_z of points O, F and S, and the horizontal displacements u_y in point U. By the excavation of the shallow tunnel in excavation step 26 the TBM face reaches the observation cross-section, further in excavation step 32 the shield tail is passing through the cross-section. By the excavation of the deep tunnel in excavation step 50 the TBM face reaches the observation cross-section, further in excavation step 56 the shield tail is passing through the cross-section.
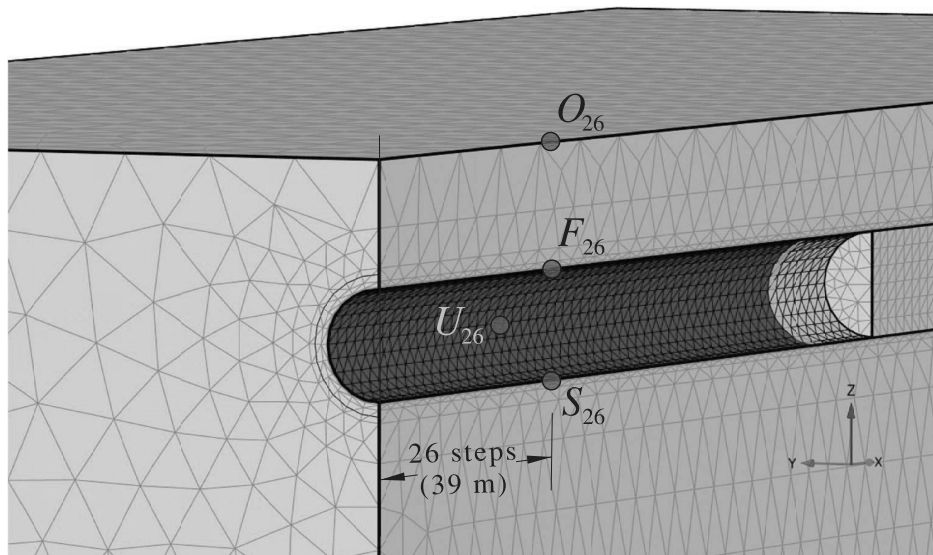
Figure 3.18.: Measurement of displacements at selected observation points (FE-nodes) during the excavation, e.g. of the shallow tunnel situated at observation cross-section 26 (i.e. located at the $39^{\text{-th}}$ m from the tunnel beginning). For the deep tunnel the observation cross-section is shifted at the $50^{\text{-th}}$ excavation stage (i.e. located at the $75^{\text{-th}}$ m from the tunnel beginning).

3.4. Results and Discussion

3.4.1. Importance of the Soil Constitutive Model

The simple MC model provides not reliable results (see e.g. Do *et al.* 2013, Hejazi *et al.* 2008a and 2008b), even for a wide range of the value of the E-modulus, as shown in Figures 3.19–3.26, because it at least doesn't distinguish between loading and unloading stress paths. It is visible the effect of unrealistic uplifting on the ground surface due to unloading during the tunnelling process when using the MC model. It is observed that without differentiating between loading and unloading regarding the values of the stiffness modulus the application of the MC model results in an unrealistic lifting (e.g. see in Fig. 3.27, 3.35 and 3.37) or in a less settlements (e.g. see in Fig. 3.28, 3.36 and 3.38) of the ground surface. The HS model gives reliable results, however the displacements – settlements during the tunnelling, longitudinal and final transverse settlements, are over-predicted, because it doesn't consider the higher soil stiffness at small stains (see additionally e.g. Brinkgreve *et al.* 2006) – see in Figures 3.27, 3.35, 3.36, 3.37, and 3.38. From the three models the most suitable for representing various real soil conditions is the HSsmall model. From the comparison of the longitudinal, and the final transverse settlements of the shallow and the deep tunnel calculated with the HSsmall model (and also these calculated just with the HS model) – see Figures 3.35, 3.36, 3.37, and 3.38 it is shown that the width of the settlements profile in case of shallow tunnelling is smaller than in case of deeper tunnelling. Moreover, the maximum inclination (i.e. slope) of the transverse and longitudinal settlements profile in case of shallow tunnel is larger than by deep tunnel. Thus, the shallow tunnels which are excavated with relatively narrow overburden depth are much more critical i.e. dangerous for the surface buildings due to these larger differential settlements (see further e.g. Ninić *et al.* 2011a, Kappen *et al.* 2013, Schindler & Mark 2013).

In Figures 3.39–3.44 there are presented the three stress invariants during the tunnelling of the shallow and deep tunnel for an observation point situated 0.10 m above the tunnel crown. The first stress invariant is defined as follow (Yu 2006):

$$I_1 = \sigma_1' + \sigma_2' + \sigma_3'. \tag{3.36}$$

The second deviatoric stress invariant is defined as follow (Yu 2006):

$$J_2 = \frac{1}{6} \left[(\sigma_1' - \sigma_2')^2 + (\sigma_2' - \sigma_3')^2 + (\sigma_3' - \sigma_1')^2 \right]. \tag{3.37}$$
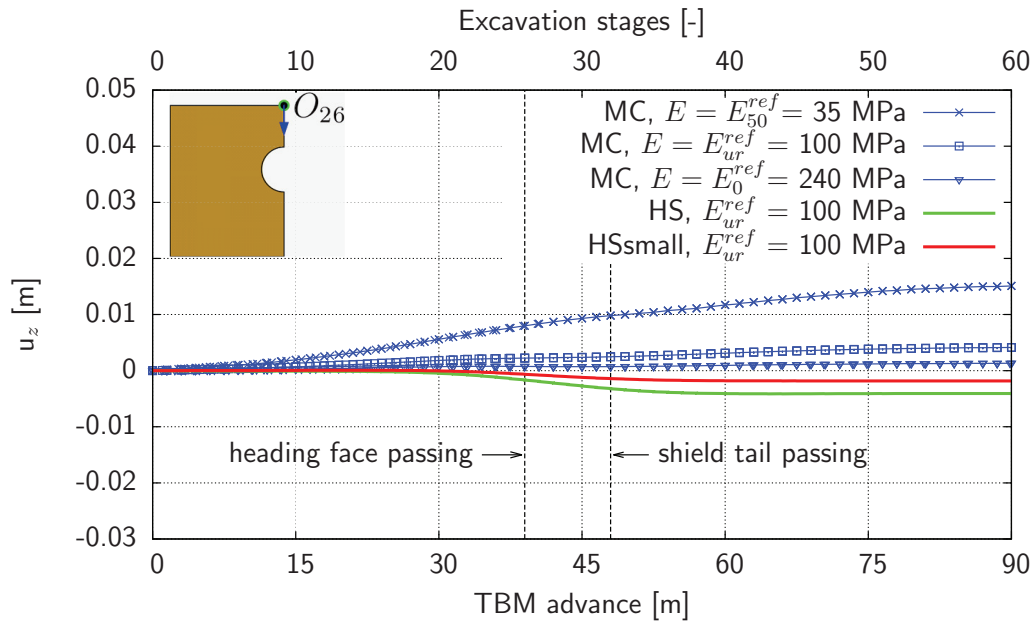
Figure 3.19.: Vertical displacements on the ground surface at observation cross-section 26 (situated at the 26th excavation stage) during the excavation of the shallow tunnel.
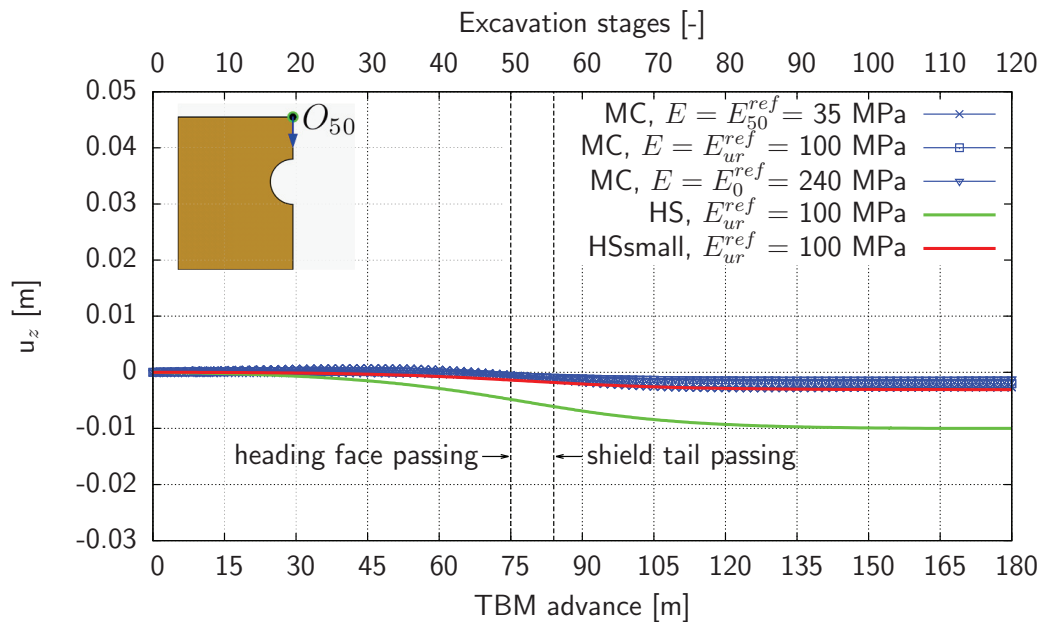
Figure 3.20.: Vertical displacements on the ground surface at observation cross-section 50 (situated at the 50th excavation stage) during the excavation of the deep tunnel.
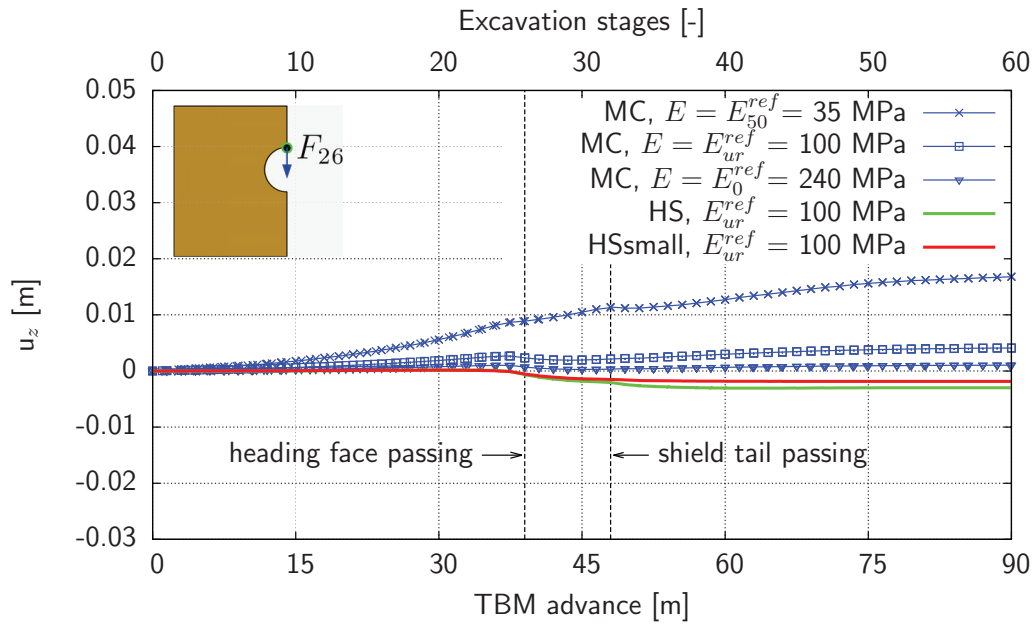
Figure 3.21.: Vertical displacements of the tunnel crown at observation cross-section 26 (situated at the 26th excavation stage) during the excavation of the shallow tunnel.
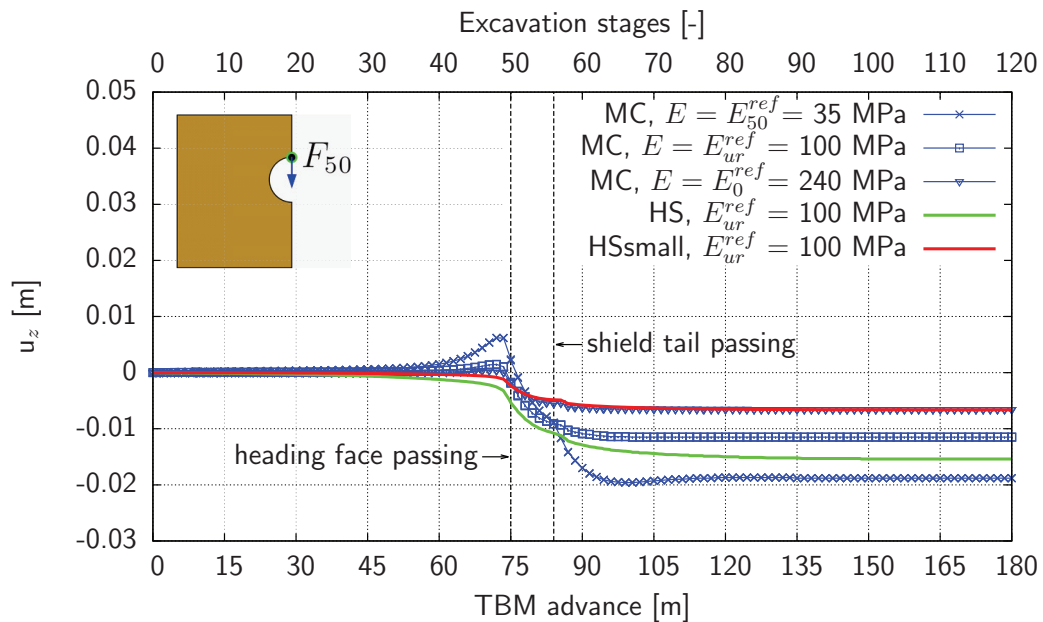
Figure 3.22.: Vertical displacements of the tunnel crown at observation cross-section 50 (situated at the 50th excavation stage) during the excavation of the deep tunnel.
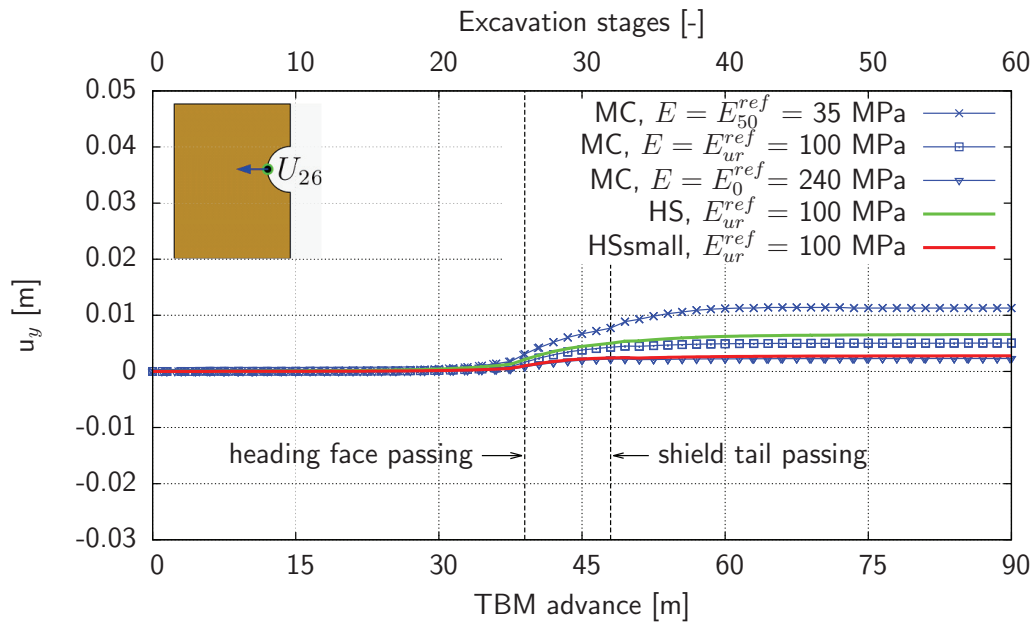
Figure 3.23.: Horizontal displacements of the tunnel side wall at observation cross-section 26 (situated at the 26th excavation stage) during the excavation of the shallow tunnel.
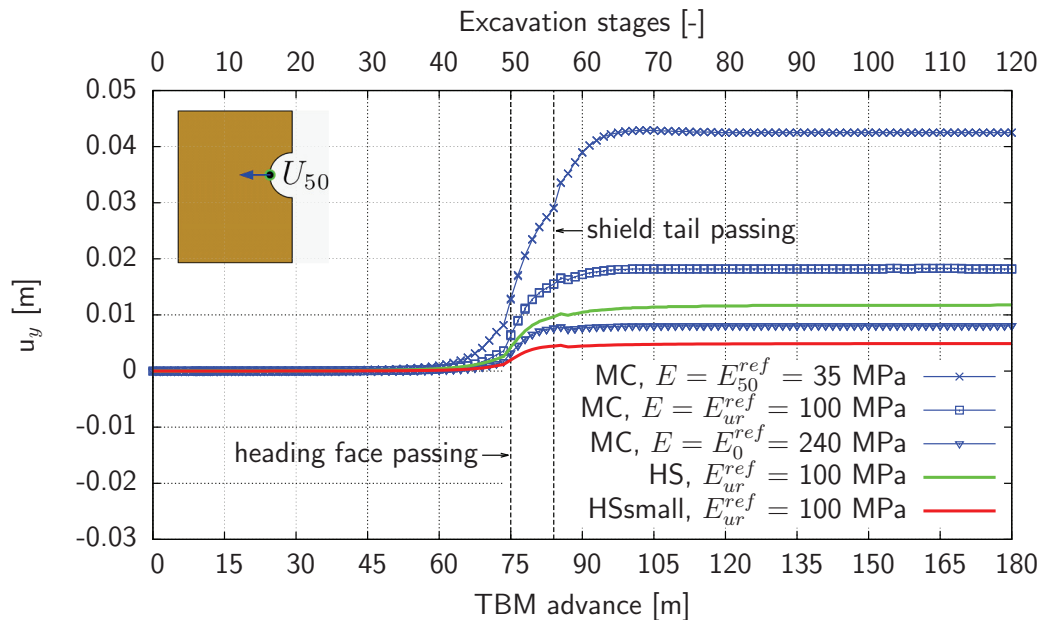
Figure 3.24.: Horizontal displacements of the tunnel side wall at observation cross-section 50 (situated at the 50th excavation stage) during the excavation of the deep tunnel.
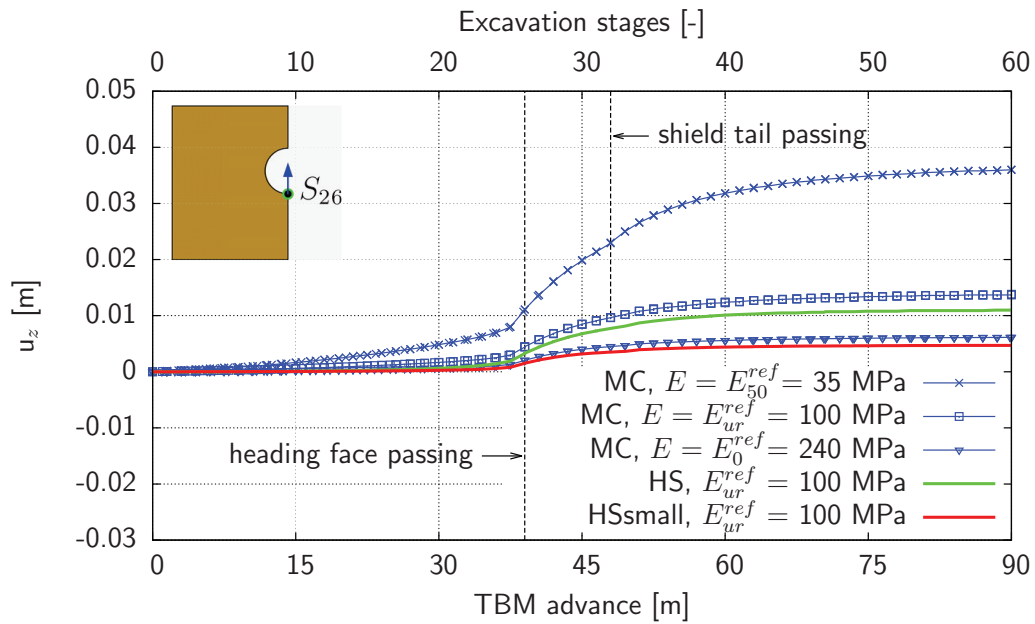
Figure 3.25.: Vertical displacements of the tunnel invert at observation cross-section 26 (situated at the 26th excavation stage) during the excavation of the shallow tunnel.
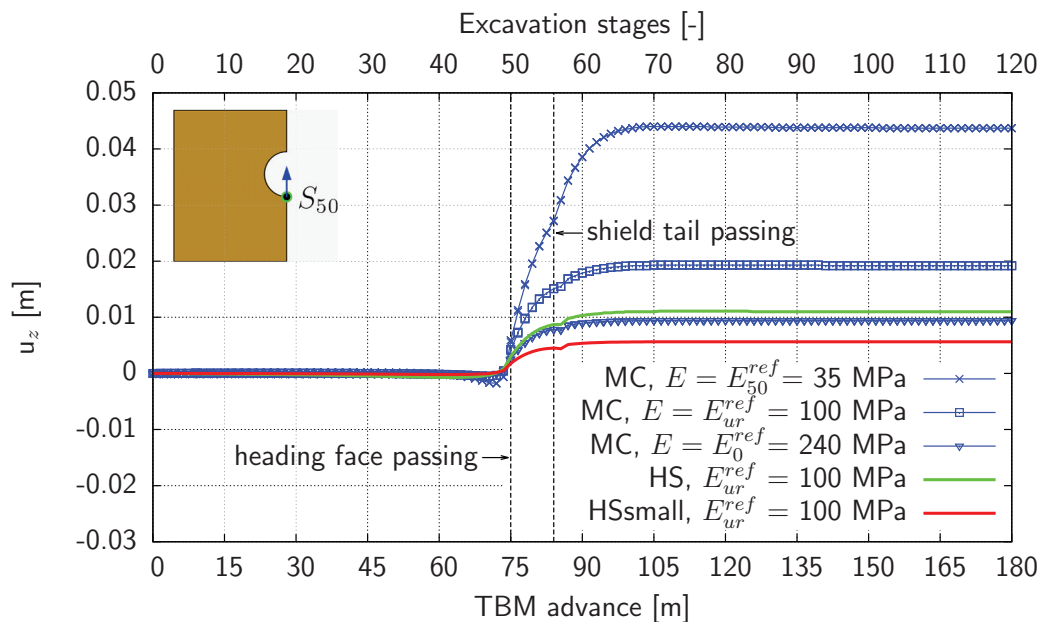
Figure 3.26.: Vertical displacements of the tunnel invert at observation cross-section 50 (situated at the 50th excavation stage) during the excavation of the deep tunnel.
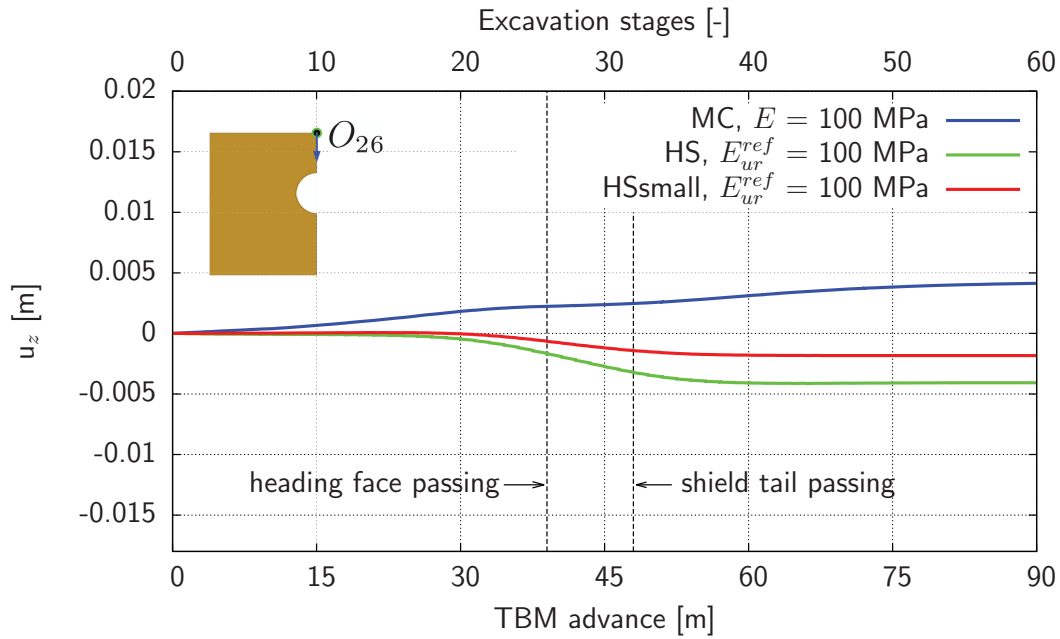
Figure 3.27.: Vertical displacements on the ground surface at observation cross-section 26 during the excavation of the shallow tunnel (overburden = $1D$).
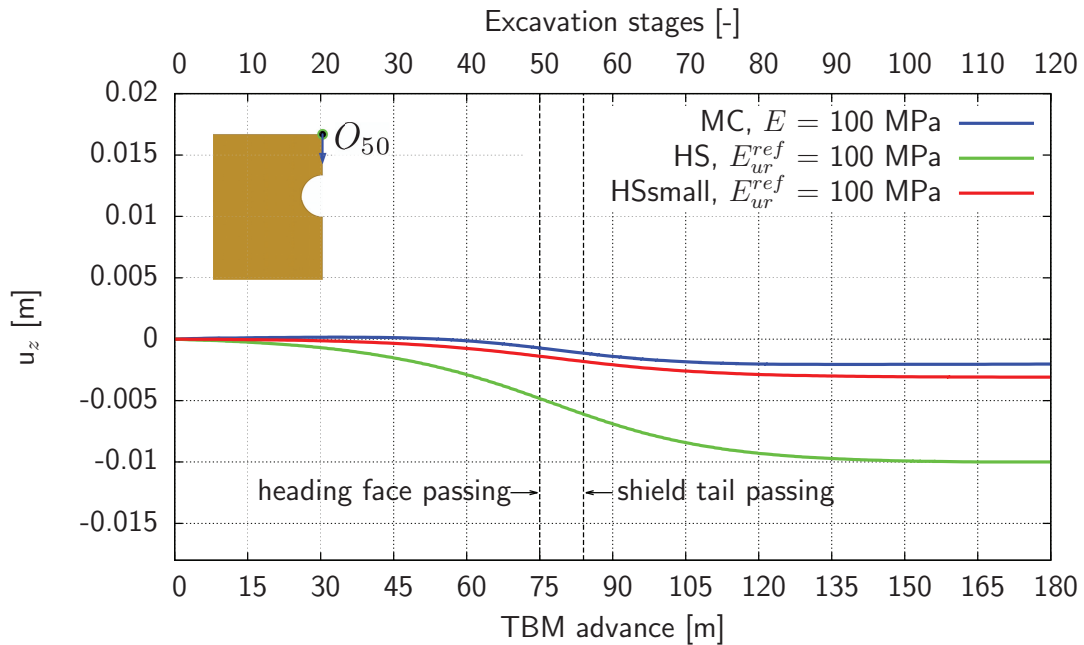
Figure 3.28.: Vertical displacements on the ground surface at observation cross-section 50 during the excavation of the deep tunnel (overburden = $5D$).
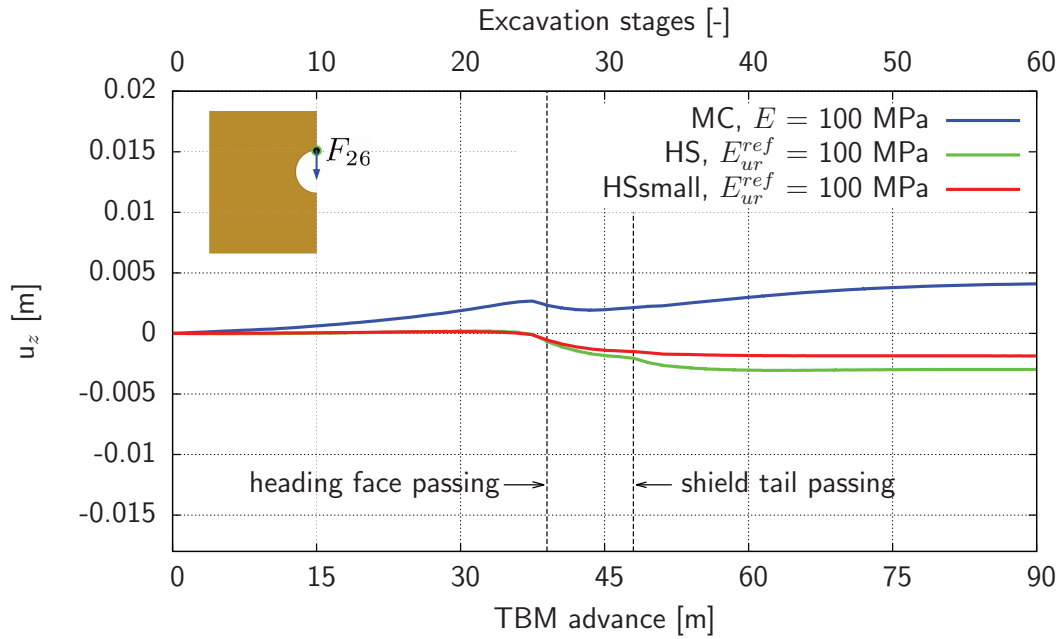
Figure 3.29.: Vertical displacements of the tunnel crown at observation cross-section 26 during the excavation of the shallow tunnel (overburden $= 1D$).
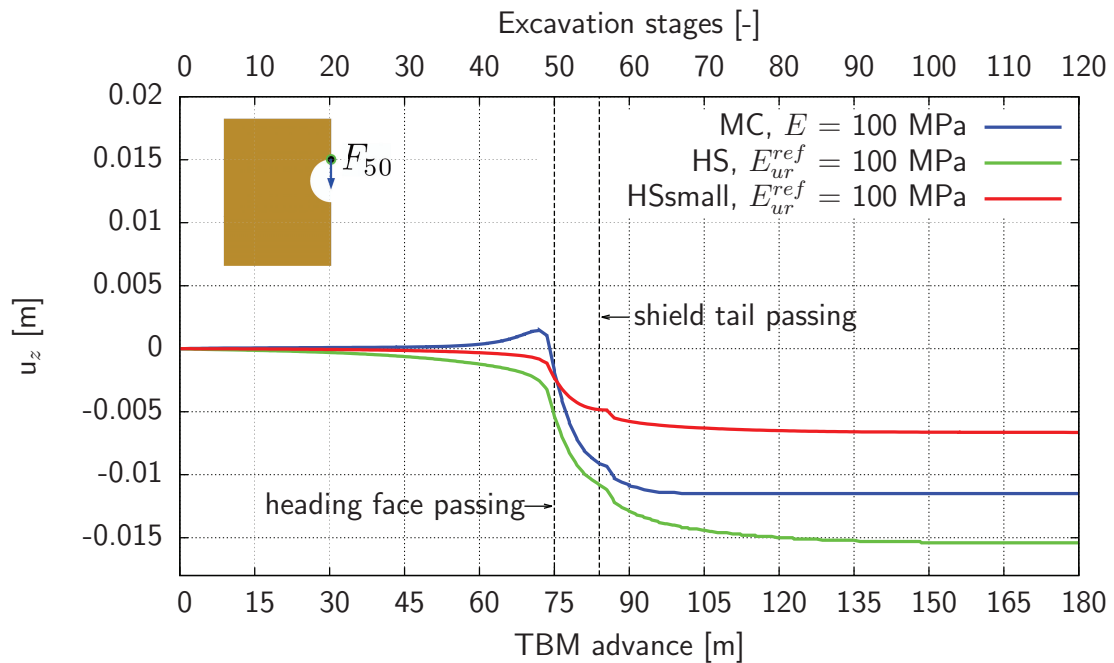
Figure 3.30.: Vertical displacements of the tunnel crown at observation cross-section 50 during the excavation of the deep tunnel (overburden $= 5D$).
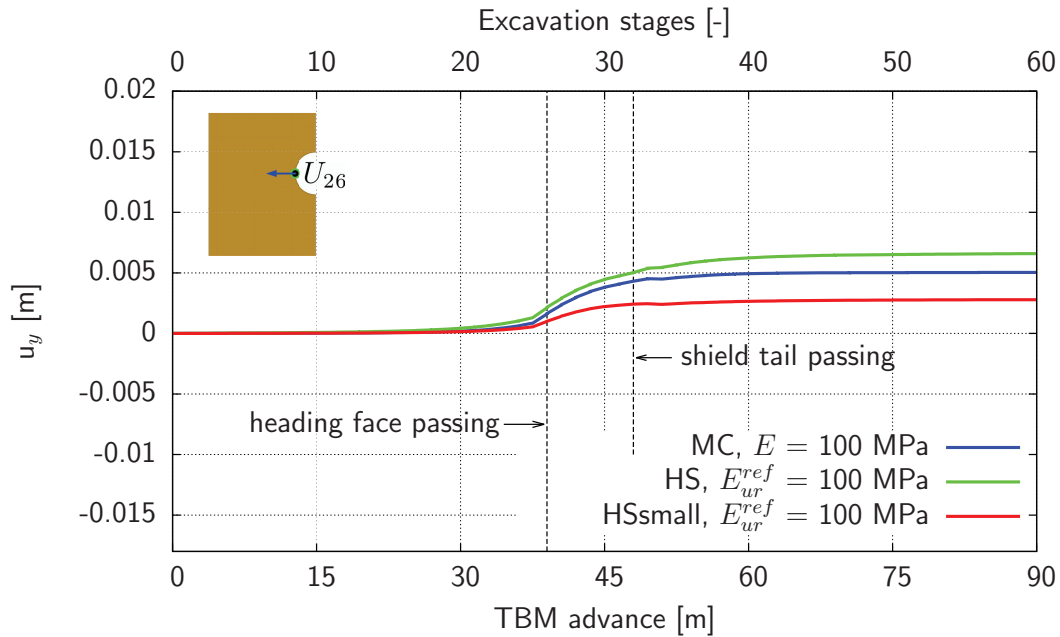
Figure 3.31.: Horizontal displacements of the tunnel side wall at observation cross-section 26 during the excavation of the shallow tunnel (overburden $= 1D$).
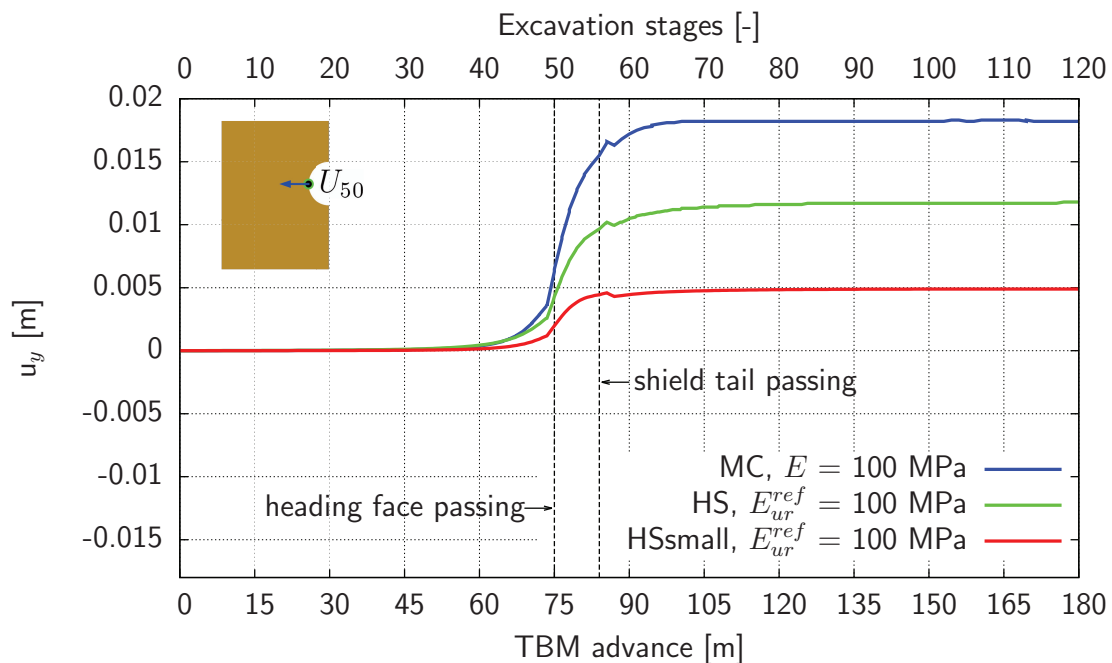
Figure 3.32.: Horizontal displacements of the tunnel side wall at observation cross-section 50 during the excavation of the deep tunnel (overburden $= 5D$).
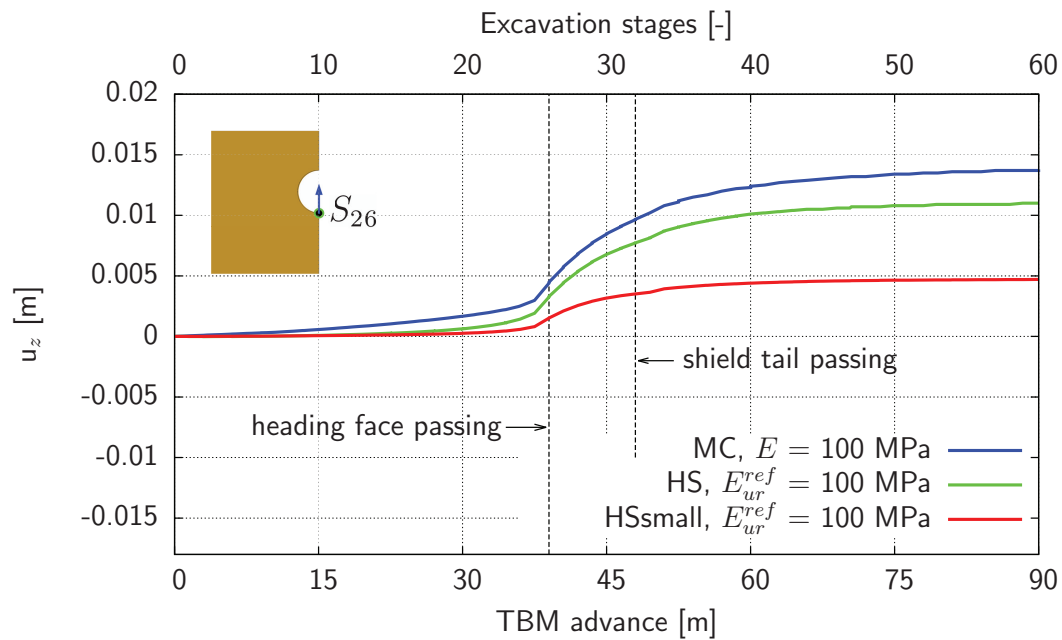
Figure 3.33.: Vertical displacements of the tunnel invert at observation cross-section 26 during the excavation of the shallow tunnel (overburden = $1D$).
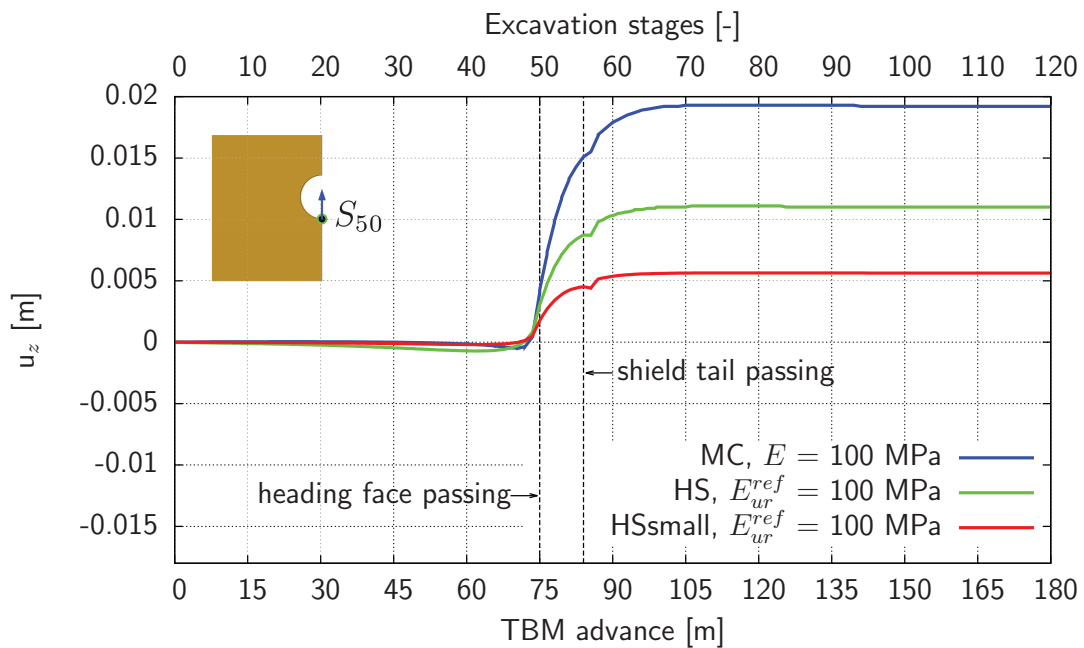
Figure 3.34.: Vertical displacements of the tunnel invert at observation cross-section 50 during the excavation of the deep tunnel (overburden = $5D$).
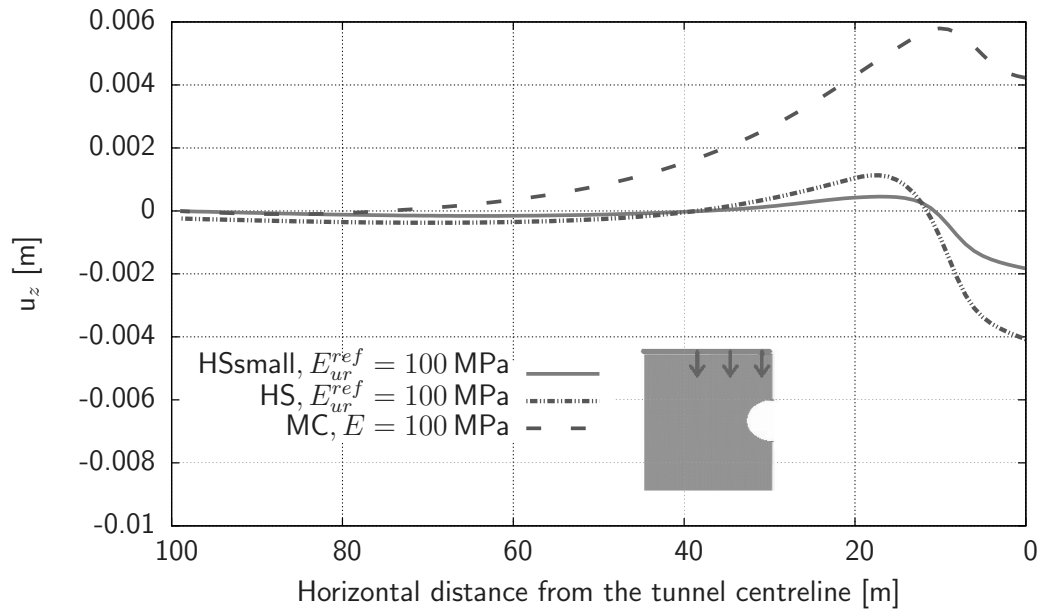
Figure 3.35.: Final transverse settlements on the ground surface (at observation cross-section 26) by the excavation of the shallow tunnel (overburden $= 1D$).
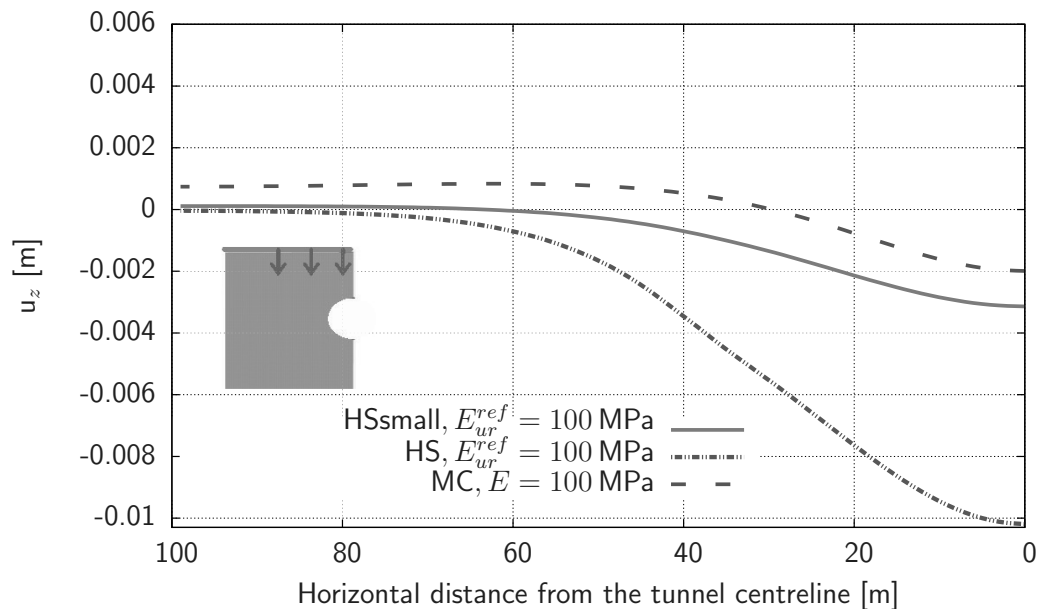
Figure 3.36.: Final transverse settlements on the ground surface (at observation cross-section 50) by the excavation of the deep tunnel (overburden $= 5D$).
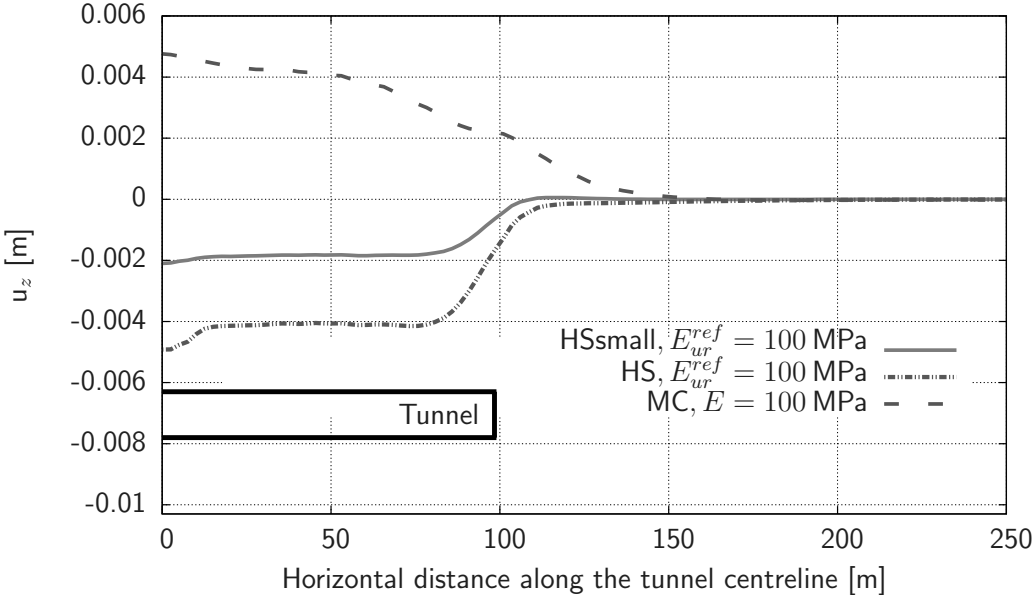
Figure 3.37.: Longitudinal surface settlements above the tunnel axis when the shallow tunnel is excavated 99 m, i.e. when the heading face is 99 m from the tunnel beginning (see also Fig. 3.2).
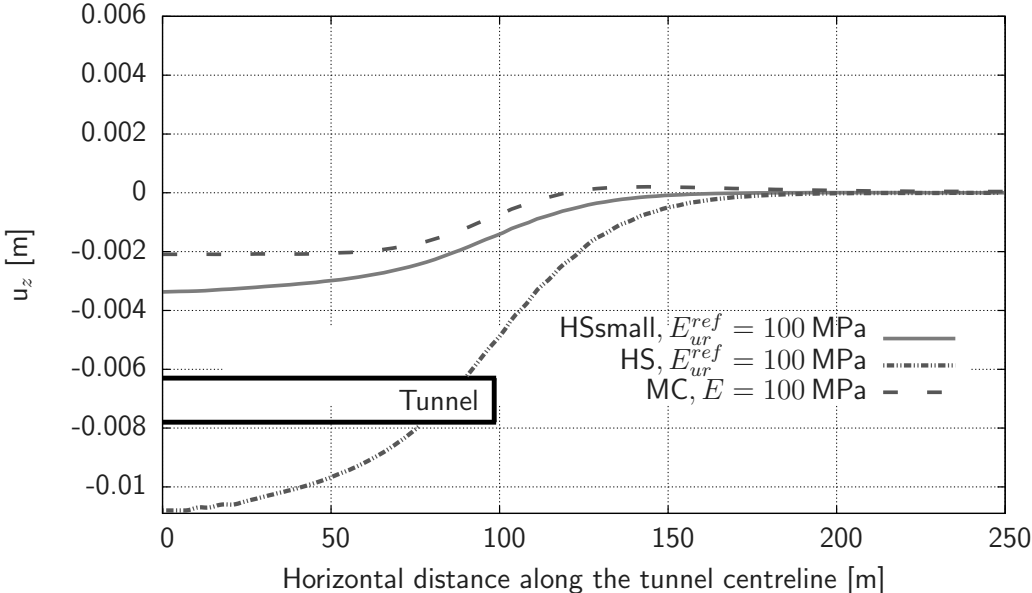
Figure 3.38.: Longitudinal surface settlements above the tunnel axis when the deep tunnel is excavated 99 m, i.e. when the heading face is 99 m from the tunnel beginning (see also Fig. 3.2).

The third stress invariant (Lode's angle) is defined as follow (Potts & Zdravkovic 1999):

$$\theta = \arctan\left[\frac{1}{\sqrt{3}}\left(2\,\frac{\sigma'_2 - \sigma'_3}{\sigma'_1 - \sigma'_3} - 1\right)\right]. \tag{3.38}$$

Physically, I_1 is the mean stress, J_2 represents the magnitude of shear stress, and θ determines the direction of shear stress.

By looking at Figures 3.39–3.40 it is visible that after passing with the TBM through the observation cross-section there is a stress reduction (in the overburden pressure) above the tunnel due to stress redistribution. This effect was demonstrated in the experiment done by Terzaghi with his famous trap door tests as mentioned already in Section 3.1 (Terzaghi 1943). In the figures it is shown that the stress reduction is well-marked by the deep tunnel where the arching is well mobilized, while, by the shallow tunnel this stress reduction is much smaller, because the arching is just partially mobilized. Arching can be defined as the stress redistribution which results in many cases in a decrease in loading over a structure.
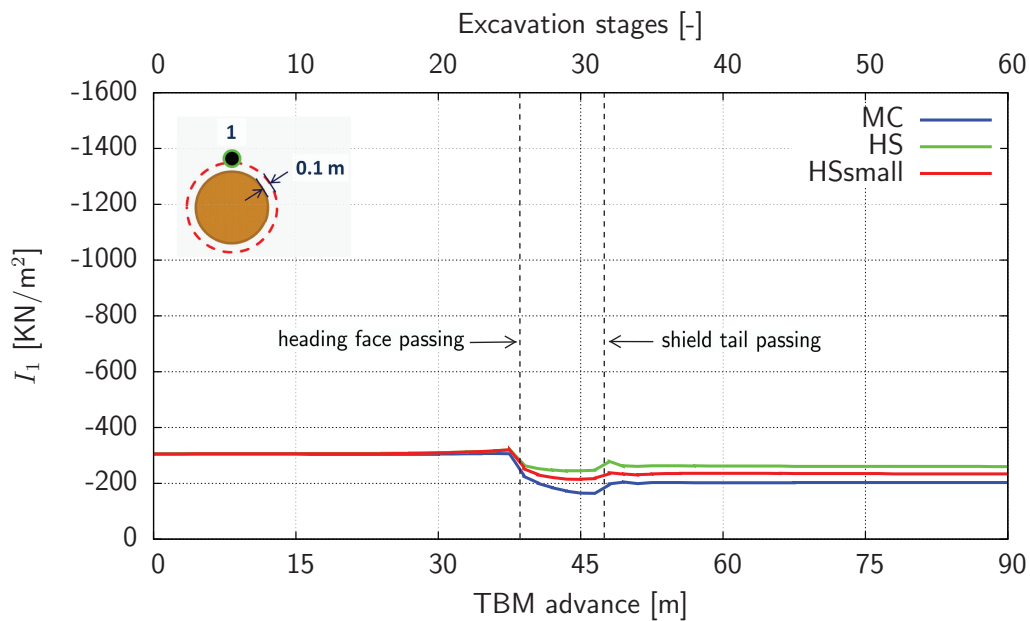
Figure 3.39.: First stress invariant (Eq. 3.36) at observation cross section 26 (overburden $= 1D$); pressure is considered to be negative.
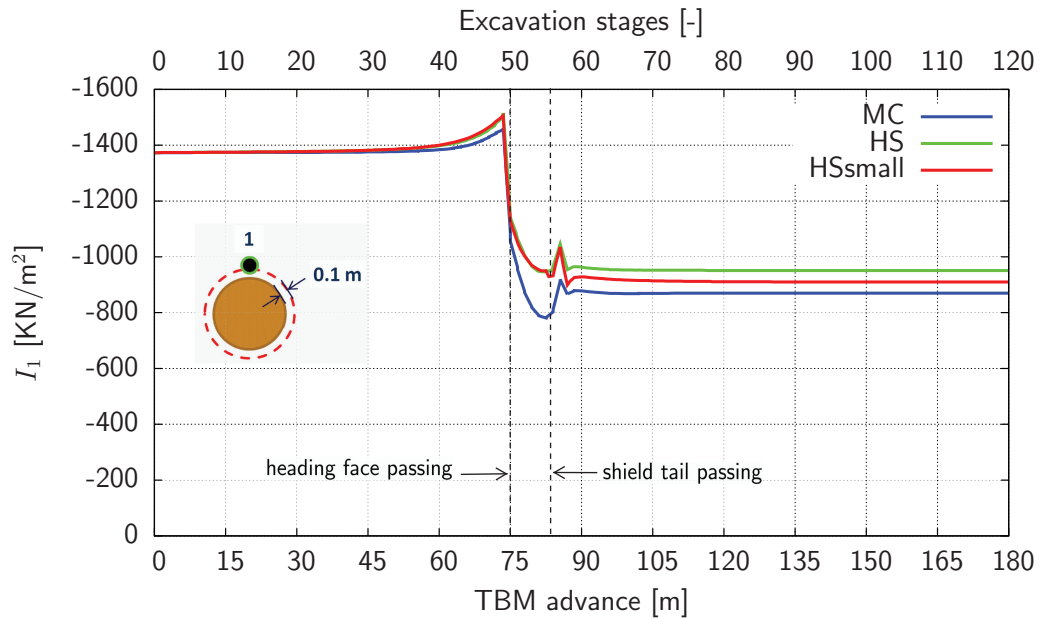
Figure 3.40.: First stress invariant (Eq. 3.36) at observation cross section 50 (overburden = 5D).
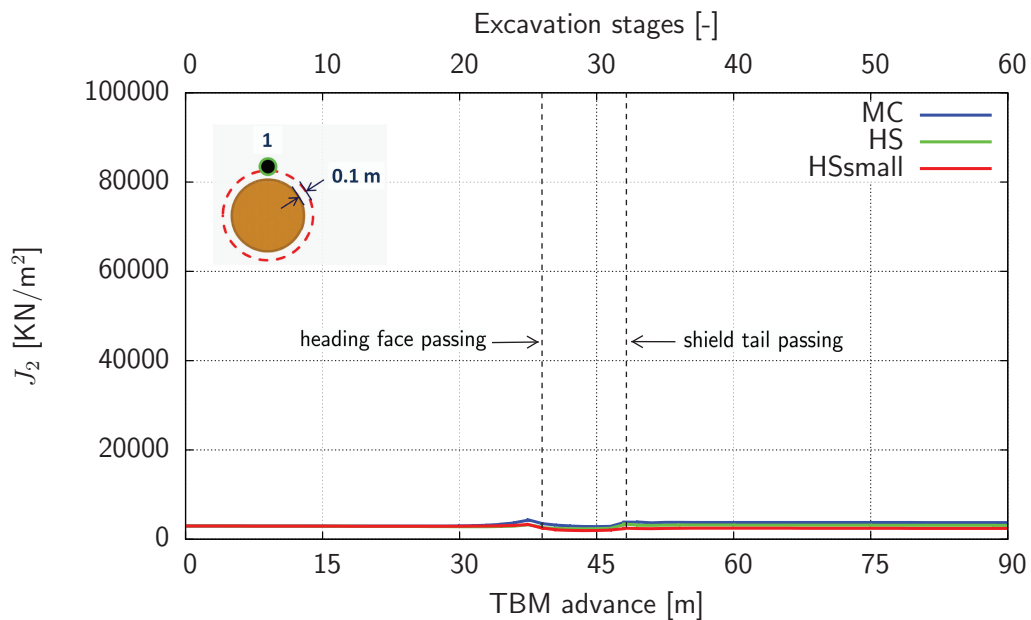
Figure 3.41.: Second deviatoric stress invariant (Eq. 3.37) at observation cross section 26 (overburden = 1D).
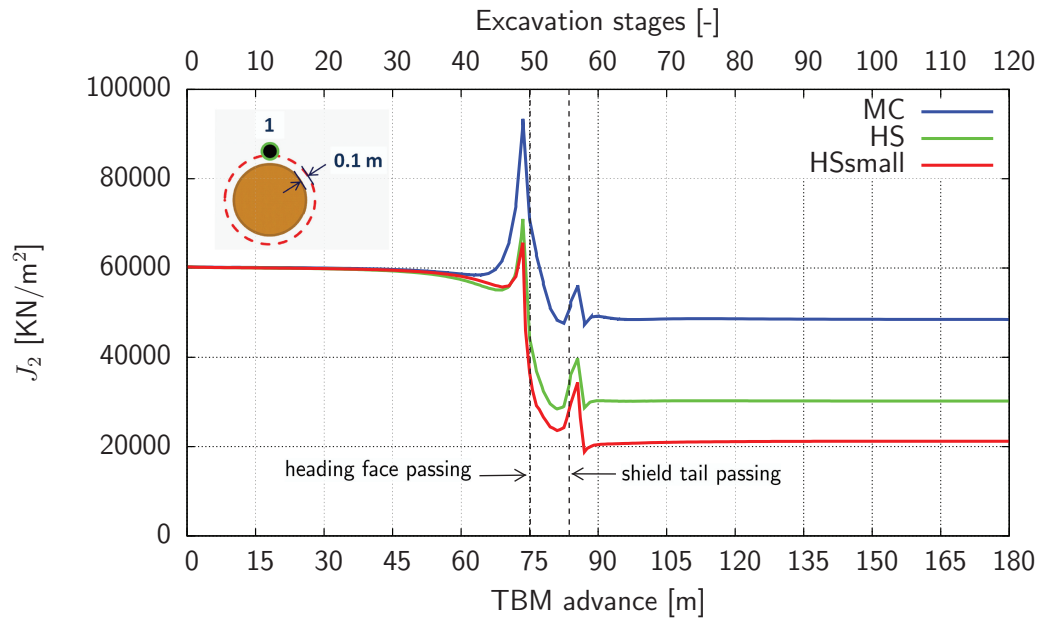
Figure 3.42.: Second deviatoric stress invariant (Eq. 3.37) at observation cross section 50 (overburden $= 5D$).
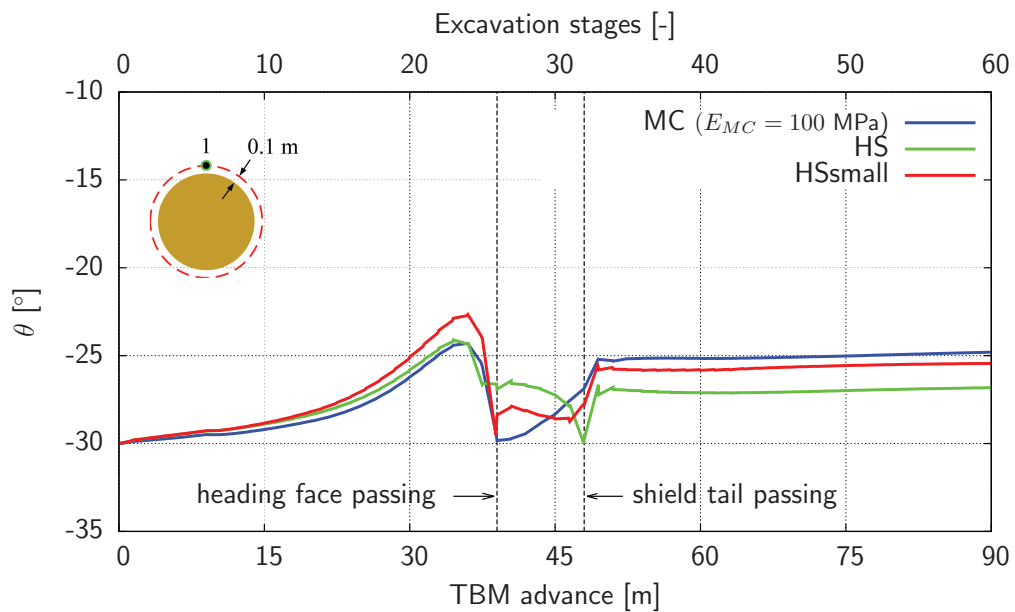
Figure 3.43.: Third stress invariant (Lode angle; Eq. 3.38) at observation cross section 26 (overburden $= 1D$).
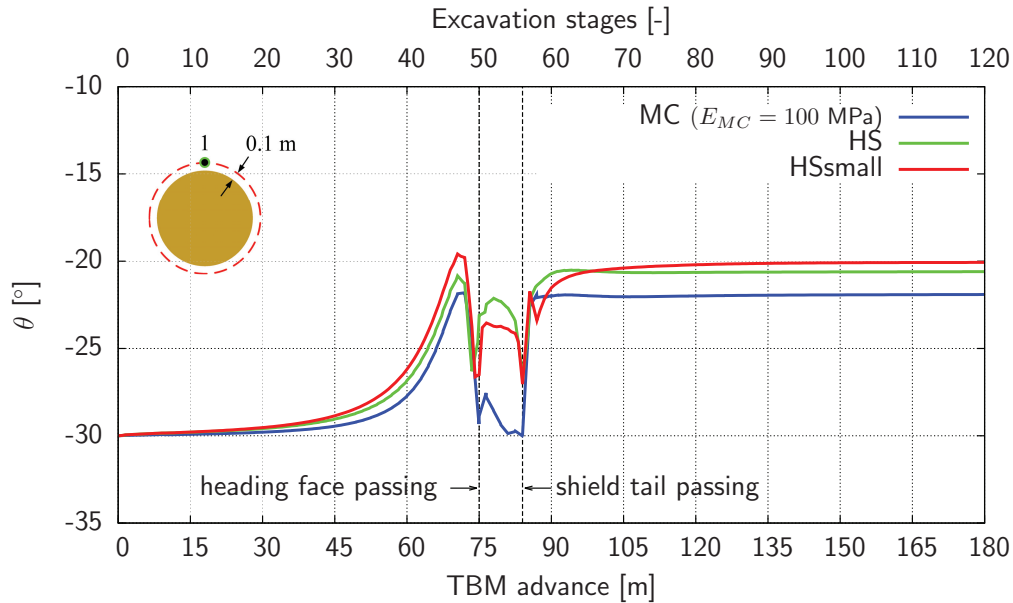
Figure 3.44.: Third stress invariant (Lode angle; Eq. 3.38) at observation cross section 50 (overburden = 5D).

3.4.2. Model Dependence on Soil Density

Looking at Figures 3.45–3.52 it is visible that the deformations are larger when tunnelling in loose ground (i.e. poor subsoil conditions). Moreover, by loose material the surface settlements are larger – see in Figure 3.45 and 3.46, and this is more visible by the deep tunnel. Thus, much more attention have to be paid during the tunnelling in such poor subsoil conditions compared with tunnelling e.g. in dense sand.

3.4.3. Interface Properties Effects

In Figures 3.53, 3.54, 3.57, 3.58, 3.61, 3.62, 3.65, and 3.66 there are given the model response for different stiffness properties of the interface elements around the tunnel. In Figures 3.55, 3.56, 3.59, 3.60, 3.63, 3.64, 3.67, and 3.68 there are given the model response for different strength properties of the interface elements. It is visible that the settlements increase with decreasing the contact properties in the interfaces. This is well-marked in Figure 3.55 where the decrease in the interface strength, i.e. of the plastic parameter φ of the interface, caused the most influence, i.e. the largest settlements by the shallow tunnel. Reason for the increase in the settlements are the increased relative displacements between the soil elements and the plate elements of the TBM and the lining when the
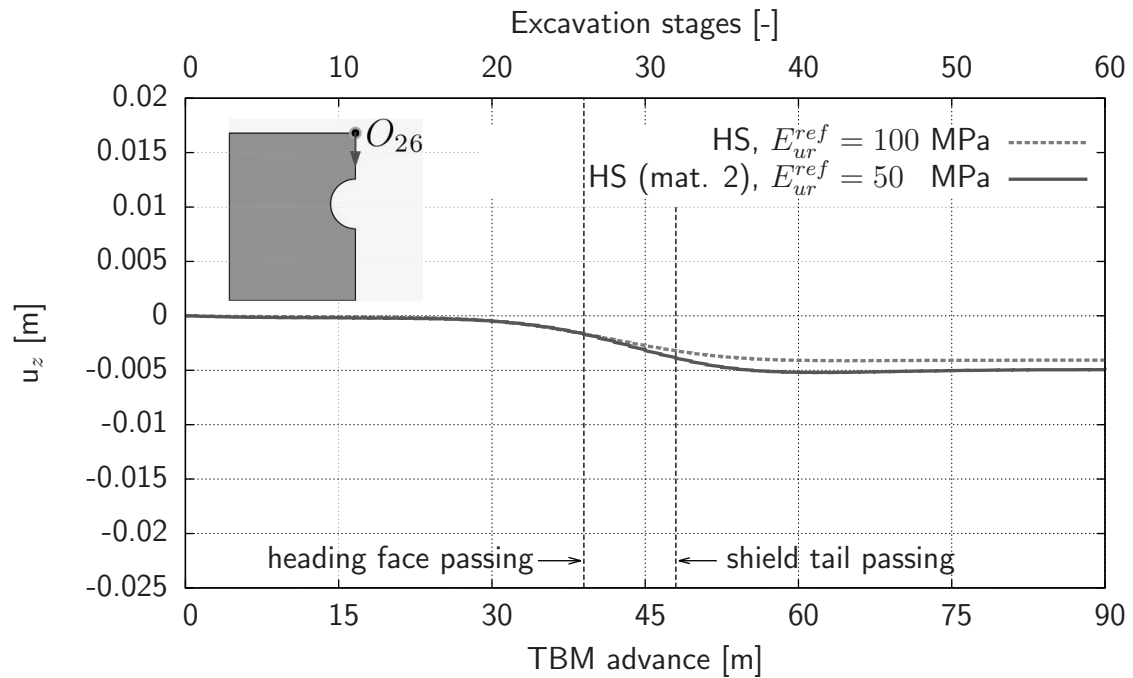
Figure 3.45.: Vertical displacements on the ground surface at observation cross-section 26 during the excavation of the shallow tunnel (overburden = $1D$).
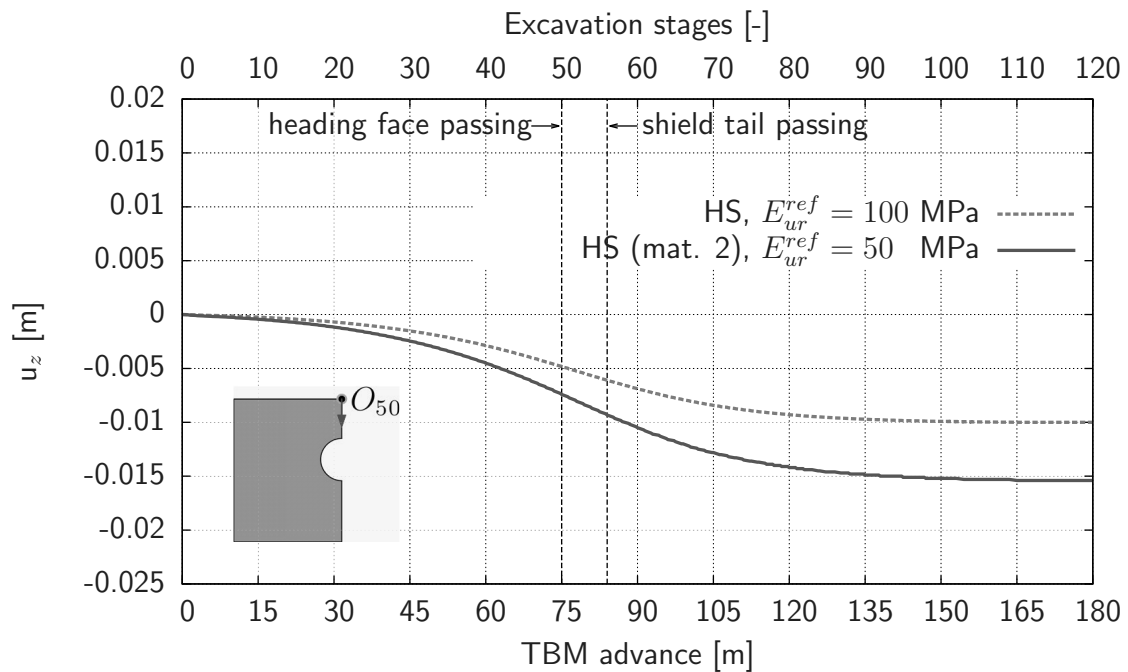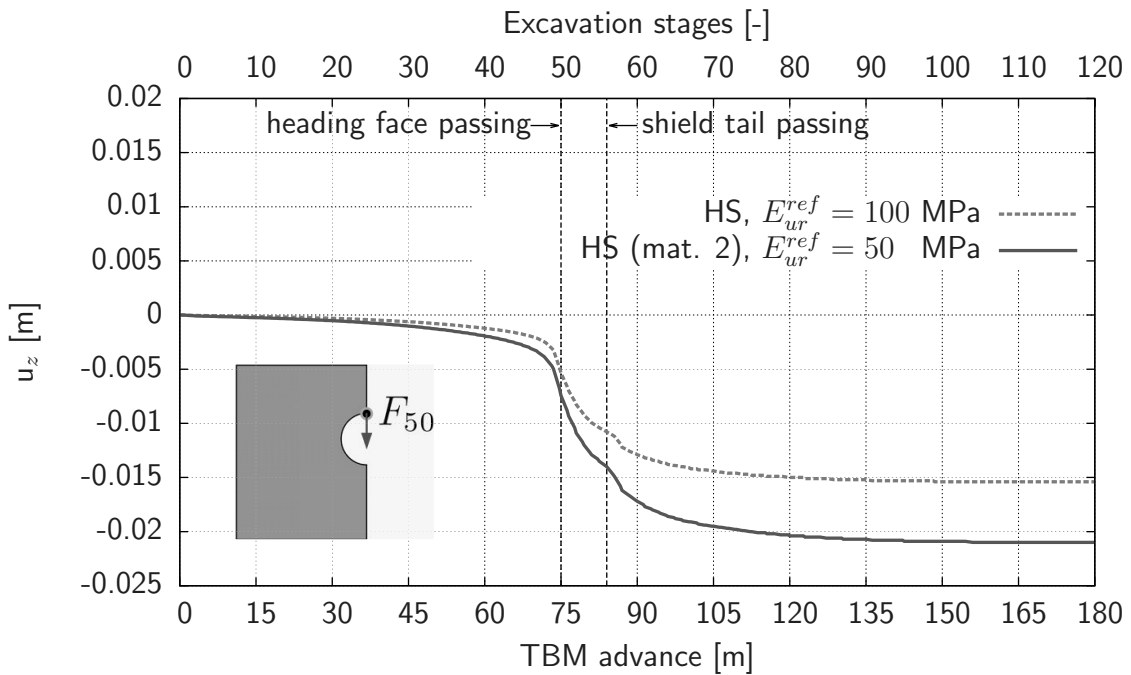

Figure 3.46.: Vertical displacements on the ground surface at observation cross-section 50 during the excavation of the deep tunnel (overburden = $5D$).
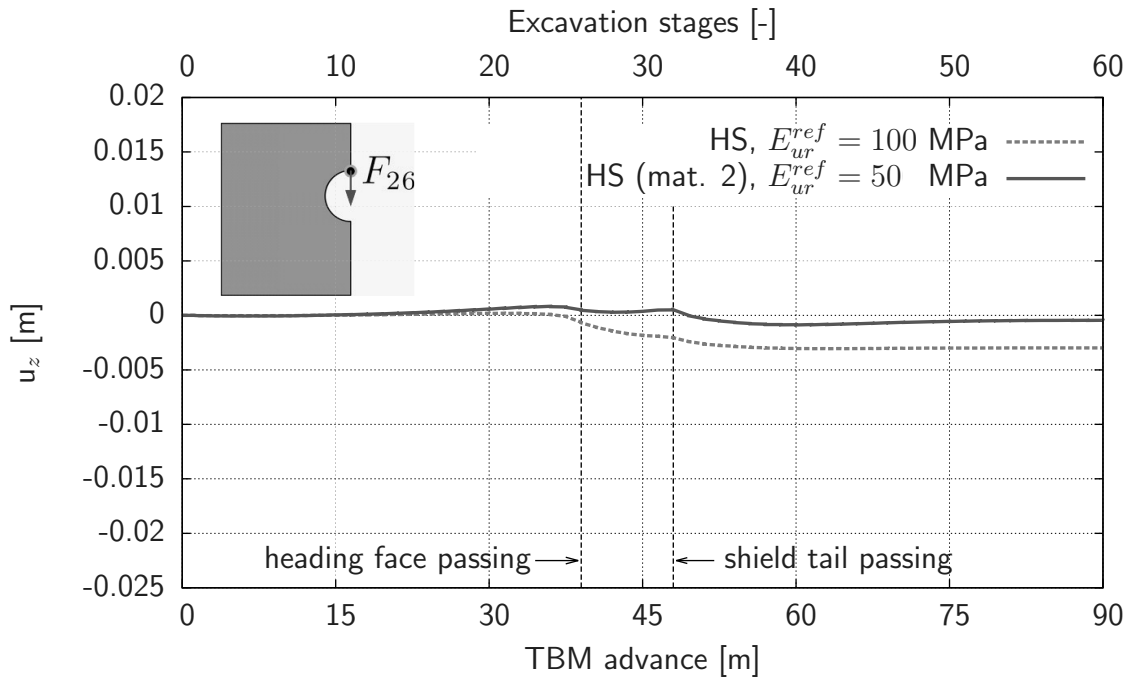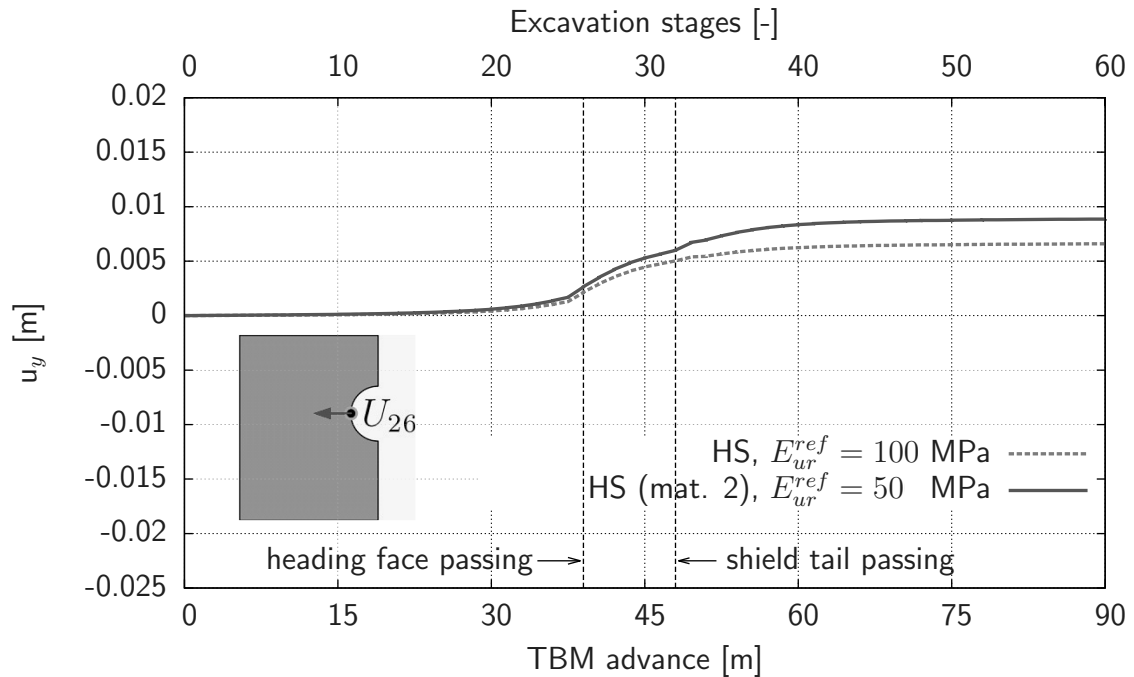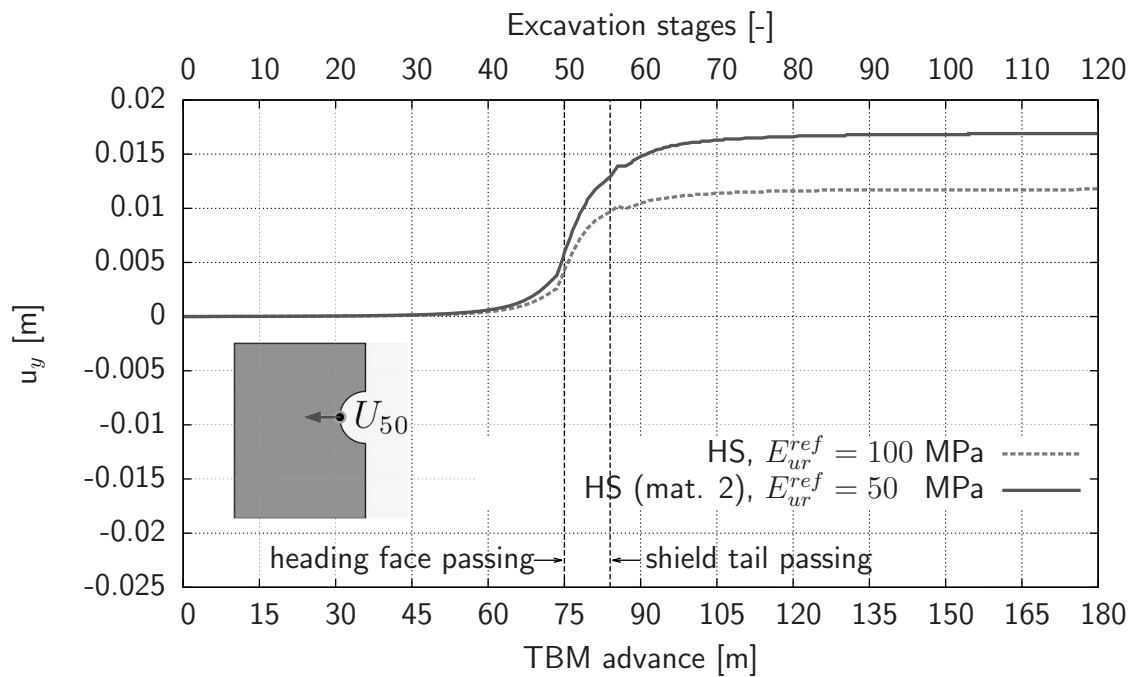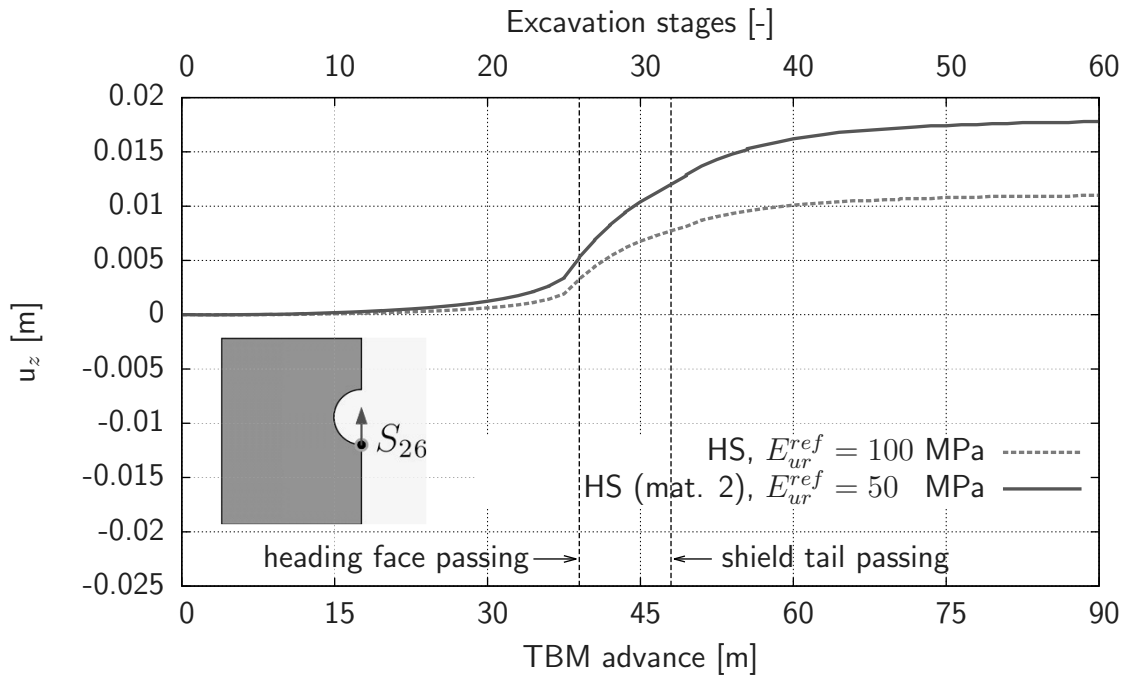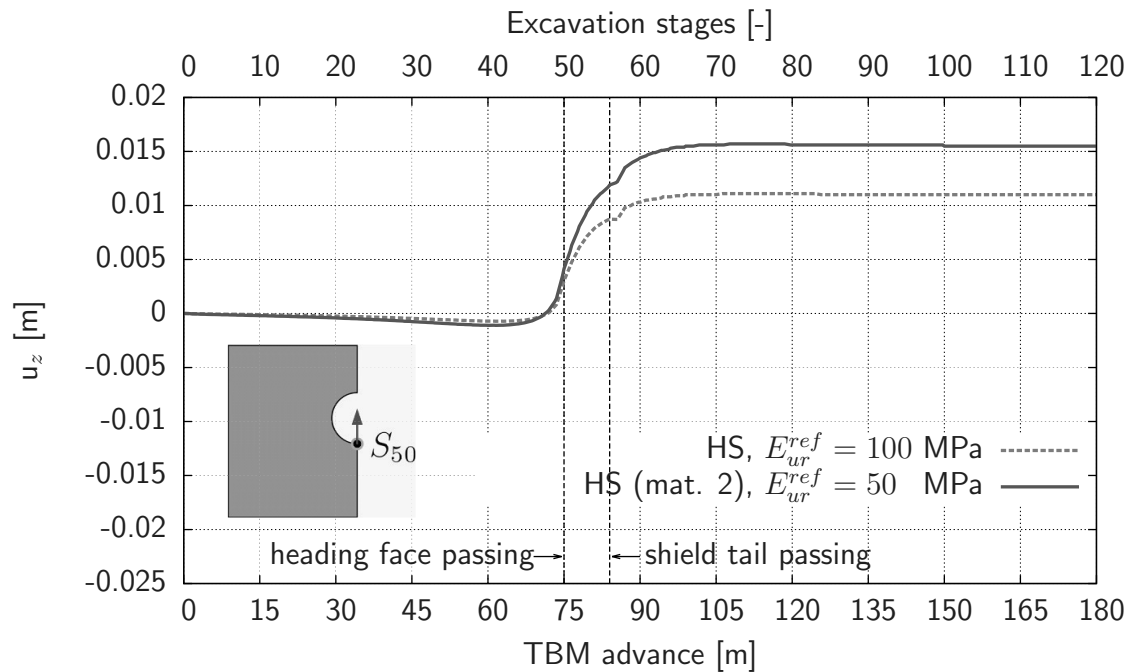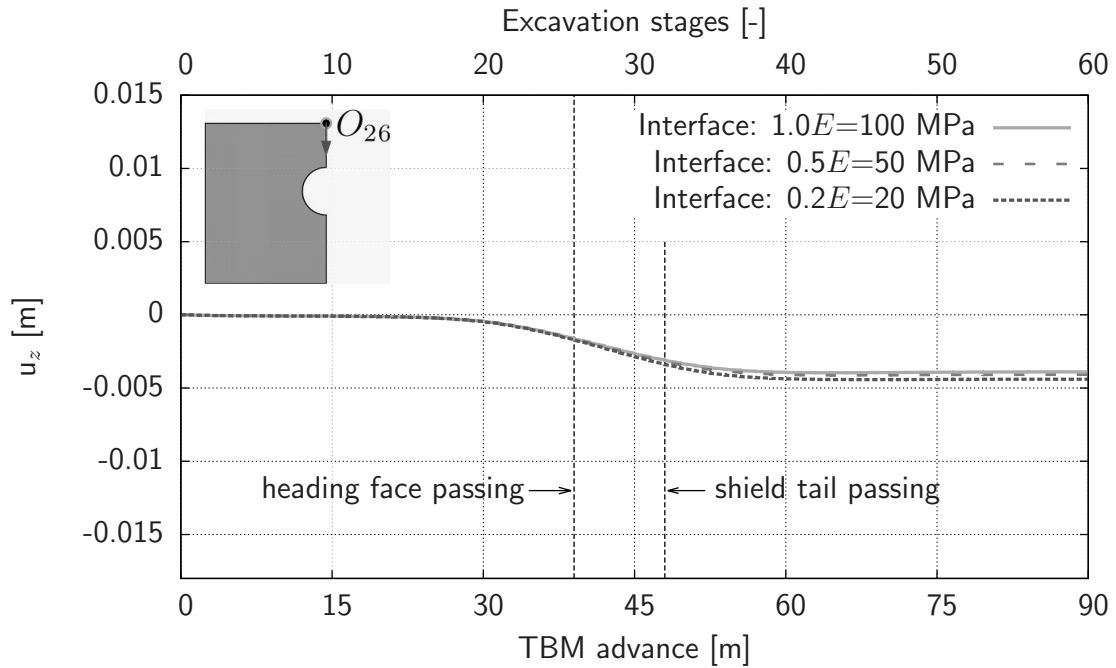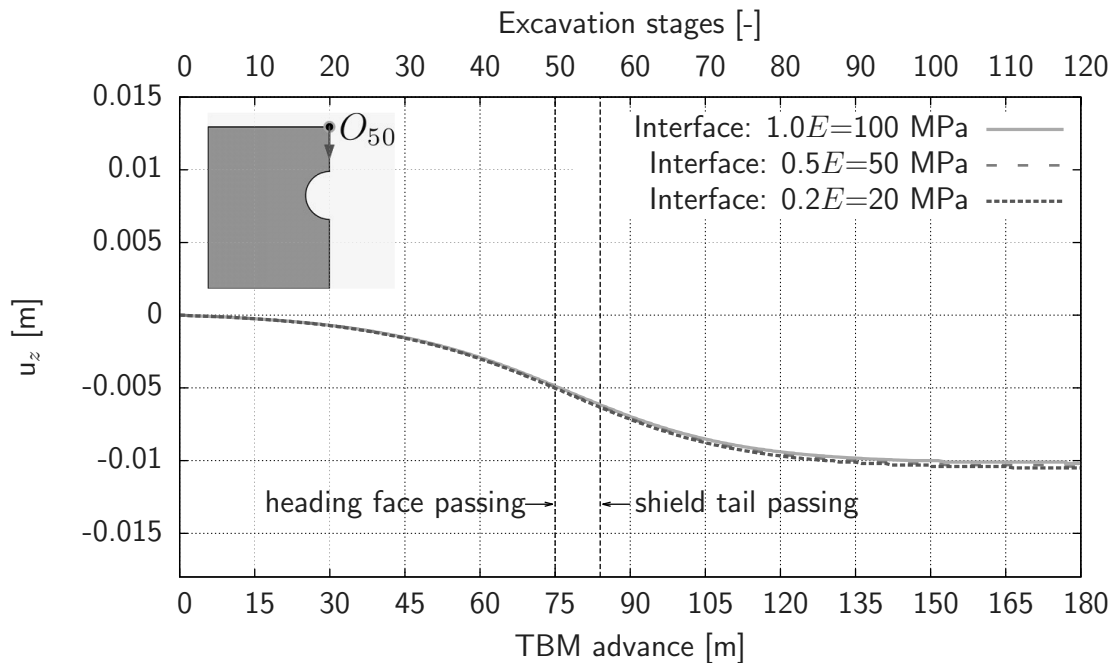
Figure 3.47.: Vertical displacements of the tunnel crown at observation cross-section 26 during the excavation of the shallow tunnel (overburden = $1D$).

Figure 3.48.: Vertical displacements of the tunnel crown at observation cross-section 50 during the excavation of the deep tunnel (overburden = $5D$).

Figure 3.49.: Horizontal displacements of the tunnel side wall at observation cross-section 26 during the excavation of the shallow tunnel (overburden = $1D$).

Figure 3.50.: Horizontal displacements of the tunnel side wall at observation cross-section 50 during the excavation of the deep tunnel (overburden = $5D$).

Figure 3.51.: Vertical displacements of the tunnel invert at observation cross-section 26 during the excavation of the shallow tunnel (overburden $= 1D$).

Figure 3.52.: Vertical displacements of the tunnel invert at observation cross-section 50 during the excavation of the deep tunnel (overburden $= 5D$).
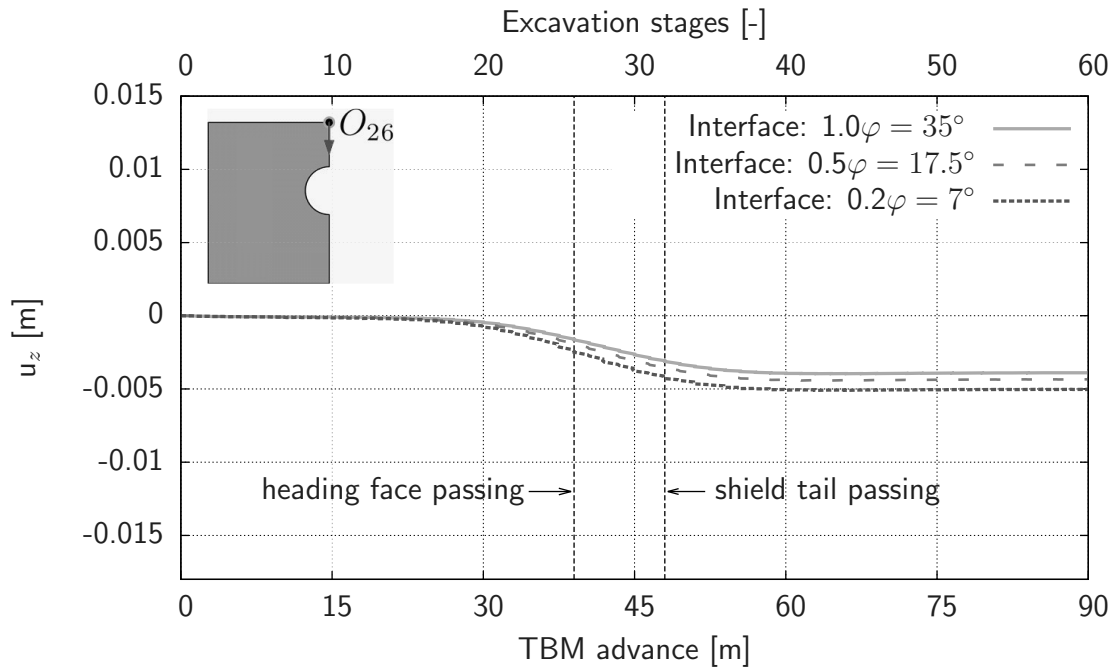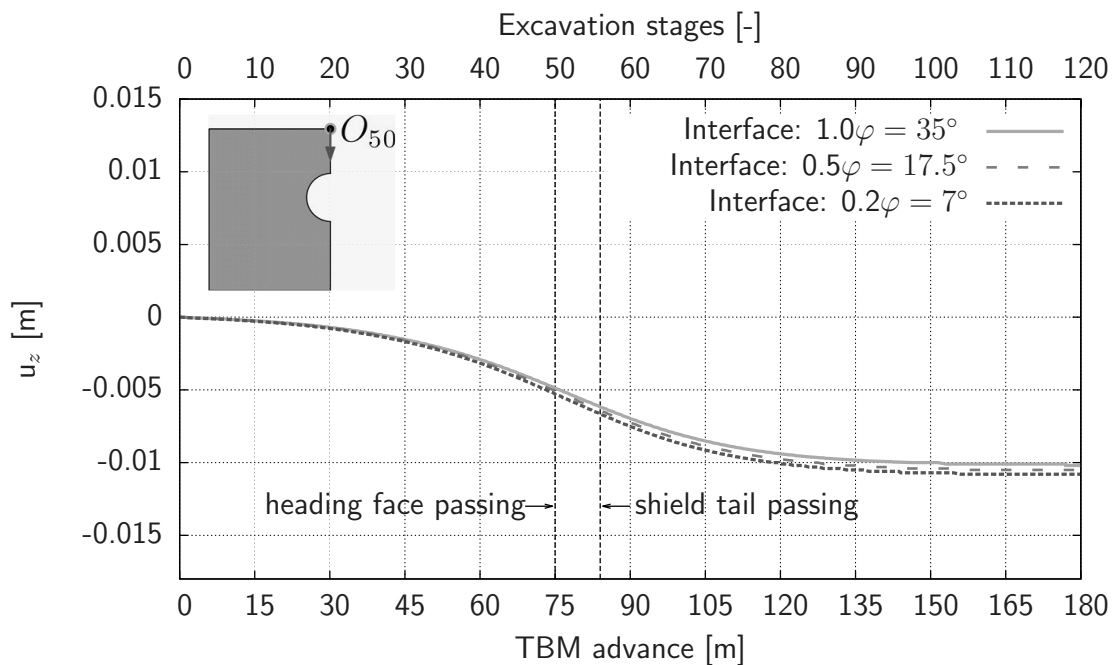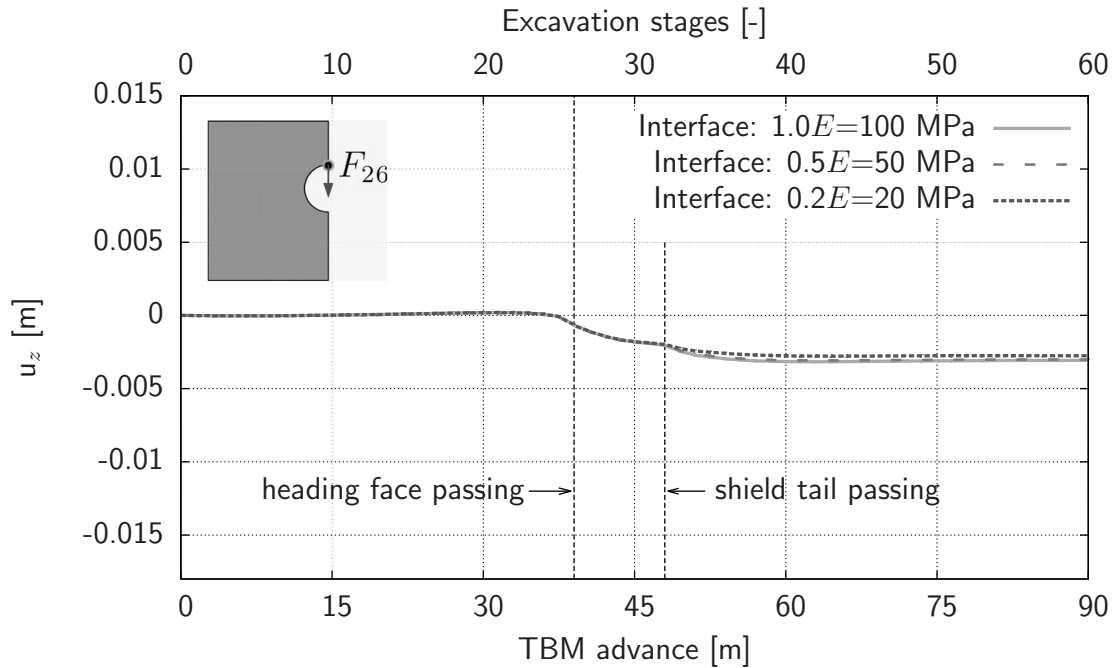
Figure 3.53.: Vertical displacements on the ground surface at observation section 26 during the excavation of the shallow tunnel. The interface strength is fixed: $\varphi = 35.0° = $ const.

Figure 3.54.: Vertical displacements on the ground surface at observation section 50 during the excavation of the deep tunnel. The interface strength is fixed: $\varphi = 35.0° = $ const.

Figure 3.55.: Vertical displacements on the ground surface at observation section 26 during the excavation of the shallow tunnel. Interface stiffness is fixed: $E = 100$ MPa $=$ const.

Figure 3.56.: Vertical displacements on the ground surface at observation section 50 during the excavation of the shallow tunnel. Interface stiffness is fixed: $E = 100$ MPa $=$ const.

Figure 3.57.: Vertical displacements on the tunnel crown at observation section 26 during the excavation of the shallow tunnel. The interface strength is fixed: $\varphi = 35.0° = $ const.
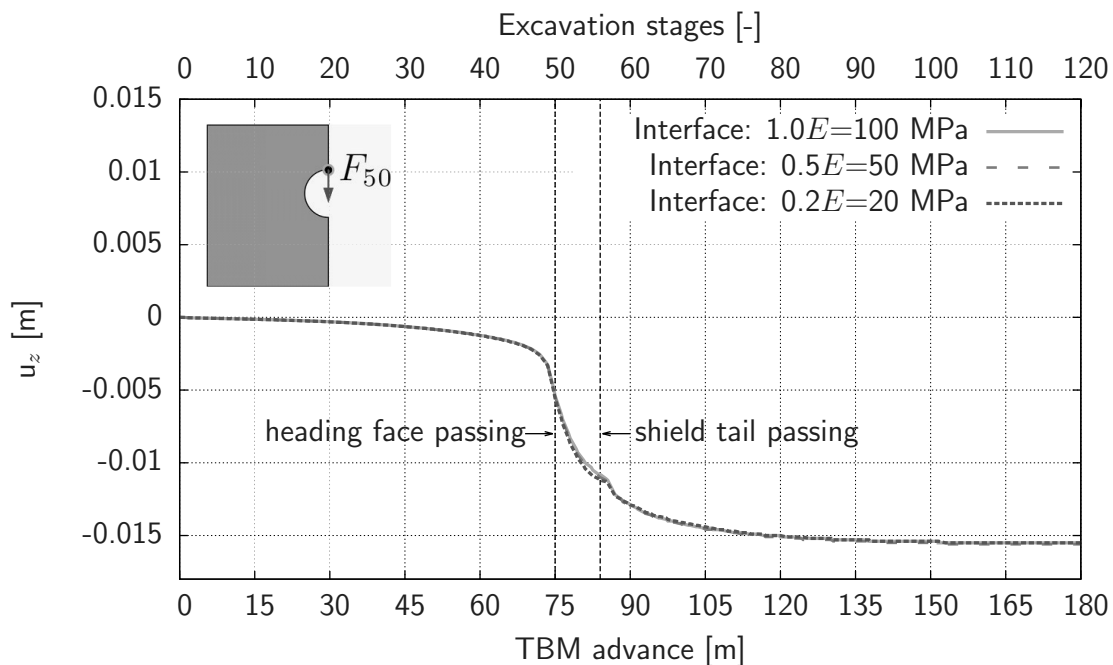

Figure 3.58.: Vertical displacements on the tunnel crown at observation section 50 during the excavation of the deep tunnel. The interface strength is fixed: $\varphi = 35.0° = $ const.
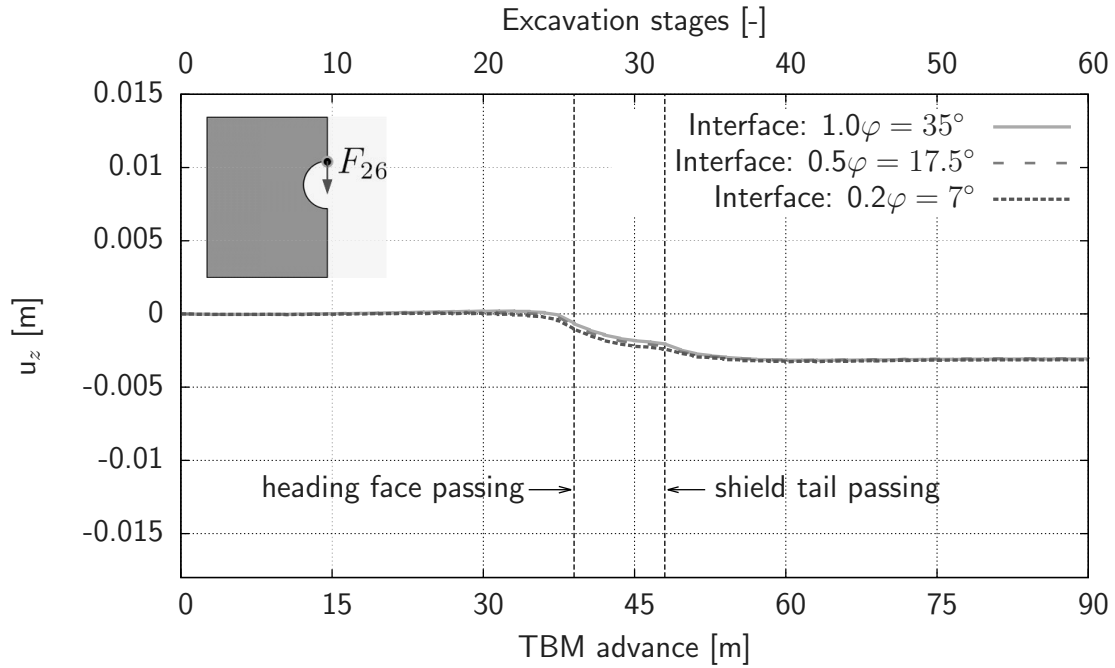
Figure 3.59.: Vertical displacements on the tunnel crown at observation section 26 during the excavation of the shallow tunnel. Interface stiffness is fixed: $E = 100$ MPa = const.
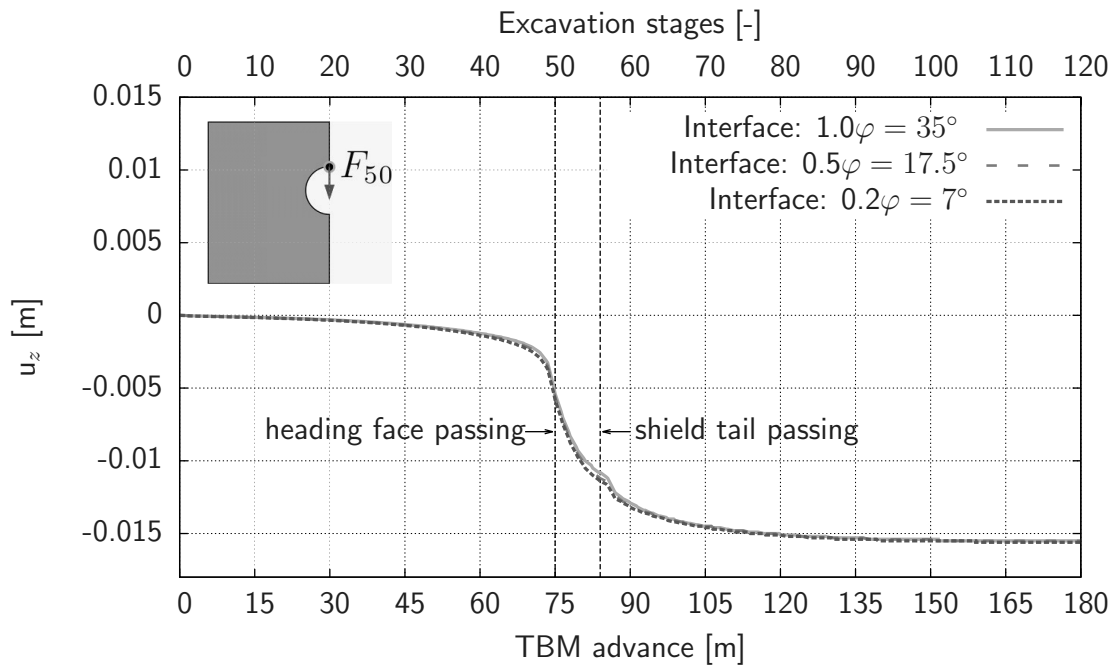

Figure 3.60.: Vertical displacements on the tunnel crown at observation section 50 during the excavation of the shallow tunnel. Interface stiffness is fixed: $E = 100$ MPa = const.
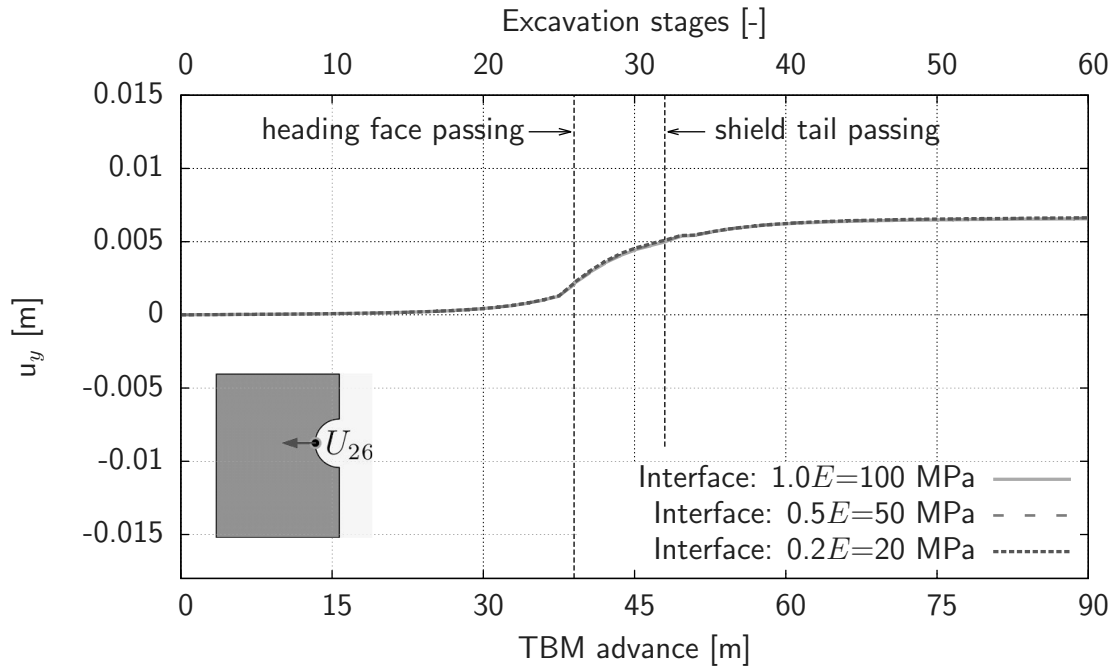
Figure 3.61.: Horizontal displ. of the tunnel side wall at observation section 26 during the excavation of the shallow tunnel. The interface strength is fixed: $\varphi = 35.0° = \text{const.}$
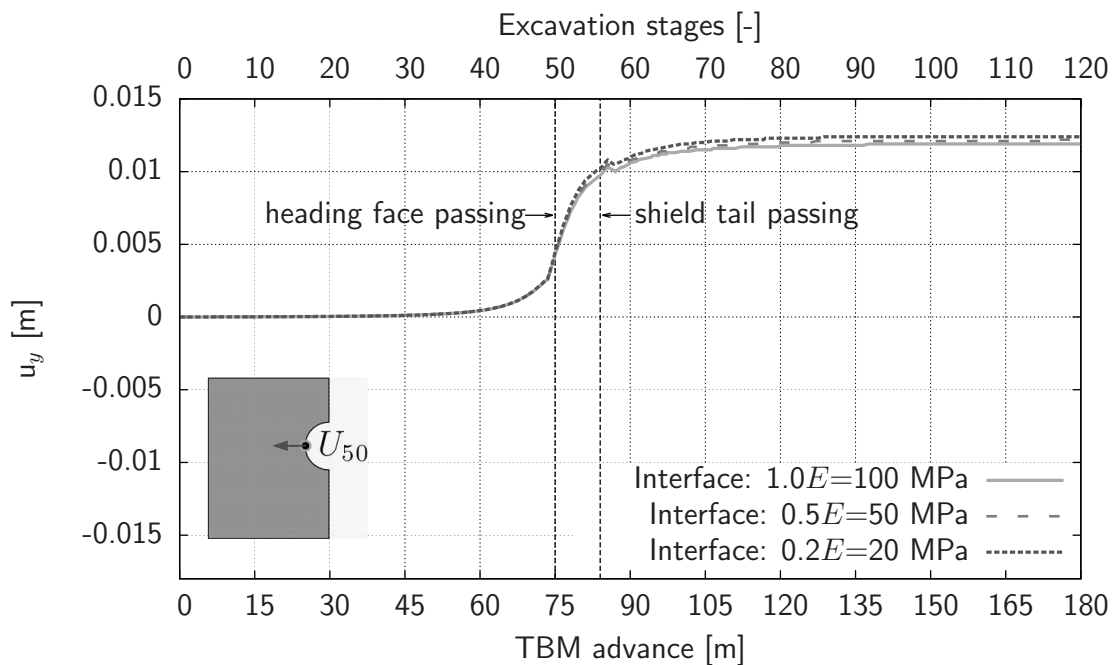

Figure 3.62.: Horizontal displ. of the tunnel side wall at observation section 50 during the excavation of the deep tunnel. The interface strength is fixed: $\varphi = 35.0° = \text{const.}$

Figure 3.63.: Horizontal displ. of the tunnel side wall at observation section 26 during the excavation of the shallow tunnel. Interface stiffness is fixed: $E = 100$ MPa $=$ const.
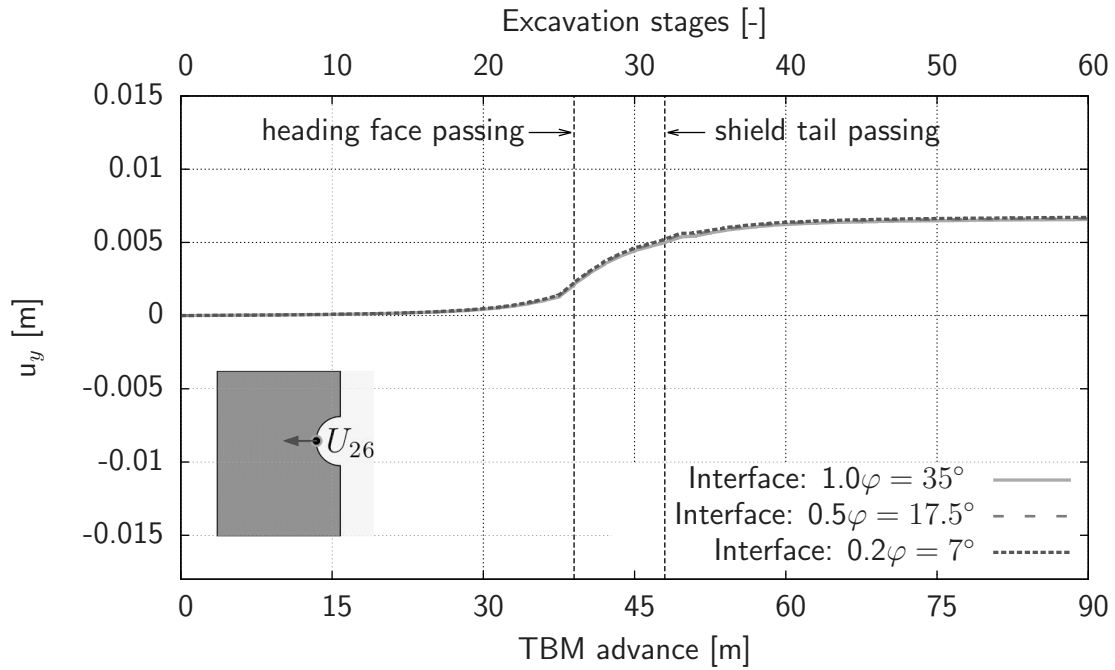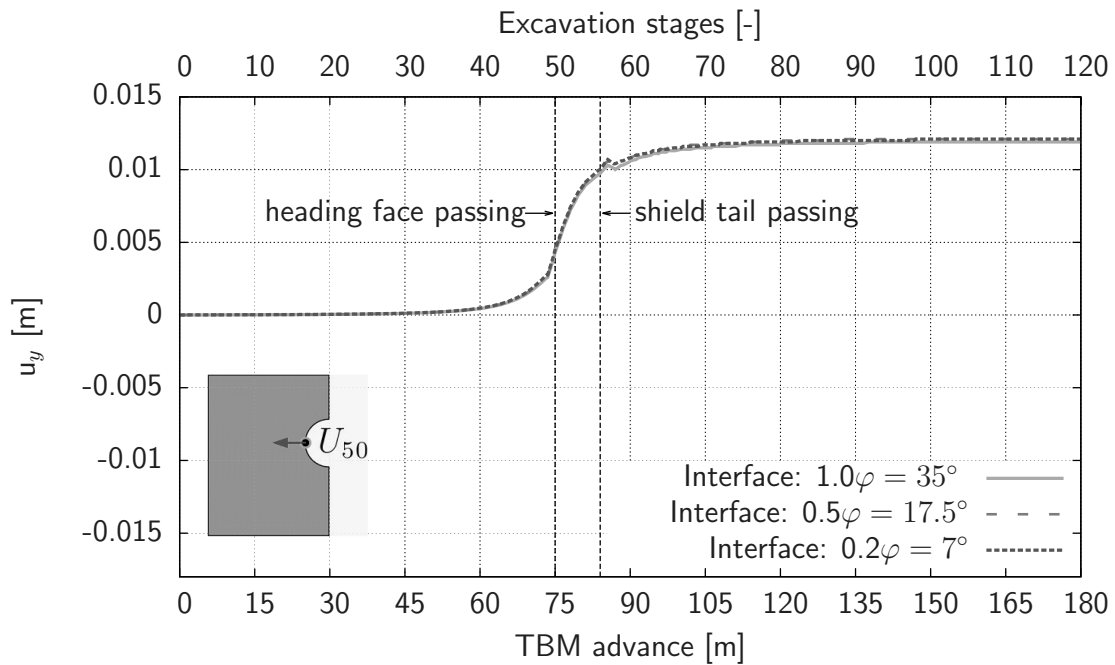

Figure 3.64.: Horizontal displ. of the tunnel side wall at observation section 50 during the excavation of the shallow tunnel. Interface stiffness is fixed: $E = 100$ MPa $=$ const.
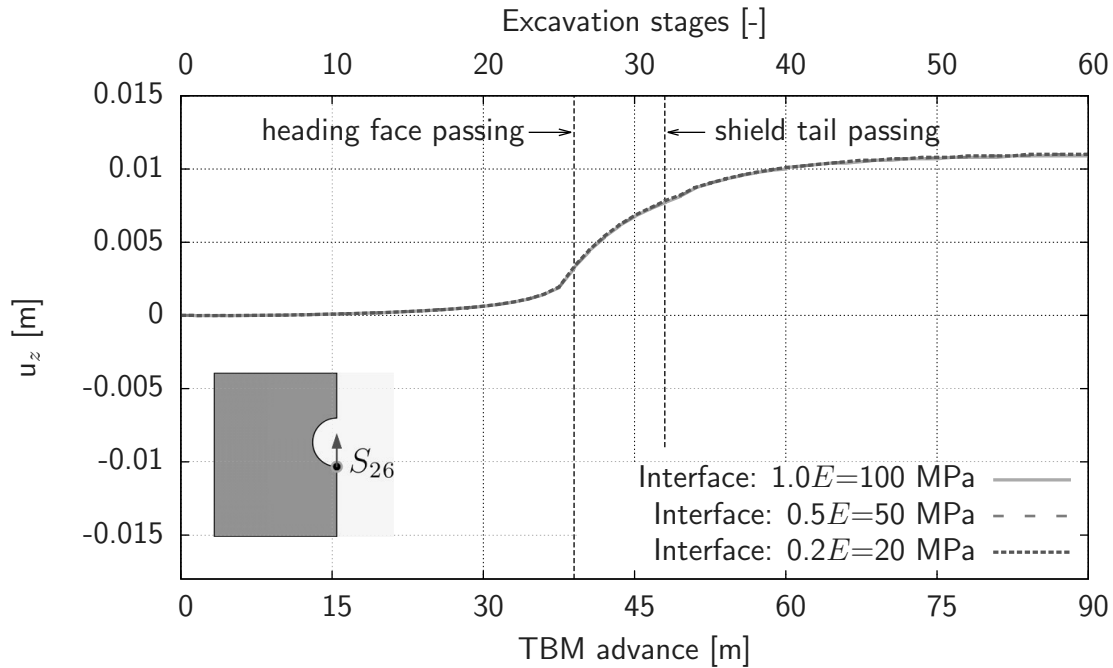
Figure 3.65.: Vertical displacements on the tunnel invert at observation section 26 during the excavation of the shallow tunnel. The interface strength is fixed: $\varphi = 35.0° = \text{const.}$

Figure 3.66.: Vertical displacements on the tunnel invert at observation section 50 during the excavation of the deep tunnel. The interface strength is fixed: $\varphi = 35.0° = \text{const.}$

Figure 3.67.: Vertical displacements on the tunnel invert at observation section 26 during the excavation of the shallow tunnel. Interface stiffness is fixed: $E = 100$ MPa $=$ const.
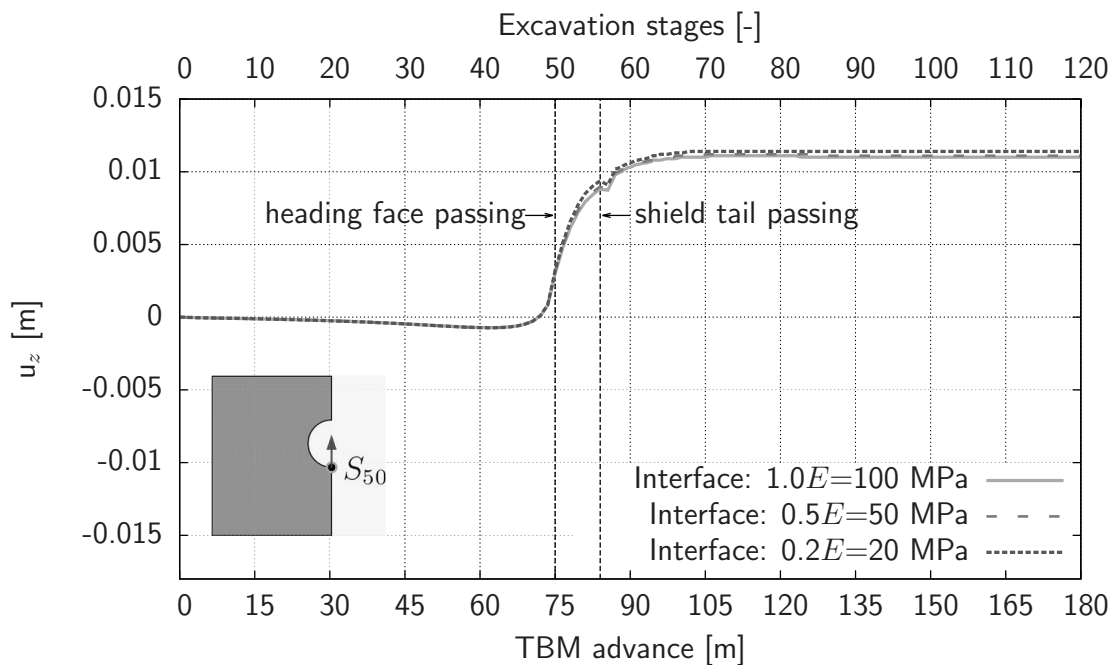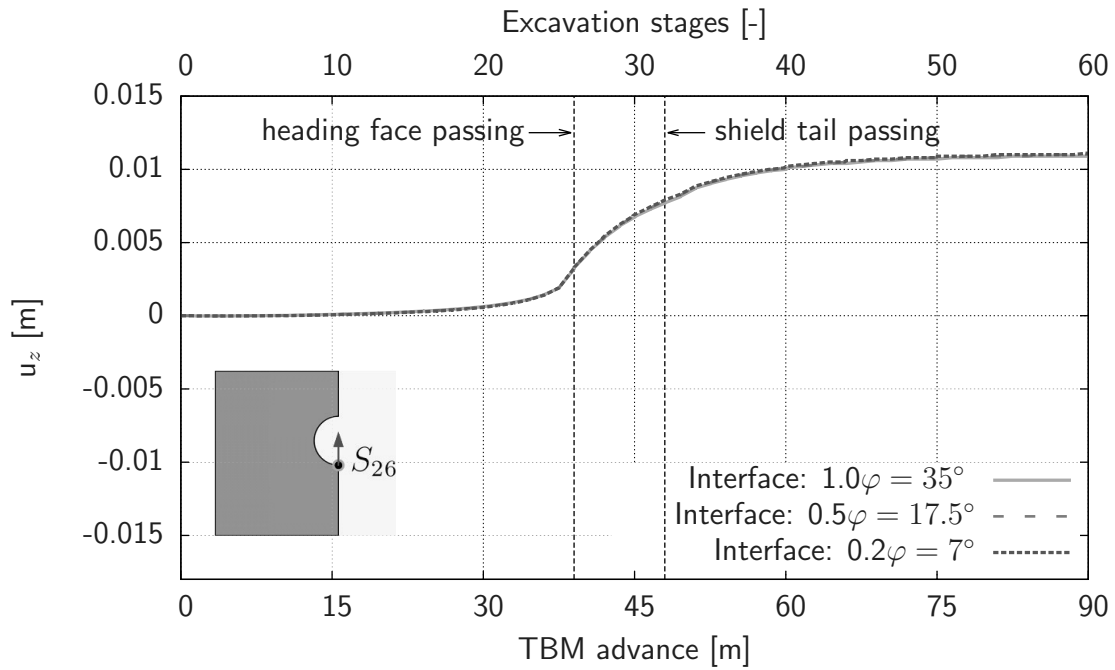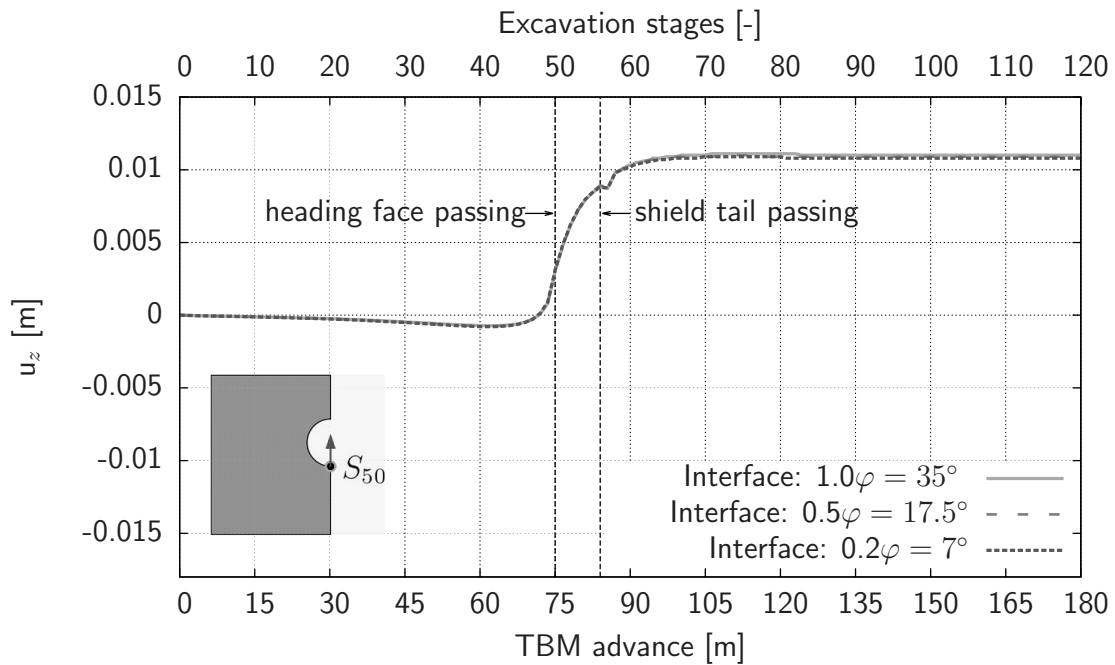

Figure 3.68.: Vertical displacements on the tunnel invert at observation section 50 during the excavation of the shallow tunnel. Interface stiffness is fixed: $E = 100$ MPa $=$ const.

interface properties are reduced. It is shown that the influence of the interface properties receding in importance with increasing the cover depth of the tunnel.

3.4.4. Steering Gap Relevancy

The results presented in Figures 3.69–3.82 show the largest influence regarding the displacements and the stresses in the subsoil. If the subsoil has the possibility to move free in the steering gap (i.e. when this gap is not filled with process mediums; called here "With TBM Conicity") than the surface settlements increase, as shown in Figures 3.69 and 3.70. That means, it is very important in the numerical simulation the actual size of the steering gap to be calculated as accurately as possible. The actual size of the steering gap is a function of the flow of the grout and bentonite around the TBM shield, which simplistically may be calculated analytically according to the concept suggested by Bezuijen (2007). However, more research is needed here for better understanding and considering the flow around the TBM and the soil-structure interaction during the advance.

Figure 3.69.: Vertical displacements on the ground surface at observation cross-section 26 during the excavation of the shallow tunnel (overburden = $1D$).

Figure 3.70.: Vertical displacements on the ground surface at observation cross-section 50 during the excavation of the deep tunnel (overburden = $5D$).
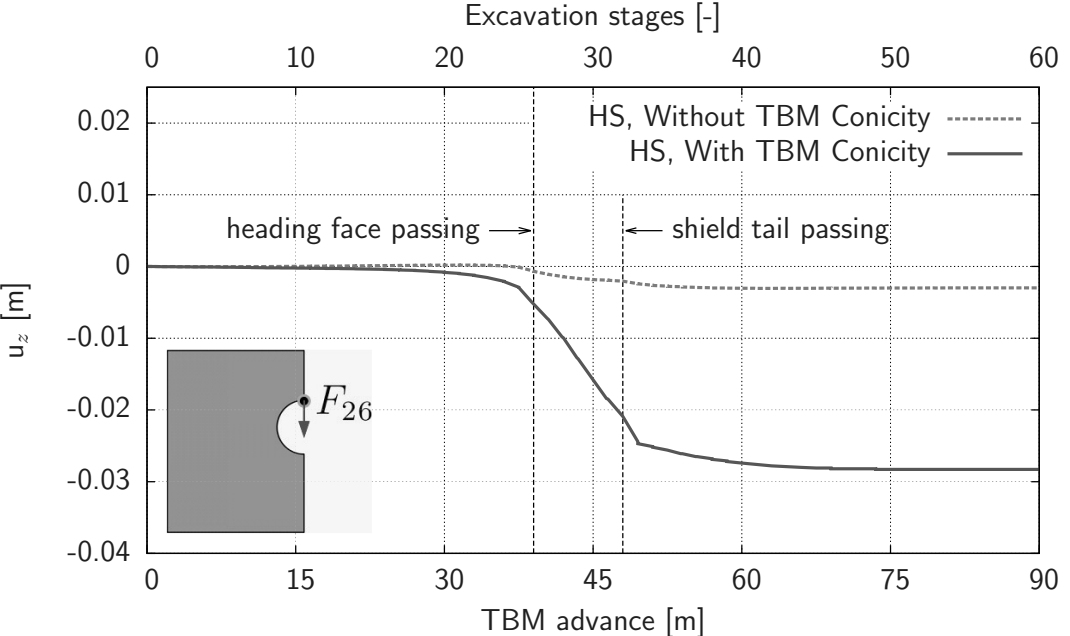
Figure 3.71.: Vertical displacements on the tunnel crown at observation cross-section 26 during the excavation of the shallow tunnel (overburden = $1D$).
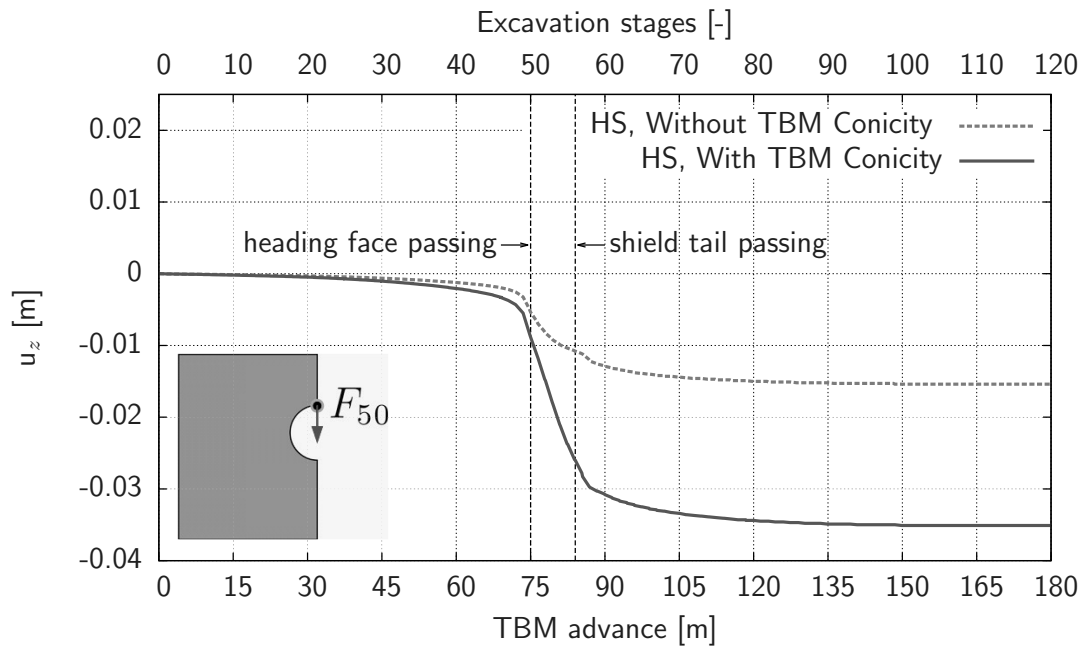
Figure 3.72.: Vertical displacements on the tunnel crown at observation cross-section 50 during the excavation of the deep tunnel (overburden = 5D).
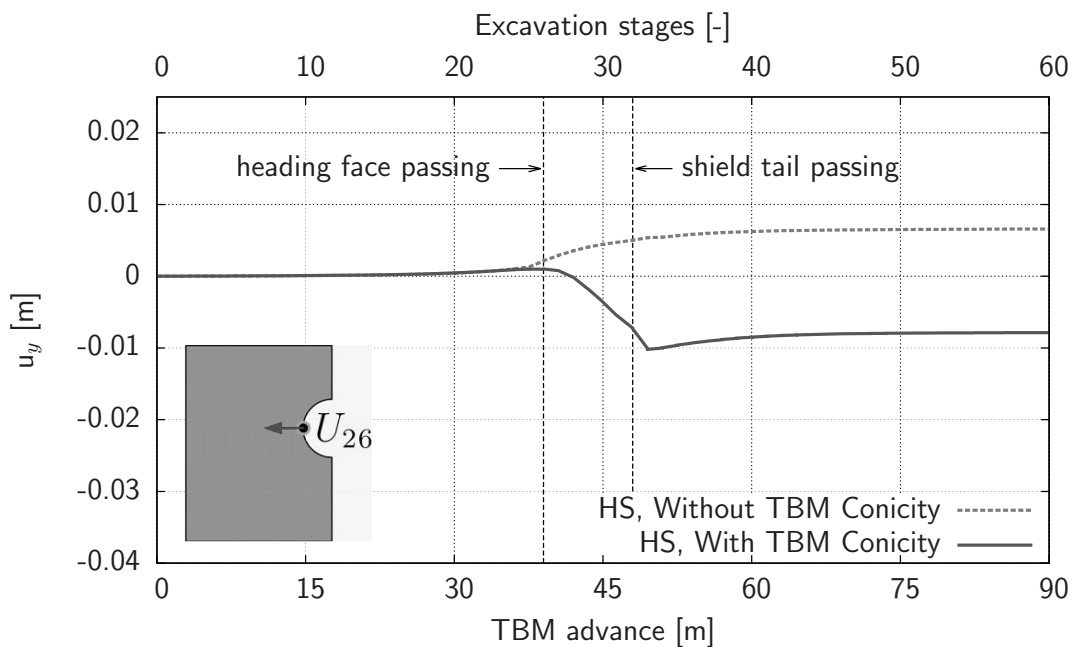
Figure 3.73.: Horizontal displacements of the tunnel side wall at observation cross-section 26 during the excavation of the shallow tunnel (overburden = 1D).
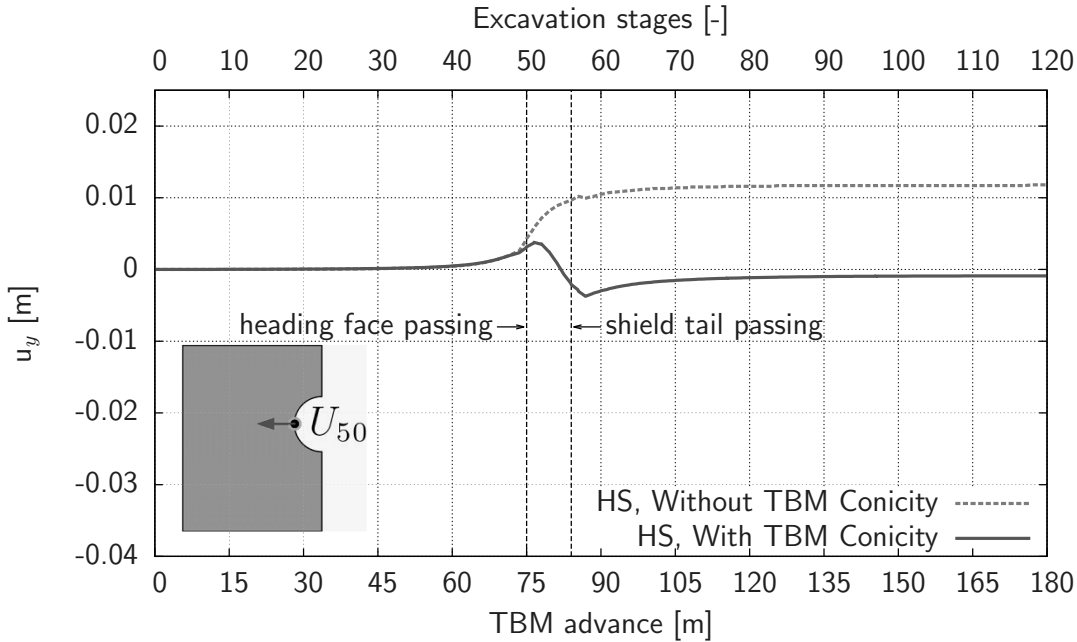
Figure 3.74.: Horizontal displacements of the tunnel side wall at observation cross-section 50 during the excavation of the deep tunnel (overburden = $5D$).
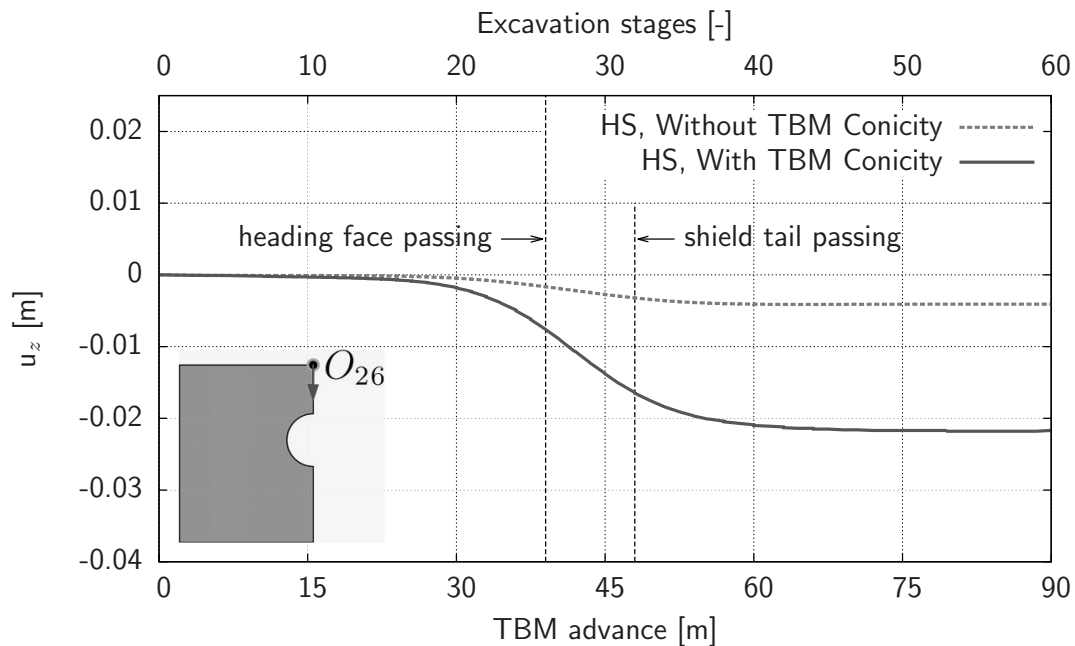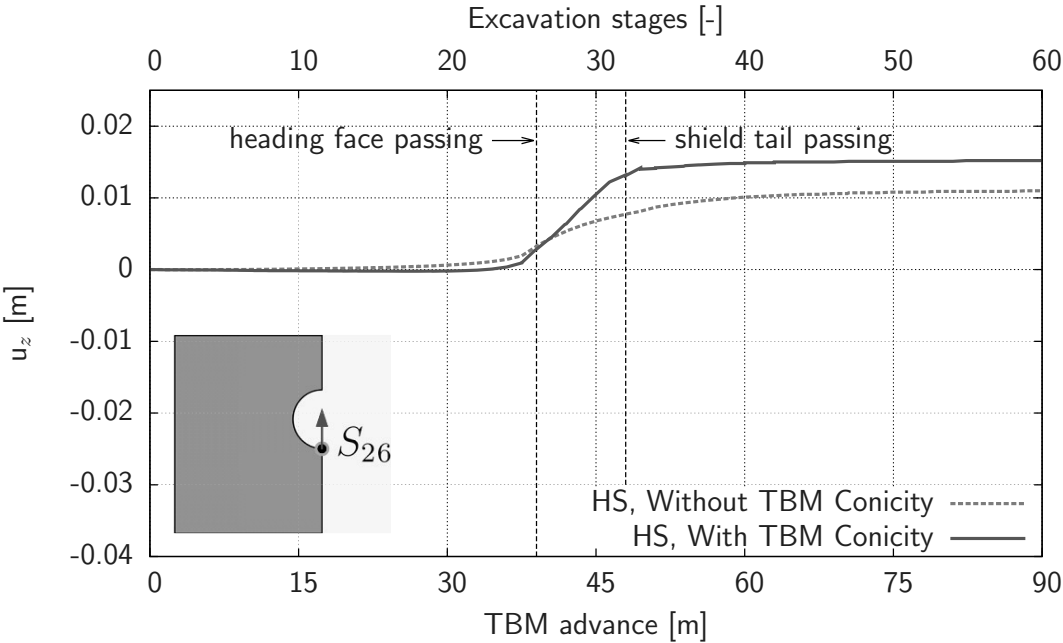

Figure 3.75.: Vertical displacements on the tunnel invert at observation cross-section 26 during the excavation of the shallow tunnel (overburden = $1D$).
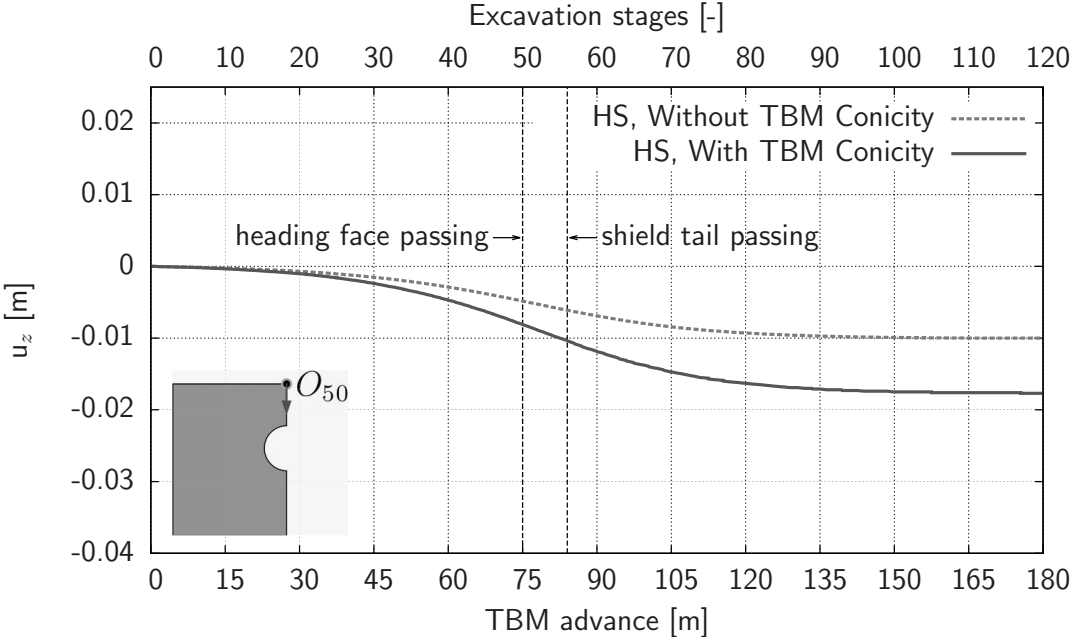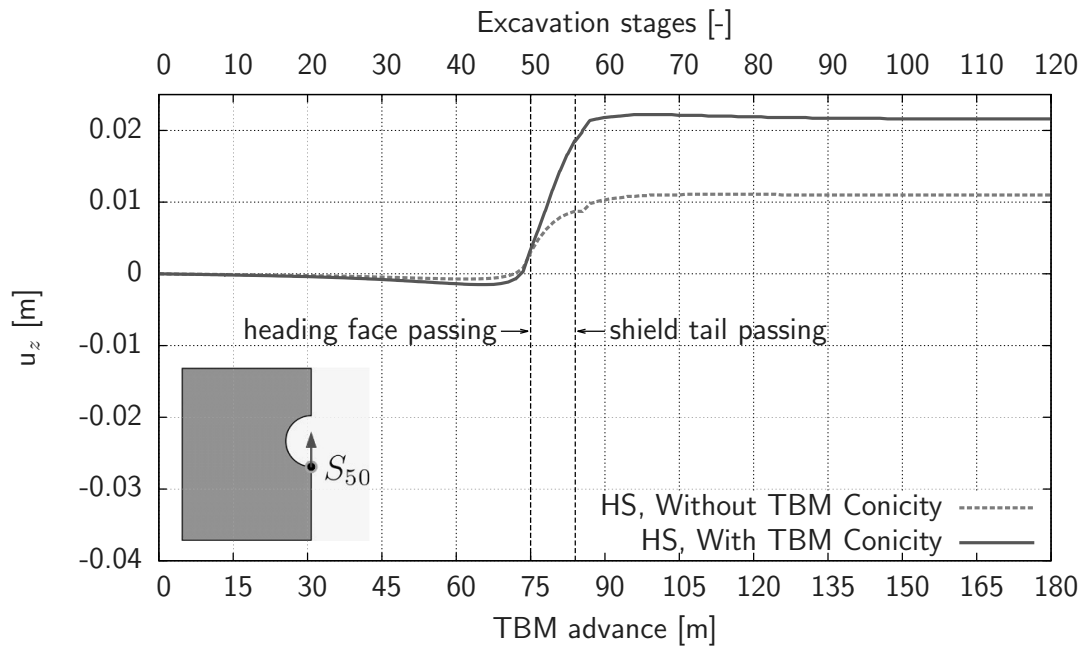
Figure 3.76.: Vertical displacements on the tunnel invert at observation cross-section 50 during the excavation of the deep tunnel (overburden = $5D$).
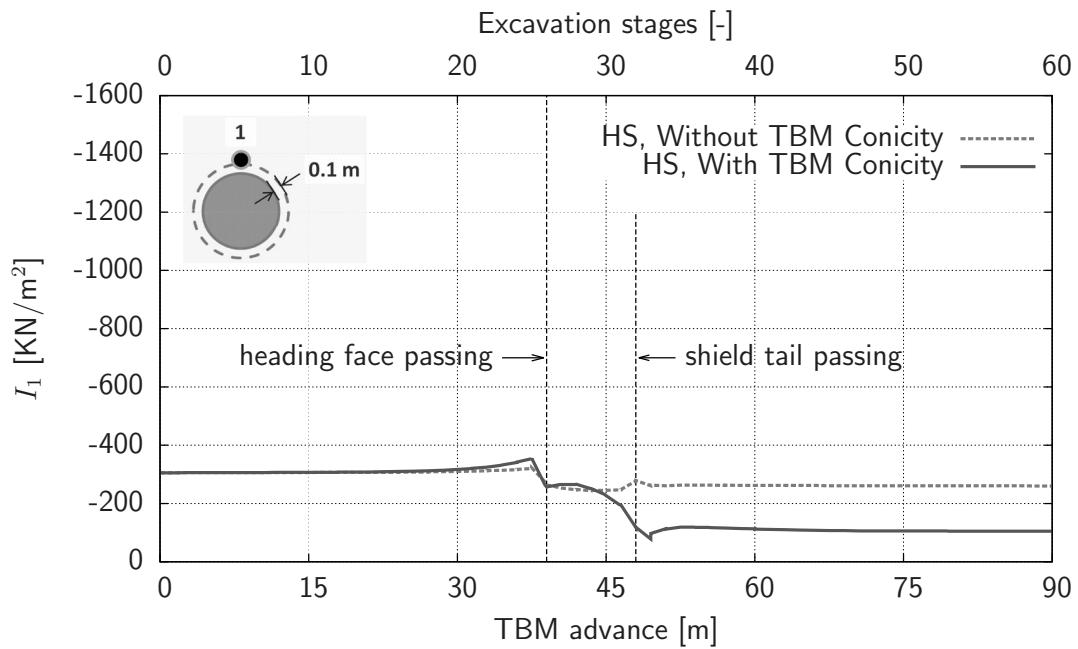
Figure 3.77.: First stress invariant at observation cross-section 26 (overburden = $1D$)
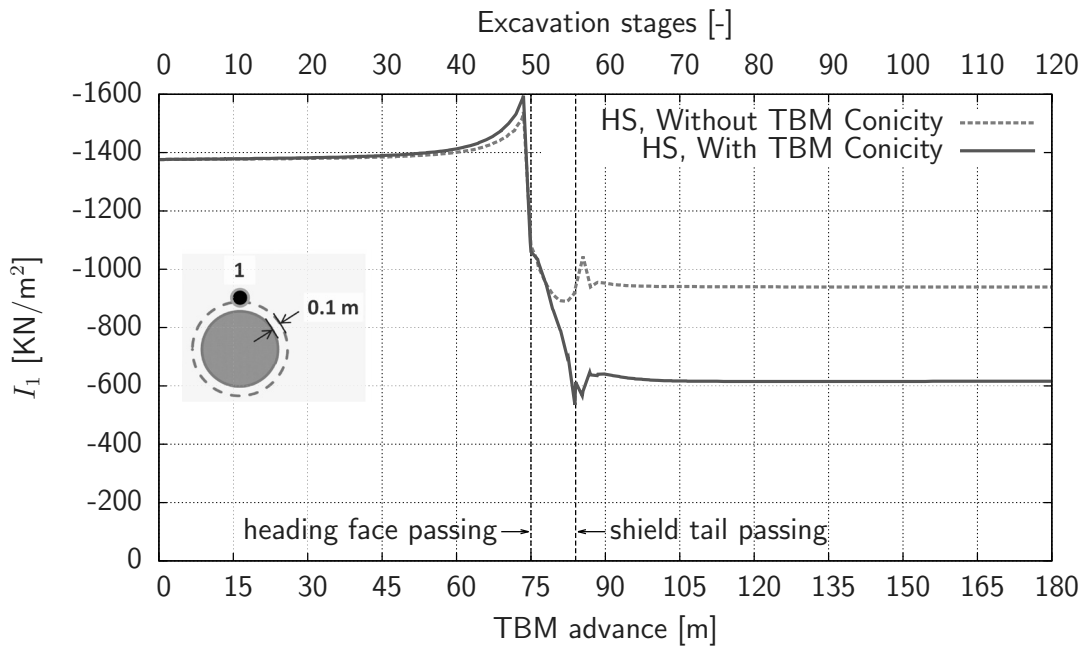
Figure 3.78.: First stress invariant at observation cross-section 50 (overburden = $5D$)
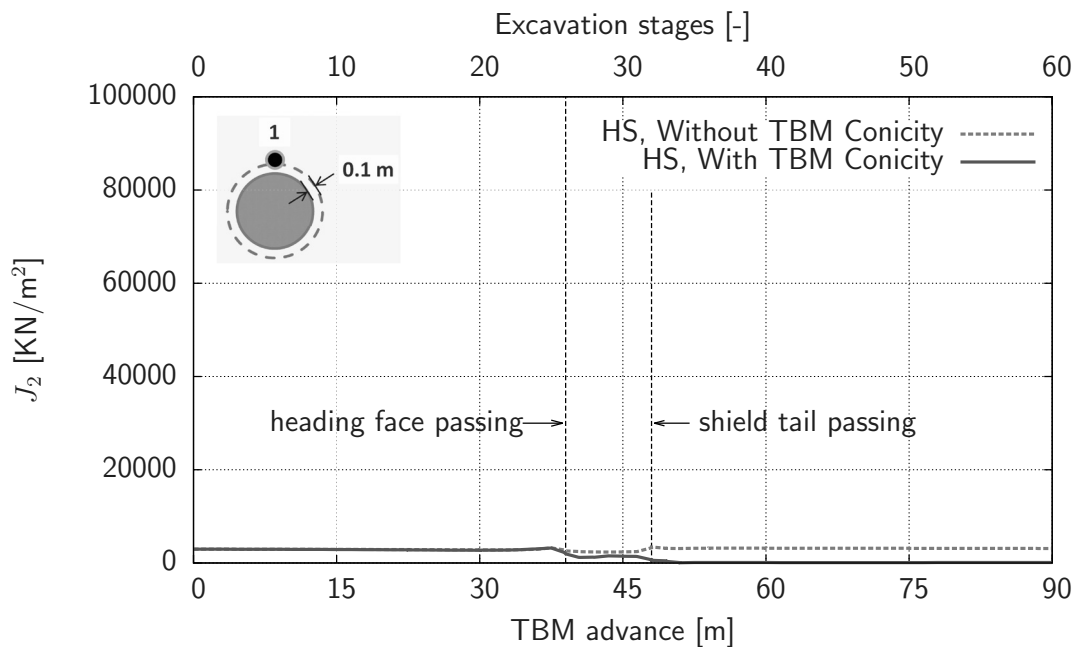
Figure 3.79.: Second deviatoric stress invariant at observation cross-section 26 (overburden = $1D$)
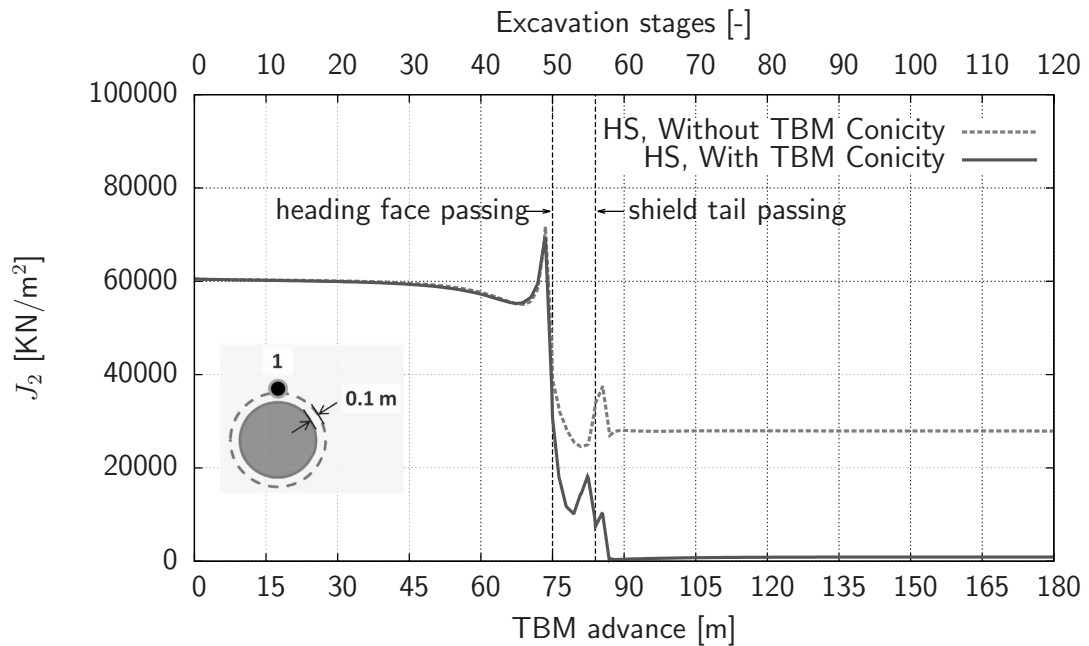
Figure 3.80.: Second deviatoric stress invariant at observation cross-section 50 (overburden $= 5D$)
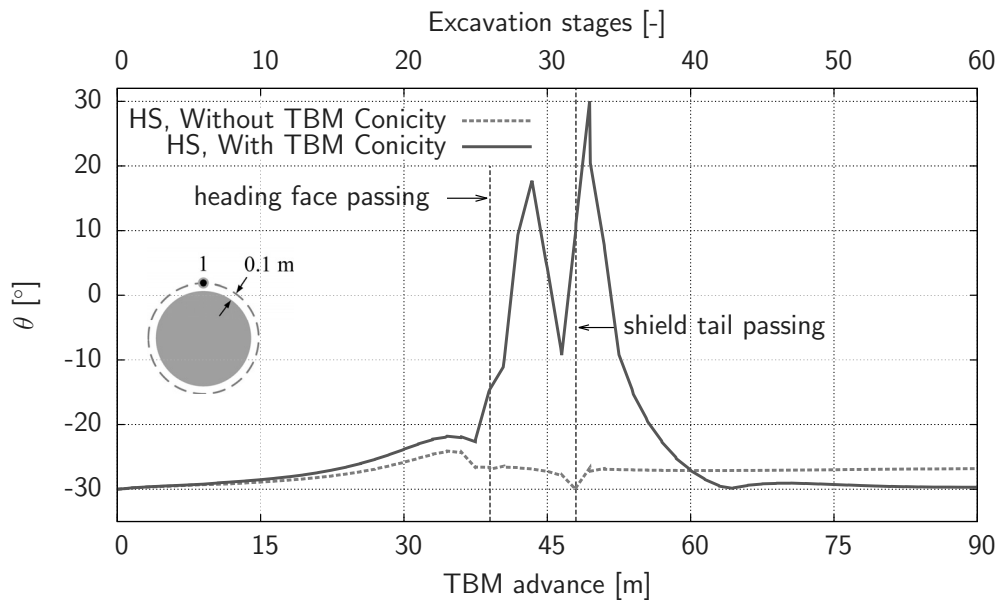
Figure 3.81.: Third stress invariant (Lode angle) at observation cross-section 26 (overburden $= 1D$)
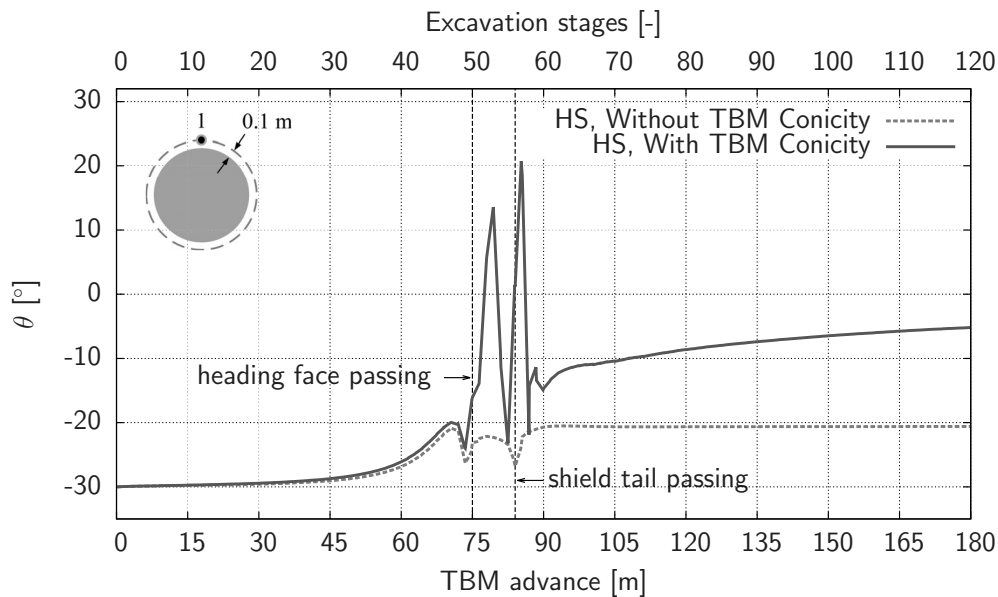
Figure 3.82.: Third stress invariant (Lode angle) at observation cross-section 26 (overburden = $5D$)

3.4.5. Annular Gap Grouting

In Figure 3.83 there are presented the calculated vertical displacements of the ground surface in O_{26} and at the tunnel invert in S_{26} at cross-section 26 during tunnelling of the shallow tunnel by using the different considered possibilities for modelling the grouting of the annular gap. This was done for a dry subsoil. The results has demonstrated that there is no significant difference in the predicted displacements (i.e. less than 1 mm) by the three variants I, II and III. Even for the last variant IV where the annular gap was not considered (Fig. 3.16, right), there are settlements, and this is due to the deformation (ovalisation) of the tunnel lining, and also due to the relative displacements between the soil and the plate elements in the interfaces. The input of the pressures is the same in the first three cases. However, the mesh is "relative large" around the tunnel, that means in variant I one plate element covers one length (in the X-direction) of 1.50 m, where the plate is not activated. That means the distributed load is applied on three FE-nodes – 2/3 of the load is applied on the middle node (i.e. direct on the soil elements), while the rest $2 \times (1/6)$ of the load on the two edge nodes (i.e. directly on the two surrounding plates, and not on the soil elements). Therefore the predicted settlements with variant I are a bit larger than these in variants II and III. However, in the presented grouting variants it is neglected the hydration of the grout material, i.e. there are neglected the time dependent material properties like the strength characteristics and the permeabilities
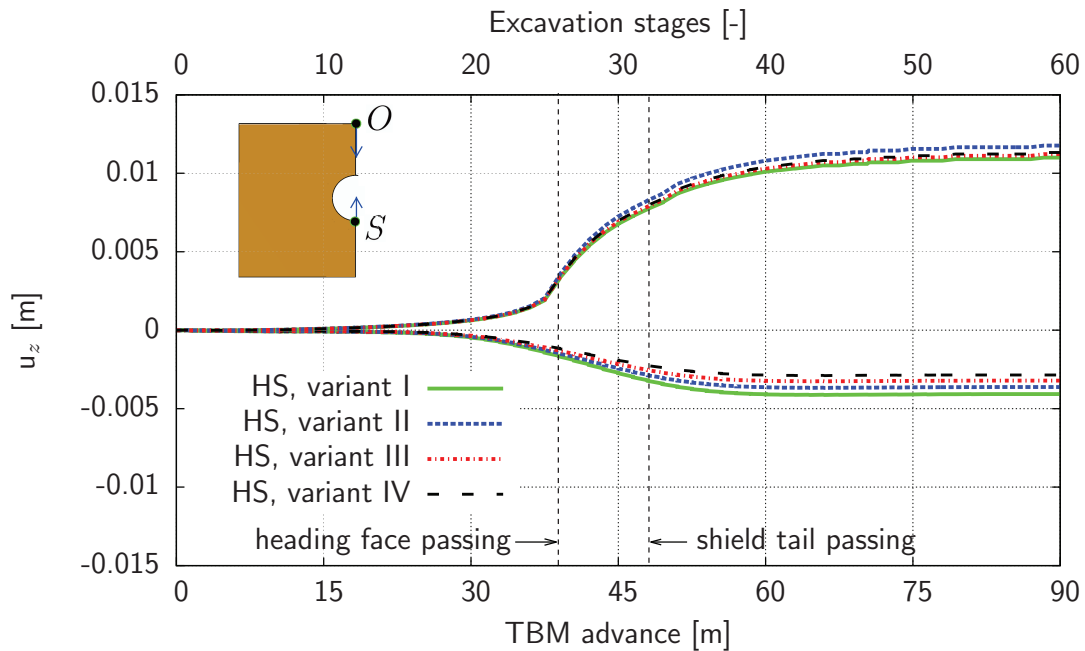
Figure 3.83.: Vertical displacements in observation points O_{26} and S_{26} during the excavation of the shallow tunnel for different variants of modelling the grouting of the annular gap. In excavation step 26 the TBM face reaches the observation cross-section.

of the grout. This may lead of underestimation of the surface settlements, e.g. in cases where the hydration time is not enough low (see e.g. Nagel 2009). Further, the flow of the grout mortar within the annular gap is not considered.

In Figure 3.84 there are presented the resulting forces – axial force N (in a direction perpendicular to the horizontal X-axis in excavation direction), and bending moment M (about the same X-axis) – in the plates (i.e. tunnel lining) at a cross section situated 2.25 m behind the shield tail, i.e. vertical cross section through the middle of the second lining ring. It is shown that the bending moments are relative similar and their value do not depends on the way of modelling the grouting. However, for the variants II and III there are the largest axial forces, which has to be expected also in the reality, while by the variants I and IV where the action of the grout pressure on the tunnel lining (plate) is not considered the axial forces are under-predicted. Just a small remark here is that for this comparison it was used the HS model and not the HSsmall, therefore the deformations of the tunnel lining are a bit larger to be expected (see in Figure 3.85), thus here the calculated bending moments may be are also overpredicted.

I

N

-418 kN/m

-813 kN/m   -128 kNm/m

-565 kN/m

M

136 kNm/m

127 kNm/m

II

N

-487 kN/m

-869 kN/m   -144 kNm/m

-639 kN/m

M

138 kNm/m

136 kNm/m

III

N

-472 kN/m

-845 kN/m   -131 kNm/m

-622 kN/m

M

135 kNm/m

134 kNm/m

IV

N

-393 kN/m

-824 kN/m   -136 kNm/m

-541 kN/m

M

135 kNm/m

127 kNm/m
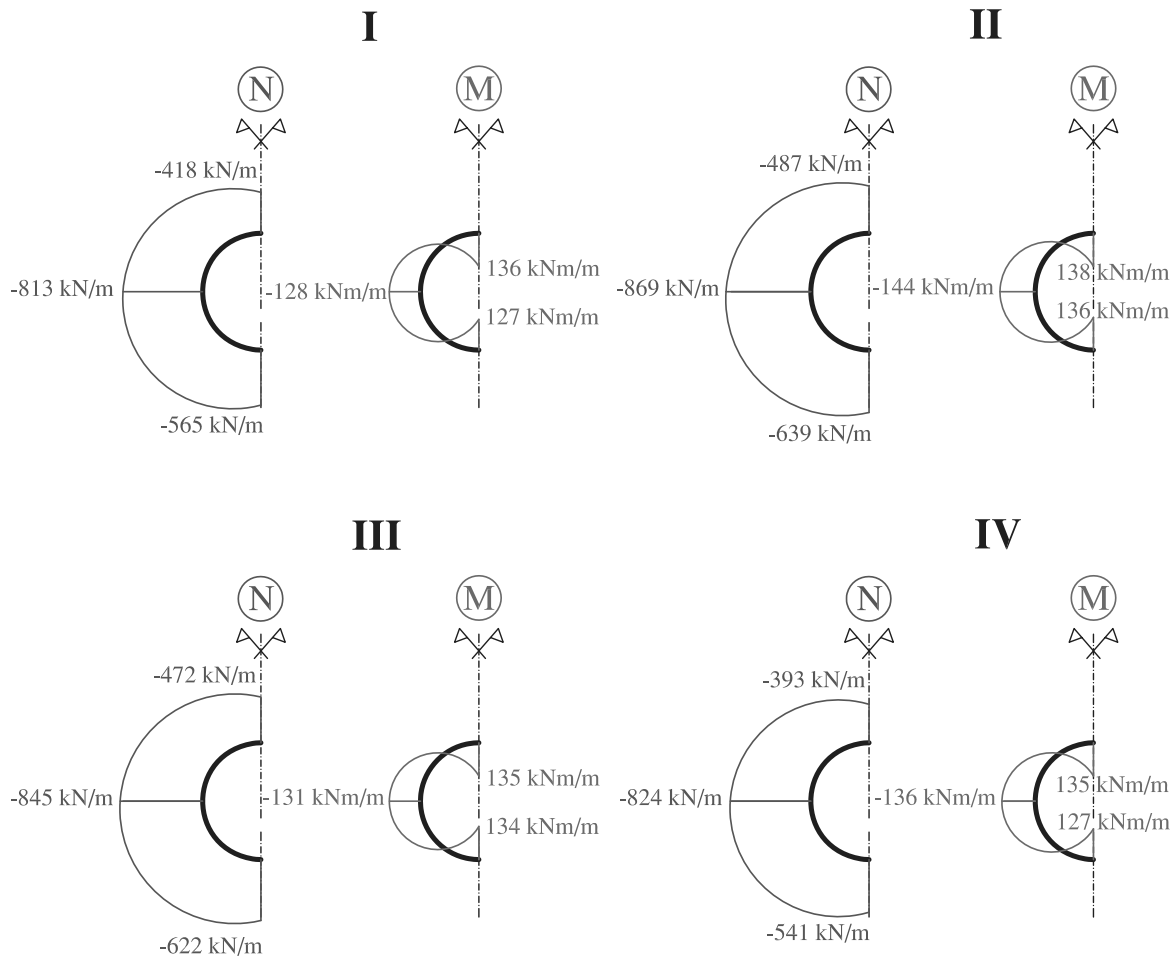
Figure 3.84.: Resulting forces – axial force N (in a direction perpendicular to the horizontal X-axis in excavation direction), and bending moment M (about the same X-axis) – in the plate (i.e. tunnel lining) at a cross section situated 2.25 m behind the shield tail, i.e. a cross section through the middle of the second lining ring. The negative axial forces N mean compression stress.

However, there is relatively no significant change in the calculated displacements in Figure 3.83 by adopting the firs three variants I, II and III, for modelling the annular gap, thereafter, variant I was selected for all other calculations done in the present thesis.

In Figure 3.85 there is presented the deformed shape of the tunnel lining – modelled with linear elastic plate elements – after the excavation of the shallow tunnel and using the HS model. This deformed shape is known as an ovalisation of the lining (i.e. squatting distortion, diametric distortion) and it is a typical deformation mode of a circular tunnel curving from a cylindrical form to an elliptical form subject to external loads like earth and grouting pressure (see Li *et al.* 2013). Generally, the ovalisation of the tunnel lining

increases when the K_0 value (see Table 3.2) is less than one, and also the magnitude of the ovalisation increases with decrease in soil stiffness (Li *et al.* 2013). It is also in the same Figure 3.85 shown the typical uplift of the tunnel lining due to the soil unloading below the tunnel invert. The weight of the placed (concrete) tunnel lining and the tunnel installation is (few times) less than the weight of the removed/excavated soil, so the structure (i.e. the tunnel lining tube) is initially not in vertical equilibrium. In order to gain equilibrium an upward movement (uplift) of the tunnel invert occur, initiating stress redistribution above, and stress relief under the tunnel (see additionally Bakker 2003); the soil was modelled as no water saturated, i.e. there was no ground water. Further, in Figure 3.86 there is shown the deformed shape of the shield of the TBM – also modelled with linear elastic plate elements. At the shield tail it is observed the maximum deformation to occur.

Figure 3.85.: Two different views of the deformed shape (ovalisation) of the tunnel lining after the excavation of the shallow tunnel (scaled up to 200 times; HS model, grouting variant I).

Figure 3.86.: Visualisation of the deformed shape of the shield of the TBM by the excavation of the shallow tunnel (scaled up to 50 times; HS model, grouting variant I).
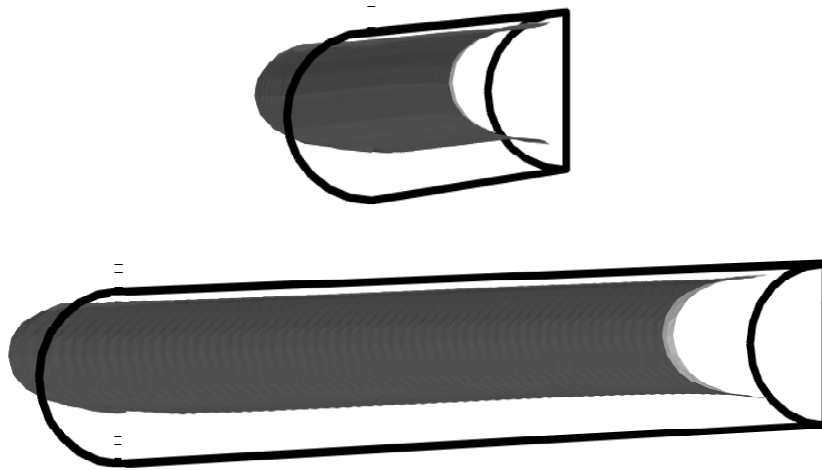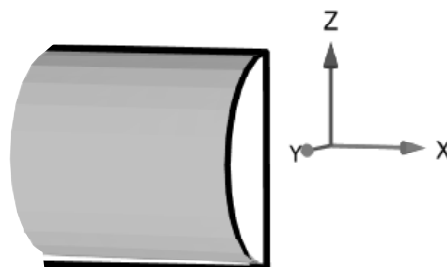
The immediate grouting, and the grouting pressure are of crucial importance and they largely influence the surface settlements. This is demonstrated with the calculated settlements in Figures 3.87 and 3.90 for dense and loose soil material (for a dry subsoil, with the HS model, and grouting variant I). The steering gap was neglected, i.e. the shield conicity and the overcutting were not considered, which leads to underestimating of the surface settlements. However, these simplified assumptions are appropriate for demonstrating here the importance of the accurate backfilling of the annular gap and its modelling. The action of the grout pressure on the surrounding subsoil is simulated via non-uniformly distributed load applied to the soil elements by deactivating the plate elements of the tunnel lining at the place grouting acts for a length of 1.50 m (i.e. grouting variant I). The used values by the excavation of the shallow tunnel are from 145 kN/m^2 at the tunnel crown linearly increased with depth up to 230 kN/m^2 at the tunnel invert. As shown in Figures 3.87 and 3.88 there are performed three additional calculations with lower grouting pressures – 45 kN/m^2 at the crown to 130 kN/m^2 at the invert, 15 kN/m^2 at the crown to 100 kN/m^2 at the invert, and finally zero at the crown to 85 kN/m^2 at the invert. Observation point (FE-node) O_{26} is fixed on the ground surface (see Fig. 3.18) where the subscribe 26 means that it is situated at the 26$^{\text{-th}}$ excavation stage, i.e. 39.00 m from the tunnel beginning (one excavation stage corresponds to 1.50 m tunnel advance). In O_{26} there are measured the vertical displacements u$_z$ during the excavation. The same idea belongs to the deep tunnel where the observation point on the ground surface is O_{50}. It is shown that the settlements are larger by the looser soil, thus, much more attention has to be paid when tunnelling in loose soil conditions.

3.5. Tunneling in Water-Saturated Subsoil

This part of the thesis is dedicated to the 3D numerical simulation of mechanized tunnelling when the ground is fully water saturated. The analyses are performed only for the shallow tunnel (see e.g. Fig. 3.4). In case of fully water saturated ground conditions a fully coupled elastoplastic consolidation analysis is performed using an advanced elastoplastic soil constitutive model – the HS model (as described in Section 3.1.3.2) with the input parameters as given in Table 3.2. Further, it has been investigated the influence of incorporating the evolution of the soil hydraulic conductivity on the predicted numerical response. Conductivity changes in the surrounding subsoil around the tunnel are caused by the infiltration process from the injected back-filled grout (Schaufler *et al.* 2013). Finally, the results are compared and discussed.

Figure 3.87.: Settlements of the ground surface at observation section 26 for different values of the grouting pressure during the excavation of the shallow tunnel in dense subsoil.

Figure 3.88.: Settlements of the ground surface at observation section 26 for different values of the grouting pressure during the excavation of the shallow tunnel in loose subsoil.

Figure 3.89.: Settlements of the ground surface at observation section 50 for different values of the grouting pressure during the excavation of the deep tunnel in dense subsoil.
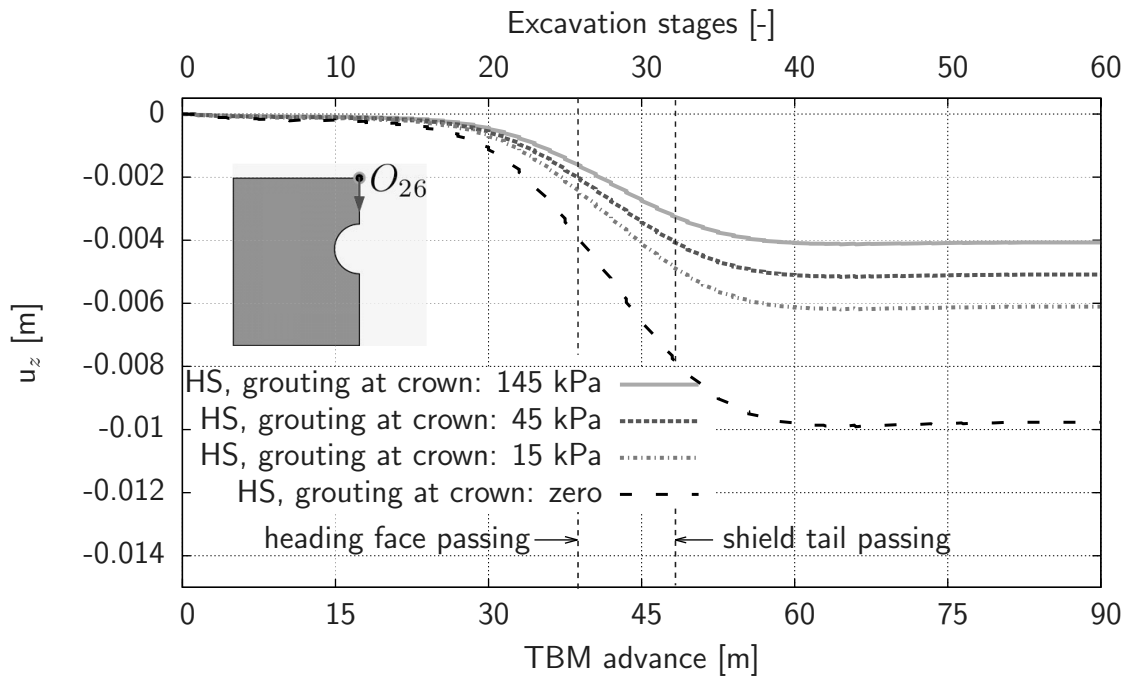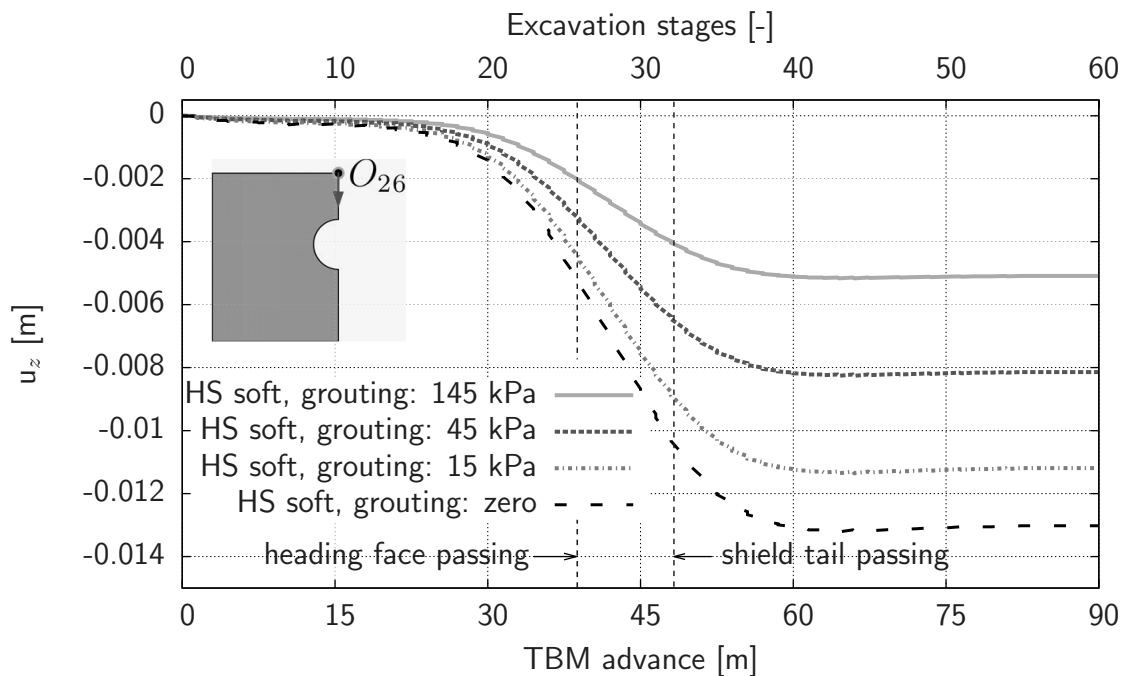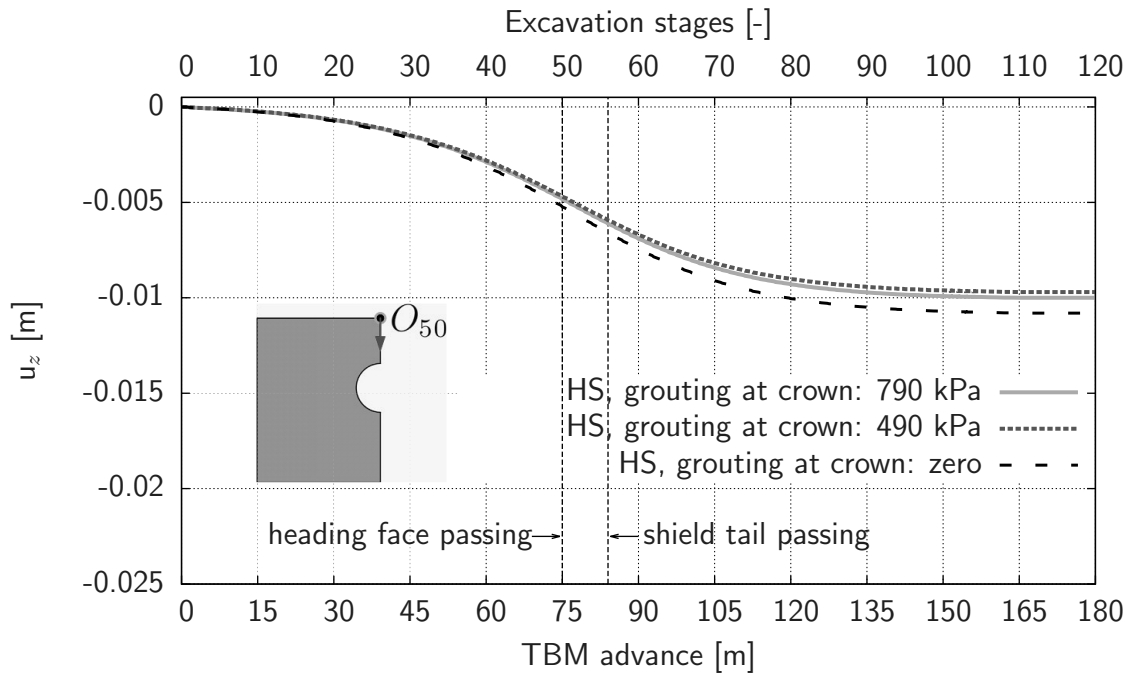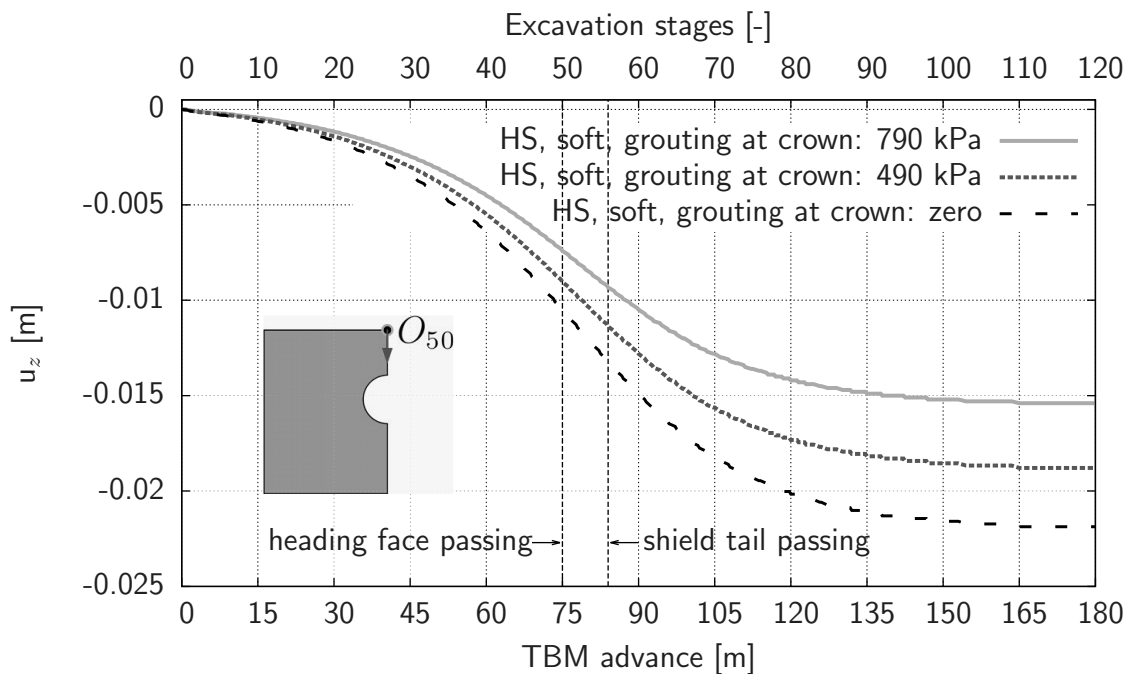

Figure 3.90.: Settlements of the ground surface at observation section 50 for different values of the grouting pressure during the excavation of the deep tunnel in loose subsoil.

3.5.1. Introduction

In a fully water-saturated soil with relatively low hydraulic conductivity the advance speed of the mechanized excavation via TBM greatly influences the development of the deformations, particularly the ground surface settlements. Generally, by a mechanized tunnelling they are generated excess pore water pressures around the tunnel heading due to the redistribution of the stresses around the TBM and additionally due to the applied support pressures – face support and grouting of the annular gap. In the same time these excess pressures are dissipating over the time causing a seepage flow in the surrounding subsoil. This changes the effective stresses in the surrounding subsoil and causes additional time-dependent deformations, i.e. soil consolidation. The higher the TBM advance speed and relatively lower the permeability of the soil, the less will the generated excess pore water pressures dissipate in the surrounding subsoil around the TBM, consequently, the smaller the deformations will be. If, otherwise, the soil permeability is relatively high and the advance rate enough low, fully drained conditions will prevail during the excavation. This behaviour was observed by Anagnostou (2008) in a 3D numerical simulation of tunnelling. Depending on the relation of the TBM advance speed to the hydraulic conductivity of the soil, the hydraulic conditions of the subsoil will be "*undrained*", fully "*drained*" or somewhere in-between. In the current study there are only investigated the two extreme cases – "undrained" or "drained". Further, the "undrained" situation can be modelled in two ways which are called here *consecutive* and *continuous* (s. additionally Section 3.5.5). By the consecutive approach each excavation step (described before in Section 3.1.2) is modelled in two single calculation phases. The first phase is an undrained effective stress analysis with input of effective soil strength and stiffness parameters, while the second phase is a consolidation type of analysis. By the continuous approach each excavation step is modelled in one single consolidation phase.

3.5.2. Annular Gap Modelling

As it was explained before in Section 3.1.7 the annular gap is backfilled with mortar (see in Fig. 3.1, 3.16, and 3.4), which is injected from a reservoir, acting as a buffer, to ensure a constant grouting pressure, independent of the excavation velocity of the TBM. The gradient between pore pressure of the surrounding soil and the grouting pressure of the mortar triggers seepage of the mortar into the surrounding soil. During this process mostly the fluid fraction of the mortar is transported. It has been assumed that the fluidized fines, i.e. small particles dissolved in the fluid fraction, are transported with the fluid.

However, different phenomena, depending on the hydraulic boundary conditions as well as on the properties of soil and mortar, can occur. Thus, an attachment of fine fluidized particles at the border in between the soil and mortar can take place. Hence, a steady growing layer appears with lower hydraulic conductivity compared to the one of the surrounding soil, which counteracts the dewatering of the mortar (Schaufler *et al.* 2012b). It means a filter cake is developed. The formation of it can be outside the filtering layer (external filter cake) or inside a filtering layer (internal filter cake).

It can be postulated, that grouting of the annular gap has a macroscopic influence on the surrounding (settlements on the surface), whereas the process is mainly driven by microstructural physical properties regarding hydraulic and geometric conditions (see Schaufler *et al.* 2012b).

In the present study it is assumed that the steering gap (described in detail in Section 3.1.6) is completely filled with the support mediums (fresh grout and bentonite). It has been considered and calculated the pressure distribution profile around the TBM shield (no nozzles considered) and the tunnel lining according to the 1D analytical models presented in Bezuijen (2007) and Bezuijen & Talmon (2003). In the presented models the fresh grout and the bentonite are assumed as Bingham liquids, which means that a certain pressure gradient is needed to start a flow along the tunnel. Further, the pressure drop is calculated – independently for the fresh grout and bentonite – for slices with a thickness 1.50 m – the same length as assumed for a single tunnel lining ring in the FE-simulation. Thereafter, the fluid pressures derived from this analyses are used as input data in the derived mesoscopic model (will be described later) for computing the evolution of the soil hydraulic conductivity around the tunnel in space and time. Then, this updated conductivity around the tunnel is used again in the FE-model of the tunnelling, in order to evaluate its influence on the numerical predictions.

3.5.3. Elastoplastic Consolidation

In the following the basic equations governing the transient deformation of (water) saturated soil are presented as used for the current numerical analysis. These governing equations follow the Biot's self-consistent consolidation theory (Biot 1956). The formulation is based on small strain theory and the fluid (water in the present study) flow is assumed to obey Darcy's low (1856). In Biot's theory the saturated soil is treated as a continuum mixture.

According to Terzaghi's principle (Terzaghi 1936, 1943), total stresses $\boldsymbol{\sigma}$ in the soil are divided into effective stresses $\boldsymbol{\sigma}'$ and total pore pressures p_{active}:

$$\boldsymbol{\sigma} = \boldsymbol{\sigma}' + \mathbf{m} \underbrace{(p_{steady} + p_{excess})}_{p_{active}}, \tag{3.39}$$

where $\mathbf{m}$ is a vector containing unity terms for normal stress components and zero terms for the shear stress components, and in a three-dimensional context is given as

$$\mathbf{m} = [1\ \ 1\ \ 1\ \ 0\ \ 0\ \ 0]^{\mathrm{T}}, \tag{3.40}$$

p_{steady} is the hydrostatic pore water pressure (calculated at the beginning with the initial conditions) and p_{excess} is the excess pore water pressure – assumed to be positive for tension (vacuum) and negative for pressure; the same assumption to the effective stresses. Further, the constitutive equation (law) constitutes a relation between rates of effective stresses $\dot{\boldsymbol{\sigma}}'$ and total strains $\dot{\boldsymbol{\varepsilon}}$, and represents the material behaviour:

$$\dot{\boldsymbol{\sigma}}' = \mathbf{D}^{\mathbf{ep}}\,\dot{\boldsymbol{\varepsilon}}, \tag{3.41}$$

where $\mathbf{D}^{\mathbf{ep}}$ represents the elastoplastic stiffness matrix, and $\dot{\boldsymbol{\varepsilon}} = \dot{\boldsymbol{\varepsilon}}^e + \dot{\boldsymbol{\varepsilon}}^p$ with $\dot{\boldsymbol{\varepsilon}}^e$ and $\dot{\boldsymbol{\varepsilon}}^p$ elastic resp. plastic strain rate component.

In a multiphase medium the volumetric strains ($\varepsilon_v = \varepsilon_x + \varepsilon_y + \varepsilon_z$) are strongly coupled with the flow of the pore fluid. In order for a certain amount of volumetric strain to occur the pore fluid must flow out first (if the fluid is incompressible). The equation describing the interaction/coupling of the volumetric strains and the flow of the pore fluid is called the continuity equation, or the storage equation.

To formulate the flow problem, the continuity equation for water is adopted in the following form (Song 1990, Brinkgreve *et al.* 2011c):

$$\nabla^{\mathrm{T}}\,\mathbf{R}\,\nabla p_{excess} = -\frac{\partial \varepsilon_v}{\partial t}, \tag{3.42}$$

where $\mathbf{R}$ is a matrix

$$\mathbf{R} = \begin{bmatrix} k_x & 0 & 0 \\ 0 & k_y & 0 \\ 0 & 0 & k_z \end{bmatrix}, \tag{3.43}$$

where k_x, k_y, and k_z are the three components of the hydraulic conductivity (unit of length per unit of time, i.e. velocity, e.g. m/s) in X-, Y-, and Z-directions, respectively, and in the present study it is assumed $k_x = k_y = k_z$.

Further, in Equation 3.42 the term $-\dfrac{\partial \varepsilon_v}{\partial t} = -\mathbf{m}^{\mathbf{T}} \dfrac{\partial \boldsymbol{\varepsilon}}{\partial t}$ is the overal compression of the soil due to effective stresses and excess pore water pressure.

Considering slightly compressible water, the rate of excess pore water pressure is calculated from the volumetric strain rate, according to (Brinkgreve 2011c):

$$\dot{p}_{excess} = \frac{K_w}{e_0/(1+e_0)} \, \dot{\varepsilon}_v, \qquad (3.44)$$

where e_0 is the initial (in-situ) void ratio (used $e_0 = 0.50$), and K_w is the compression (bulk) modulus of the pore fluid which is taken as (Brinkgreve *et al.* 2011c):

$$\frac{K_w}{e_0/(1+e_0)} = \frac{3(\nu_u - \nu_{ur})}{(1-2\nu_u)(1+\nu_{ur})} K_{skeleton}, \qquad (3.45)$$

where $K_{skeleton}$ is the bulk modulus of the solid particles forming the soil skeleton, ν_u is the undrained Poisson's ratio (used $\nu_u = 0.495$), and $\nu_{ur}(= 0.20)$ was the unloading/reloading Poisson's ratio (see in Tab. 3.2).

The excess pore water pressure is changing during the time and is the cause of the flow of water – according to Darcy's empirical low (see the first therm in Eq. 3.42) – in the porous medium. As it is there seen the water outflow is equal to the divergence of the specific discharge $\nabla^{\mathrm{T}} \mathbf{R} \, \nabla p_{excess} \equiv \nabla^{\mathrm{T}} \mathbf{q}$, where $\mathbf{q}$ is the rate of flow, or specific discharge (fluid velocity).

3.5.4. Evolution of the Soil Hydraulic Conductivity

The time dependent hydraulic conductivity in the region close to the annular gap is accounted for by introducing an additional 1D mesoscopic model (see Schaufler *et al.* 2012b, Schaufler *et al.* 2013). This model has a strong interaction with the macroscopic model, i.e. the tunnel simulation, as described before. The 1D mesoscopic model was performed within the framework of the theory of porous media (TPM). The TPM was used to describe the ongoing physical processes of the grouting mortar and the surrounding soil during the backfilling process of the annular gap. The TPM is describing the phenomena at the continuum scale, accounting for the micro structure of the corresponding domain.

It is assumed that the mortar and the surrounding soil are represented by a mixture of spherical particles of different types and a pore fluid. Therefore, the domain is described by four constituents φ^α with $\alpha = \{\mathfrak{f}, \mathfrak{a}, \mathfrak{sn}, \mathfrak{sa}\}$, which can be described by their volume fractions $n^\alpha = \mathrm{d}v^\alpha/\mathrm{d}v$. Basically, the volume is divided into a fractions which are: the

Table 3.4.: Material properties and used boundary conditions for calculating the time dependent soil hydraulic conductivity using the 1D mesoscopic model (see Fig. 3.91).

Length of domain 1	l	0.15	m
Length of domain 1 and 2	L	1.15	m
Concentration of fines	c_{02}	0.01	
Concentration of fines	c_{01}	0.1	
Effective dynamic viscosity	$\eta_0^{\mathfrak{f}R}$	1	mPa s
Initial porosity	ϕ_{02}	0.4	
Initial porosity	ϕ_{01}	0.4	
Material parameter	β_{01}	0.001	
Material parameter	β_{02}	0.004	
Calculation time	T	18000	s
a) Initial intrinsic permeability	$k_{01}^{\mathfrak{f}} = k_{02}^{\mathfrak{f}}$	1.02×10^{-16}	m^2
b) Initial intrinsic permeability	$k_{01}^{\mathfrak{f}} = k_{02}^{\mathfrak{f}}$	1.02×10^{-12}	m^2

rigid skeleton $\varphi^{\mathfrak{sn}}$, the fines which are attached to the skeleton $\varphi^{\mathfrak{sa}}$, the fluid dissolved fines $\varphi^{\mathfrak{a}}$, and the pore fluid $\varphi^{\mathfrak{f}}$ (Steeb 2008, de Boer 2000, Ehlers & Bluhm 2002).

Evolution of hydraulic properties during the backfilling process of grouting mortar can be traced back to infiltration of fines. Whereas infiltration processes can be interpreted as phase transition from fluidized fines to fines attached to the rigid skeleton ($\varphi^{\mathfrak{a}} \to \varphi^{\mathfrak{sa}}$). Due to an increase of the solid volume fraction by infiltration, the hydraulic conductivity decreases.

An initial and boundary value problem (IBVP) for the analysis of infiltration problems in porous materials was defined (see Fig. 3.91) and a FEM code is used to solve it. For a more detailed derivation of the governing equations and the numerical implementation the reader is referred to Schaufler *et al.* (2012a and 2012b).

In Figure 3.91(b) the situation during the process of grouting of the annular gap mortar is shown. The injection of the annular gap grouting mortar takes place in axial direction, e.g. by gap holes in the tail skin. In contrast the dewatering process, which is responsible for the evolution of hydraulic and mechanical properties, is mainly oriented in radial di-

(a) Illustration of the simulation of the grouting process

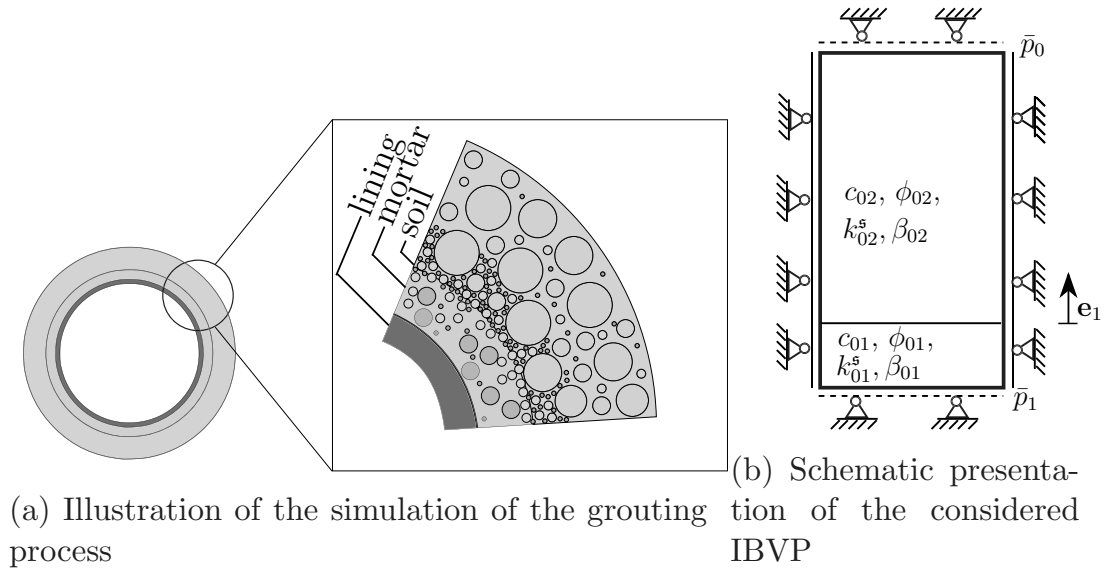(b) Schematic presentation of the considered IBVP

Figure 3.91.: Grouting of the annular gap during mechanized shield tunnelling.

rection around the tunnel axis. Therefore, the presented simulation capturing infiltration phenomena is reduced to a 2D model. Due to the symmetrical boundary conditions and homogeneous material properties, the problem is further reduced to 1D model. Therefore, the evaluation of the hydraulic properties takes place along the coordinate $\mathbf{e}_1$. The calculated IBVP is graphically summarized in Figure 3.91(a). It consists of two domains, simulating the fully filled annular gap (domain 1) and the surrounding soil (domain 2). In consequence of the pressure boundary conditions, $\bar{p}_1$ at the lower and $\bar{p}_0$ at the upper edge, a pressure gradient arises which leads to a material flow. The corresponding pressure distribution is shown in Figure 3.92. The input parameter of the calculated 1D mesoscopic model are given in Table 3.4. Hence, the evolution of the hydraulic properties of the soil, takes place in domain 2.

Aiming a better insight in the physics related to infiltration phenomena, two different examples were studied, where the initial hydraulic conductivity $k_0^{\mathfrak{f}}$ was varied. The evolution of the hydraulic conductivity caused by infiltration strongly depends on its initial value. In the first case ($k_0^{\mathfrak{f}} = 1 \times 10^{-9} \frac{m}{s}$) no significant change of hydraulic conductivity in terms of mechanized tunnelling can be observed after infiltration time of 5 h. In the second case ($k_0^{\mathfrak{f}} = 1 \times 10^{-5} \frac{m}{s}$) a distinct evolution of the hydraulic conductivity in space and time is observed.

In Figure 3.93 the evolution of the hydraulic conductivity in space and time of the surrounding soil is presented in a contour plot. It has to be noted, that with increasing
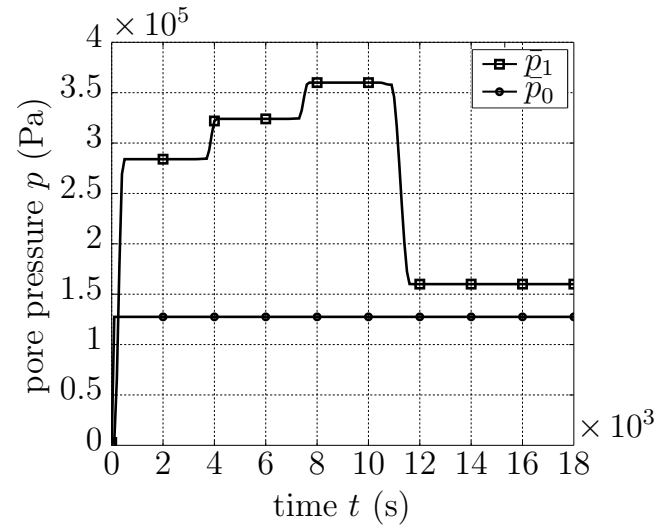
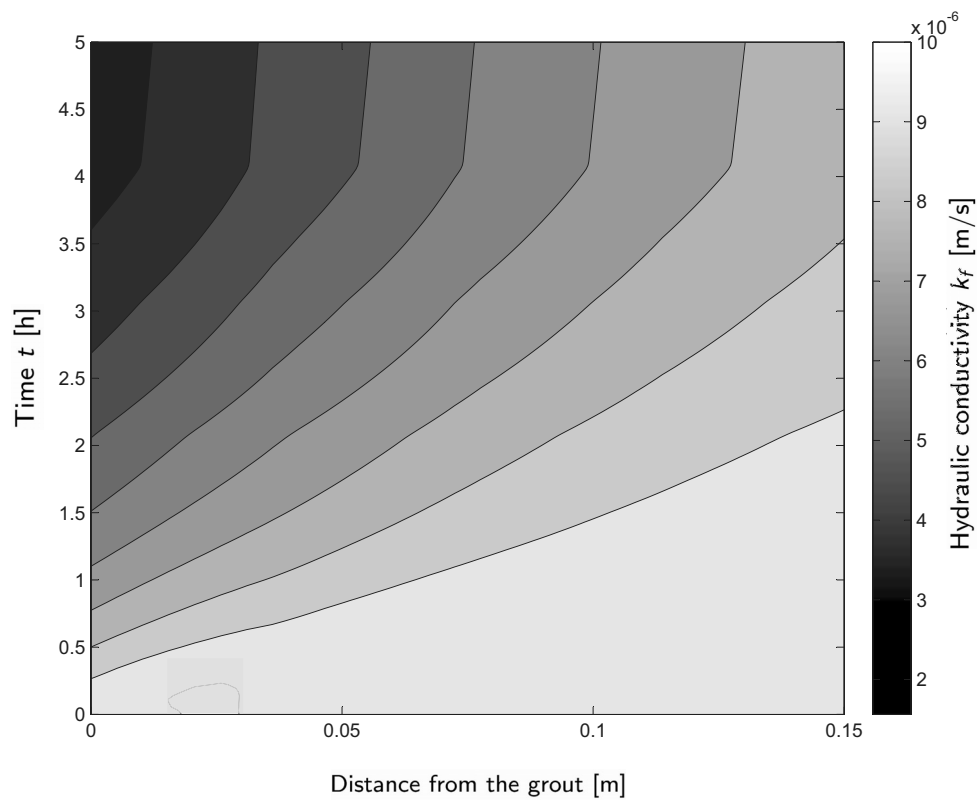Figure 3.92.: Boundary pressure distribution for the IBVP of infiltration.

Figure 3.93.: Evolution of the soil hydraulic conductivity in time and space around the tunnel. Initial hydraulic conductivity 1×10^{-5} m/s (corresponding to sand). For this relatively high initial conductivity practically there is relatively very small change in the conductivity over the time and space.

time of dewatering of the annular gap grouting mortar the hydraulic conductivity of the surrounding soil is reduced. This phenomenon occurs due to infiltration of fine particles from the grout into the soil. The influence of the infiltration process on the soil hydraulic conductivity is diminishing within a distance of approximately 15 cm. Thus the formation of a so-called internal filter cake occurred in the surrounding soil. Hence, the surrounding soil acts in the case of grouting as a filter.

In the following sections the influence of the hydraulic conductivity evolution in the 3D tunnel simulation will be investigated.

3.5.5. Construction and Consolidation Phases

There are modelled and investigated the two extreme cases regarding to the hydraulic conditions of the subsoil:

- **A** – "undrained" soil response. In the reality this corresponds to a relative high TBM advance speed and/or relative low soil permeability. There are two possibilities for modelling of this soil behaviour

  - **A.1** – *consecutive*; Each excavation step is modelled in two single calculation phases. The first phase is an undrained (no volumetric deformations of the soil, $\varepsilon_v = 0$) effective stress analysis with effective soil strength and stiffness parameters and it is used for generating the excess pore water pressures resulting from the excavation, and additionally from the support pressures acting directly on the surrounding soil. The second phase is a consolidation type of analysis with a time duration equal to 1.00 hour. This time interval is chosen so that it realistically represents the excavation speed and means that for 1.00 h the TBM advances with 1.50 m;

  - **A.2** – *continuously*; Each excavation step is modelled in one single consolidation phase with the same time of duration equal to 1.00 hour, in which concurrently the excess pore water pressures are generated and dissipated by following deformations of the subsoil.

- **B** – "drained" soil response. In the reality this corresponds to a relative low TBM advance speed and/or relative high soil permeability. By such hydraulic conditions of the soil no excess pore water pressures will be generated.

The above assumptions are equivalent to an assumed excavation speed of 1.50 m/h, i.e. for 1.00 hour the TBM excavates 1.50 m in the front of the tunnel, and erects the next

tubbing ring of the lining. The governing equations of consolidation as used here follow
the Biot's theory (Biot (1941), Biot (1956)). However, the mechanical field is considered
as an *elasto-plastic* type, when it is used an elasto-plastic soil constitutive model like the
HS model in the present study (as already explained in Section 3.1.3.2).

3.5.6. Results

3.5.6.1. Significance of the Soil Hydraulic Conditions

In Figures 3.94 to 3.101 there are presented the observed displacements in the four obser-
vation points – at the ground surface, at the tunnel crown, at the tunnel side wall, and at
the tunnel invert – by tunnelling in a soil with low hydraulic conductivity $k_f = 1 \times 10^{-9}$
m/s. At the time of 26^{-th} hour the heading face of the TBM reaches the observation
cross-section 26. Six hours later at the time of 32^{-nd} hour the shield tail passes through
the observation cross-section. There are calculated larger displacements at the observation
points at fully "drained" soil conditions (i.e when the advance rate is enough slow, and/or
the soil permeability is enough high that no excess pore water pressures are generated).
This difference is coming from the difference in the effective stresses in the subsoil due to
the change of the total pore water pressures during the tunnelling (s. e.g. Fig. 3.106) by

Figure 3.94.: Vertical displacements on the ground surface at observation cross-section 26
during the excavation in a soil with low hydraulic conductivity $k_f = 1 \times 10^{-9}$ m/s.

Figure 3.95.: Vertical displacements on the ground surface at observation cross-section 26 over a long period of time (hydraulic conductivity $k_f = 1 \times 10^{-9}$ m/s).

Figure 3.96.: Vertical displacements of the tunnel crown at observation cross-section 26 during the excavation in a soil with low hydraulic conductivity $k_f = 1 \times 10^{-9}$ m/s.

the "undrained" situation. So, by increasing the total pore water pressures the effective stresses in the soil ahead the tunnel face become smaller if compared with the "drained" situation. Thereafter, the soil deformations around the TBM at each moment of time are larger in comparison with the same at "undrained" soil conditions. Consequently, the

Figure 3.97.: Vertical displacements of the tunnel crown at observation cross-section 26 over a long period of time (hydraulic conductivity $k_f = 1 \times 10^{-9}$ m/s).
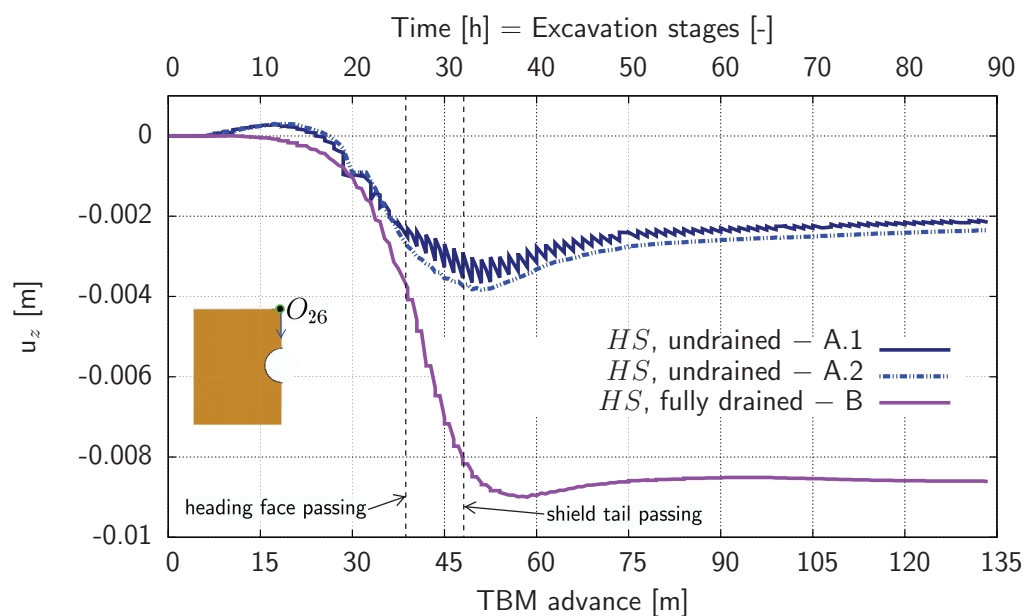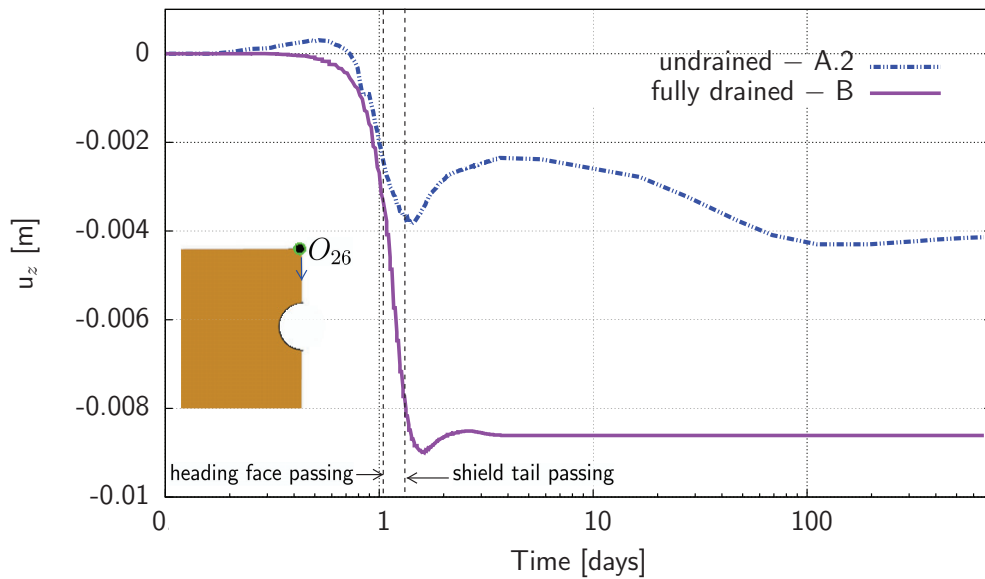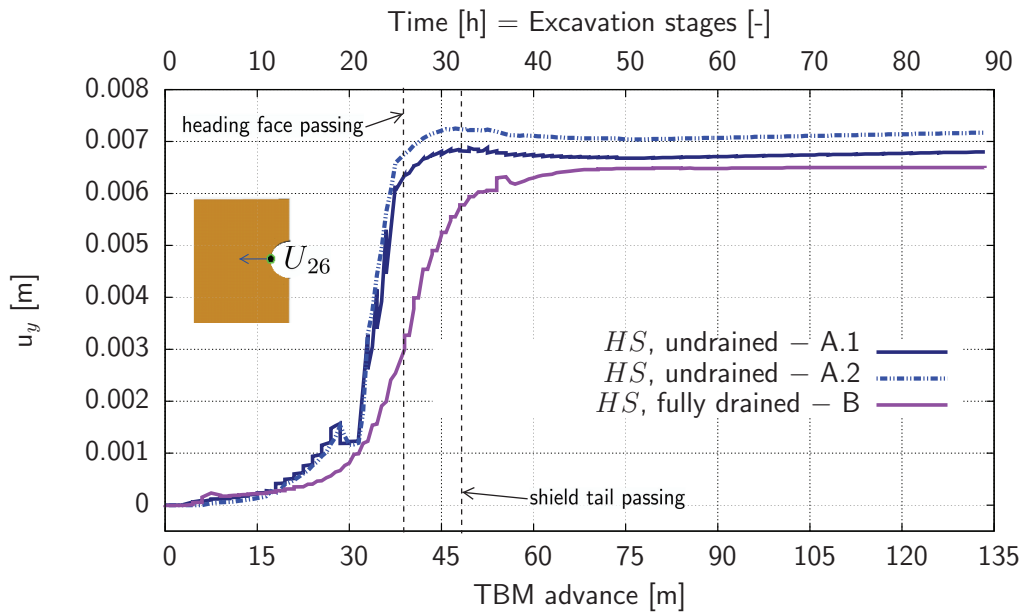

Figure 3.98.: Horizontal displacements of the tunnel side wall at observation cross-section 26 during the excavation in a soil with low hydraulic conductivity $k_f = 1 \times 10^{-9}$ m/s.

high advance rate reduces the deformations close to the TBM heading face and the final surface settlements when the soil conductivity is relative low. It is shown also in the same Figures 3.94–3.101 that the predicted displacements by the "undrained" soil hydraulic
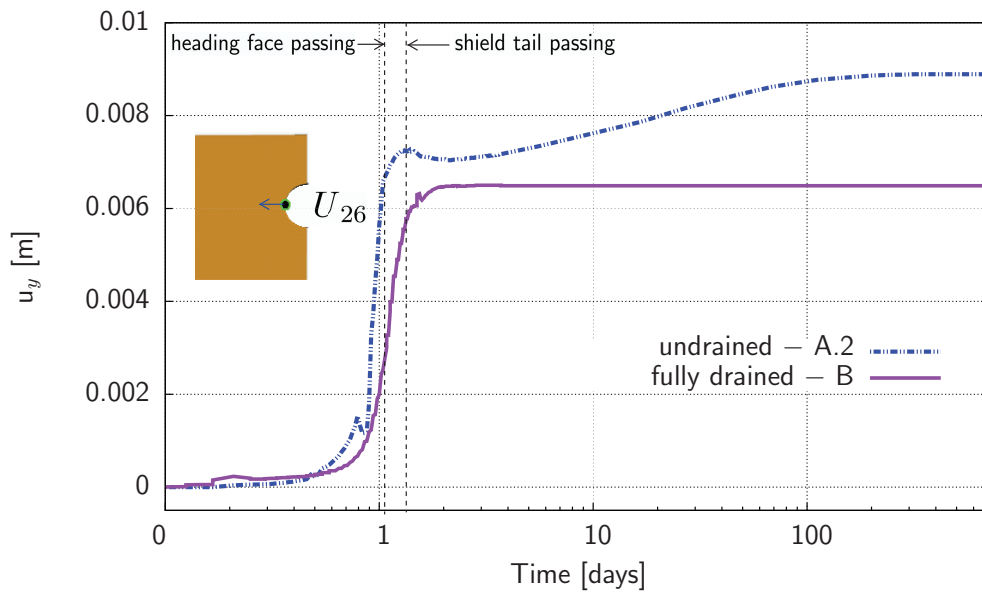
Figure 3.99.: Horizontal displacements of the tunnel side wall at observation cross-section 26 over a long period of time (hydraulic conductivity $k_f = 1 \times 10^{-9}$ m/s).
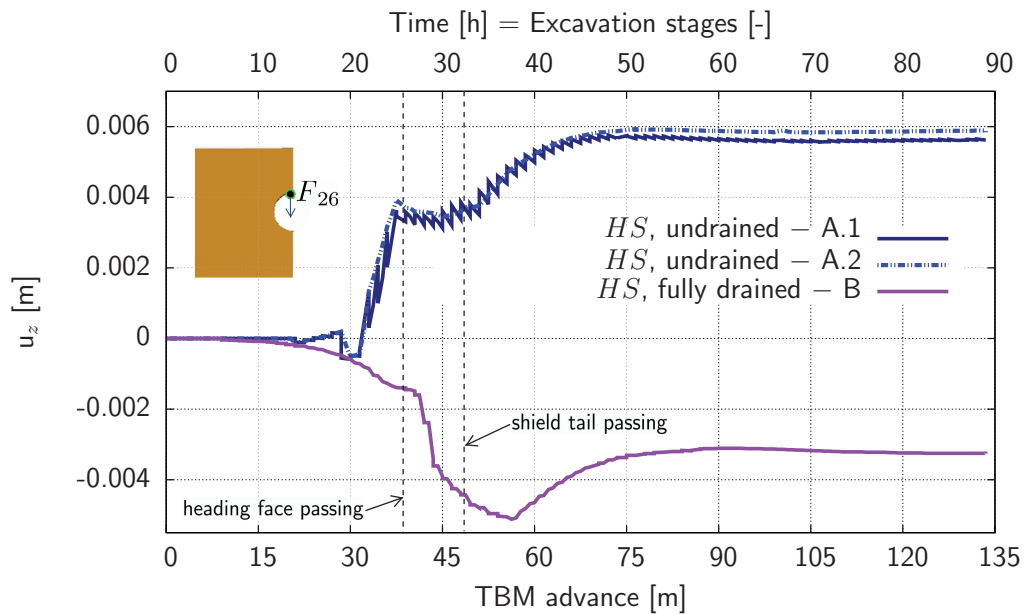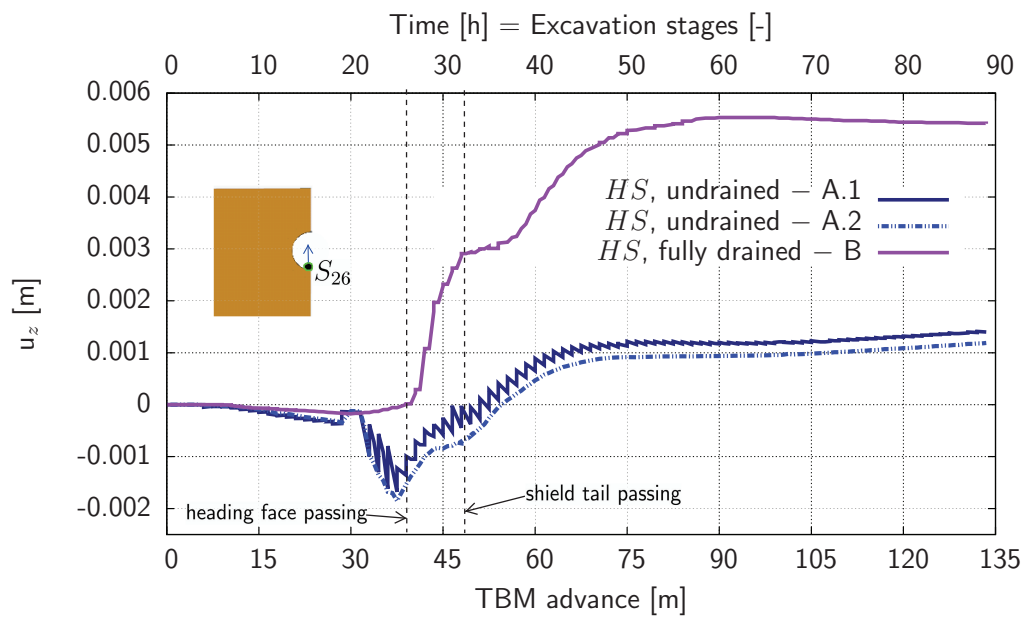

Figure 3.100.: Vertical displacements of the tunnel invert in the observation cross section during the excavation in a soil with low hydraulic conductivity $k_f = 1 \times 10^{-9}$ m/s.

condition modelled with the two variants A.1 (consecutive) and A.2 (continuously) are relatively identical.
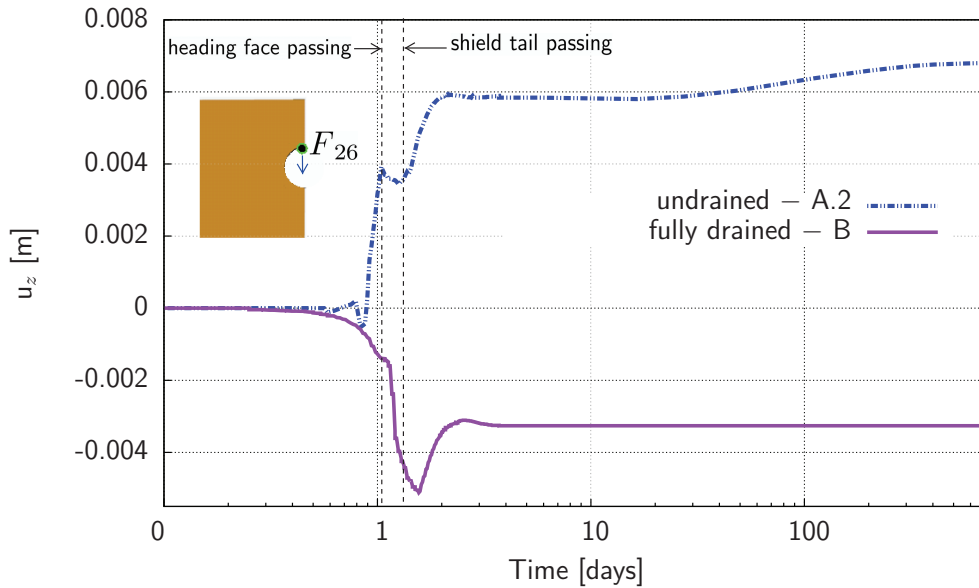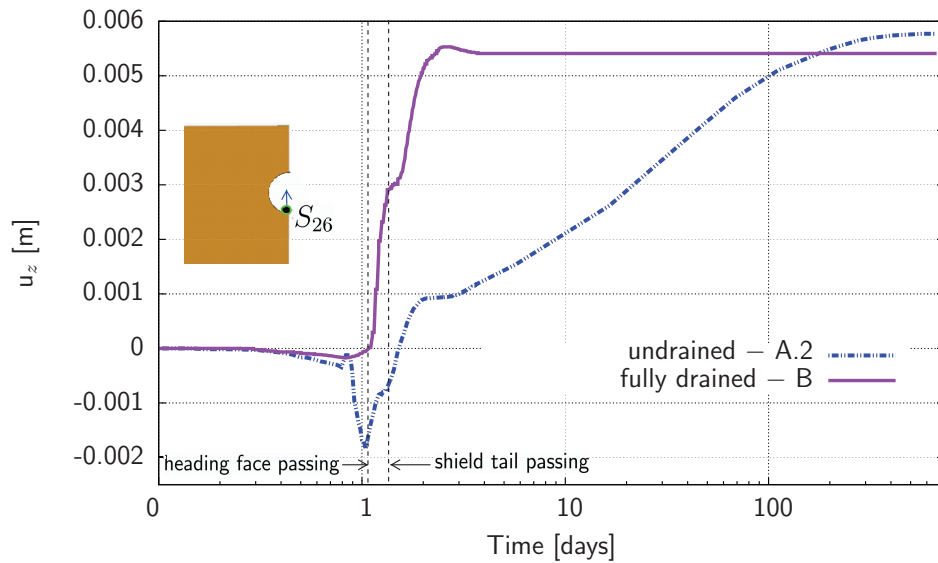
Figure 3.101.: Vertical displacements of the tunnel invert in the observation cross section over a long period of time (hydraulic conductivity $k_f = 1 \times 10^{-9}$ m/s)
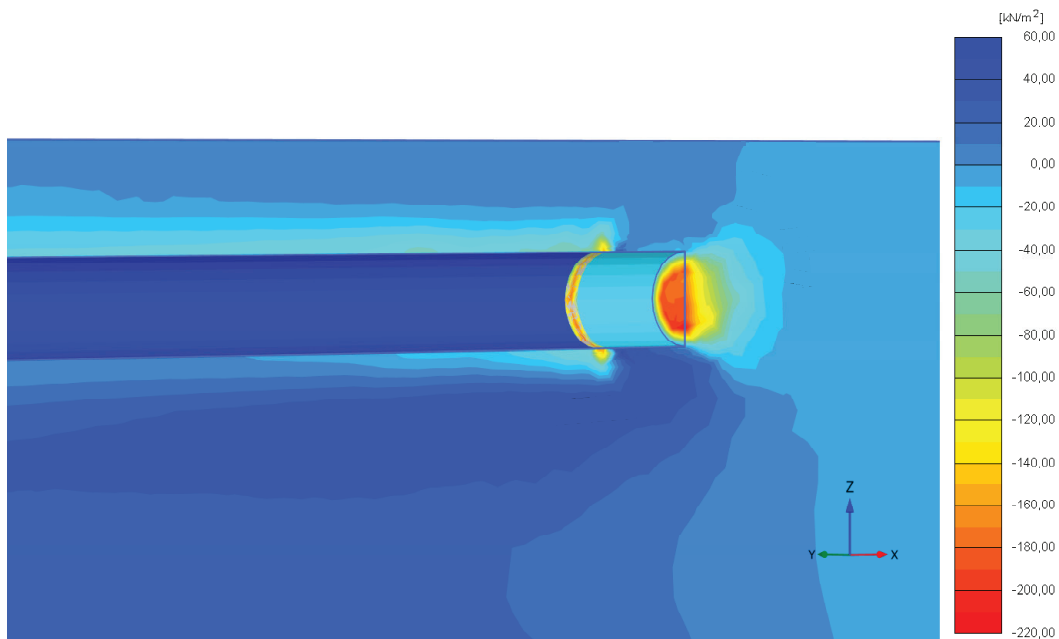

Figure 3.102.: Calculated excess pore water pressures at the last excavation stage. Pressure is negative. Hydraulic conductivity $k_f = 1 \times 10^{-9}$ m/s.

In Figure 3.102 there are shown the generated excess pore water pressures at the last excavation stage. Pressures are considered to be negative. In the next Figure 3.103 there are shown the excess pore water pressures in the observation cross-section 26 when the shield tail passes through. There are observed also during the excavation below the tunnel invert
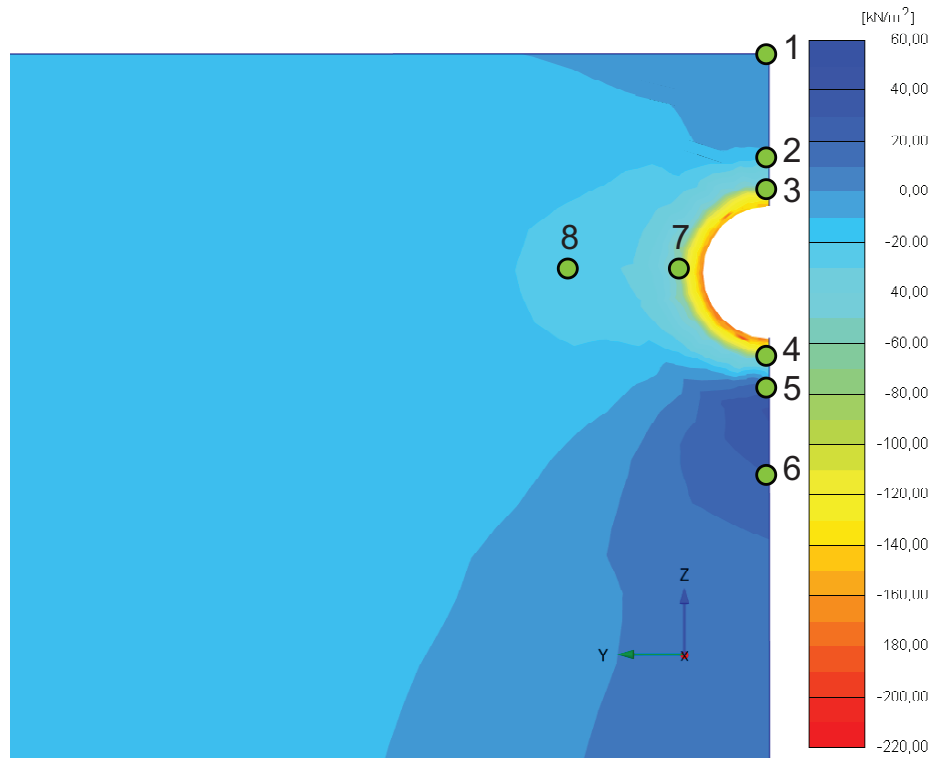
Figure 3.103.: Observed stress points and calculated excess pore water pressures in the observation cross-section 26 (located at the 39$^{\text{-th}}$ m from the tunnel beginning) when the shield tail passes through. Pressure is negative. The area with positive values (in dark blue) below the tunnel invert indicates development of tensile pore pressures (suction). Hydraulic conductivity $k_f = 1 \times 10^{-9}$ m/s.

areas of positive pore pressures (suction), because the soil in these areas was unloaded through the excavation (i.e. removal or deactivation) of soil volumes. In Figures 3.104–3.108 there are shown the calculated total pore water pressures p_{active} in stress points at different locations around the tunnel perimeter in the observation cross-section 26. The total pore water pressure is defined as

$$p_{active} = p_{steady} + p_{excess},$$

where p_{steady} is the steady state pore pressure, i.e. in this case the hydrostatic pore water pressure.

In Figure 3.112 there are shown the calculated total pore water pressures in front of the tunnel face, measured at one cross-section by the excavation of the shallow tunnel. The measurements start when the TBM is 18 m before the observed stress point up to reaching it after 12 hours.

Figure 3.104.: Calculated total pore pressures in the observation cross-section during the excavation in a stress point on the ground surface (shallow tunnel).

Figure 3.105.: Calculated total pore pressures in the observation cross-section during the excavation in a stress point 1 m above the tunnel crown (shallow tunnel).

Figure 3.106.: Calculated total pore pressures in the observation cross-section during the excavation in a stress point 0.1 m above the tunnel crown (shallow tunnel).
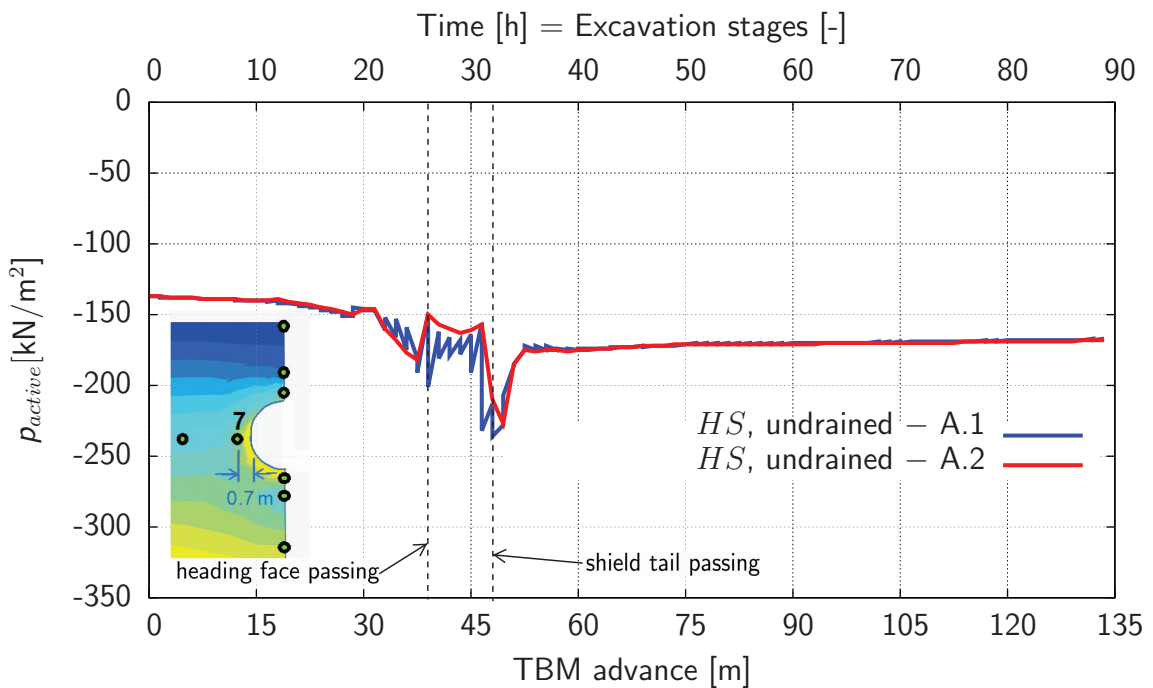
Figure 3.107.: Calculated total pore pressures in the observation cross-section during the excavation in a stress point 0.7 m apart the tunnel side wall (shallow tunnel).
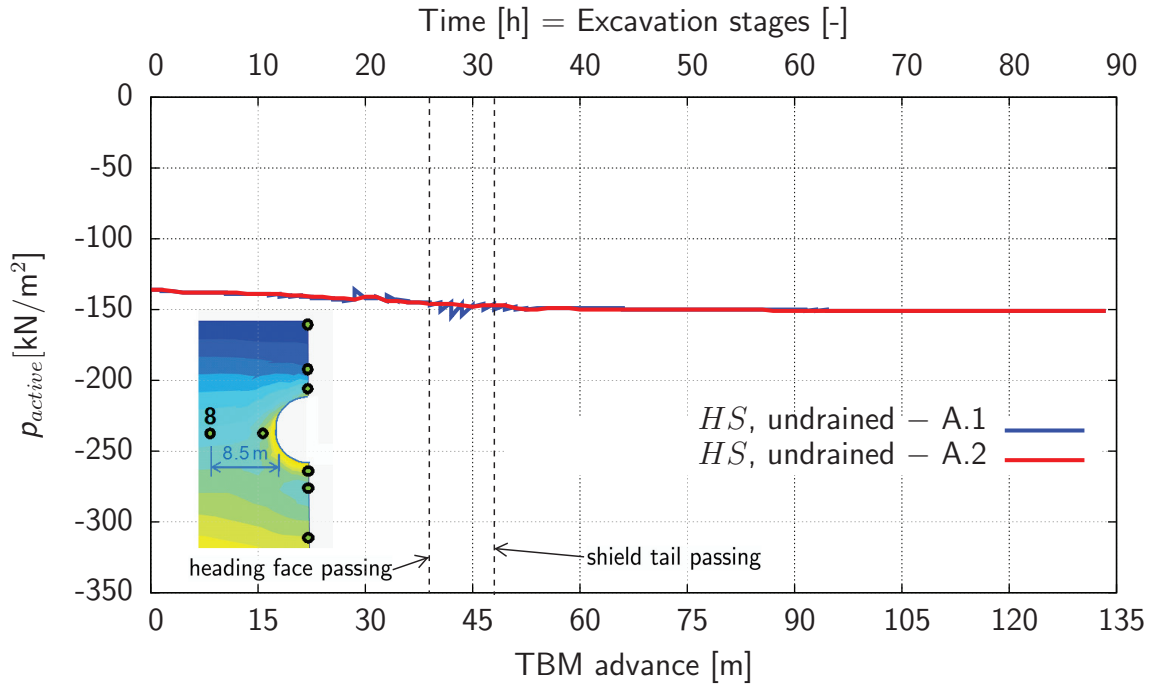
Figure 3.108.: Calculated total pore pressures in the observation cross-section during the excavation in a stress point 8.5 m apart the tunnel side wall (shallow tunnel).
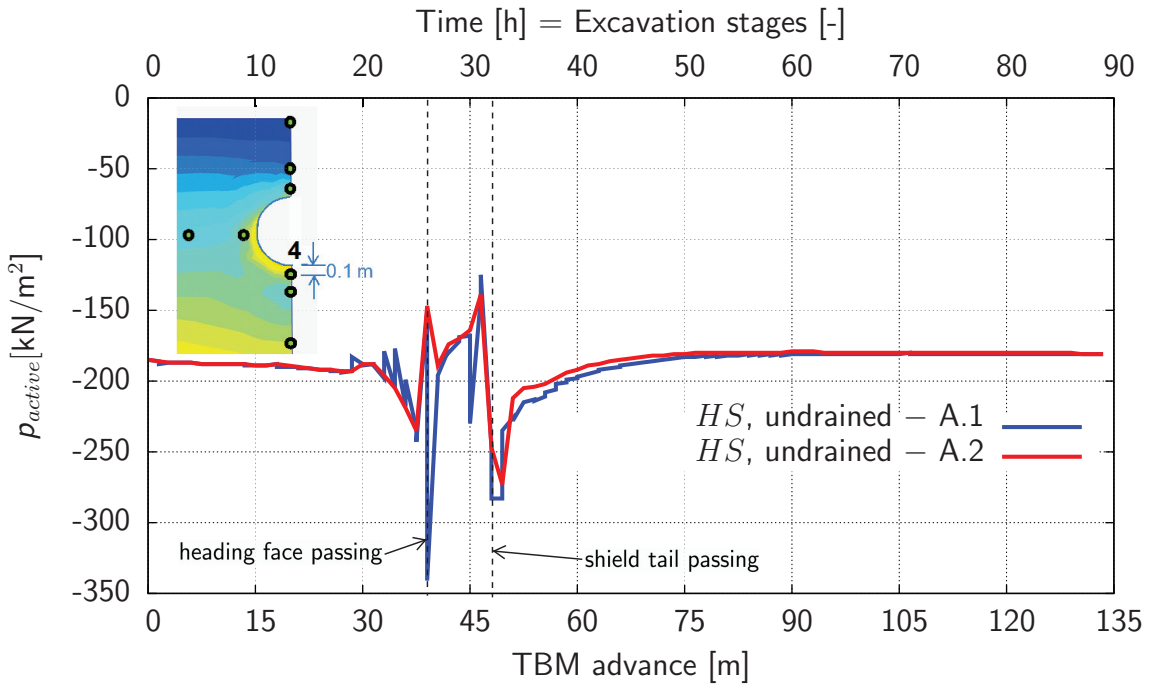
Figure 3.109.: Calculated total pore pressures in the observation cross-section during the excavation in a stress point 0.1 m below the tunnel invert (shallow tunnel).

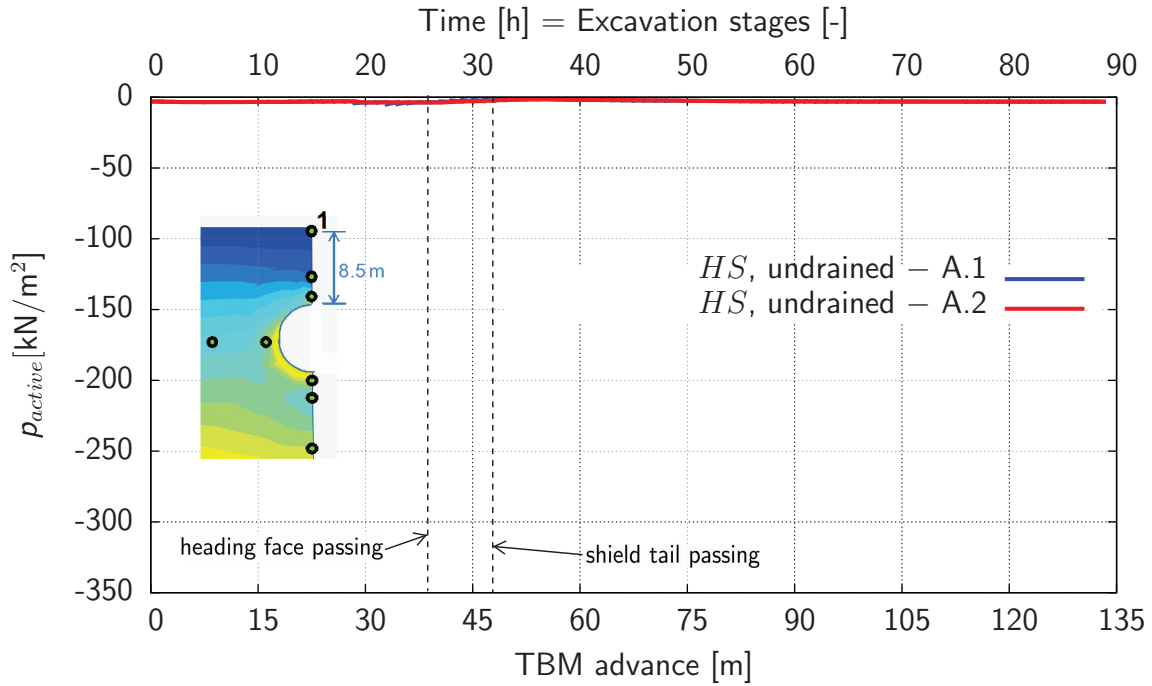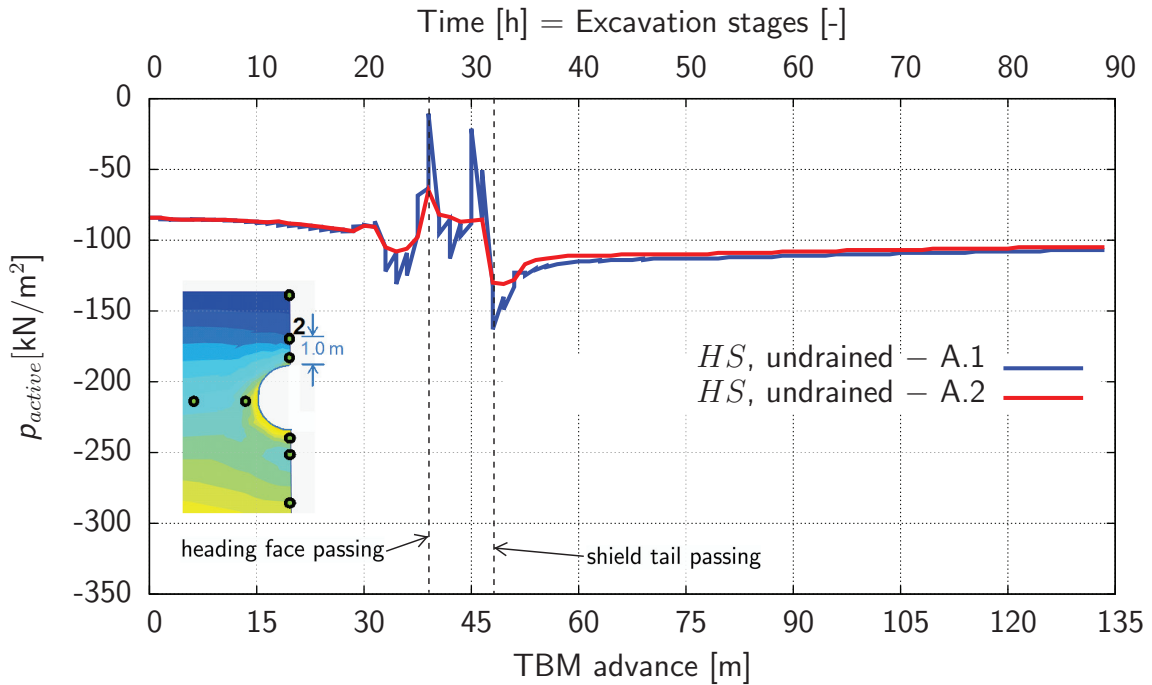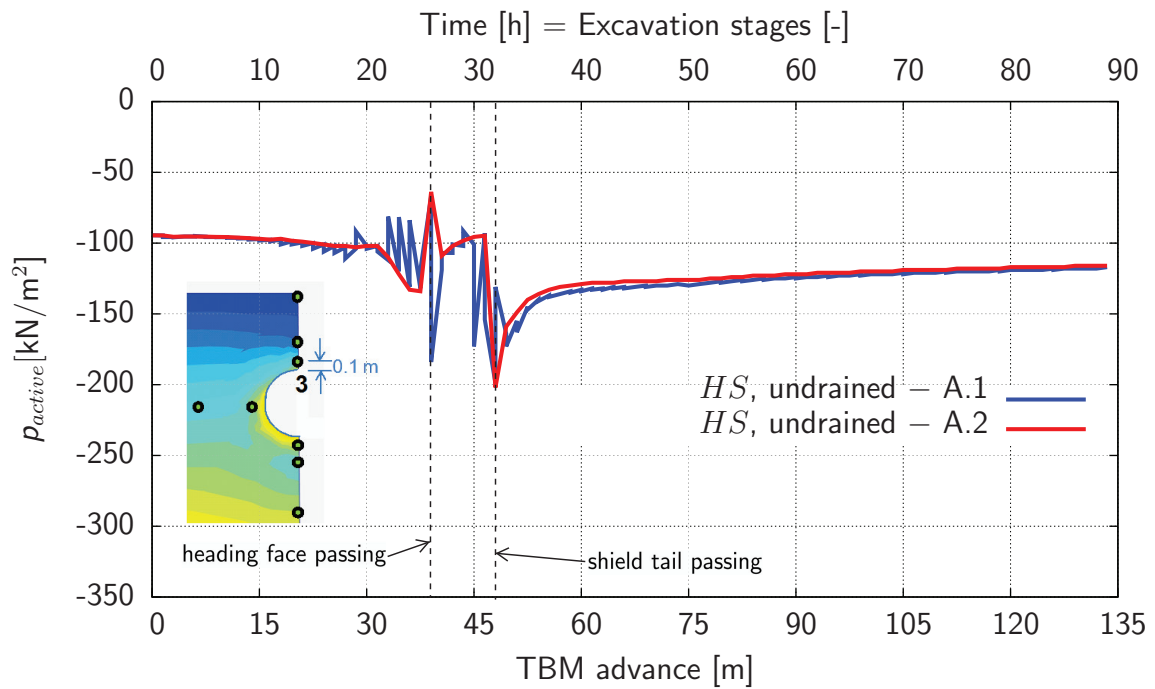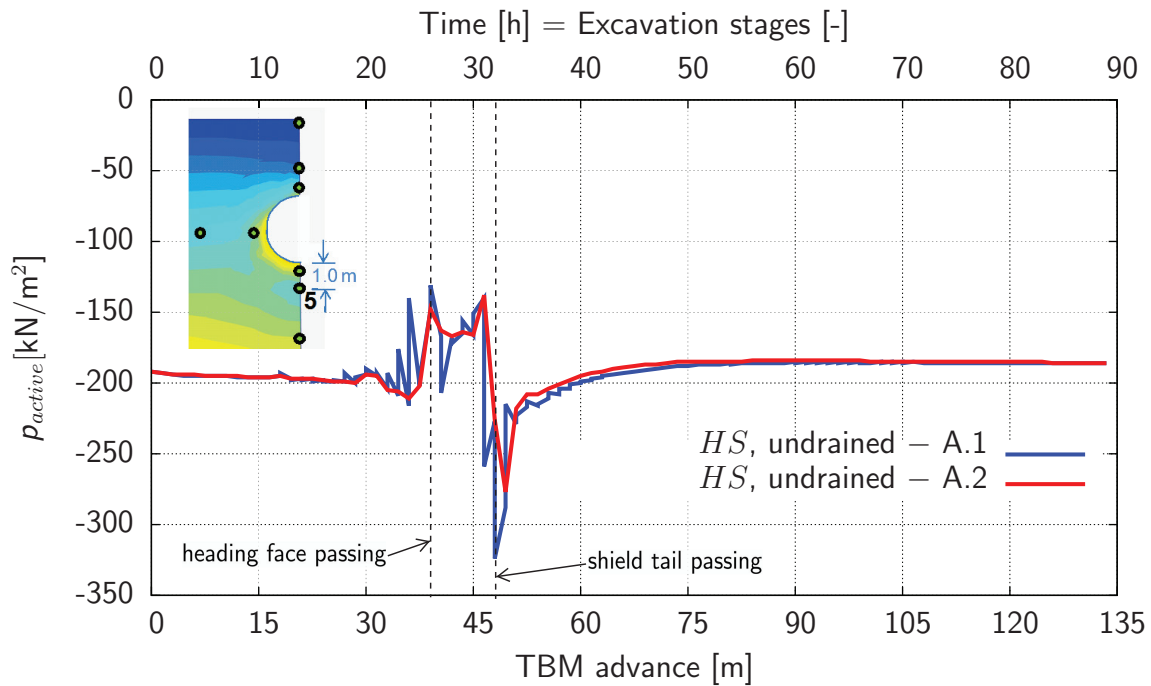Figure 3.110.: Calculated total pore pressures in the observation cross-section during the excavation in a stress point 1.0 m below the tunnel invert (shallow tunnel).
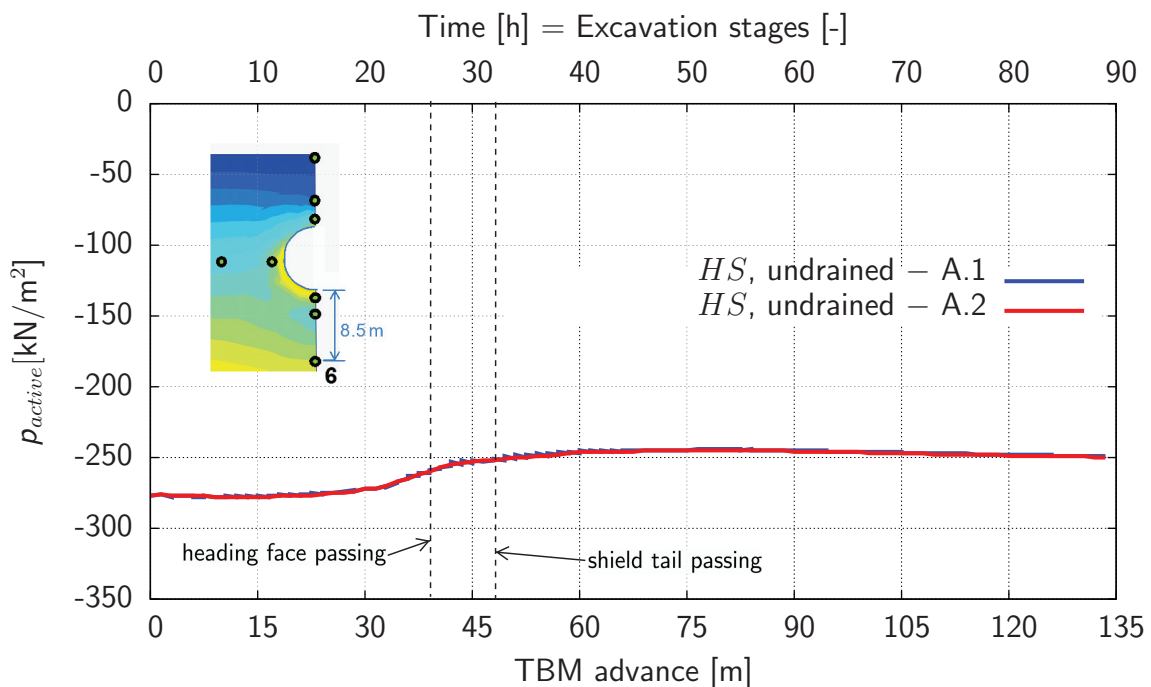
Figure 3.111.: Calculated total pore pressures in the observation cross-section during the excavation in a stress point 8.5 m below the tunnel invert (shallow tunnel).
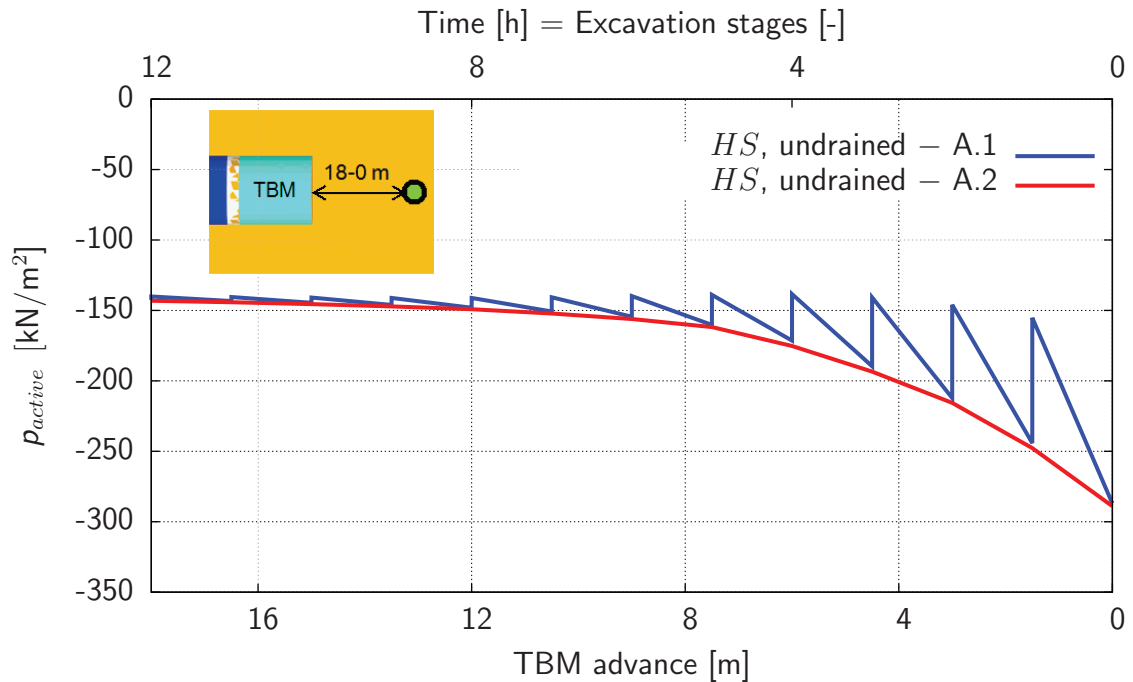
Figure 3.112.: Calculated total pore water pressures in front of the tunnel face measured at cross-section 26 by the excavation of the shallow tunnel.

In Figures 3.113–3.115 there are presented the three stress invariants during the tunnelling of the shallow and deep tunnel for an observation point situated 0.10 m above the tunnel crown. Physically, I_1 indicates the effect of mean stress, J_2 represents the magnitude of shear stress, and θ determines the direction of shear stress.

3.5.6.2. Significance of the Soil Hydraulic Conductivity

Additionally to the current used low hydraulic conductivity $k_f = 1 \times 10^{-9}$ m/s corresponding e.g. to clay, there are performed calculations for comparison with a higher conductivity -1×10^{-5} m/s corresponding e.g. to sand. The vertical displacements in observation points O_{26} and S_{26} during the excavation are given in Figures 3.118 and 3.119. It is shown that with this higher conductivity $k_f = 1 \times 10^{-5}$ m/s, and by the assumed excavation speed of 1.5 m/h, the soil hydraulic response is close to the fully drained behaviour.

In Figure 3.116a) there is presented the excess pore water pressure distribution above and sideways of the tunnel in a length of one times the tunnel radius, $R = 4.25$ m, in the moment when the shield tail is passing through, i.e. in the moment when the grouting is acting in the observation cross-section. The generated excess pore water pressures in the sand (in red) are much smaller and they dissipate very fast in the surrounding subsoil. In
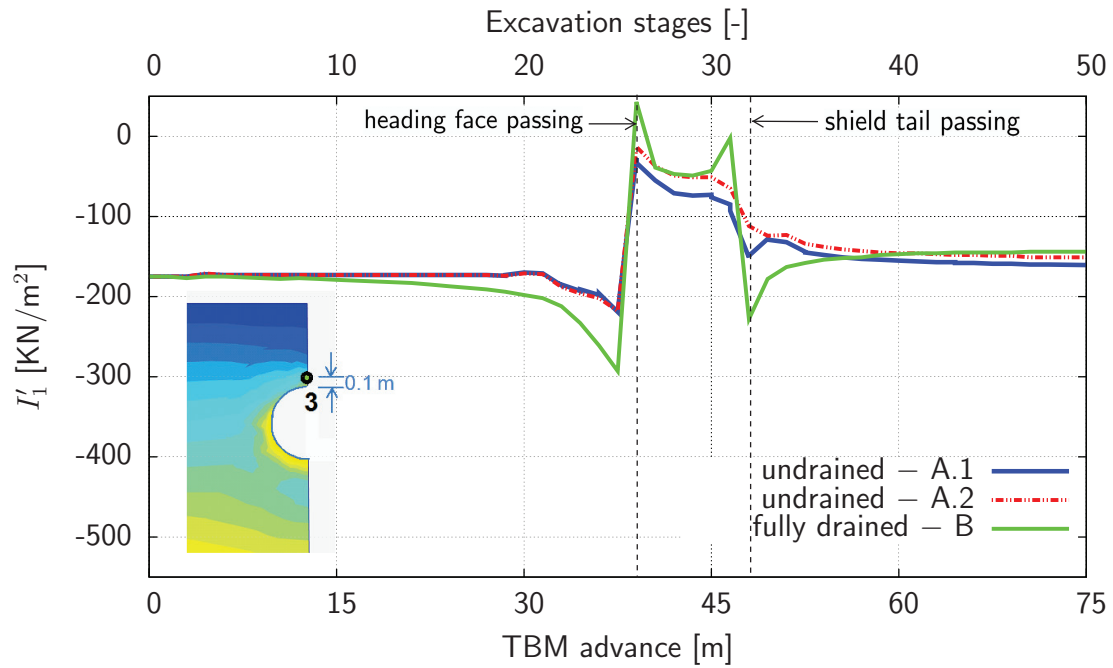
Figure 3.113.: First stress invariant (Eq. 3.36) at observation cross section 26 (shallow tunnel, overburden = $1D$); pressure is considered to be negative.
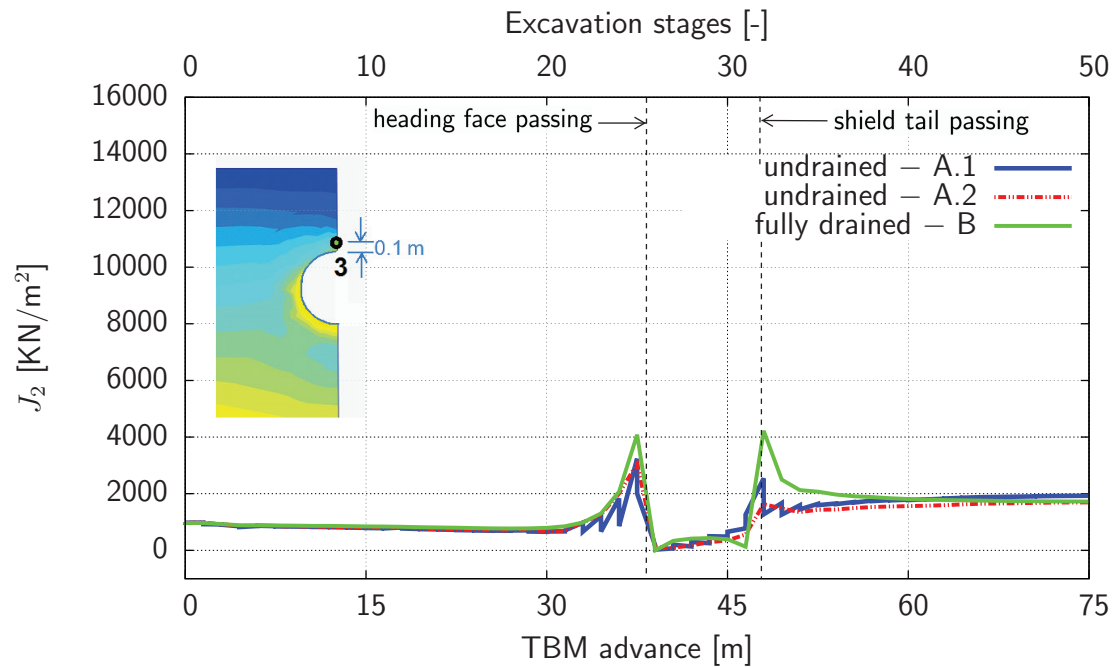
Figure 3.114.: Second deviatoric stress invariant (Eq. 3.37) at observation cross section 26 (shallow tunnel, overburden = $1D$).
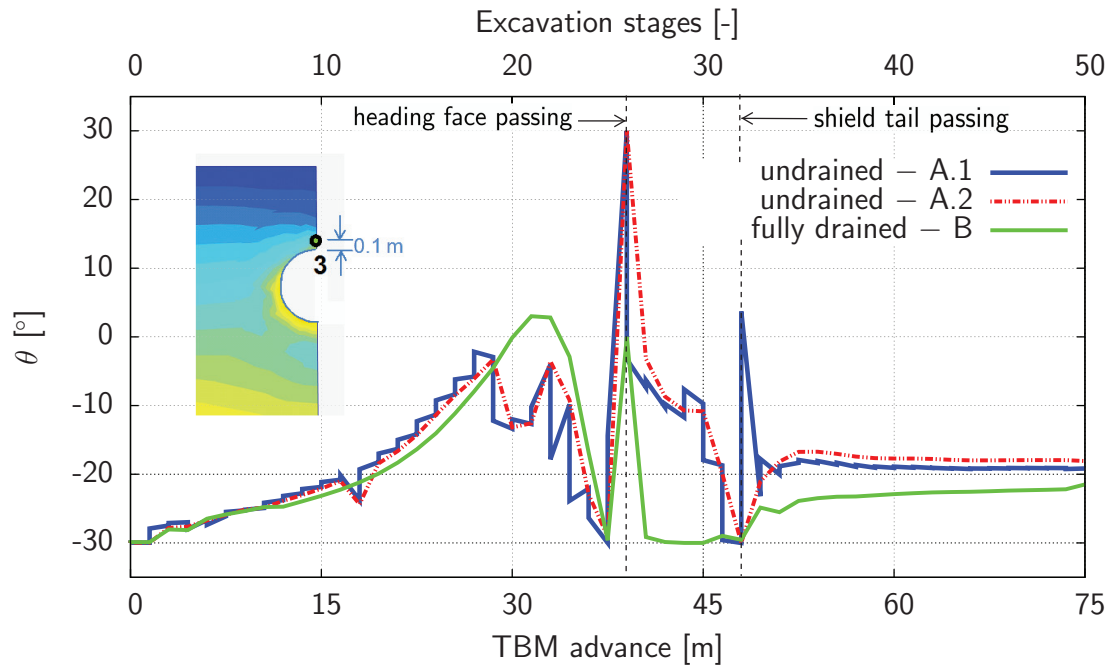
Figure 3.115.: Third stress invariant (Lode angle; Eq. 3.38) at observation cross section 26 (shallow tunnel, overburden = $1D$).

the same Figure 3.116b) in an observation point on the tunnel side wall ($R = 0$) there is presented the excess pore water pressure distribution over time t. The observation starts when the shield tail is passing ($t = 0$). Again here it is shown that the generated excess pressures in the sand (in red) are smaller and they dissipate very fast over the time (immediately in the very first few minutes). The excess pore water pressures in the clay (in blue) dissipate faster in the first few hours, and after the 10-th hour the dissipation is slower. The remaining excess pore water pressures dissipate slowly after that over a time of almost one year. This statement is indicated for example in Figure 3.101 (the dark-blue dashed curve) where the displacements attenuate also after about one year.

3.5.6.3. Significance of the Evolution of the Soil Hydraulic Conductivity

Bezuijen (2007) and Bezuijen & Talmon (2003) investigated analytically the flow and the pressure distribution of the support mediums – grout and bentonite – between the shield and the subsoil, and the grout pressure distribution (i.e. reduction) around the tunnel lining due to bleeding (or consolidation) of the grout, as already explained before in Section 3.5.2. In Figure 3.117 there is presented the calculated pressure distribution profile around the tunnel according to their analytical methods. It was assumed that the
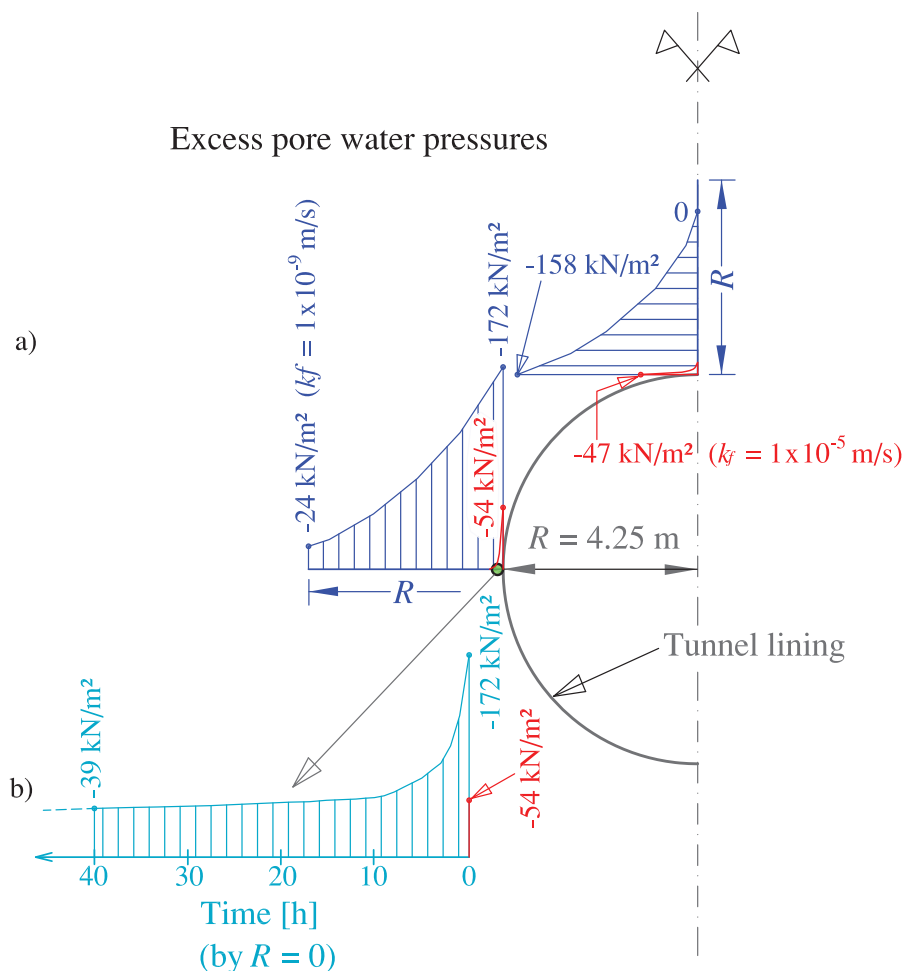
Figure 3.116.: Calculated excess pore water pressures in the observation cross-section 26 located at the 39th m from the shallow tunnel beginning: a) above and sideways of the tunnel in a length of one times the tunnel radius R when the shield tail passes through; b) in an observation point on the tunnel side wall over the time t. Pressure is negative.

fresh grout flows from the shield tail to the tunnel face and bentonite flows from the tunnel face back to the shield tail in the steering gap. The TBM conicity, i.e. the diameter reduction over the shield was assumed to be 0.4 % in order to define the geometrical dimensions of the steering gap. Further assumption is that there are no nozzles around the TBM for a direct injection of a bentonite, i.e. no active support of the steering gap. In order to achieve more visible influence in the results calculated with the mesoscopic model the grouting pressure is slightly increased to values of 300 kN/m² at the crown to 420 kN/m² at the invert.

Further, with the obtained grout pressure profile (see in Fig. 3.117) there are calculated the evolution (i.e. the change) of the soil hydraulic conductivity in space and time (time
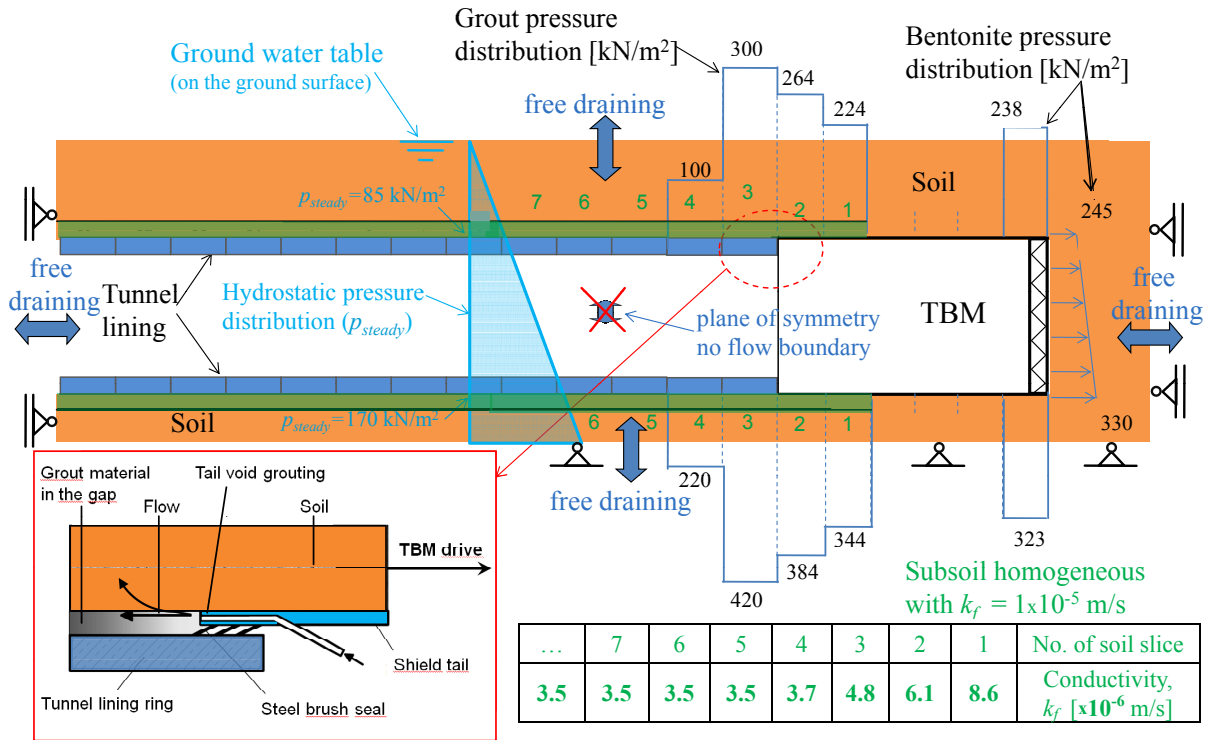
Figure 3.117.: Analytically calculated pressure distribution profile around the shallow tunnel (overburden $= 1D$), and thereafter numerically calculated with the 1D mesoscopic model spacial distribution of the soil hydraulic conductivity after "homogenization" for each hour around the tunnel according to the results presented on Figure 3.93. In the numerical simulation the changed hydraulic conductivities are assigned to soil clusters with thickness 0.15 m and length 1.50 m around the tunnel (shown in green).

duration of 5 hours) around the tunnel with the 1D mesoscopic model of Schaufler *et al.* (2012b). This was done for a soil with relative high initial hydraulic conductivity $- 1 \times 10^{-5}$ m/s, and for a soil with relative low initial hydraulic conductivity $- 1 \times 10^{-9}$ m/s. The results are presented in Figure 3.93 for the high permeable soil, while no change of the hydraulic conductivity of the soil with an initial $k_f = 1 \times 10^{-9}$ m/s was found. Thereafter, the hydraulic conductivity evolution in space and time, only for the soil with an initial $k_f = 1 \times 10^{-5}$ m/s, is homogenized for each hour and for the whole investigated soil thickness of 0.15 m. Here "homogenized" means that from Figure 3.93 at time $t_1 = 0.5$ h, $t_2 = 1.5$ h, $t_3 = 2.5$ h, $t_4 = 3.5$ h, and $t_5 = 4.5$ h there is taken the average hydraulic conductivity for the whole investigated soil thickness of 0.15 m. Next, with these homogenized conductivities the initial conductivity in a soil layer with thickness of 0.15 m around the tunnel is updated at each excavation step, i.e. each hour, as presented in Figure 3.117. The FE-model is calculated now again considering the
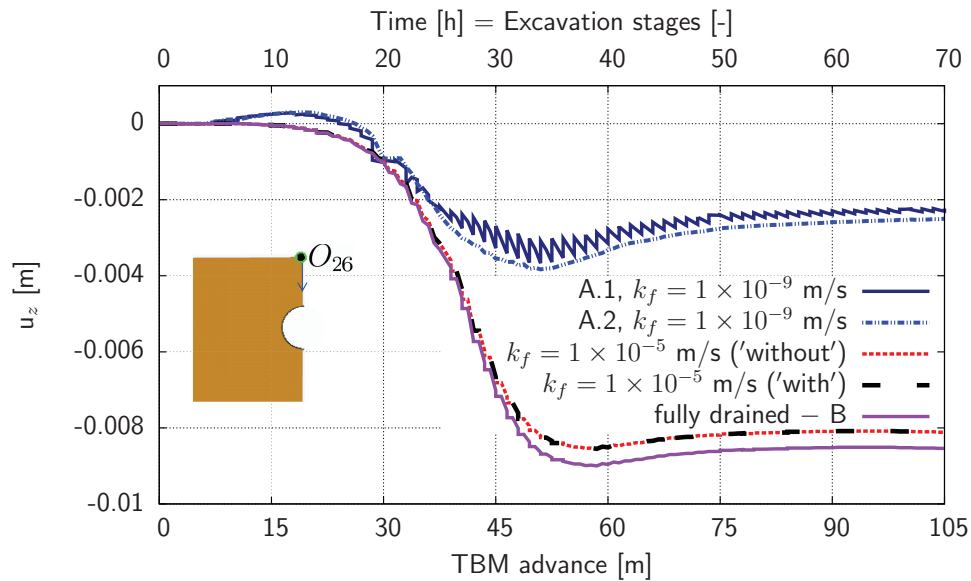
Figure 3.118.: Vertical displacements on the ground surface in the observation cross section 26 during tunnelling. Considering the evolution of the soil hydraulic conductivity around the tunnel ("with") resulting from the grouting there is no change in the calculated displacements, the displacements are fully identical.
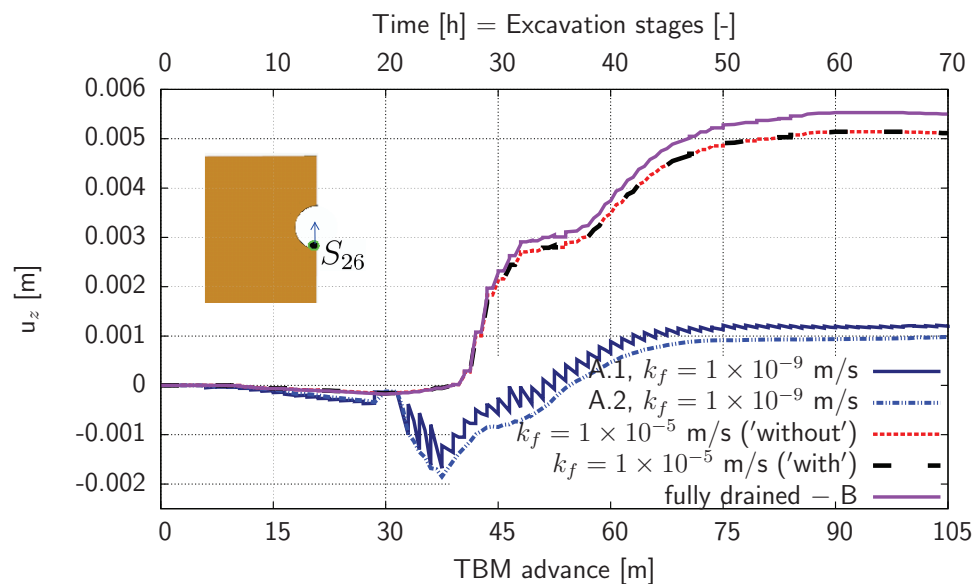
Figure 3.119.: Vertical displacements of the tunnel invert in the observation cross section 26 during tunnelling. Considering the evolution of the soil hydraulic conductivity around the tunnel ("with") resulting from the grouting there is no change in the calculated displacements, the displacements are fully identical.

conductivity change. Comparison of the results is made for the two FE-models – with (termed "with" in Fig. 3.118 and 3.119) and without (termed "without" in Fig. 3.118 and 3.119) considering the evolution of the soil hydraulic conductivity around the tunnel. The predicted displacements of points O_{26} and S_{26} presented in Figures 3.118 and 3.119 have demonstrated that there is no influence coming from the change of the conductivity around the tunnel. This results was expected because the zone around the tunnel in which the change of the hydraulic conductivity take place is very limited – only 0.15 m according to the results obtained with the 1D mesoscopic model.

In Figure 3.120 there are presented the generated excess pore water pressures by the excavation of the shallow tunnel in the observation cross-section 26 when the shield tail is passing through. Drown are the results at the tunnel side wall in a horizontal distance from the lining of ones the tunnel radius R. The results shown no meaningful difference with and without considering the change of the soil hydraulic conductivity around the tunnel.

3.6. Summary and Conclusions

First, a 3D numerical model of the closed face shield supported mechanized tunnelling was created. Researched was the influence of several components of the mechanized tunnelling process in the simulation. Next, it has been demonstrated that the advance speed of the tunnel excavation in water-saturated ground has a large influence on the deformations and the settlements of the ground. The higher the excavation speed of the TBM in a water-saturated subsoil with enough low permeability, the lower are the surface settlements, which is very important for the building construction safety in urban areas. Further, using the 1D analytical models derived by Bezuijen (2007) and Bezuijen & Talmon (2003) the pressure distribution of the supports – grout and bentonite – between the shield and the subsoil, and the grout pressure distribution around the tunnel lining were obtained. In addition to this, the 1D numerical model of the mesoscopic approach elaborated by Schaufler *et al.* (2012b) within the framework of the theory of porous media is used. In this mesoscopic model the calculated pressure distribution is used as an input data for calculating the soil hydraulic conductivity evolution (change) in the soil around the tunnel during the time. This was done for a soil with high hydraulic conductivity – 1×10^{-5} m/s (e.g. sand), and for a soil with low hydraulic conductivity – 1×10^{-9} m/s (e.g. clay). For the clay type of soil (i.e. low conductivity) no change of the hydraulic conductivity was observed. The explanation for this is that the infiltration in the soil is very limited due

Excess pore water pressures

without considering the soil
hydraulic conductivity evolution

with considering the soil
hydraulic conductivity evolution

$(k_f = 1 \times 10^{-5}\text{m/s})$

$R = 4.25$ m | $R = 4.25$ m

-24 kN/m² $(k_f = 1 \times 10^{-9}$ m/s)

-172 kN/m²

-54 kN/m²

-172 kN/m²

-61 kN/m²

-24 kN/m² $(k_f = 1 \times 10^{-9}$ m/s)
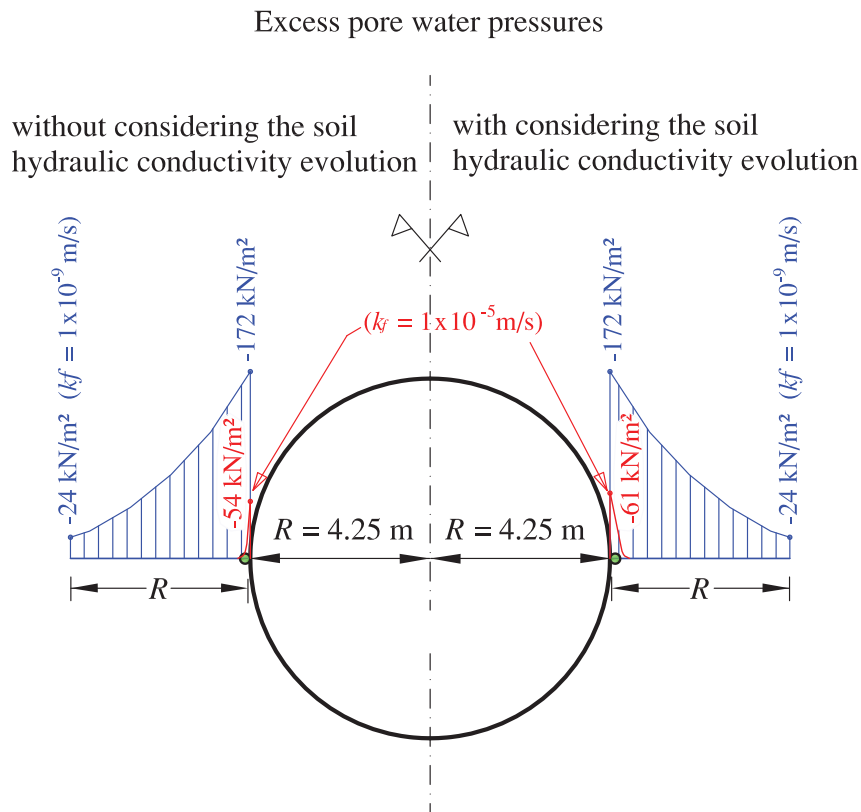
Figure 3.120.: Generated excess pore water pressures by the excavation of the shallow tunnel in the observation cross-section 26 when the shield tail is passing through. There is no, or no meaningful influence when considering the soil hydraulic conductivity evolution around the tunnel perimeter.

to the low conductivity. Thereafter, the calculated hydraulic conductivity evolution in space and time, only for the soil with an initial hydraulic conductivity $k_0^{\text{f}} = 1 \times 10^{-5}$ m/s (e.g. sand), was used in the 3D tunnel model to update the initial conductivity in a soil layer with thickness of 0.15 m around the tunnel at each excavation step, i.e. each hour. Comparison of the results is made for the two FE tunnel simulations – with and without considering the conductivity evolution around the tunnel. The obtained results have demonstrated that there is no meaningful influence coming from the change of the conductivity around the tunnel. This results were expected because the zone around the tunnel in which the change of the hydraulic conductivity take place is very limited – only 0.15 m according to the results obtained with the 1D mesoscopic model.

4. Soil Model Parameters Identification

4.1. Sensitivity Analysis

4.1.1. Derivative Based Local Sensitivity Analysis

The local SA investigates the local impact of each input parameter x_j on the model output (response) y_i. For this reason the partial derivatives of the model output with respect to an individual input for a specific local point (called: nominal point) in the input domain have to be calculated.

The goal of the mechanized tunnelling is to keep the ground displacements as low as possible. Therefore, when measuring displacements, the measurement points have to be placed at such places where the displacements are expected to be large enough and therefore can be measured reliably with the available instruments like e.g. extensometers, inclinometers, leveling instruments. In Figure 4.1 there are given the vertical and the horizontal displacements at the last excavation stage of the shallow tunnel. There are selected the observation points O_{12} (on the ground surface) and S_{12} (at the tunnel invert) as they belong to the zone with significant vertical displacements. The meaning of the subscript 12 is that the observation points mark the position of the 12th excavation stage and are located at 12×1.50 m from the beginning of the tunnel.

Here for the numerical model the vector of the chosen five input parameters of the HS model is $X = (\varphi, c, E_{50}^{ref}, E_{oed}^{ref}, E_{ur}^{ref})$, and the vector of model response (i.e. vertical displacements) is $Y = (u_z(O_{12}), u_z(S_{12}))$. In Figure 4.2 there are given the vertical displacements in observation points O_{12} and S_{12} during the excavation of the shallow tunnel.

A basic and classical technique for calculating the partial derivatives is the *finite-difference approximation*. In the present work the *first-order forward-difference approximation* is used defined as

$$y_i'(x_j) \approx \frac{\Delta y_i}{\Delta x_j} = \frac{y_i(x_j + \Delta x_j) - y_i(x_j)}{\Delta x_j} \equiv \omega(y_i, \Delta x_j). \tag{4.1}$$
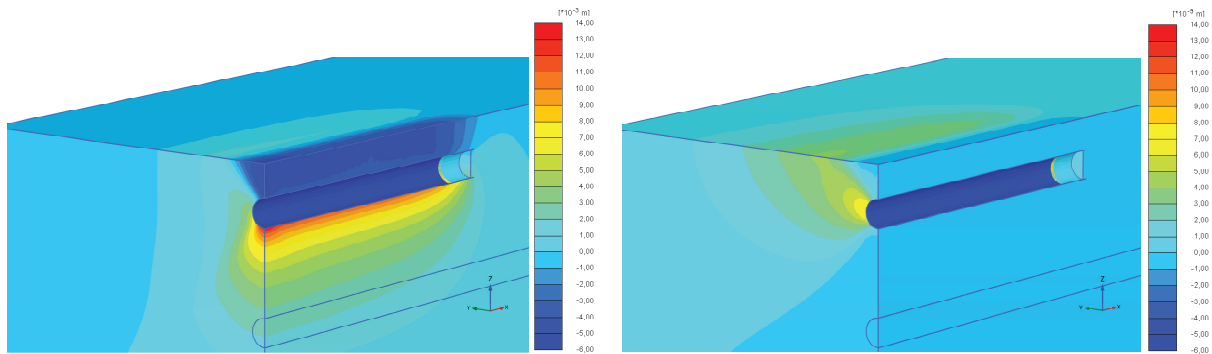
Figure 4.1.: Displacement field at the last excavation stage by the excavation of the shallow tunnel. *Left*: vertical displacements (in Z-direction); *Right*: horizontal displacements (in Y-direction).
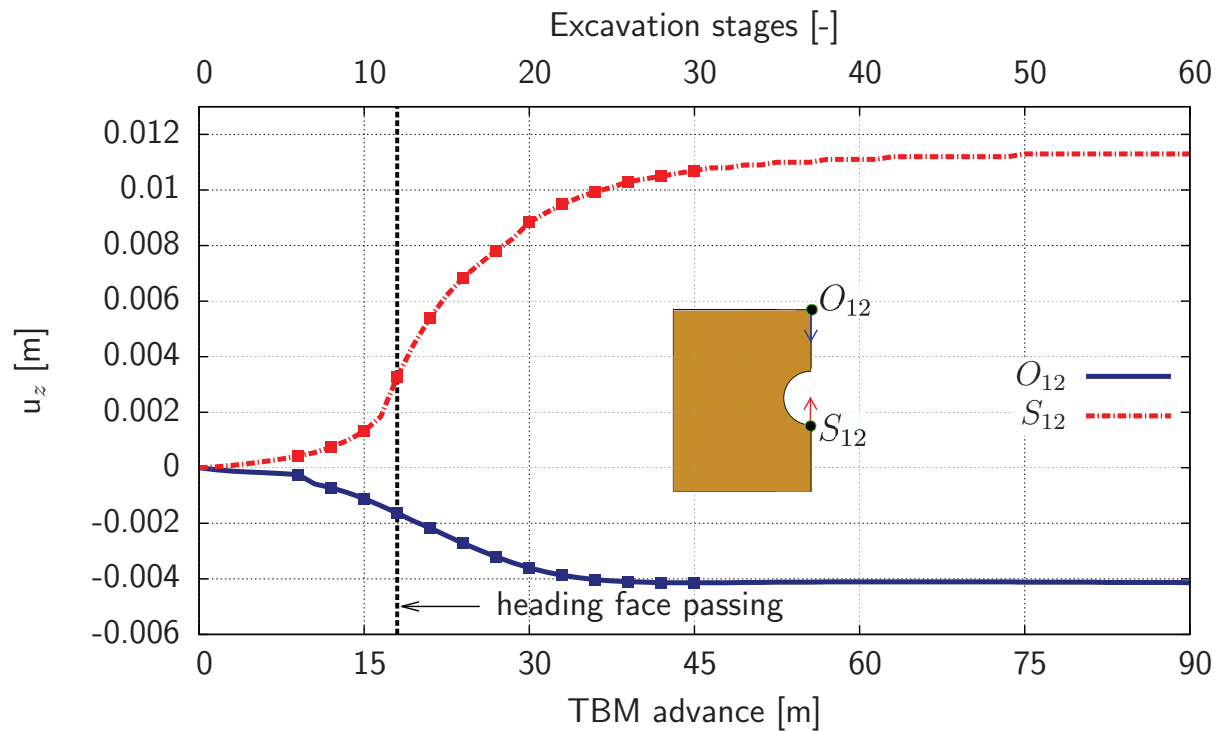
Figure 4.2.: Vertical displacements in observation points O_{12} and S_{12} during the excavation of the shallow tunnel (overburden $= 1D$). In an excavation step 12 the TBM face reaches the observation cross-section.

However, it is also possible to use higher order finite-difference approximations in calculating the derivatives.

4.1.1.1. Accuracy and Step Size Selection

Unfortunately, finite-difference approximations often have accuracy problems, associated directly with the choice of the used *finite-difference interval* (*step size*, Δx_j). The step size can contribute to two types of errors – *truncation error* and *condition error*, which are described in the next two subsections. This problem of selecting an optimum step size for calculating the derivatives is discussed in Curtis & Ried (1974), Lyness (1977), Gill *et al.* (1983), Gill *et al.* (1989) and others, and it is summarized also in Haftka & Gardal (1992), Iott *et al.* (1985). However, there are given only the used final formulas in the thesis for these errors taken from the above authors.

4.1.1.1.1. Truncation Error

The *Taylor's theorem* is of fundamental importance because it shows that if the function (i.e. $y_i(x_j)$) and its derivatives are known at a single (nominal) point, than it is possible to compute approximations to the function at all points in the immediate neighborhood of that point.

Taylor's theorem. *If $y_i(x_j) \in \mathbb{R}^r$ then there exists a scalar ζ ($0 \leq \zeta \leq 1$), such that*

$$y_i(x_j + \Delta x_j) = y_i(x_j) + \Delta x_j y_i'(x_j) + \frac{1}{2}\Delta x_j^2 y_i''(x_j) + \cdots$$
$$+ \frac{1}{(r-1)!}\Delta x_j^{r-1} y_i^{(r-1)}(x_j) + \frac{1}{r!}\Delta x_j^r y_i^{(r)}(x_j + \zeta \Delta x_j), \quad (4.2)$$

where $y_i^{(r)}(x_j)$ denotes the r-th derivative of y_i evaluated at x_j in an interval $\mathbb{R}^r$.

Using order notation, the Taylor-series of y_i about the nominal point x_j can be written as:

$$y_i(x_j + \Delta x_j) = y_i(x_j) + \Delta x_j y_i'(x_j) + \frac{1}{2}\Delta x_j^2 y_i''(x_j) + \cdots$$
$$+ \frac{1}{(r-1)!}\Delta x_j^{r-1} y_i^{(r-1)}(x_j) + T(\Delta x_j^r), \quad (4.3)$$

assuming that $|y_i^{(r)}|$ is finite in the interval $[x_j, x_j + \Delta x_j]$. The last term

$$T(\Delta x_j^r) = \frac{1}{r!}\Delta x_j^r y_i^{(r)}(x_j + \zeta \Delta x_j) \tag{4.4}$$

is termed *truncation error* and it is a result of the neglected terms in the Taylor-series expansion of the perturbed function $y_i(x_j + \Delta x_j)$.

From Eq. 4.2 it follows that the truncation error for the first-order forward-difference approximation (see Eq. 4.1) is

$$T(\Delta x_j) \equiv \frac{1}{2} \Delta x_j y_i''(x_j + \zeta \Delta x_j), \qquad 0 \le \zeta \le 1. \tag{4.5}$$

In general, ζ is unknown, and it is possible only to compute or estimate an upper bound on the truncation error, i.e. it leads to

$$T(\Delta x_j) \equiv \frac{1}{2} \Delta x_j y_i''(x_j + \Delta x_j). \tag{4.6}$$

4.1.1.1.2. Condition Error

By looking at the *forward-difference formula* (see Eq. 4.1), the computed function values to be used in calculating ω will be subject to error. Let the positive quantity ϵ_A denotes a *bound on the absolute error* in the computed function values at x_j and $x_j + \Delta x_j$. This quantity ϵ_A is known also as a *noise level* in the computed function values (see Lyness 1977). Let $\hat{y}_i(x_j)$ and $\hat{y}_i(x_j + \Delta x_j)$ denote the computed values of $y_i(x_j)$ and $y_i(x_j + \Delta x_j)$ (including errors that may results from the precision of the numerical iterations in the used FE-code). By assumption, the computed function values satisfy

$$\hat{y}_i(x_j) = y_i(x_j) + \theta_n \epsilon_A \tag{4.7}$$

and

$$\hat{y}_i(x_j + \Delta x_j) = y_i(x_j + \Delta x_j) + \theta_{\Delta x} \epsilon_A, \tag{4.8}$$

where $|\theta_n| \le 1$ and $|\theta_{\Delta x}| \le 1$. If the inexact function values are used in Eq. 4.1 and no other errors are made, it follows that

$$\omega(\hat{y}_i, \Delta x_j) - \omega(y_i, \Delta x_j) = \frac{2\alpha \epsilon_A}{\Delta x_j} \equiv C(\Delta x_j) \tag{4.9}$$

for some α, $|\alpha| \le 1$. The error $C(\Delta x_j)$ in the value of $\omega(\hat{y}_i, \Delta x_j)$ due to inaccurate values of y_i is termed the *condition error*; However α is unknown, it is possible only to compute or estimate an upper bound on the condition error (Gill *et al.* 1983, Gill *et al.* 1989):

$$|C(\Delta x_j)| \le \frac{2}{\Delta x_j} \epsilon_A. \tag{4.10}$$

4.1.1.1.3. Condition Error – Evaluation of the Bound on the Absolute Error ϵ_A

The used in the present study nonlinear, elastoplastic soil constitutive model – the HS model – is a mathematical relationship (i.e. equations) between rates of stress and strain.

In such nonlinear analysis where the load is applied incrementally, and where a finite number of calculation steps are used there will be some error from the exact solution. The purpose of an iterative solution algorithm is to ensure that the equilibrium errors, both local and global, become smaller than some acceptable predefined *tolerance*. This predefined tolerance in the used FE-code PLAXIS 3D (version 2011) is linked to the so called *tolerated error*, which is a criterion for terminating the iterations in the current step, within some predefined accuracy. The tolerated error is an user defined value in the FE-code.

Below it is given a description of the automatic error checking in the used FE-code of the global equilibrium error and the local error (Brinkgreve *et al.* 2011b). The both errors are needed as indicators for the implicit (see also Brinkgreve *et al.* 2011c) iterative algorithm when to terminate in the current load step.

Global error check

The global error checking parameter used in the Plaxis calculation kernel is related to the sum of the magnitudes of the out-of-balance nodal forces. The term "out-of-balance nodal forces" refers to the difference between the external loads and the forces that are in equilibrium with the current stresses. The global error is defined as shown below:

$$\text{Global error} = \frac{\sum |\text{Out-of-balance nodal forces}|}{\sum |\text{Active loads} + \text{CSP} \times \text{Inactive loads}|}. \tag{4.11}$$

The abbreviation CSP in the above equation is the current value of the *Stiffness* parameter, defined as:

$$\textit{Stiffness} = \int \frac{\Delta\varepsilon \cdot \Delta\sigma}{\Delta\varepsilon D^e \Delta\varepsilon} \tag{4.12}$$

which is a measure for the amount of plasticity that occurs during the calculation. In the above equation D^e represents the elastic material stiffness matrix according to Hooke's law for the current stress increment $\Delta\sigma$, and $\Delta\varepsilon$ is the strain increment.

Local error check

Local errors refer to the errors at each individual stress integration point. In Figure 4.3 there are shown the changes in one of the stress components that occur during the iterative process. At the end of each iteration, two important values of stress are calculated by the FE-code Plaxis. The first of these, the *equilibrium stress*, is the stress calculated directly from the stiffness matrix (i.e. point **A** in Figure 4.3). The second important stress, the
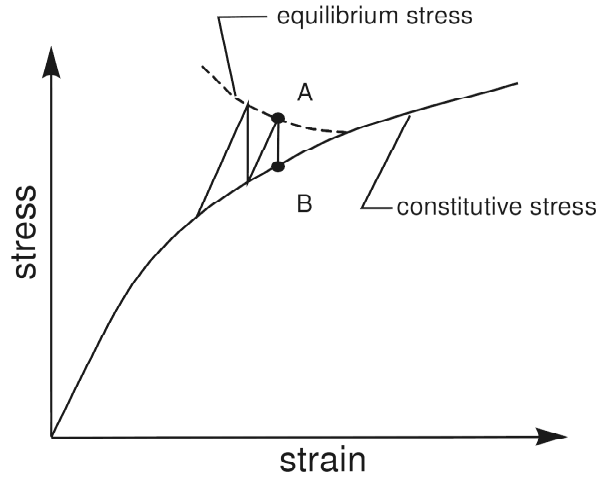
Figure 4.3.: Equilibrium and constitutive stresses (Brinkgreve *et al.* 2011c).

constitutive stress, is the value of stress on the material stress-strain curve at the same strain as the equilibrium stress, i.e. point **B** in Figure 4.3.

The dashed line in Figure 4.3 indicates the path of the equilibrium stress. In general this equilibrium stress path depends on the nature of the stress field and the applied loading. For the case of a soil element obeying the Mohr-Coulomb criterion, the local error for the particular stress point at the end of the iteration is defined:

$$\text{Local error} = \frac{|\sigma^e - \sigma^c|}{T_{\max}}. \tag{4.13}$$

In the above equation the numerator is a norm of the difference between the equilibrium stress tensor, σ^e, and the constitutive stress tensor, σ^c. This norm is defined by:

$$|\sigma^e - \sigma^c| = \left[(\sigma^e_{xx} - \sigma^c_{xx})^2 + (\sigma^e_{yy} - \sigma^c_{yy})^2 + (\sigma^e_{zz} - \sigma^c_{zz})^2 + \cdots \right.$$
$$\left. + (\sigma^e_{xy} - \sigma^c_{xy})^2 + (\sigma^e_{yz} - \sigma^c_{yz})^2 + (\sigma^e_{zx} - \sigma^c_{zx})^2 \right]^{1/2}. \tag{4.14}$$

The denominator ($T_{\max}$) of Eq. 4.13 is the maximum value of the shear stress as defined by the Coulomb failure criterion.

When the stress point is located in an interface element the following expression is used:

$$\text{Local error} = \frac{\sqrt{(\sigma^e_n - \sigma^c_n)^2 + (\tau^e - \tau^c)^2}}{c_i - \sigma^c_n \tan \varphi_i}, \tag{4.15}$$

where σ_n and τ^e represent the normal and the shear stresses respectively in the interface. To quantify the local accuracy, the concept of *inaccurate plastic points* is used. A plastic

point is defined to be inaccurate if the local error exceeds the value of the user defined *tolerated error*.

Termination of the iterations

For the used FE-code Plaxis to terminate the iterations in the current load step, all of the following three error checks must be satisfied (Brinkgreve *et al.* 2011b).

$$\text{Global error} \leq \text{Tolerated error;} \tag{4.16}$$

$$\text{No. of inaccurate soil points} \leq 3 + \frac{\text{No. of plastic soil points}}{10}; \tag{4.17}$$

$$\text{No. of inaccurate interface points} \leq 3 + \frac{\text{No. of plastic interface points}}{10}; \tag{4.18}$$

For further details of these error-checking procedures, see Vermeer & van Langen (1989).

For obtaining an appropriate value of ϵ_A for calculating the condition error in Eq. 4.1, the FE-model of constructing the shallow tunnel, i.e. of $y_i(x_j)$, is computed in lower (i.e. the normal default used value of the tolerated error $= 1 \cdot 10^{-2}$) and in much higher precision (i.e. with a tolerated error $= 1 \cdot 10^{-8}$); see further Section 4.1.2.1.1. The calculation time increases around 150 times when switching to this higher precision, because the iterations are performed with much smaller load increments in smaller steps.
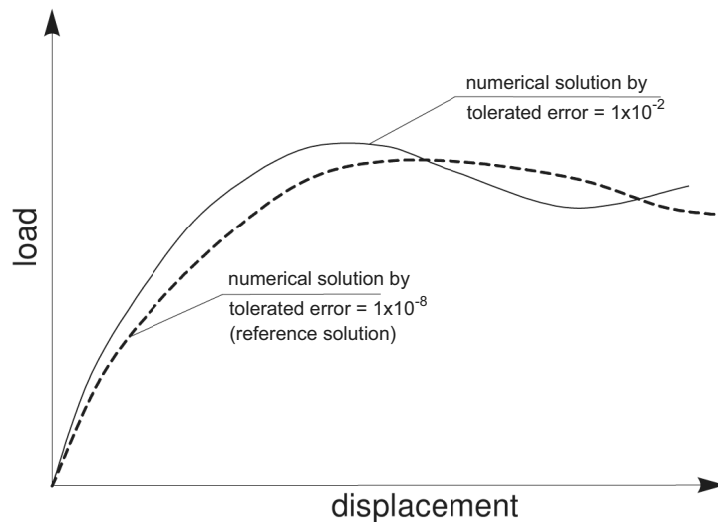
Figure 4.4.: Influence on the numerical solution dependent from the accuracy of the iterative procedure in the FE-code, when it is used a nonlinear soil constitutive model like the HS model (adopted from Brinkgreve *et al.* 2011c).

4.1.1.1.4. Total Error

Finally, the *total error* e is the sum of the truncation and condition error:

$$e(\Delta x_j) = T(\Delta x_j) + C(\Delta x_j). \tag{4.19}$$

For example in the *forward-difference formula* (Eq. 4.1) it is

$$e(\Delta x_j) = \frac{\Delta x_j}{2}|y_i''| + \frac{2}{\Delta x_j}\epsilon_A, \tag{4.20}$$

where $|y_i''|$ is the second derivative in the interval $[x_j, x_j + \Delta x_j]$. Here it is used the central finite difference approximation for evaluating the second derivative:

$$y_i''(x_j) \approx \Phi_i(x_j) = \frac{y_i(x_j + \Delta x_j) - 2y_i(x_j) + y_i(x_j - \Delta x_j)}{\Delta x_j^2}, \tag{4.21}$$

so that

$$e(\Delta x_j) = \underbrace{\frac{\Delta x_j}{2}|\Phi_j|}_{\text{truncation error}} + \underbrace{\frac{2}{\Delta x_j}\epsilon_A}_{\text{condition error}}. \tag{4.22}$$

It would be noted that Eq. 4.21 is an approximation to y_i'' in the interval $[x_j, x_j + \Delta x_j]$ only if y_i'' changes slightly around x_j.

The *optimum step size* Δx_j is the one, which minimizes the sum of the errors defined in Eq. 4.19. Therefore, the optimum step size is the one which balances the truncation and condition error, i.e. which solves the so called "step-size-dilemma"; If the step size is selected to be small, so as to reduce the truncation error, this may results in excessive condition error. By definition the condition error is a decreasing function of the of the step size Δx_j.

4.1.1.2. Computing the Sensitivity Measures

After calculating the partial derivatives (i.e. the sensitivities / sensitivity derivatives), further useful transformation is to calculate the dimensional *scaled sensitivities* (Hill & Tiedeman 2007, Hill 1998)

$$SS_{ij} = \left(\frac{\Delta y_i}{\Delta x_j}\right) x_j. \tag{4.23}$$

When the observations are only one single type (i.e. in the present study it was decided only displacements to be measured) the *dimensional* scaled sensitivities are calculated,

because they do not need the predetermination of statistical weighting factors associated with each type of observation, like when using the *dimensionless* scaled sensitivities for different type of observation data (see Zhang *et al.* 2003). The observation points with relative large SS_{ij} are likely to provide more information about parameter x_j compared to observations associated with low SS_{ij}.

The SS_{ij} are accumulated for each parameter x_j to produce the *composite scaled sensitivities* (Hill & Tiedeman 2007, Hill 1998)

$$CSS_j = \sqrt{\frac{1}{N} \sum_{i=1}^{N} (SS_{ij})^2} \tag{4.24}$$

where N is the number of the observations (measurements) in the numerical model, and can include not only displacements, but also stresses, pore water pressures, and others, depending on the particular geotechnical problem. The composite scaled sensitivity gives the overall model sensitivity (of course only overall the chosen observation points; therefore these points must be preselected very careful) to a single input model parameter. They can be calculated for some or all observation points.

4.1.2. Results of the Performed Sensitivity Analysis

4.1.2.1. Step Size Selection

In the present study there is evaluated an optimum step size for calculating the derivatives using the first-order forward-difference approximation (Eq. 4.1).

4.1.2.1.1. Evaluation of the Bound on the Absolute Error ϵ_A

Firstly, it has been tested the influence of the *tolerated error* in PLAXIS 3D (version 2011) on the simulation of Oedometer test (Fig. 4.5). The modelled soil sample has an initial height of $h_0 = 1$ m. There are used two kinds of constitutive models for representing the soil behaviour: a linear-elastic material with input parameters $\gamma_{\mathsf{unsat}} = 17.00$ kN/m^3, $\nu = 0.30$, $E = 7326$ kN/m^2 ($\equiv E_{oed} = 10\,000$ kN/m^2) and the HS model with parameters with the same values like for the tunnel, according to Table 3.2. On the top of the cube it is applied a vertical loading $\sigma_v = 25$ kN/m^2. The results are presented in Table 4.1 and 4.2, respectively in Figure 4.6. There is no meaningfully influence by using a linear-elastic constitutive model, however by using the nonlinear elastoplastic HS model this influence

Table 4.1.: Influence of the *tolerated error* in the FE-code on the vertical displacements of a soil in a simulation of Oedometer test by using a linear-elastic model.

Tolerated error	Δh [m]
$1 \cdot 10^{-2}$	-0.00249994430097585
$1 \cdot 10^{-3}$	-0.00249994430096918
$1 \cdot 10^{-4}$	-0.00249994430096915
$1 \cdot 10^{-5}$	-0.00249994430096915
$1 \cdot 10^{-6}$	-0.00249994430096915
$1 \cdot 10^{-7}$	-0.00249994430096915
$1 \cdot 10^{-8}$	-0.00249994430096915
$1 \cdot 10^{-9}$	-0.00249994430096915

Table 4.2.: Influence of the *tolerated error* in the FE-code on the vertical displacements of a soil in a simulation of Oedometer test by using the elastoplastic HS model.

Tolerated error	Δh [m]
$1 \cdot 10^{-2}$	-0.0013192125539891
$1 \cdot 10^{-3}$	-0.00131024780511905
$1 \cdot 10^{-4}$	-0.00130301120862241
$1 \cdot 10^{-5}$	-0.00125361297695836
$1 \cdot 10^{-6}$	-0.00124654434472835
$1 \cdot 10^{-7}$	-0.00124476360075673
$1 \cdot 10^{-8}$	-0.00124308399399264
$1 \cdot 10^{-9}$	-0.00124280205197854
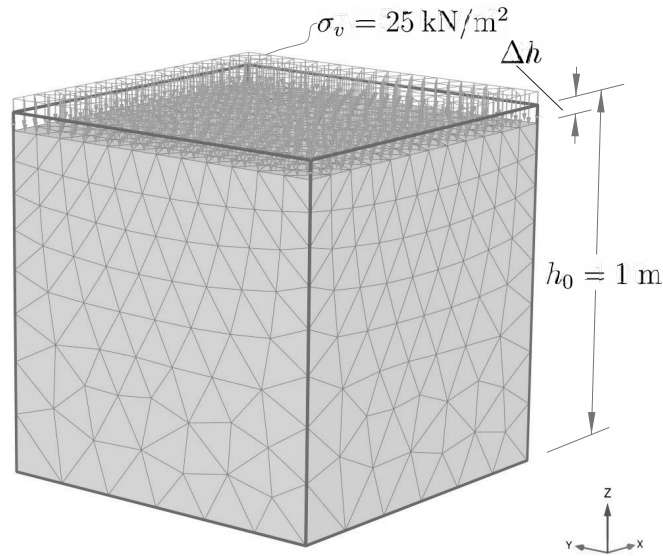
Figure 4.5.: Simulation of Oedometer test for testing the influence of the *tolerated error* in the FE-code on the vertical displacements/settlements u$_z$ (or Δh). Used are a linear-elastic and the elastoplastic HS model for simulating the soil behaviour.
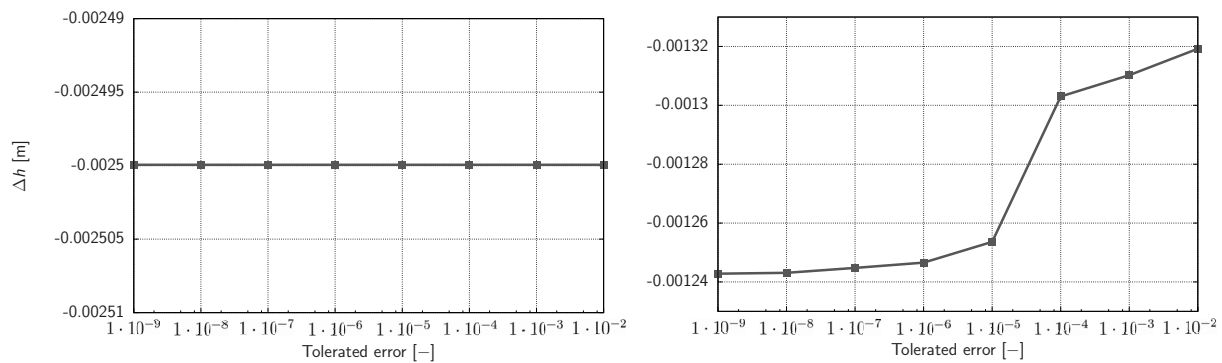
Figure 4.6.: Influence of the *tolerated error* in the FE-code on the vertical displacements in the Oedometer test by using a linear-elastic model (left) and by using the elastoplastic HS model (right).

is evident, and for small values of the tolerated error, i.e. increased accuracy of the iterative procedure, the relative change in the displacements becomes smaller.

In the next Figure 4.7 the results for the tunnel model are presented. It is evident that for values of the *tolerated error* in PLAXIS smaller than $1 \cdot 10^{-7}$ there is relatively no change in the displacements, i.e. there is no significant influence of the tolerated error any more. Therefore, one may use the numerical solution obtained with a tolerated error $= 1 \cdot 10^{-8}$ as a "reference solution" for calculating the bound on the absolute error ϵ_A.
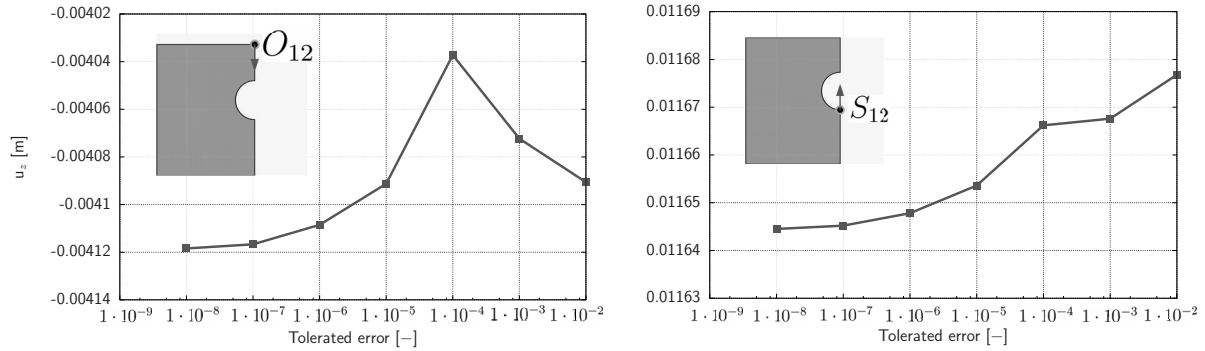
Figure 4.7.: Influence of the *tolerated error* in the FE-code on the final vertical displacements in the observed points O_{12} and S_{12}.

The calculated values of the final vertical displacements in the observed points by tolerated error $= 1 \cdot 10^{-2}$ (default solution) are

$$u_z^{-2}(O_{12}) = -0.00409159531773043 \text{ m},$$
$$u_z^{-2}(S_{12}) = 0.01167684002320828 \text{ m},$$

and by tolerated error $= 1 \cdot 10^{-8}$ (reference solution, with a higher numerical accuracy) they are

$$u_z^{-8}(O_{12}) = -0.00411842423141335 \text{ m},$$
$$u_z^{-8}(S_{12}) = 0.01164457153191562 \text{ m}.$$

Hence, it has been assumed the bound on the absolute error to be of order (see also Section 4.1.1.1.3)

$$\epsilon_A = |u_z^{-2}(O_{12}) - u_z^{-8}(O_{12})|/2 + |u_z^{-2}(S_{12}) - u_z^{-8}(S_{12})|/2 \qquad (4.25)$$
$$\epsilon_A = 0.00002954870248779 = 2.955 \cdot 10^{-5} \text{ m}.$$

Because the error bound ϵ_A may be not precisely evaluated under the above assumptions, additionally, the effect of ϵ_A on the total error is investigated, respectively on the step size evaluations. To test this effect ϵ_A is varied – to be 10-times larger or 10-times smaller for each single input parameter. The results from this variation for the investigated input parameters of the HS model are presented in Figures 4.18, 4.20, 4.22, 4.24, and 4.26. The results shown in Figures 4.18 and 4.20 represent very well the two extreme results. For the parameter $x_1 = c = 10$ kN/m² the modified values of ϵ_A has no meaningful influence on the range of appropriate step sizes (because of its low sensitivity; see Section 4.1.2.2). For the another parameter $x_2 = \varphi = 35°$ there is a noticeable (because of its large sensitivity; see Section 4.1.2.2) but still acceptable effect on the results.

4.1.2.1.2. Influence of the Step Size on the Errors in the Finite Difference Approximation

There are calculated the derivatives in nodes O_{12} and S_{12} for each of the observed five input parameters of the HS model, and for different step sizes Δx_j, by using the forward-difference formula (Eq. 4.1). The results are shown in Figures 4.8 and 4.9. Additionally, the derivatives are normalized logarithmically using the relation (Haftka 1992)

$$\Psi = \frac{\Delta y_i}{\Delta x_j}\frac{x_j}{y_i}. \tag{4.26}$$

The above relation is also known as sensitivity index. So the normalized derivatives can be easily compared to each other, and their relative magnitude can be evaluated. When the normalized derivative is larger than unity (see Fig. 4.8 and 4.9) the relative change in y_i is larger than the relative change in x_j and the derivative can be considered to be large. When the same is much smaller than unity the derivative is considered to be small, and in general, it would be difficult to evaluate it accurately using finite-difference differentiation (Haftka & Gardal 1992).

In Figures 4.8 and 4.9 it is marked the range of appropriate step sizes regarding all input parameters together, separately for the two observation nodes O_{12} and S_{12}. The straight horizontal lines of the values of the derivatives in the both figures represents this optimum range – from about 0.05 % up to about 15 %. Outside this range the step sizes are not appropriate, because for smaller steps the total error is dominated significantly by the condition error (oscilations, see in Fig. 4.8 and 4.9), while for larger steps it is dominated by the truncation error (see additionally Fig. 4.17 and 4.19).

For the purpose of an identification of the soil constitutive parameters via subsequent back analysis, with some prior knowledge of the soil properties, for each input parameter a search space with lower and upper bound is defined. For each parameter it is assumed its *nominal point*, for which the sensitivity is calculated, to be in the middle of the corresponding search interval. Additionally, here it is investigated the effect of variation of the nominal point on the derivatives. The value of the nominal point is varied in a chosen reliable nominal range of ±30 %, and the results are presented separately for point O_{12} and S_{12} in Figures 4.10 and 4.11. The both graphs show that the derivatives calculated for different points around the nominal point of each input parameter (chosen nominal points: $x_1 = c = 10$ kN/m², $x_2 = \varphi = 35°$, $x_3 = E_{ur}^{ref} = 100000$ kN/m², $x_4 = E_{oed}^{ref} = 35000$ kN/m² and $x_5 = E_{50}^{ref} = 35000$ kN/m²), with chosen constant step size $\Delta x = 10\%$, are smooth functions and that means that these chosen nominal points
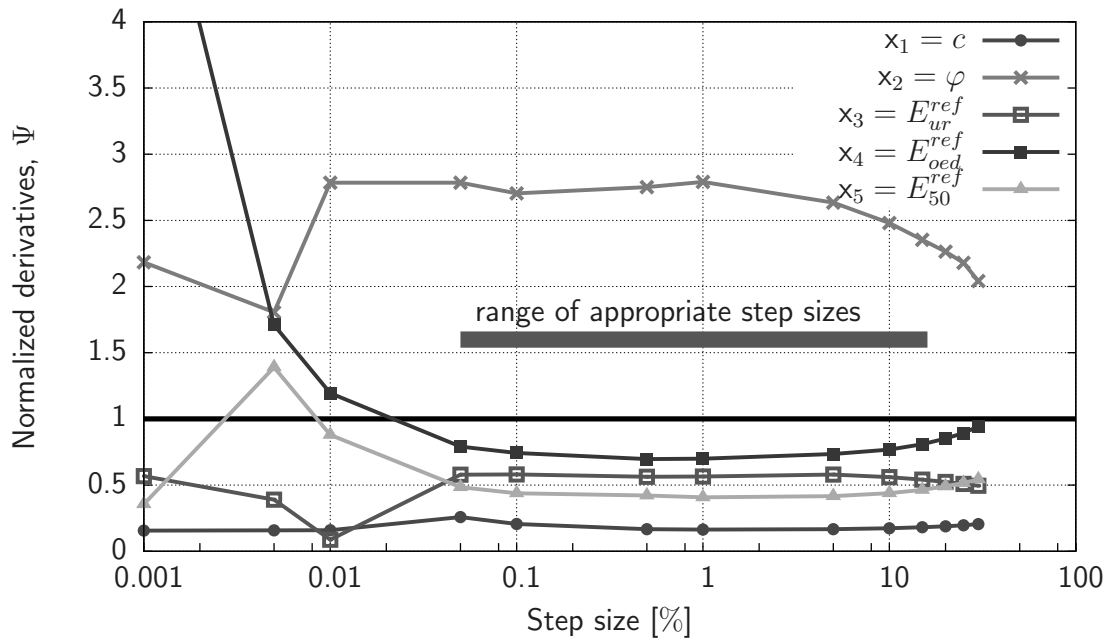
Figure 4.8.: Normalized derivatives Ψ of u_z for different step sizes in node O_{12} (calculated by Eq. 4.26).
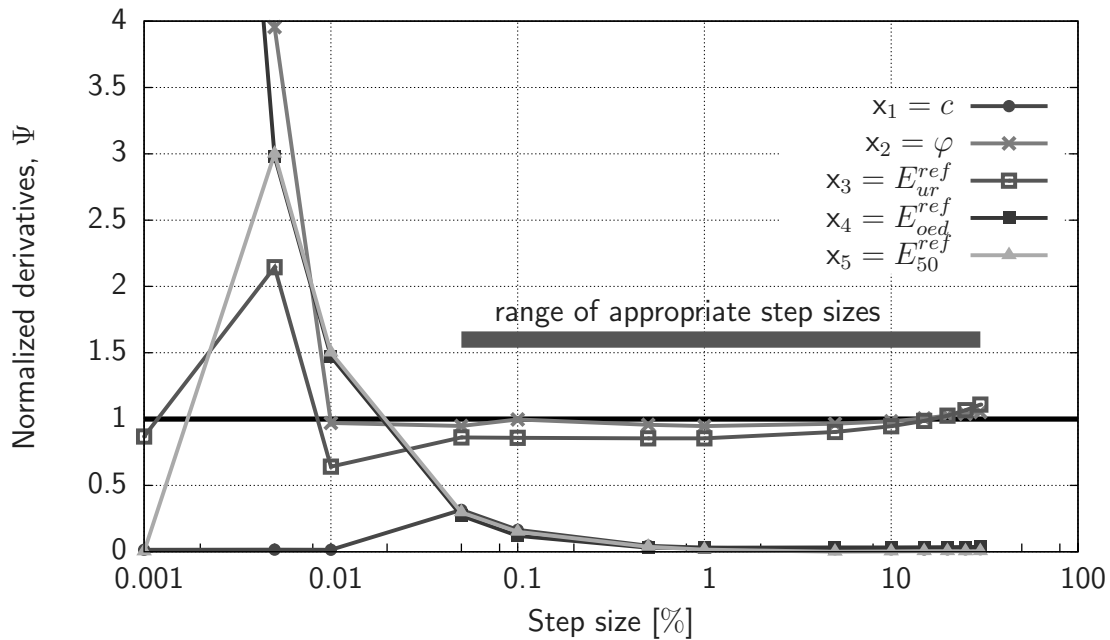
Figure 4.9.: Normalized derivatives Ψ of u_z for different step sizes in node S_{12} (calculated by Eq. 4.26).
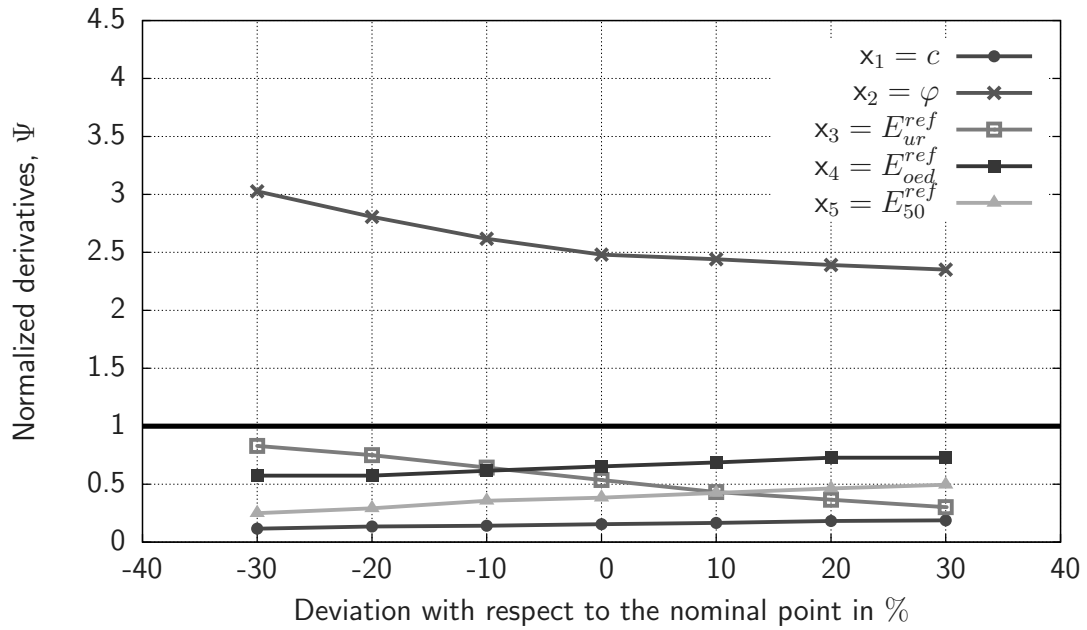
Figure 4.10.: Normalized derivatives Ψ of u_z for different points around the *nominal point* in node O_{12} (calculated by Eq. 4.26).
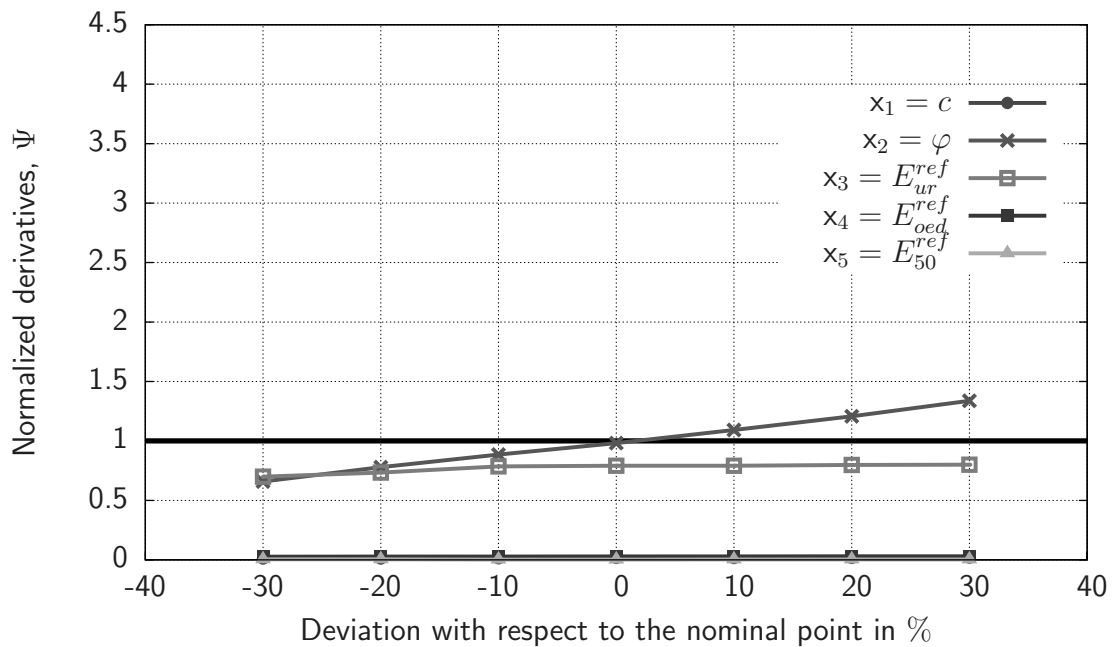
Figure 4.11.: Normalized derivatives Ψ of u_z for different points around the *nominal point* in node S_{12} (calculated by Eq. 4.26).
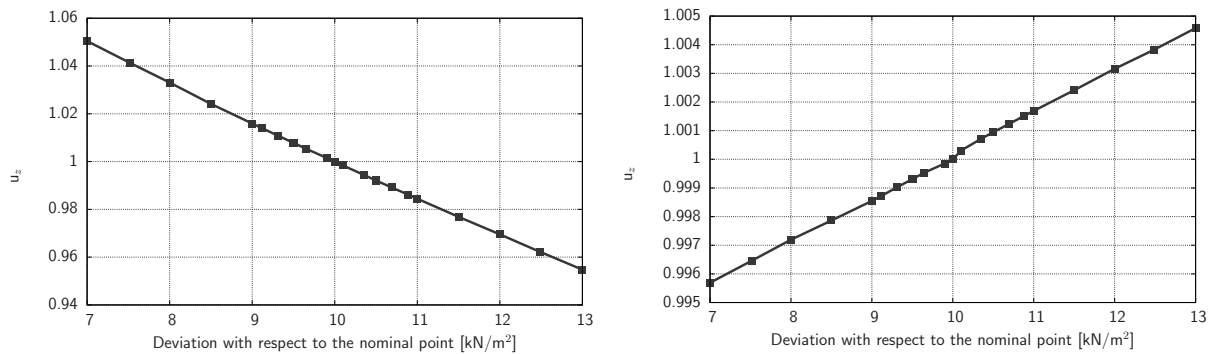
Figure 4.12.: Normalized vertical displacements u_z of observation point O_{12} (left) and S_{12} (right) regarding the parameter c with a nominal point $x_1 = c = 10$ kN/m^2, and deviation in a chosen nominal range ± 30 % around its nominal point.
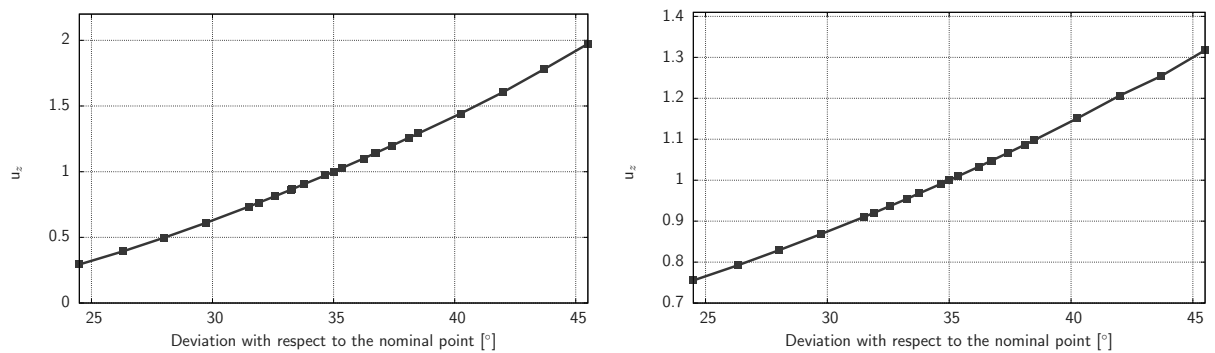
Figure 4.13.: Normalized vertical displacements u_z of observation point O_{12} (left) and S_{12} (right) regarding the parameter φ with a nominal point $x_2 = \varphi = 35°$, and deviation in a chosen nominal range ± 30 % around its nominal point.
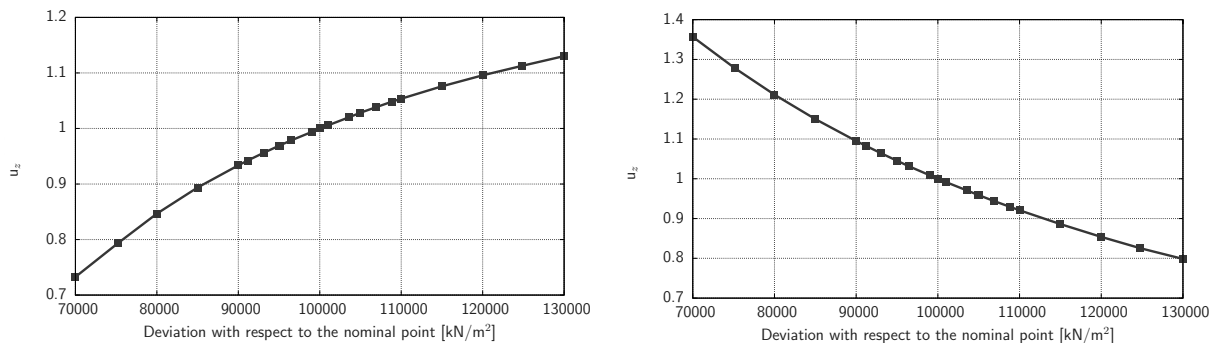
Figure 4.14.: Normalized vertical displacements u_z of observation point O_{12} (left) and S_{12} (right) regarding the parameter E_{ur}^{ref} with a nominal point $x_3 = E_{ur}^{ref} = 100000$ kN/m^2, and deviation in a chosen nominal range ± 30 % around its nominal point.
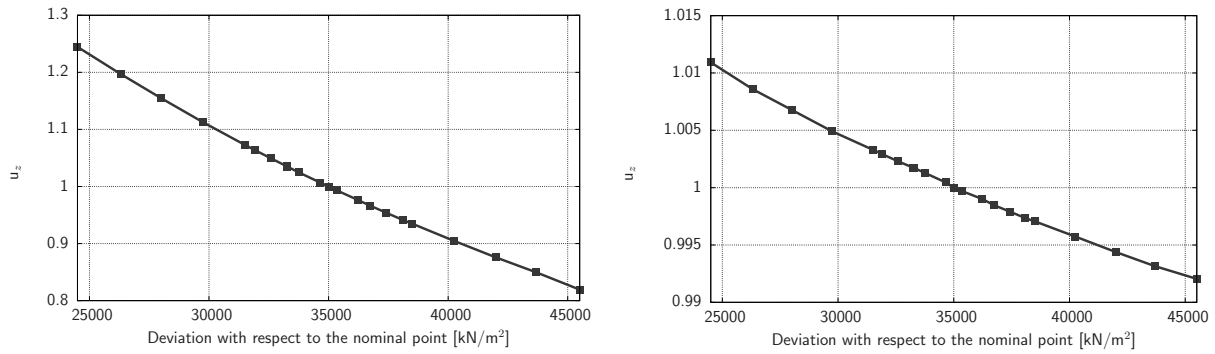
Figure 4.15.: Normalized vertical displacements u_z of observation point O_{12} (left) and S_{12} (right) regarding the parameter E_{oed}^{ref} with a nominal point $x_4 = E_{oed}^{ref} = 35\,000$ kN/m^2, and deviation in a chosen nominal range ± 30 % around its nominal point.
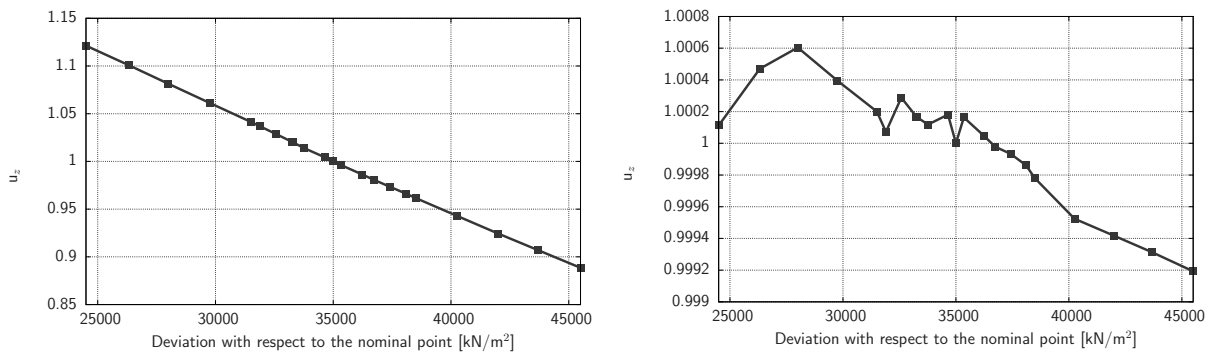
Figure 4.16.: Normalized vertical displacements u_z of observation point O_{12} (left) and S_{12} (right) regarding the parameter E_{50}^{ref} with a nominal point $x_5 = E_{50}^{ref} = 35\,000$ kN/m^2, and deviation in a nominal range ± 30 % around its nominal point.
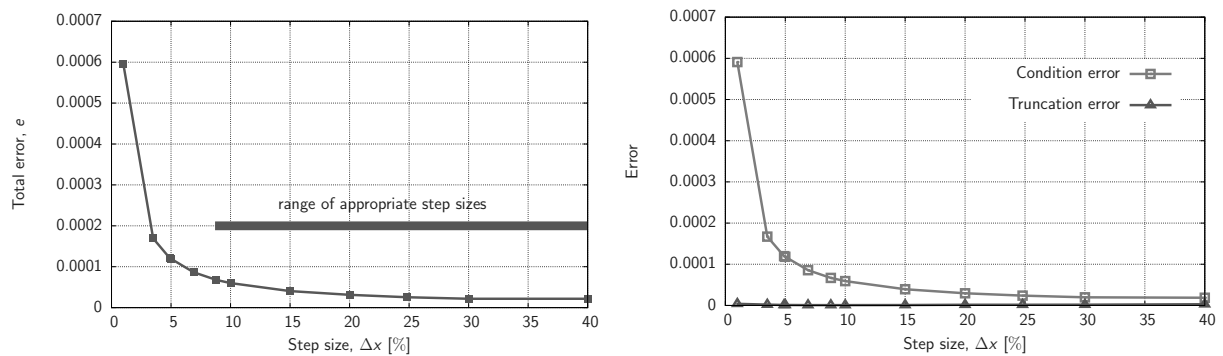
Figure 4.17.: Optimum Step Size for the parameter $x_1 = c = 10$ kN/m^2 (left: *Total error* calculated by Eq. 4.22; right: *Truncation error* and *Condition error* calculated from Eq. 4.22).
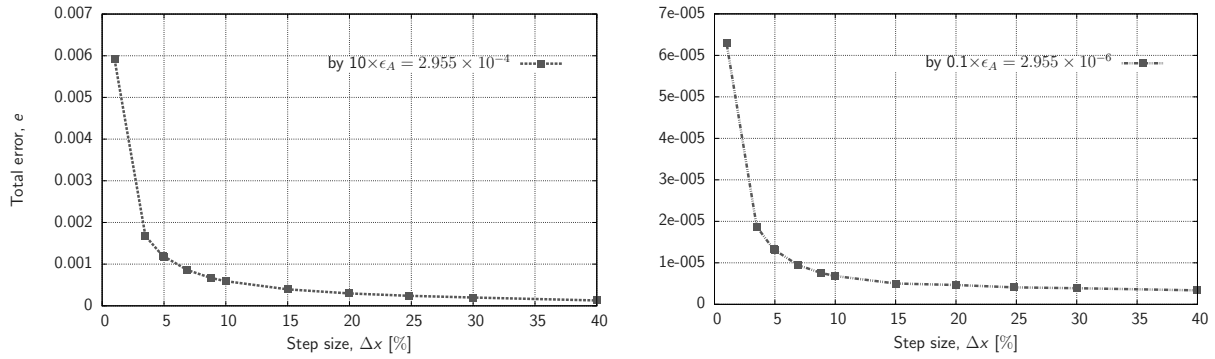
Figure 4.18.: Influence of ϵ_A on the total error (i.e on the optimum step size) in the first-order forward difference approximation of the derivatives regarding the parameter $x_1 = c = 10$ kN/m^2 (calculated by Eq. 4.22).
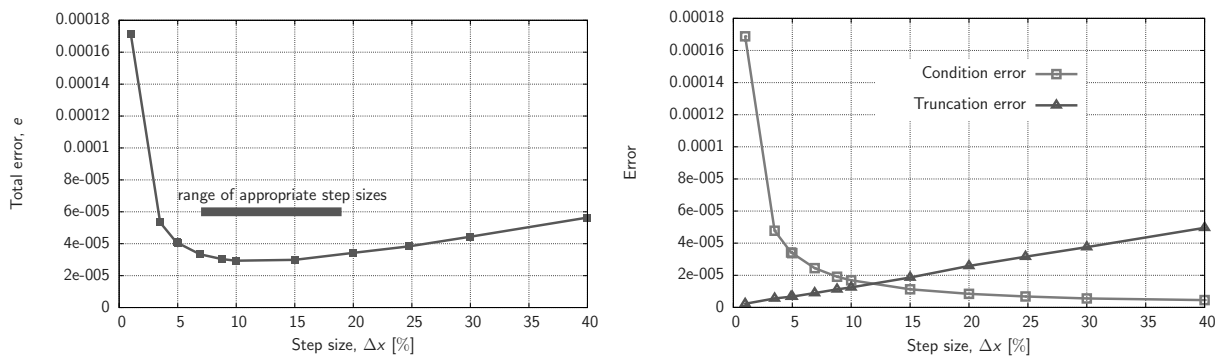
Figure 4.19.: Optimum Step Size for the parameter $x_2 = \varphi = 35°$ (left: *Total error* calculated by Eq. 4.22; right: *Truncation error* and *Condition error* calculated from Eq. 4.22).
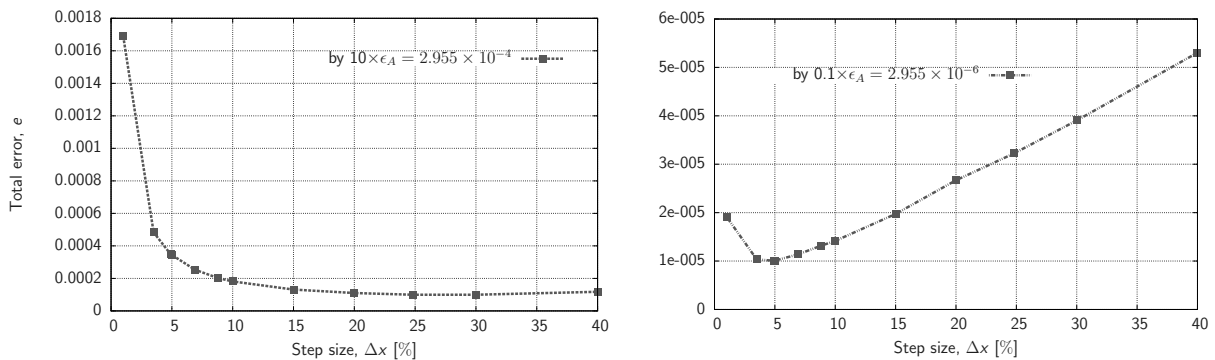
Figure 4.20.: Influence of ϵ_A on the total error (i.e on the optimum step size) in the first-order forward difference approximation of the derivatives regarding the parameter $x_2 = \varphi = 35°$ (calculated by Eq. 4.22).
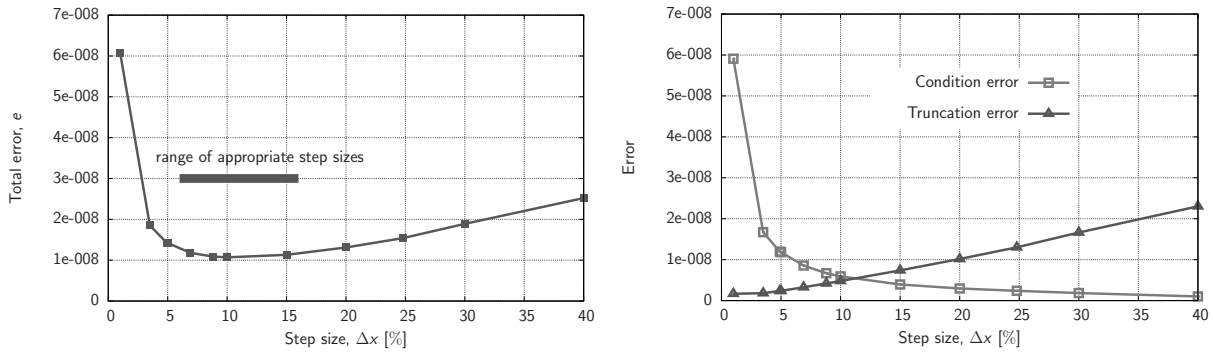
Figure 4.21.: Optimum Step Size for the parameter $x_3 = E_{ur}^{ref} = 100\,000$ kN/m^2 (left: *Total error* calculated by Eq. 4.22; right: *Truncation error* and *Condition error* calculated from Eq. 4.22).
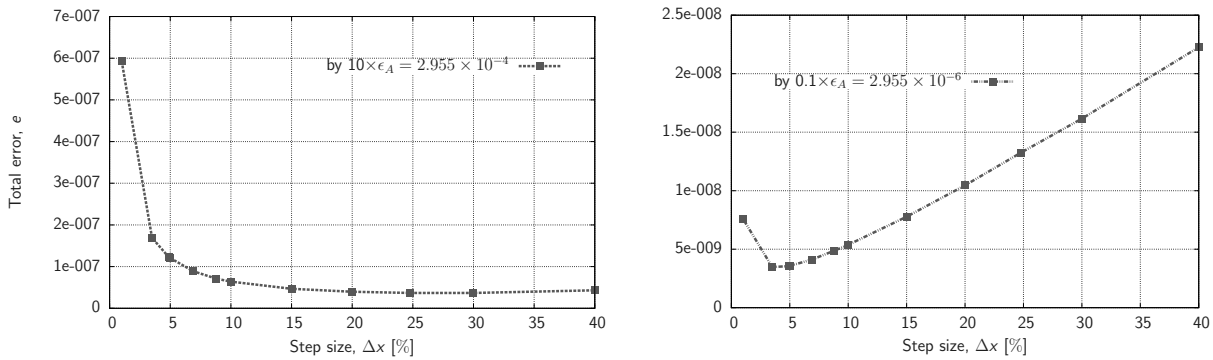
Figure 4.22.: Influence of ϵ_A on the total error (i.e on the optimum step size) in the first-order forward difference approximation of the derivatives regarding the parameter $x_3 = E_{ur}^{ref} = 100\,000$ kN/m^2 (calculated by Eq. 4.22).
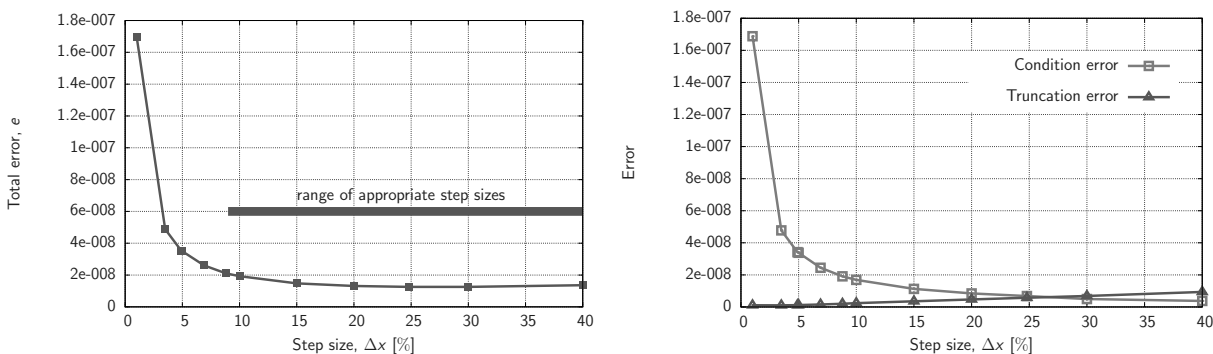
Figure 4.23.: Optimum Step Size for the parameter $x_4 = E_{oed}^{ref} = 35\,000$ kN/m^2 (left: *Total error* calculated by Eq. 4.22; right: *Truncation error* and *Condition error* calculated from Eq. 4.22).
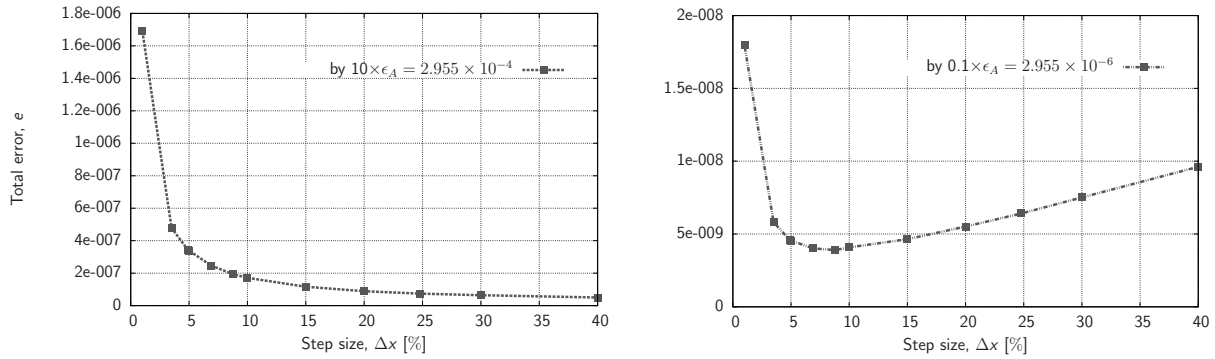
Figure 4.24.: Influence of ϵ_A on the total error (i.e on the optimum step size) in the first-order forward difference approximation of the derivatives regarding the parameter $x_4 = E_{oed}^{ref} = 35\,000$ kN/m^2 (calculated by Eq. 4.22).
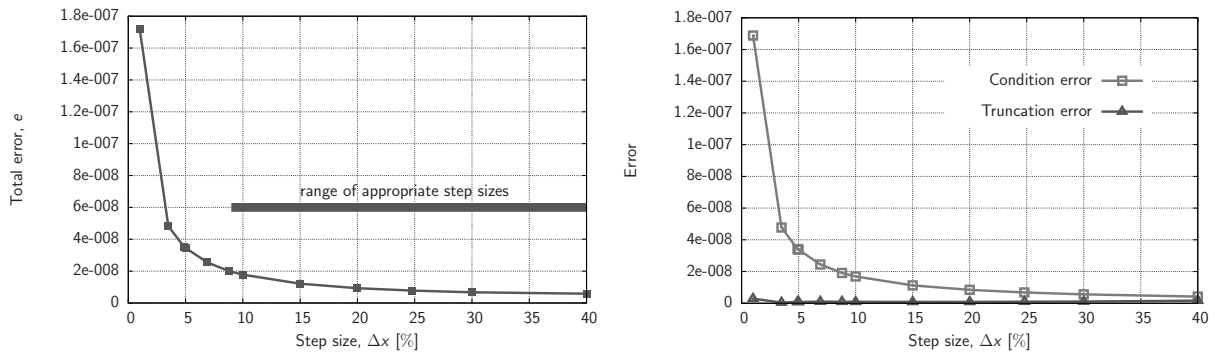
Figure 4.25.: Optimum Step Size for the parameter $x_5 = E_{50}^{ref} = 35\,000$ kN/m^2 (left: *Total error* calculated by Eq. 4.22; right: *Truncation error* and *Condition error* calculated from Eq. 4.22).
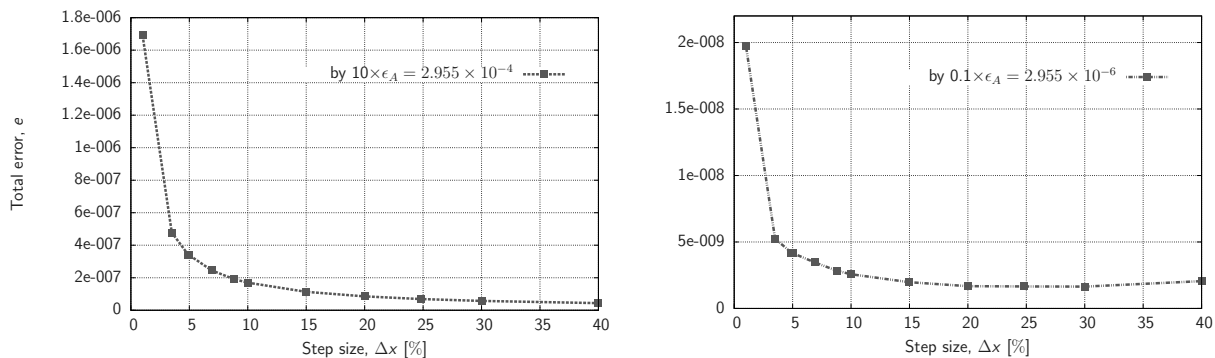
Figure 4.26.: Influence of ϵ_A on the total error (i.e on the optimum step size) in the first-order forward difference approximation of the derivatives regarding the parameter $x_5 = E_{50}^{ref} = 35\,000$ kN/m^2 (calculated by Eq. 4.22).

are appropriate and reliable for calculating the sensitivities. The normalized derivatives in the same two Figures 4.10 and 4.11 show also that for each parameter the model, i.e. the response is monotonic. The same results, i.e monotonic response, is shown also in Figures 4.12–4.16. There the final vertical displacements in O_{12} and S_{12} are normalized with the displacements calculated with the nominal value of the parameter. In Figure 4.12, right, there are shown some numerical oscillations, because the sensitivity of the parameter E_{50}^{ref} in S_{12} is low (see additionally Fig. 4.27). The results are presented in a chosen nominal range $\pm 30\,\%$ around the nominal point of each parameter. Similar monotonic response is observed also by Kasper & Meschke(2004b) in a 3D elasto-plastic numerical simulation of the same geotechnical problem – closed face shield supported mechanized tunnelling in soft ground with low overburden.

4.1.2.1.3. Optimum Step Size

For each of the investigated input parameters of the Hardening Soil model an optimum step size Δx_{opt} is selected. This is done by intersecting together the appropriate interval of each input parameter (see Fig. 4.17, 4.19, 4.21, 4.23, 4.25, 4.8, and 4.9). Thereafter, the chosen optimum step sizes of the parameters are: $\Delta x_{opt}(\varphi) = 10\,\%$, $\Delta x_{opt}(c) = 15\,\%$, $\Delta x_{opt}(E_{ur}^{ref}) = 8\,\%$, $\Delta x_{opt}(E_{50}^{ref}) = 14\,\%$, $\Delta x_{opt}(E_{oed}^{ref}) = 14\,\%$.

4.1.2.2. Local Sensitivities

In Figure 4.27 there are shown the calculated composite scaled sensitivities, CSS_j, of the investigated five input parameters of the HS model regarding the final vertical displacements by the shallow tunnel excavation separately for points O_{12} and S_{12}. In Figure 4.28 there are presented the overall sensitivities in O_{12} and S_{12}. The parameter $x_2 = \varphi$ has the largest sensitivity, i.e. this parameter is the most important in the HS model for this geotechnical problem. The second important parameter is $x_3 = E_{ur}^{ref}$. Its sensitivity (i.e. influence) is larger at the tunnel invert, i.e. in point S_{12} because the (mechanized) tunnelling is an unloading process, because soil volumes are excavated (removed) from the subsoil. This statement is shown first in Figure 4.29 where the current isotropic over-consolidation ratio, OCR, in the model is presented, which in the HS model is the ratio between the isotropic pre-consolidation stress p_p and the equivalent isotropic stress p_{eq} (see Brinkgreve *et al.* 2011a). In the areas in yellow (i.e. where the current OCR is larger than unity) bellow the tunnel invert the stresses in the soil are reduced, i.e. the soil is unloaded. In Figure 4.30 it is shown the value of the current stress-dependent stiffness E_{ur} for
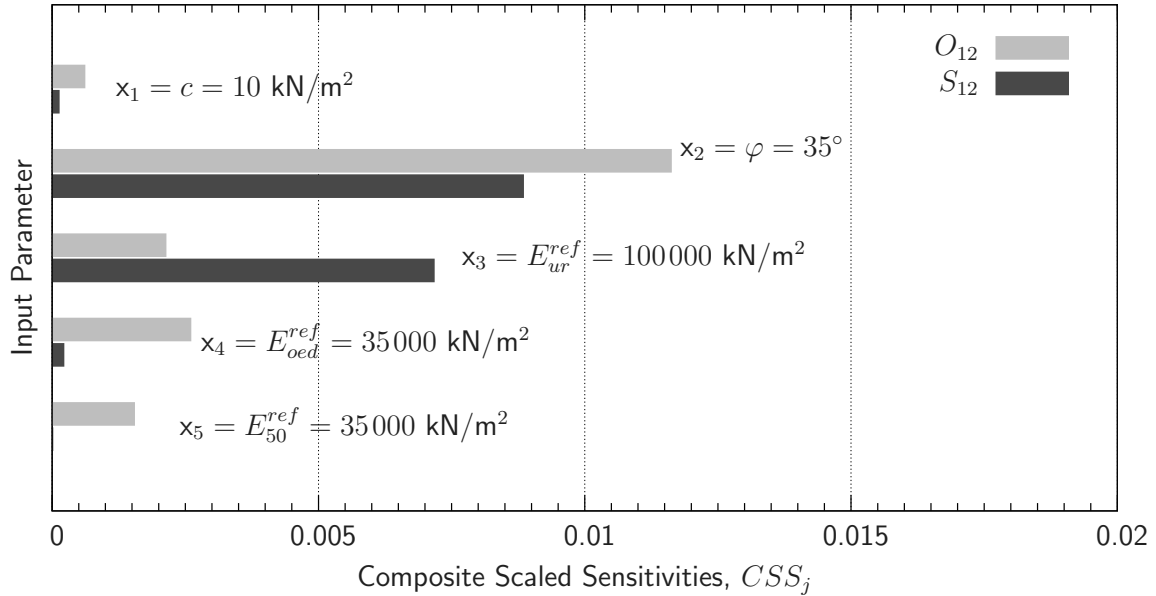
Figure 4.27.: Sensitivities for the shallow (overburden height $= 1D$) tunnel separately in observation points O_{12} and S_{12} (calculated by Eq. 4.23, with the final vertical displacements, i.e. $N = 1$).

unloading (and reloading) in the model. The two stiffnesses $x_4 = E_{oed}^{ref}$ and $x_5 = E_{50}^{ref}$ for primary loading have low sensitivity in observation point S_{12}. Finally, the least sensitive parameter is $x_1 = c$.

Additionally, the SA is performed using a softer material (e.g. loose sand) for modelling the subsoil, i.e. there are decreased the three stiffnesses and the angle of internal friction of the soil of the HS model as used up to now (corresponding to a hard soil, e.g. dense sand; see Table 3.2). Subsequently, the new chosen parameters for this loose sand are $E_{oed}^{ref} = E_{50}^{ref} = 15\,000$ kN/m², $E_{ur}^{ref} = 50\,000$ kN/m², $\varphi = 27°$, and $\psi = 0$; all the other parameters remain unchanged, also the support pressures are the same. The results of the sensitivity with a softer (looser) and harder (denser) soil are compared in Figure 4.31 which shows that generally the sensitivities of the investigated constitutive input parameters increase with decrease of the strength and stiffness properties of the subsoil.

As an additional explanation, only for understanding, it have to be stated that the sensitivity calculated for the angle of internal friction of the soil φ (see Fig. 4.28 and 4.27) is largely influenced (i.e. about five times increased) by the contribution coming from the coefficient of lateral earth pressure at rest K_0^{nc}, because in the sensitivity calculations, and also later in the subsequent soil parameters identification there is used the Jaky's semi-empirical relation ($K_0^{nc} = 1 - \sin\varphi$) for identifying the initial soil conditions. That

Figure 4.28.: Calculated overall sensitivities in O_{12} & S_{12} regarding the investigated five input parameters of the soil constitutive model (the HS model) by the shallow (overburden height $= 1D$) tunnel (calculated by Eq. 4.23, with the final vertical displacements, i.e. $N = 2$).
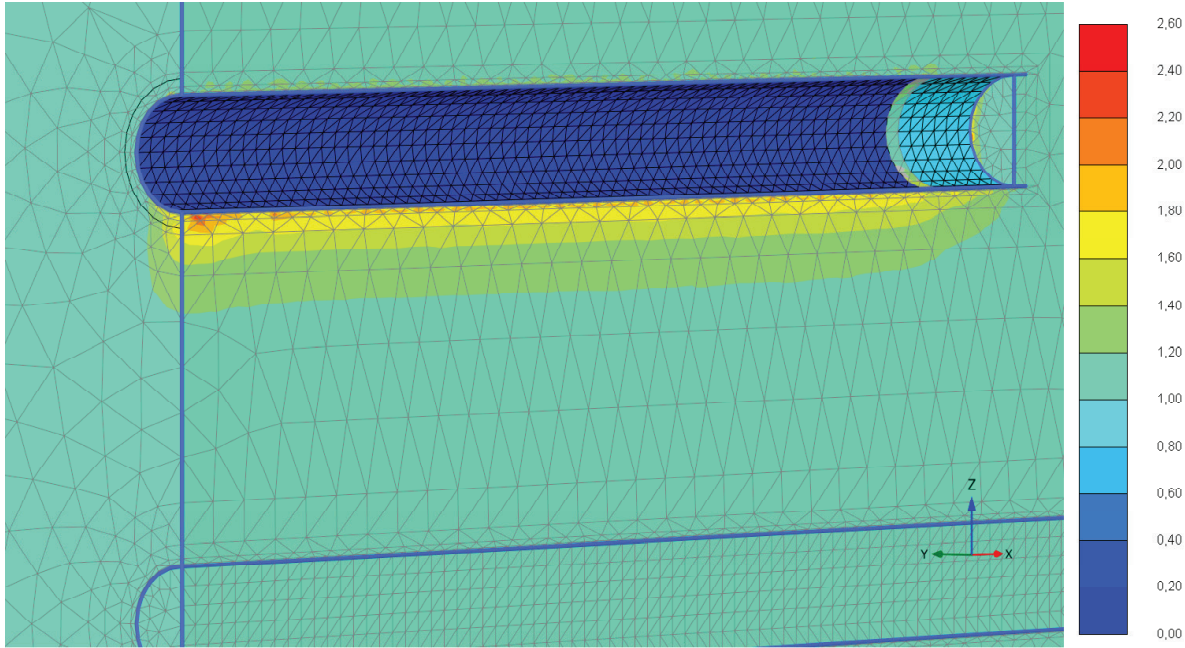
Figure 4.29.: Distribution of the isotropic overconsolidation ratio in the model.
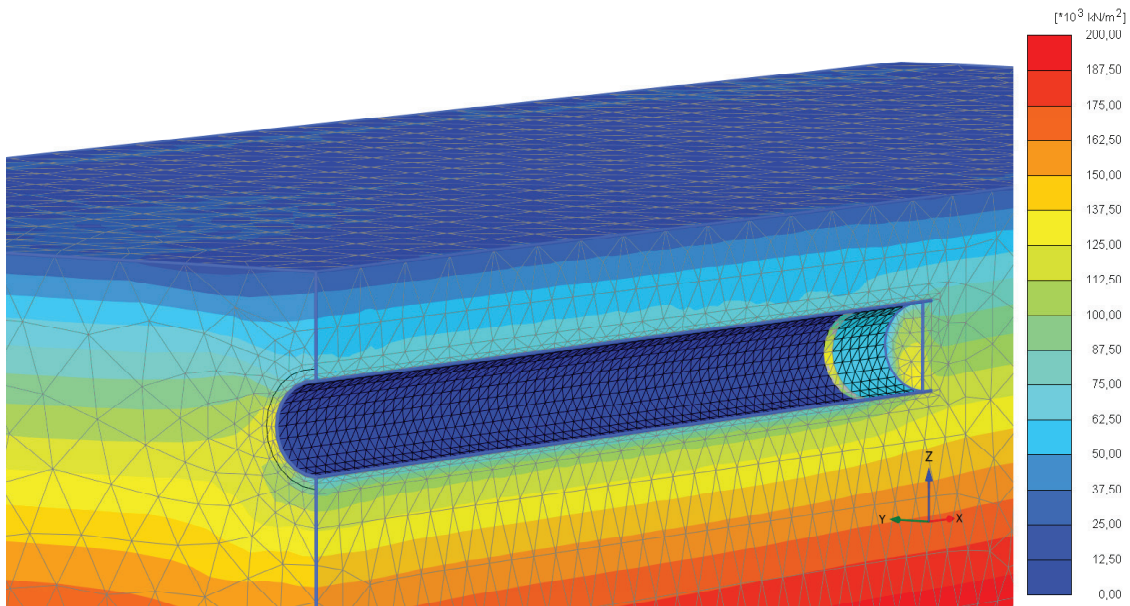
Figure 4.30.: Distribution of the current stiffness E_{ur} for unloading (and reloading).

Figure 4.31.: Calculated overall sensitivities in O_{12} and S_{12} regarding the investigated five input parameters of the HS model by the shallow tunnel (calculated by Eq. 4.24, with the final vertical displacements, i.e. $N = 2$) for a hard (denser) subsoil (as used up to now, values written in the graph), and additionally with a softer (looser) subsoil.

means that the initial soil conditions have large influence on the predicted displacements by the mechanized tunnel excavation. Furthermore, the perturbation of φ with a step size 10 % corresponding to 3.5° (i.e. from 35.0° to 38.5°) results directly in a change in the values of the three stiffnesses of the HS model (see Eqs. 3.4, 3.5, and 3.24). For an appropriate range of the minor principle effective stress σ_3' from zero to -600 kN/m^2 (pressure is negative) in the numerical model, in Figure 4.34 it is given the relative deviation of the threes stiffnesses resulting from the perturbation of φ. For calculating E_{oed} the value of K_0^{nc} was cept unchanged (see Eq. 3.24), so this is only the direct contribution of φ. It is shown that the relative deviation, calculated through the relation (known as an equation for the relative error)

$$\frac{E_{oed/50/ur}(\varphi = 38.5°) - E_{oed/50/ur}(\varphi = 35°)}{E_{oed/50/ur}(\varphi = 35°)} \, 100 \qquad (4.27)$$

in %, is relatively small, i.e. less than 1 % increase of each of the three stiffnesses (see in Fig. 4.34), so that the perturbation of the input parameter φ with a step size 10 % results in small, but still noticeably direct change in E_{oed}, E_{50} and E_{ur}. In Figure 4.32 there are presented the calculated values of the three soil stiffnesses and in Figures 4.33 and 4.34 it is given the nominal (i.e. $E_{oed/50/ur}(\varphi = 38.5°) - E_{oed/50/ur}(\varphi = 35°)$), respectively the relative deviation (Eq. 4.27) resulting directly from the perturbation of φ.

Later, in the identification procedure (see in Section 4.2) for the shallow tunnel it will be investigated the influence of adding three additional observation points – K_{12}, L_{12} and M_{12} (see Fig. 4.36) – in the observation cross-section 12. In K_{12} and L_{12} the vertical displacements during the excavation can be measured by an extensometer device in the reality, while in M_{12} the horizontal displacements can be measured by an inclinometer device.

In Figures 4.37–4.39 there are presented separately the sensitivities for each of the above investigated five observation points – O_{12}, S_{12}, K_{12}, L_{12} and M_{12} during the excavation of the shallow tunnel. It is shown, that φ has the largest sensitivity in all five points. Further E_{ur}^{ref} has its largest influence in point S_{12}, because the tunnelling is dominated by soil unloading, as discussed above. The sensitivities in O_{12}, K_{12}, L_{12} and M_{12} are very similar, however, later in Section 4.2.2.3 it will be demonstrated that the used number of points during the excavation have a significant influence in the parameter identification procedure.

The results of the local SA – Figure 4.40 – are compared with these calculated by Miro *et al.* (2012a) – Figure 4.41, right – obtained via the global Variance based SA (Sobol 1993) performed with the same FE-model (but with smaller dimensions of the discretized
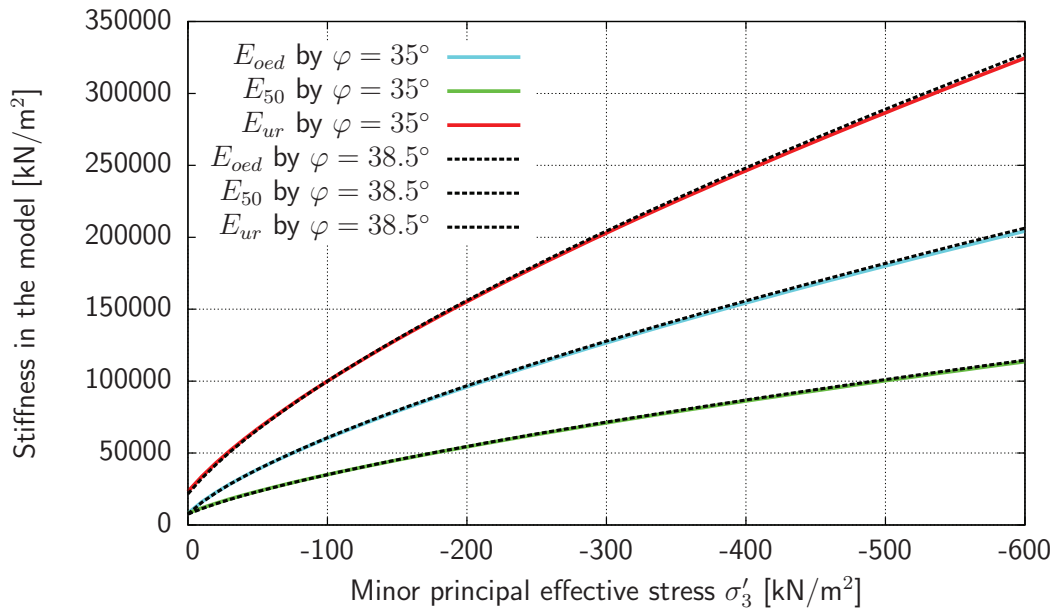
Figure 4.32.: Stress dependent stiffnesses of the HS model in the numerical model for an appropriate stress range (calculated through Eqs. 3.4, 3.5, and 3.24).
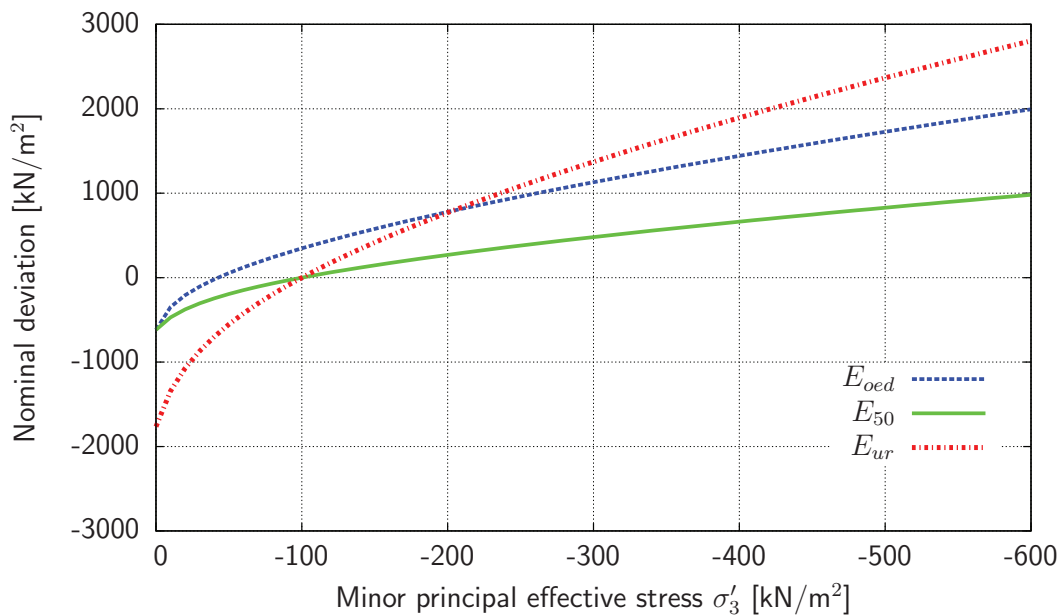
Figure 4.33.: Nominal deviation $(E_{oed/50/ur}(\varphi = 38.5°) - E_{oed/50/ur}(\varphi = 35°))$ of the soil stiffnesses of the HS model as a result of the perturbation with a step size 10 % or 3.5° (i.e. from 35.0° to 38.5°) of the input parameter $x_2 = \varphi$.
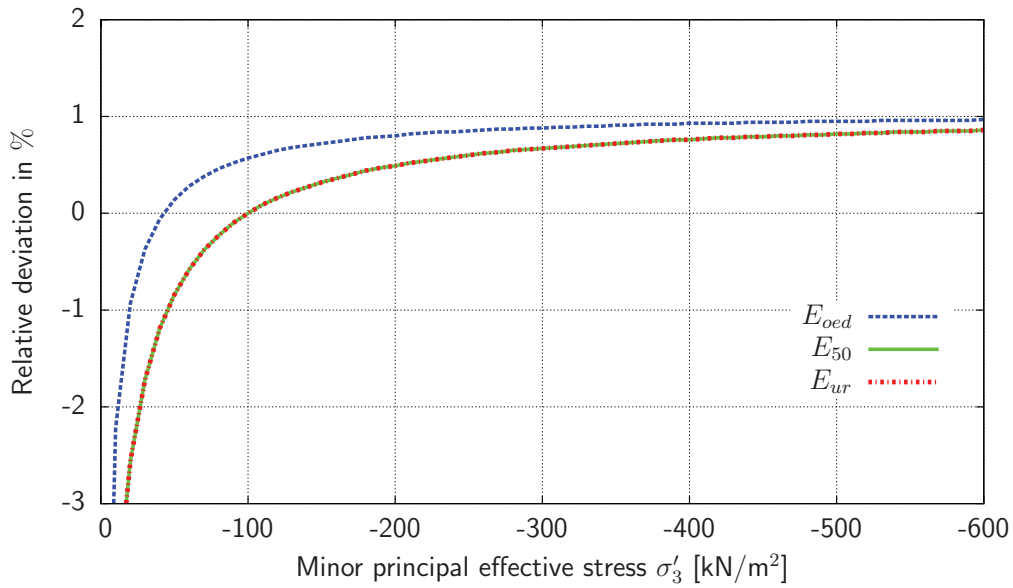
Figure 4.34.: Relative deviation (Eq. 4.27) of the three soil stiffnesses of the HS model as a result of the perturbation with a step size 10 % or 3.5° (i.e. from 35.0° to 38.5°) of the input parameter $x_2 = \varphi$.
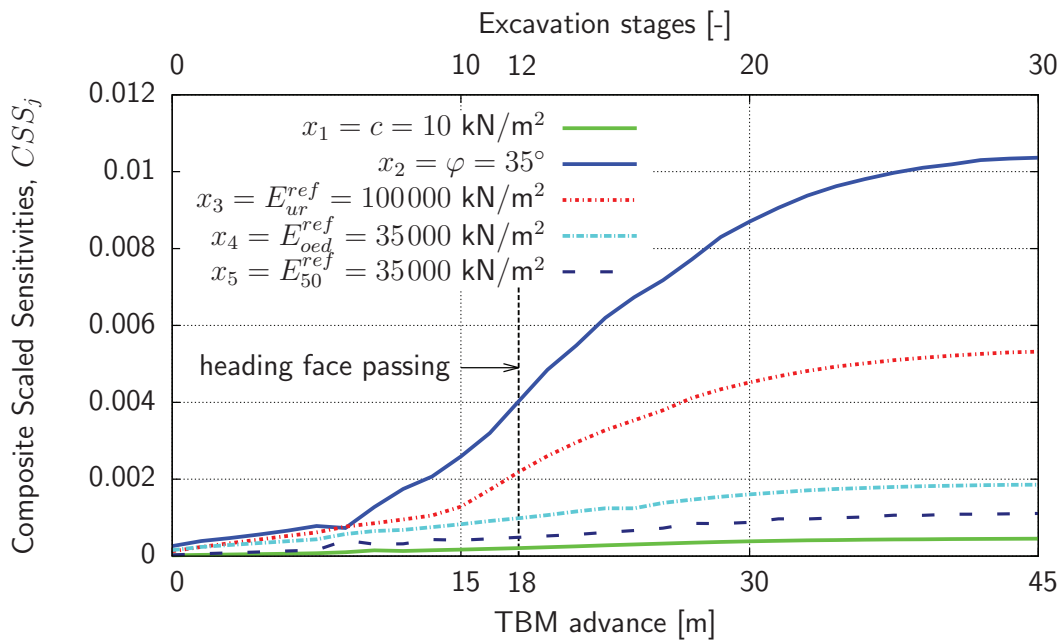
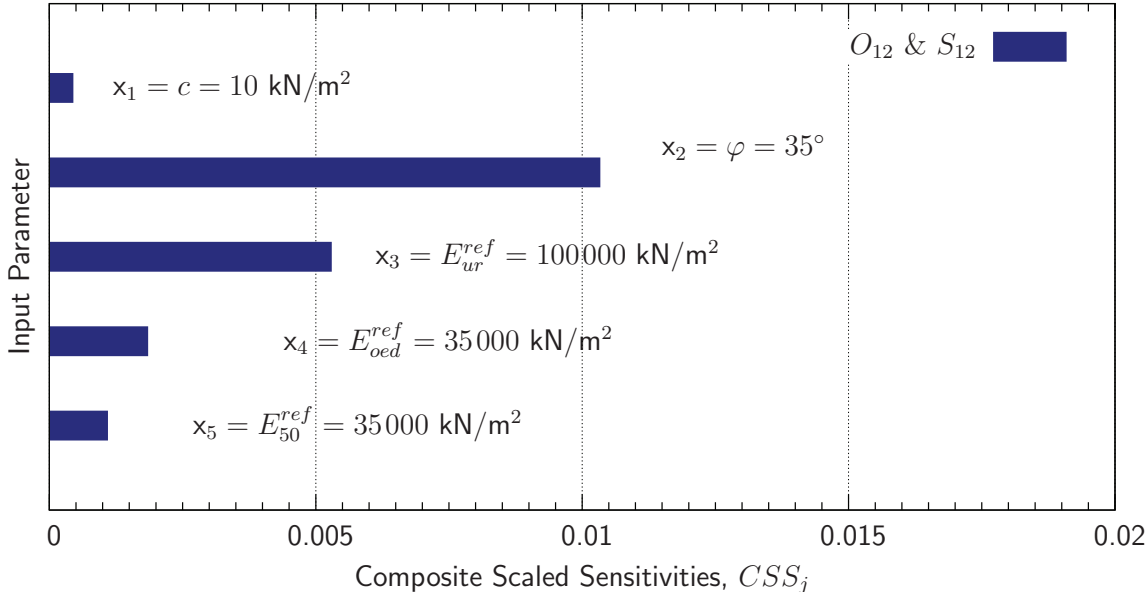

Figure 4.35.: Calculated overall sensitivities in O_{12} and S_{12} regarding the investigated input parameters of the HS model by the shallow tunnel, calc. by Eq. 4.24, with the vertical displacements after each excavation stage ($N = 2$) during the tunnelling.
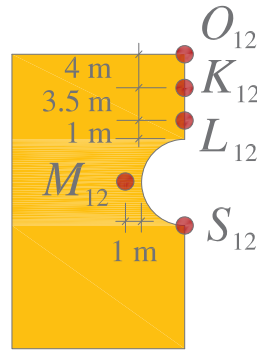
Figure 4.36.: Observed points in cross-section 12 during the excavation of the shallow tunnel.
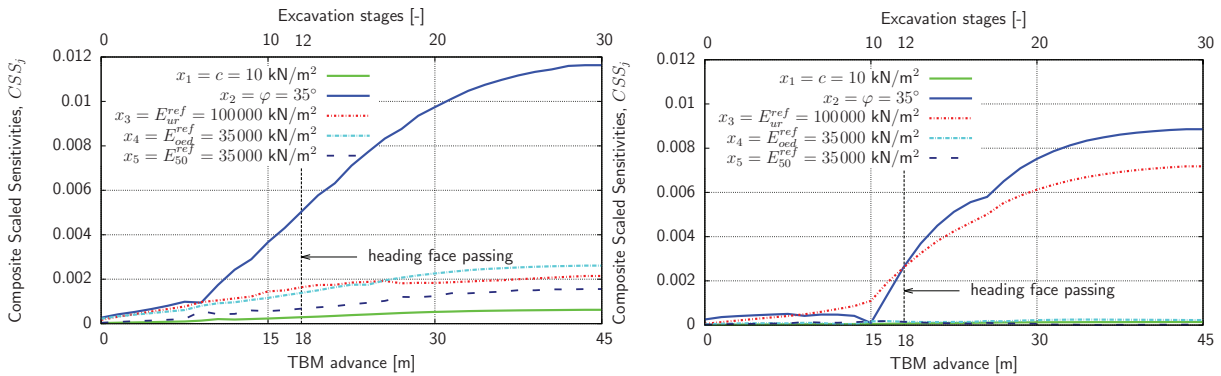
Figure 4.37.: Calculated sensitivities in O_{12} (left) and in S_{12} (right) regarding the investigated five input parameters of the soil constitutive model (the HS model) by the shallow tunnel, calculated by Eq. 4.24, with the vertical displacements after each excavation stage ($N = 1$) during the tunnelling up to the 30th excavation stage.
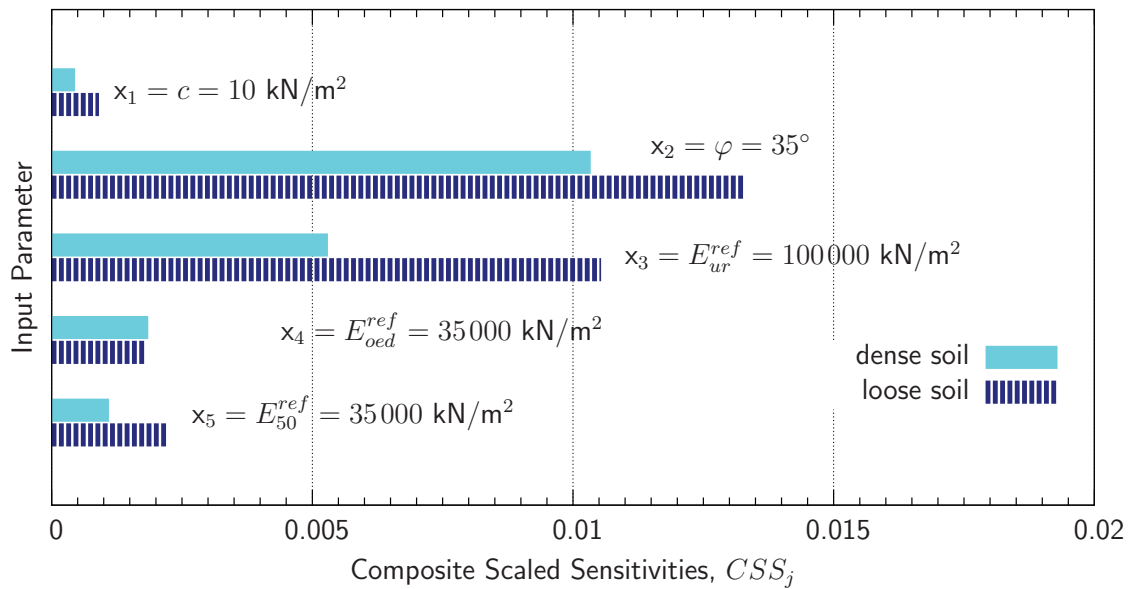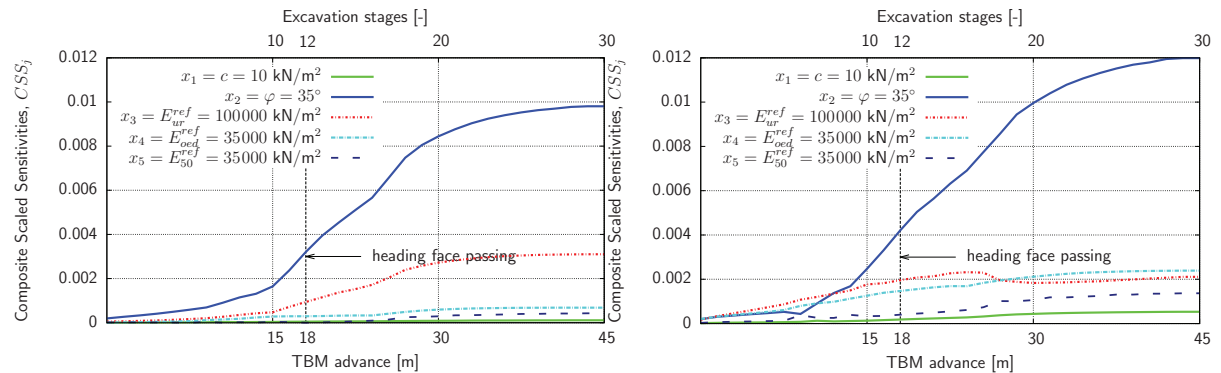

Figure 4.38.: Calculated sensitivities in K_{12} (left) and in L_{12} (right) regarding the investigated five input parameters of the soil constitutive model (the HS model) by the shallow tunnel, calculated by Eq. 4.24, with the vertical displacements after each excavation stage ($N = 1$) during the tunnelling up to the 30th excavation stage.
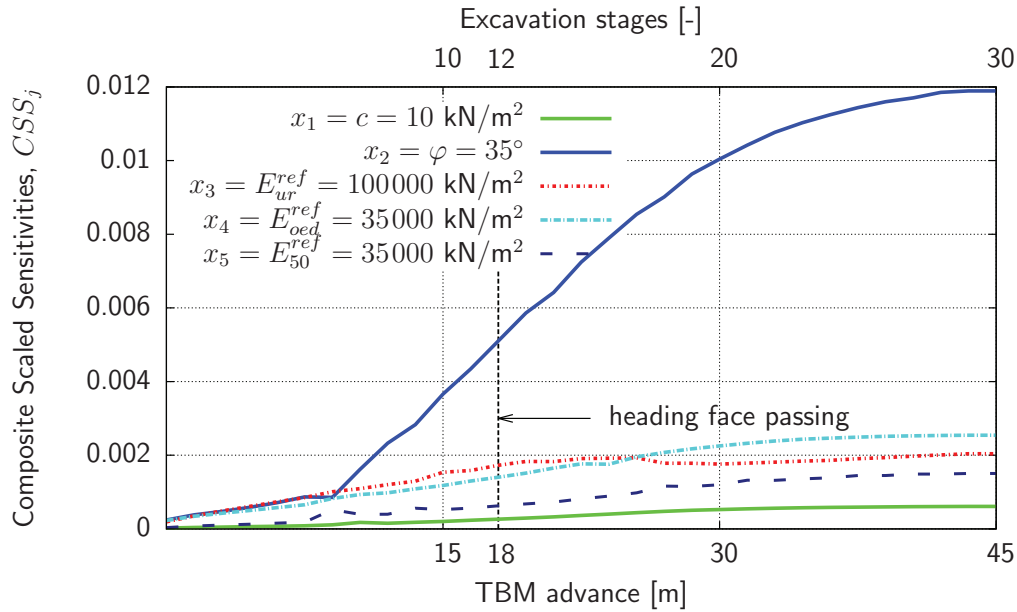
Figure 4.39.: Calculated sensitivities in M_{12} regarding the investigated 5 input parameters of the HS model (shallow tunnel), calculated by Eq. 4.24, with the horiz. displ. after each excavation stage ($N = 1$) during the tunnelling up to the 30th excavation stage.
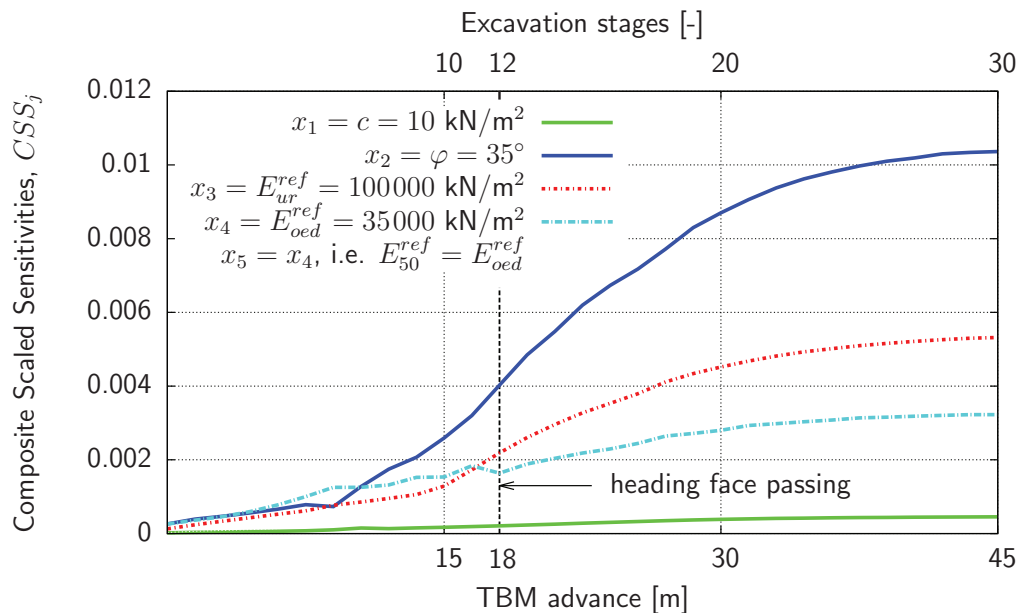
Figure 4.40.: Calculated overall sensitivities in O_{12} and S_{12} regarding the investigated five input parameters of the soil constitutive model (the HS model) by the shallow tunnel, calculated by Eq. 4.24, with the vertical displacements after each excavation stage ($N = 2$) during the tunnelling up to the 30th excavation stage; assumed $E_{50}^{ref} = E_{oed}^{ref}$.

(a)   (b)
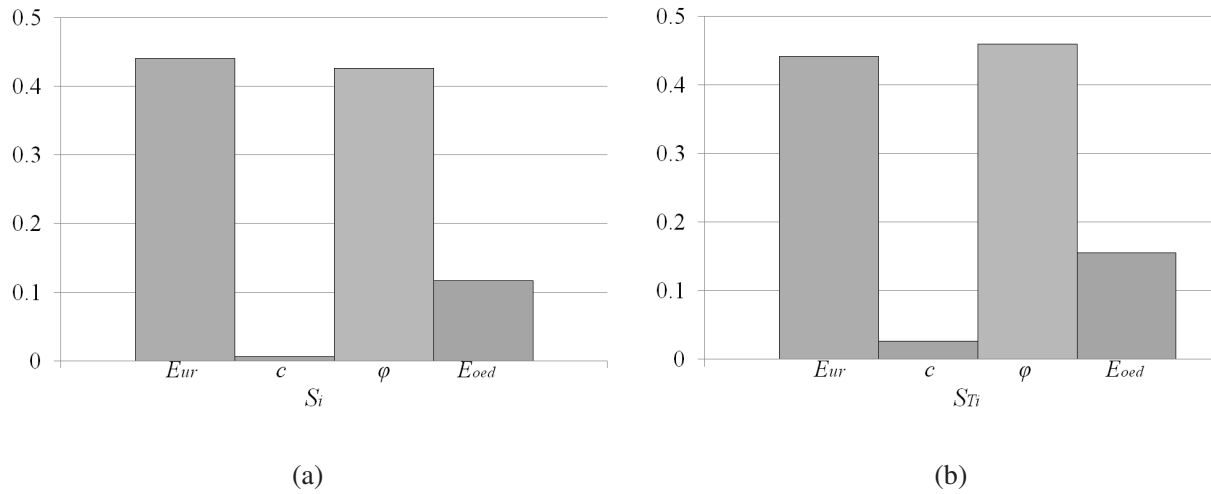
Figure 5: First order and total effect sensitivity indices of the soil parameters.

Figure 4.41.: Results by Miro *et al.* (2012a): Calculated overall sensitivities in O_{12} and S_{12} regarding the investigated input parameters of the soil constitutive model (the HS model) by the shallow tunnel using a global variance based SA; assumed $E_{50}^{ref} = E_{oed}^{ref}$.

domain) and for the same soil constitutive parameters of the HS model. The comparison shows similar qualitatively ranging of the parameters. However, the global SA give additional information like interaction between the different input parameters (Dimov & Georgieva 2010, Sobol 1993, Homma & Saltelli 1996, Saltelli *et al.* 2008).

4.1.3. Summary and Conclusions

In the first part of this study it has been demonstrated that the adopted local SA may be appropriate for this particular geotechnical problem. In the same time an appropriate step size was selected for calculating the partial derivatives via first-order finite difference scheme for the investigated input parameters of the adopted elastoplastic soil constitutive model (the HS model).

The local SA, and also the performed global SA in Miro *et al.* (2012a), have shown similar ranking (sensitivity, CSS_j) of the input parameters:

$$CSS(\varphi) > CSS(E_{ur}^{ref}) > CSS(E_{oed}^{ref}) \gg CSS(c).$$

The most important (i.e. sensitive) parameters are $x_2 = \varphi$ and $x_3 = E_{ur}^{ref}$, $x_4 = E_{oed}^{ref}$ has moderate sensitivity, while the least sensitive parameter is $x_1 = c$ which may be excluded from the subsequent identification procedure.

In this particular geotechnical problem – mechanized tunnelling in an assumed homogeneous, normally consolidated and dry subsoil – of main interest is the identification of the basic constitutive input parameters for soil stiffness E_{50}^{ref}, E_{oed}^{ref}, E_{ur}^{ref}, and for soil strength φ, ψ, c of the adopted HS model. The initial soil conditions have also to be identified. This is done through the angle of internal friction φ using the Jaky's semi-empirical relation: $K_0^{nc} = 1 - \sin\varphi$.

As discussed above for identifying the initial soil conditions one may identify the coefficient of lateral earth pressure at rest K_0^{nc} (normally consolidated soil) through the angle of internal friction φ by

$$K_0^{nc} = 1 - \sin\varphi. \tag{4.28}$$

The K_0-values have also to satisfy that the initial stresses in the subsoil are not in a state of failure. Therefore to avoid failure K_0^{nc} is conservatively (i.e. for cohesionless soils) bounded by:

$$K_a = \frac{1 - \sin\varphi}{1 + \sin\varphi} < K_0^{nc} < \frac{1 + \sin\varphi}{1 - \sin\varphi} = K_p, \tag{4.29}$$

with K_a, resp. K_p Rankine's coefficient of active, resp. passive earth pressure. Further, for the dilatancy angle it is used the relation:

$$\psi = \varphi - 30°, \quad \text{and} \quad \psi = 0 \text{ if } \varphi < 30°. \tag{4.30}$$

The dilatancy of sand depends on both the density and on the friction angle φ. In general, ψ is much smaller than φ. However, for quartz sands Equation 4.30 is a realistic measure. For further information between the link between the friction angle and dilatancy, see Bolton (1986).

According to the experimental results presented in Schanz & Vermeer (1998) and Schanz (1998) in the subsequent identification procedure it is used the following equality for the two primary loading module expressed as the empirical relation:

$$E_{50}^{ref} = E_{oed}^{ref}. \tag{4.31}$$

Another inequality which is used is:

$$E_{50}^{ref} < \frac{1}{2} E_{ur}^{ref}. \tag{4.32}$$

Subsequently, the input parameters of the HS model to be identified directly become four: φ, c, E_{oed}^{ref} and E_{ur}^{ref}.

For these four unknown soil constitutive parameters it is defined very conservatively a search space D: about $\pm 50\,\%$ of the "exact" input parameters (except for φ) used at the beginning only for the generation of the synthetic measurements. The exact values, and the lower/upper bounds of each parameter are listed in Table 4.3.

In order to avoid unrealistic combinations of the input parameters during the iterative identification procedure, i.e. relatively low soil strength with relative high soil stiffness and vice versa, it is useful to define additional constraints and relations relating the soil stiffness to the soil strength in a certain realistic manner. However, further constraints and relations between the parameters are not considered in the present study.

4.2. Back Analysis

In the present Section 4.2 a parameter optimization technique (direct back analysis) is applied to examine the possibility to fit simulated results and observed (measured) data during the tunnelling, expressed in the form of displacements. It is shown based on the applied back analysis procedure that in case the numerical model is too large it is worth to explore equivalent reduced numerical model for soil-model parameters identification (see further Section 4.2.1.1).

4.2.1. Concept of the Direct Back Analysis

In principle any problem of parameters identification may be solved in two different ways, defined as *inverse back analysis* and *direct back analysis* (see Cividini *et al.* 1981). The inverse back analysis consists in inverting the model equation with respect to the input

Table 4.3.: Search space of the input soil constitutive parameters of the adopted HS model to be identified.

Parameter	Lower bound	Exact value	Upper bound	Unit
φ	31	35	46	[°]
c	5	10	15	[kN/m^2]
E_{oed}^{ref}	17 000	35 000	53 000	[kN/m^2]
E_{ur}^{ref}	48 000	100 000	150 000	[kN/m^2]
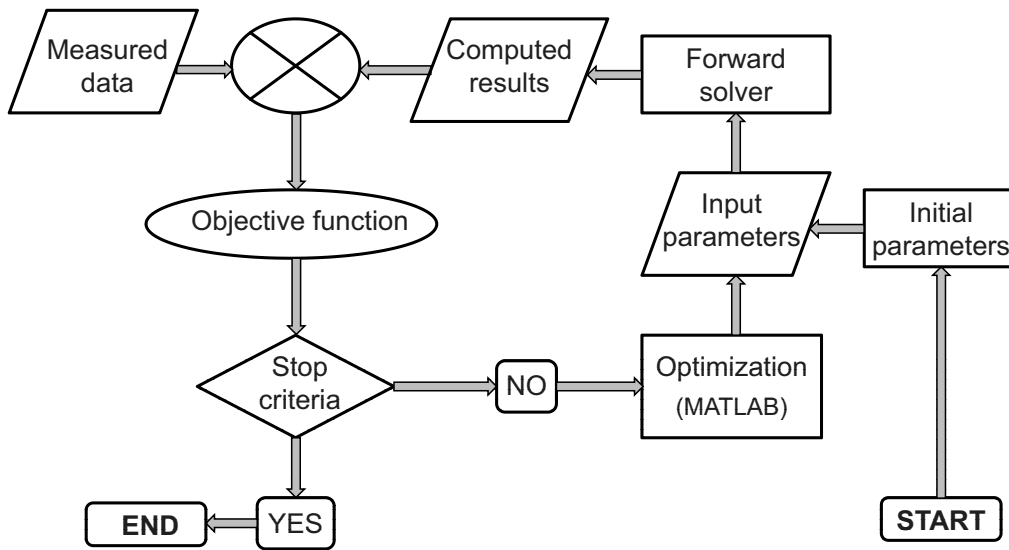
Figure 4.42.: Concept of the applied direct back analysis.

parameters that are unknown and subject to identification. The direct approach is based on an iterative procedure correcting the trial values of the unknown parameters by minimizing an error (objective) function. This way the model response data are provided by iterative trail forward solutions of the problem used for model parameters identification. For the analysis presented here the iterative direct approach has been chosen.

In Figure 4.42 there is presented the concept of the adopted direct back analysis. The iterations start with an initial guess of the input parameters which are subject to identification. In the present study the initial guess is randomly generated (in the predefined search space), i.e. no a priori information regarding the parameters is considered. The forward numerical model of the mechanized tunnelling is executed and the needed values of the nodal displacements of the observation points are read (by MATLAB) and compared with the (synthetic) measurements during the excavation process of the shallow tunnel. This comparison is made in a form of an objective function (will be defined later in Section 4.2.1.1) which has to be iteratively minimized by the adopted optimization algorithm (will be described also later in Section 4.2.1.2). If some predefined stop criteria are satisfied, such as reaches of some predefined enough small value of the objective function, or allowed maximum number of iterations, or others, the iterations are stopped, otherwise the optimization algorithm sets a new parameters vector $X = (\varphi, c, E_{oed}^{ref}, E_{ur}^{ref})$ in a next iteration, by modifying the input parameters of the forward model.
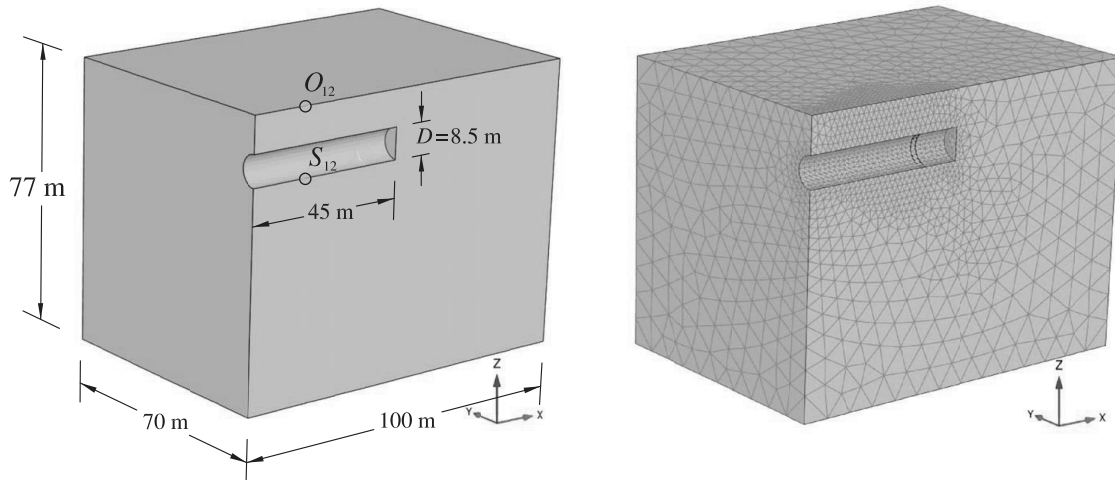
Figure 4.43.: Dimensions of the small FE-model (left) and FE discretization (right).

4.2.1.1. Definition of the Objective Function

Because each run of the forward solver (the FE-model of the mechanized tunnelling) is time expensive, when it comes to parameter identification via back analysis, it is very helpful to replace it, i.e. to approximate its response with a some kind of surrogate model. One possibility is to approximate its response with a surrogate model in a form of an analytical functions. Another possibility is to reduce the discretized domain of the numerical model having the same performance as the original large FE-model.

The possibility, which is used in the current thesis, is to reduce the discretized domain of the main large FE-model (Fig. 3.2) with a smaller one. This equivalent small model (Fig. 4.43) have the same performance as the original large FE-model, as demonstrated in Figure 4.44.

Subsequently, the iterative model parameters identification is done using this equivalent small FE-model (Fig. 4.43). The large main large FE-model (Fig. 3.2) is used to collect the synthetic measurement data based on the simulation of excavation of solely the shallow tunnel.

In the identification procedure via direct back analysis the objective (or error, or merritt, or fitness) function is used as a comparison criterion between the calculated results and the measurement data. A relative small value of the objective function corresponds to better agreement between the calculated results and the measurements. Therefore, the goal in the back analysis procedure is to minimize this objective function. Meier (2008) has investigated several types of objective functions and their suitability for identification
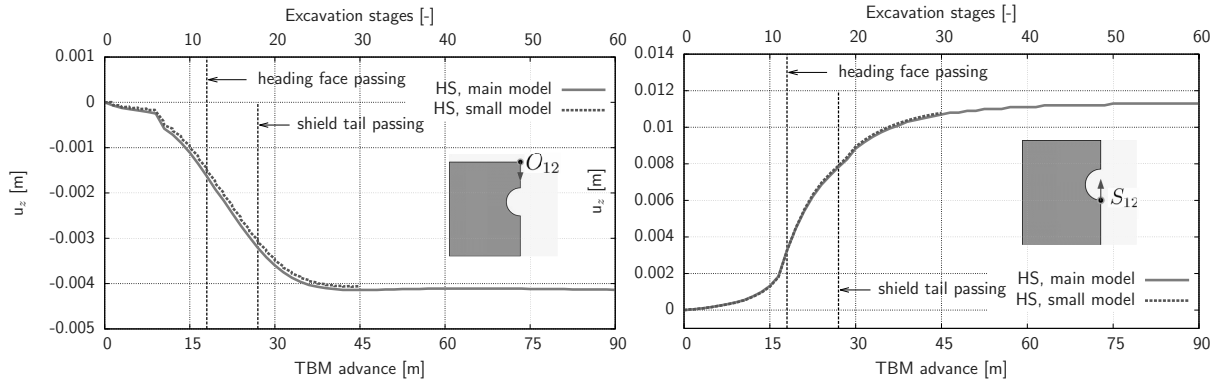
Figure 4.44.: Comparison of the vertical displacements in observation points O_{12} and S_{12} during the excavation of the shallow tunnel calculated with the small FE-model (Fig. 4.43), and with the main large FE-model (Fig. 3.2).

problems. He founds the *mean squared error* as suitable for geotechnical problems:

$$f(X) = \frac{1}{N} \sum_{i=1}^{N} \left(y_i^{calc}(X) - y_i^{meas} \right)^2 \tag{4.33}$$

with

X – vector of the input parameters to be identified (i.e. dimensions of the problem),
$y_i^{calc}(X)$ – calculated data, i.e. nodal displacements with the parameter set X,
y_i^{meas} – observed (measured) data,
N – total number of measurements/observations = (used number of points in the observation cross-section) × (used number of records during the excavation).

So, the constrained optimization problem can be now formulated:

$$\text{minimize} \quad f(X)$$

$$\text{subject to} \quad g_s(X) \leq 0, \ s = 1, \ldots, u \quad \text{Inequality constraints}$$

$$h_t(X) = 0, \ t = 1, \ldots, v \quad \text{Equality constraints}$$

where $\mathbf{g}(X)$ and $\mathbf{h}(X)$ are a set of inequality resp. equality constraints. Additionally, each of the input parameters contained in the parameter set X is restricted to a predefined search space defined by lower and upper bound:

$$x_{j,\min} \leq x_j \leq x_{j,\max}, \qquad j = 1, \ldots, m.$$

4.2.1.2. Description of the Optimization Algorithm

Recently, a family of optimization algorithms (population-based methods) has been developed based on the simulation of social interactions among members of a specific species looking for food sources. According to Meier *at al.* (2007), from this family of algorithms, the two most promising are the Ant Colony Optimization and the Particle Swarm Optimizer (PSO). Therefore, in the present thesis the PSO is the algorithm chosen for minimizing the objective function.

The PSO was first introduced by Kennedy & Eberhart (1995), Eberhart & Kennedy (1995), Eberhart *at al.* (1996), and Kennedy (1997). The algorithm is a population-based stochastic optimization technique, inspired by the social-psychological behaviour of bird flocking or fish schooling. It is based on swarm intelligence using a population (swarm) of individuals (particles), and it is gradient-free and no rigorous convergence theory is needed. The main strength of the PSO is its faster convergence, compared with other widely used global optimization algorithms like the Genetic Algorithm or the Simulated Annealing. Next the original (basic) PSO – in its global version – is presented.

The PSO has two primary operations: Velocity update and Position update. Each particle adjust its flying according to its own flying experience and its companions' flying experience. Each particle, in fact, represents a potential solution to the problem and it is treated as a point in a D-dimensional search space (in the present study 4-dimensional, i.e. 4 input parameters of the HS model subjected to identification – $\varphi, c, E_{oed}^{ref}$, and E_{ur}^{ref}). The k-th particle at the current t-th generation (i.e. iteration) is represented as a vector containing all the input parameters to be identified: $X_k(t) = (x_1, x_2, \ldots, x_D)$, where $x_j \in [x_{j,\min}, x_{j,\max}]$, $1 \leq j \leq D(= 4)$, where $x_{j,\min}$ and $x_{j,\max}$ is lower and upper bound for the j-th dimension, i.e. the j-th input parameter, respectively. The best previous position (the position giving the best, i.e. the minimum value of the objective function) of the k-th particle at current iteration is recorded and represented as X_k^L (also known as *pbest*). The best particle among all the particles in the swarm is represented as X^G. Actually, according to the different possible definitions of X^G, there are two different versions of the PSO. If X^G is the best position among all the particles in the swarm (also known as *gbest*), such a version is called the global version (this version was implemented in MATLAB and used in the present thesis). If X^G is taken from some smaller number of adjacent particles of the population (also known as *lbest*), such a version is called the local version. The rate of position change (velocity) for particle k is represented as $V_k(t) = (v_1, v_2, \ldots, v_D)$. The particles for each point j (i.e. input parameter to be identified) in the search space
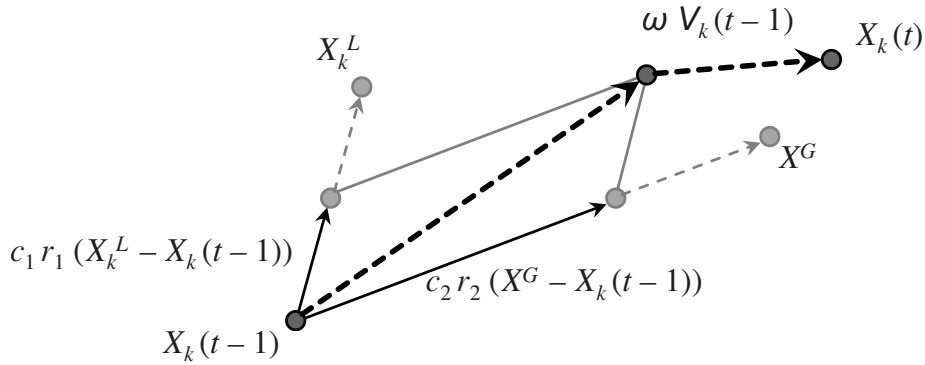
Figure 4.45.: PSO velocity and position update.

are manipulated according to the following two Equations 4.34 and 4.35 given below and represented also in Figure 4.45.

Updated particle velocity:

$$V_k(t) = \underbrace{V_k(t-1)}_{\text{momentum}} + \underbrace{c_1 r_1 \left(X_k^L - X_k(t-1) \right)}_{\text{cognitive component}} + \underbrace{c_2 r_2 \left(X^G - X_k(t-1) \right)}_{\text{social component}} \quad (4.34)$$

Updated particle position:

$$X_k(t) = X_k(t-1) + V_k(t) \quad (4.35)$$

where $k = 1, 2, 3, \ldots, K_p$, and K_p is the total number of particles,

X_k^L and X^G as described above,

c_1 and c_2 are two positive constants – cognitive and social parameter, respectively, or known also as acceleration coefficients,

r_1 and r_2 are two independent random functions in the range $[0, 1]$,

t is the current iteration step, and

$(t-1)$ is the previous iteration step.

The positions X_k^L and X^G are given by the following equations, respectively:

$$X_k^L = \begin{cases} X_k^L : & f(X_k) \geq f(X_k^L) \\ X_k : & f(X_k) < f(X_k^L) \end{cases} \quad (4.36)$$

$$X^G \in \{x_1, x_2, x_3, \ldots, x_{K_p}\} | f(X^G) = \min \left(f(x_1), f(x_2), f(x_3), \ldots, f(x_{K_p}) \right), \quad (4.37)$$

where f is the objective function.

The second part of Equation 4.34 is the "cognition" part, which represents the private thinking of the particle itself. The third part is the "social" part, which represents the collaboration among the particles. Equation 4.34 is used to calculate the particle's new

velocity according to its previous velocity and the distance of its current position from its own best experience (position) and the group's best experience. Then the particle flies toward a new position according to Equation 4.35 (see also Fig. 4.45). The performance of each particle is measured according to the predefined objective function, as shown e.g. according to Equations 4.36 and 4.37. The parameters c_1 and c_2 are configuration parameters that play very important role in the PSO convergence behaviour, as will be discuss later. They represent "trust" settings which respectively indicate the degree of confidence in the best solution found by each individual particle (c_1) and by the swarm as whole (c_2).

In the present thesis it is used an updated version of Equation 4.34 by adding a new parameter for balancing the global and local search, called inertia weight ω (or sometimes damping weight), into the basic original PSO, as introduced by Shi & Eberhart (1998a, 1998b). So Equation 4.34 now becomes:

$$V_k(t) = \underbrace{\omega(t)\, V_k(t-1)}_{\text{momentum}} + \underbrace{c_1 r_1 \left(X_k^L - X_k(t-1) \right)}_{\text{cognitive component}} + \underbrace{c_2 r_2 \left(X^G - X_k(t-1) \right)}_{\text{social component}} \qquad (4.38)$$

Generally, the inertia weight ω could be a constant or decreasing function over the time of iterations (e.g. linear or nonlinear function over the time). In the current implementation it have been chosen to be used a linearly decreasing $\omega(t)$ with each iteration (see Eq. 4.39), where $\omega(t)$ is multiplied by the previous velocity $V_k(t-1)$ and has characteristics that are reminiscent of the temperature parameter in the Simulated Annealing (Eberhart & Shi 1998). A large inertia weight facilitates a global search while a small inertia weight facilitates a local search. By linearly decreasing the inertia weight from a relatively large value to a smaller value through the course of PSO run, the PSO tends to have more global search ability at the first iterations, while having more local search ability near the last iterations, in order to get more refined solutions. Therefore, it is used a variation of the inertia weight defined by linearly decreasing ω at each iteration, as suggested by She & Eberhart (1998a):

$$\omega(t) = \omega_{max} - \frac{\omega_{max} - \omega_{min}}{T_{max}} \cdot (t-1), \qquad (4.39)$$

where an initial value ω_{max} is linearly decreased up to end value ω_{min} during T_{max} number of iterations. The inertia weight ω is critical for the convergence behaviour of the PSO. By its introduction into the original PSO, the performance of PSO has been greatly improved (Shi & Eberhart 1998a, 1998b).

As a summarization the PSO algorithm consists in the following steps:

Initialization of the swarm

1. Generate randomly distributed vector of particle k's positions $X_k(0)$ at iteration 0 (zero) and velocities $X_k(0)$ through the search pace D bounded by the lower and upper bound. By doing this consider all equalities (i.e. Eq. 4.31) and inequalities (i.e. Eq. 4.32);

Iterations

2. Calculate the objective function for each particle k from the current performed iteration. A total number of K_p objective function calculations will be performed at each iteration (K_p is the total number of particles within the swarm);

3. Update the optimum particle position X_k^L at current iteration step t and global optimum particle position X^G;

4. Update the velocity vector $V_k(t)$ according to Equation 4.38 and update the position of each particle $X_k(t)$ using its previous position by Equation 4.35.

5. Repeat steps 2–4 until some predefined stop criteria is satisfied.

Further, the PSO algorithm has undergone a huge number of modifications since it was first proposed in 1995. Most of these modifications vary in some way the velocity-update rule, in an attempt to improve the optimization performance. Such modifications are presented for example by Fourie & Groenwold (2002), with a dynamic decrease of the inertia weight value. Løberg *et al.* (2001) presented a hybrid PSO model with breeding (a core element in the Genetic Algorithm) and subpopulations. He *et al.* (2004) proposed a PSO with passive congregation, similar as idea to the introduced stochastic variable (turbulence) by Fieldsend & Singh (2002). Other important variant is presented by Clerc (2002) – a PSO with construction coefficient (playing similar role as the inertia weight ω used in Equation 4.38). Another investigations on improving the performance of the PSO are undertaken by Kennedy (2000) using cluster analysis, and by Shi & Eberhart (2001) using fuzzy adaptive inertia weight.

4.2.1.3. Parameters of the Adopted Particle Swarm Optimization

Perez & Behdinan (2007) did an algorithm analysis and demonstrated that the PSO is only stable if the following set of stability conditions are satisfied:

$$0 < (c_1 + c_2) < 4, \tag{4.40}$$

$$\frac{(c_1 + c_2)}{2} - 1 < \omega_{\max} < 1. \tag{4.41}$$

If the above two conditions are satisfied this guarantees convergence for the PSO to a stable equilibrium point. However, it is not a guarantee that this point in the search space is the global optimum, i.e. the global minimum of the objective function topology.

In conclusion the successful and efficient performance of the adopted PSO version – a PSO with inertia – is steered by:

- the total number of particles K_p;

- the distribution of the initial particle positions $X_k(0)$;

- the value of the constants c_1 and c_2 giving weight to either the local or the global best information, i.e. how far a particle will move in a single iteration;

- the value of the weighting factor ω, i.e. the values of ω_{max}, ω_{min} und T_{max}, which influence the trade-off between the global and local exploration abilities during search;

- the size of the search space D (restricted by lower and upper bound);

- the stopping criteria: maximum number of allowed iterations T_{max}, reaching enough small value of the objective function, or no remarkable deviation of the objective function.

That means that the choose of reasonable PSO input parameters is crucial for its convergence behaviour, and strongly depends on the optimization problem. The PSO input parameters can also be tuned by using another overlaying optimizer, a concept known as a *meta-optimization* (see Meissner *at al.* 2006, Pedersen 2009 & 2010). However, this was not done in the present thesis and the PSO parameters were selected manually after few trials.

4.2.1.3.1. Verification of the Implemented Optimization Algorithm on a Simple Geotechnical Problem – Oedometer Test

To test and verify the performance of the implemented PSO with inertia it have been performed an identification of the oedometer modulus E_{oed} by assuming a simple linear elastic material model for the soil sample. The Oedometer test was modelled as a cube in the FE-code PLAXIS 3D, version 2011, (see again Fig. 4.5) with initial height $h_0 = 1$ m and soil constitutive parameters $\gamma_{\texttt{unsat}} = 17.00$ kN/m^3, $\nu = 0.30$, $E = 7326$ kN/m^2 ($\equiv E_{oed} = 10\,000$ kN/m^2). On the top of the soil sample it is applied a vertical loading $\sigma_v = 50$ kN/m^2. Here there exist the known analytical relation $E_{oed} = \frac{\sigma_v}{\Delta h/h_0} = \frac{50.0}{0.005/1.00} = 10000$ kN/m^2. However, the Oedometer test have been calculated numerically and the

vertical settlement of the top surface Δh equals to $u_z = -0.00499988860168609$ m. This value have been used in the objective function (Eq. 4.33) as a single measurement y_i^{meas} (i.e. $N = 1$). Further, E_{oed} is treated as unknown and the goal is to be back-calculated. The search space D for E_{oed} is predefined to be in the interval $[5\,000, 15\,000]$. The PSO parameters used for this example are given in Table 4.4.

The two adopted stopping criteria are the deviation of the objective function $f(X_k)$ and the allowed maximum number of iterations $T_{\max}$, as shown in the same Table 4.4.

Table 4.4.: PSO parameters used in the back calculation of the simulation of the Oedometer test.

PSO parameters	Value [-]
K_p	6
$\omega_{\max}$	0.9
$\omega_{\min}$	0.4
c_1	0.7
c_2	1.4
$T_{\max}$	80
Min. deviation of $f(X_k)$	1×10^{-28}

4.2.1.3.2. Application to the Mechanized Tunnelling

The PSO parameters used for the soil constitutive parameters identification for the mechanized tunnelling of the shallow tunnel are listed in Table 4.5.

Investigated are eight identification variants (defined in the next Section 4.2.1.3.3), regarding the used number of observation points in the observation cross-section 12 (see Fig. 4.36), and recorded information during the excavation of the shallow tunnel (see Fig. 4.46). The shallow tunnel is excavated from the beginning, however, the measurements starts from the 6th excavation stage, each 3th meter (i.e. each 2nd excavation stage), up to the 30th excavation stage, because before that the displacements in observation cross-section 12 are still relatively small.

Table 4.5.: PSO parameters used in the back calculation of the mechanized excavation of the shallow tunnel.

PSO parameters	Value [-]
K_p	20
$\omega_{\max}$	0.9
$\omega_{\min}$	0.4
c_1	0.5
c_2	1.25
$T_{\max}$	300
Min. deviation of $f(X_k)$	1×10^{-26}

4.2.1.3.3. Application to the Mechanized tunnelling – Design of Experiment

Below are described the investigated eight (8) identification variants, regarding the used number of observation points in the observation cross-section 12 (see Fig. 4.36), and recorded information during the excavation of the shallow tunnel (see Fig. 4.46):

(1) In the objective function (Eq. 4.33) the information provided by observation points O_{12}, and S_{12} from the 6th to the 30th excavation stage each 3th meter (i.e. each 2nd excavation stage) during the excavation is used, i.e. totally $N = 2 \times 13 = 26$ measurements;

(2) In the objective function (Eq. 4.33) the information provided by observation points O_{12}, and M_{12} from the 6th to the 30th excavation stage each 3th meter during the excavation is used, i.e. totally $N = 2 \times 13 = 26$ measurements;

(3) and (4) In the objective function (Eq. 4.33) the information provided by observation points O_{12}, and M_{12} from the 6th to the 12th excavation stage during the excavation up to the observation cross-section 12 (i.e. 0 m before it), and 3.0 m before it (from the 6th to the 10th excavation stage) is used, i.e. totally $N = 2 \times 4 = 8$, respectively $N = 2 \times 3 = 6$ measurements.

(5) In the objective function (Eq. 4.33) the information provided by observation points O_{12}, K_{12}, L_{12}, and M_{12} from the 6th to the 30th excavation stage during the excavation is used, i.e. totally $N = 4 \times 13 = 52$ measurements.
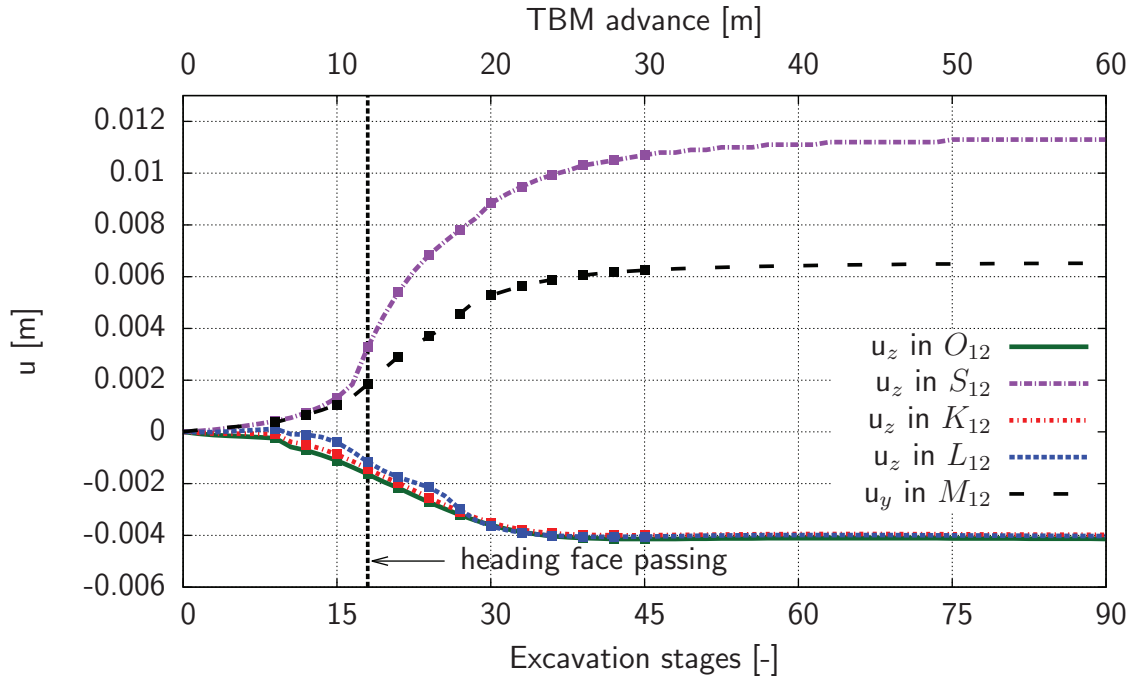
Figure 4.46.: Vertical displacements in observation points O_{12}, K_{12}, L_{12}, S_{12}, and horizontal in M_{12} (see Fig. 4.36) during the excavation of the shallow tunnel (using the nominal values of the input parameters of the HS model, as given in Table 3.2). Shown are also the used measurements in the range 6th to 30th excavation stage each 3th meter for the investigated 8 identification variants.

(6) There are used the same number of observations like in (5), but to these measurements it is added 20 % statistical noise calculated according to Equation 4.42.

(7) and (8) In the objective function (Eq. 4.33) the information provided by observation points O_{12}, K_{12}, L_{12}, and M_{12} from the 6th to the 12th excavation stage during the excavation up to the observation cross-section 12 (i.e. 0 m before it), and 3.0 m before it (from the 6th to the 10th excavation stage), i.e. totally $N = 4 \times 4 = 16$, respectively $N = 4 \times 3 = 12$ measurements.

In variant (6) it is added 20 % statistical noise to the measurements according to:

$$y_i^{meas,error} = y_i^{meas} + (\xi - 0.5) \cdot H, \tag{4.42}$$

where ξ is a uniformly distributed random number between 0 and 1 (generated via the MATLAB (pseudo)random number generator), and H is a disturbing factor – a variable which depends from the measured value of the corresponding displacement as: $H = 0.20 \cdot y_i^{meas}$.

In order to investigate the variation of the parameters subject to identification – i.e. to validate their sensitivity calculated in the previous Section 4.1, or to evaluate their "confidence intervals", the probability distribution of the residual values is calculated. This is done for each of the eight (8) identification variants, whilst for each variant the PSO is ran four times ($p = 1, 2, \ldots, P$, and $P = 4$) with different initial random swarms. The normalized residual values of each of the four investigated input parameters of the HS model $x_{j,p}^{norm}$ ($j = 4$, as there are 4 parameters involved in the analysis) is given in % by

$$x_{j,p}^{norm} = \frac{x_{j,p} - \overline{x}_j}{\overline{x}_j} \times 100, \tag{4.43}$$

where $\overline{x}_j$ is the arithmetic mean of the parameter x_j. Further, the standard deviation of the parameters is calculated through

$$\sigma_{sd,j} = \sqrt{\frac{1}{P-1} \sum_{p=1}^{P} \left(x_{j,p}^{norm}\right)^2}, \tag{4.44}$$

with $P = 4$. By the assumption of normal probability distribution of the parameters, finally, the probability density function (PDF) of each investigated parameter x_j^{norm} reads:

$$PDF(x_j^{norm}|\sigma_{sd,j}) = \frac{1}{\sigma_{sd,j}\sqrt{2\pi}} \exp\left(-\frac{(x_j^{norm})^2}{2\sigma_{sd,j}^2}\right). \tag{4.45}$$

4.2.2. Discussion of the Back Analysis Results

4.2.2.1. Verification of the Back Analysis Procedure

In the present example the Oedometer modulus E_{oed} is successfully back calculated (i.e. identified) to its "exact" value with a zero final relative error. In Figure 4.49 it is presented the performance of the PSO regarding the maximum and minimum value of E_{oed} at each iteration. Shortly before the 60th iteration the PSO has converged, i.e. for this they were needed around 360 (6 particles × 60 iterations) runs of the FE-model. In Figures 4.47-4.48 it is presented the minimum value of the objective function at each iteration.

4.2.2.2. Application to Mechanized Tunneling Modelling

First, there are presented the results from identification variant (1) as described above in Section 4.2.1.3.3, i.e. using the vertical displacements in the two observation points O_{12} (on the ground surface) and S_{12} (at the tunnel invert) during the excavation of the shallow

tunnel. In Figures 4.50-4.53 there are presented the performance of the PSO regarding the maximum and minimum value of the input soil constitutive parameters φ, c, E_{oed}^{ref} and E_{ur}^{ref} at each iteration. After about 100 iterations the PSO has converged and about 40 iterations later the iterations were aborted according to the stop criterion (min. deviation of the objective function $= 1 \times 10^{-26}$). The deviation between the optimized and exact parameters φ, E_{oed}^{ref}, and E_{ur}^{ref} is small. Remarkable is that the parameter c which has the smallest sensitivity (Fig. 4.37) has the largest final relative error – 22.80 % (Fig. 4.50), while the parameter φ which has the largest sensitivity has the smallest final relative error
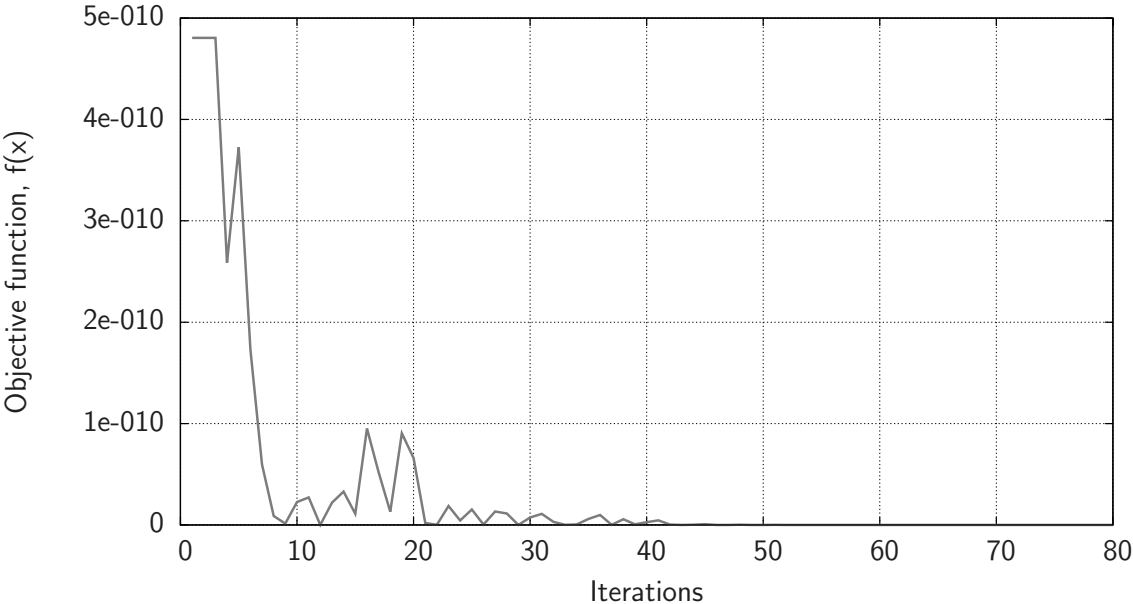
Figure 4.47.: Minimum value of the objective function in each iteration in the identification of the Oedometer modulus E_{oed}.
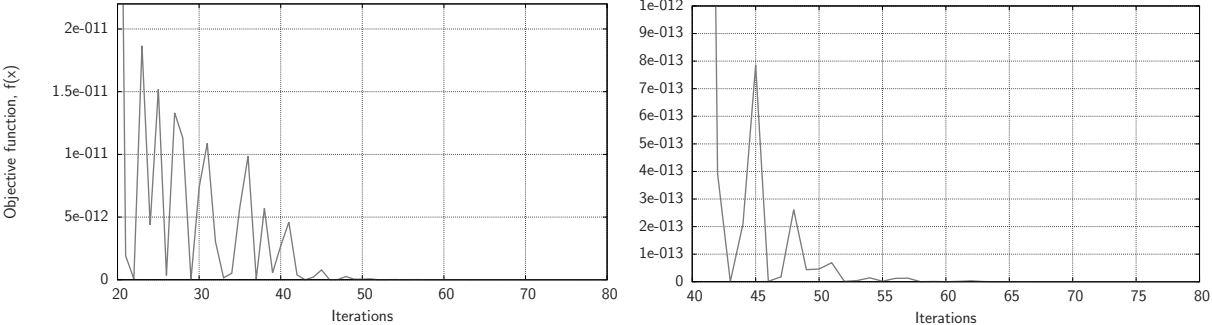
Figure 4.48.: Minimum value of the objective function in each iteration (zoomed) in the identification of the Oedometer modulus E_{oed}.
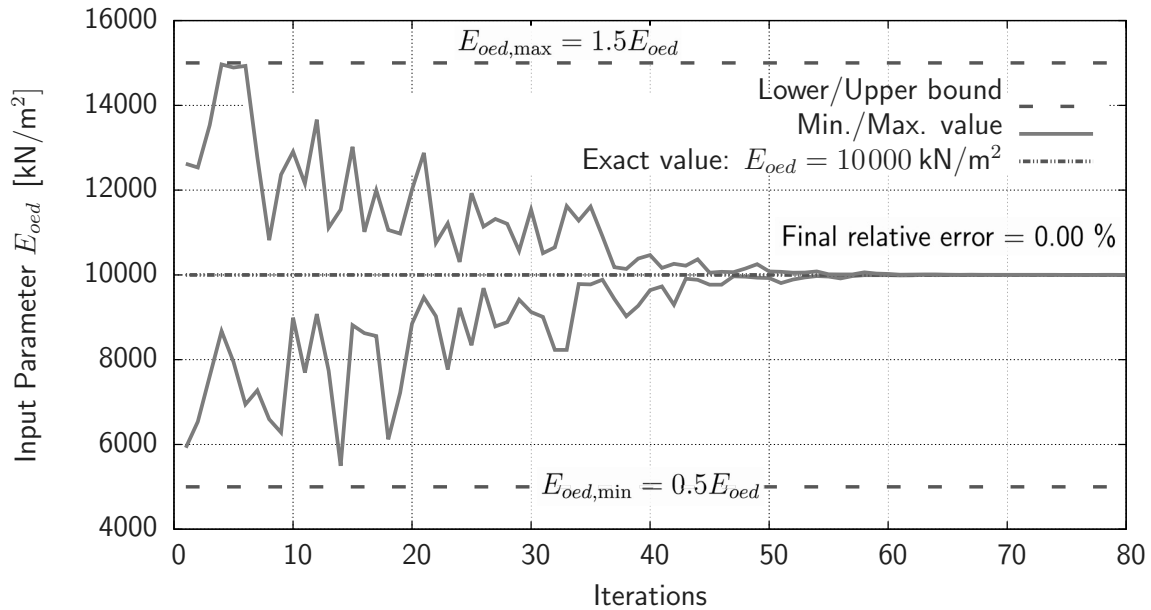
Figure 4.49.: Identification of the Oedometer modulus E_{oed}.
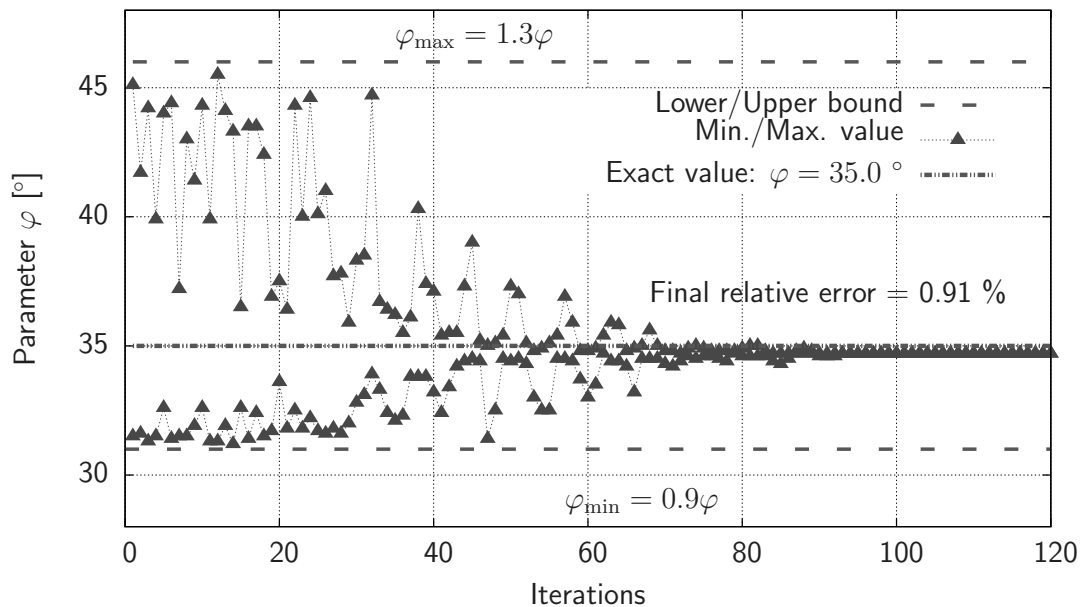
Figure 4.50.: Identification of the soil angle of internal friction φ in identification variant (1).

– 0.91 %. In Figure 4.54 it is presented the minimum value of the objective function at each iteration.

Further, in Table 4.6 there are summarized the relative errors of the identified HS parameters (the cohesion c is not included, due to its relatively very low sensitivity), when
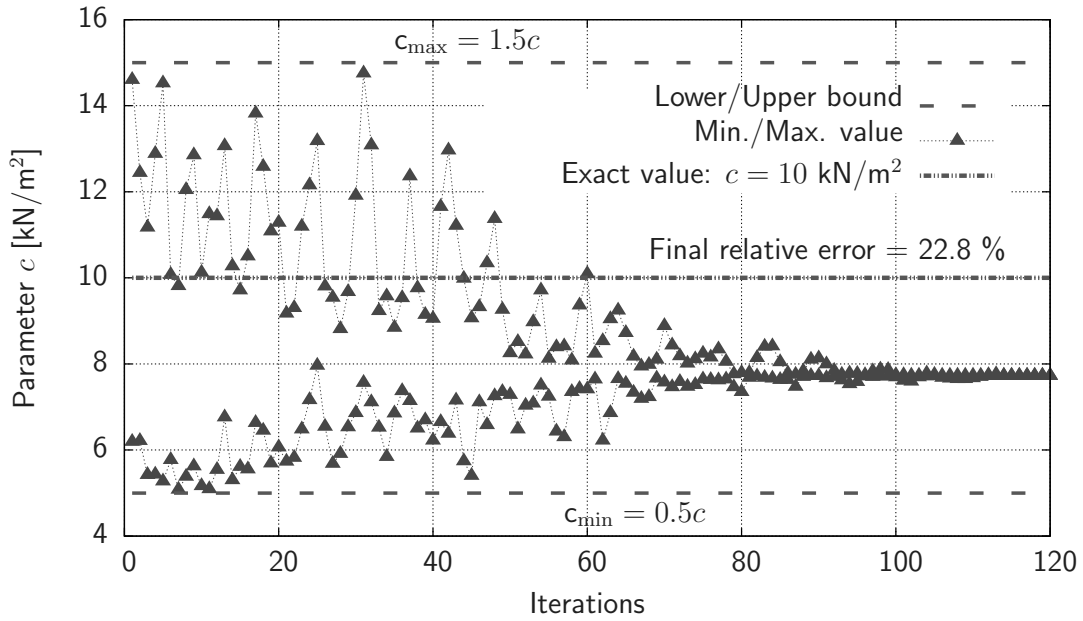
Figure 4.51.: Identification of the cohesion c in identification variant (1).
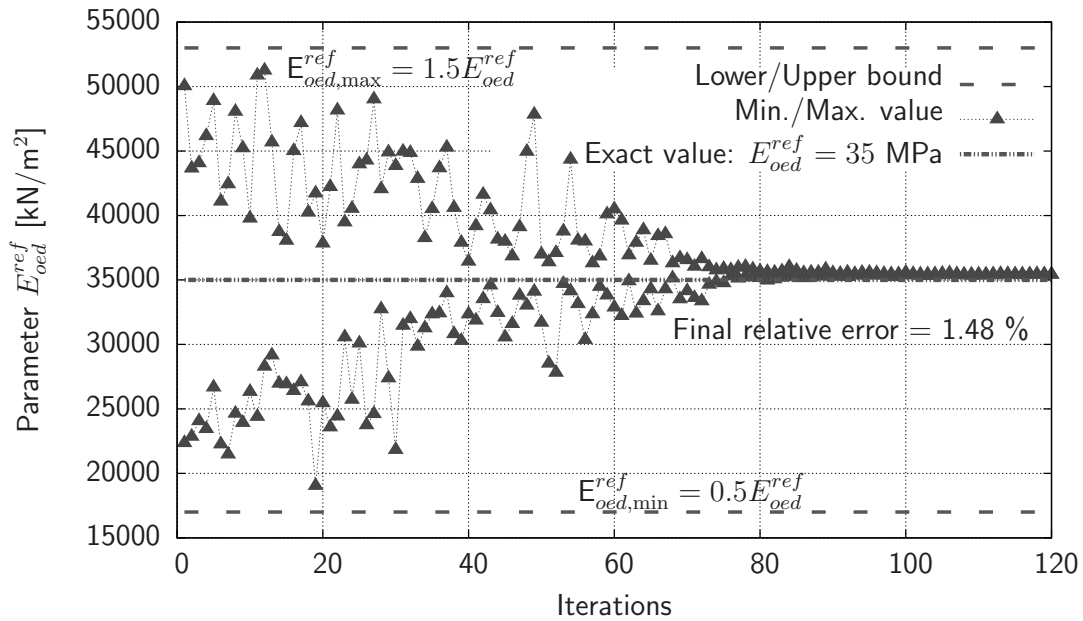
Figure 4.52.: Identification of the soil modulus for primary loading E_{oed}^{ref} in identification variant (1).

there are started with the same initial random generated population (swarm). As already explained before in Section 4.2.1.3.3, in column (1) there is used in the objective function (Eq. 4.33) the information provided by observation points O_{12} and S_{12} (see Fig. 4.36) during the excavation for each 3th meter, i.e. totally $N = 2 \times 13 = 26$ measurements.
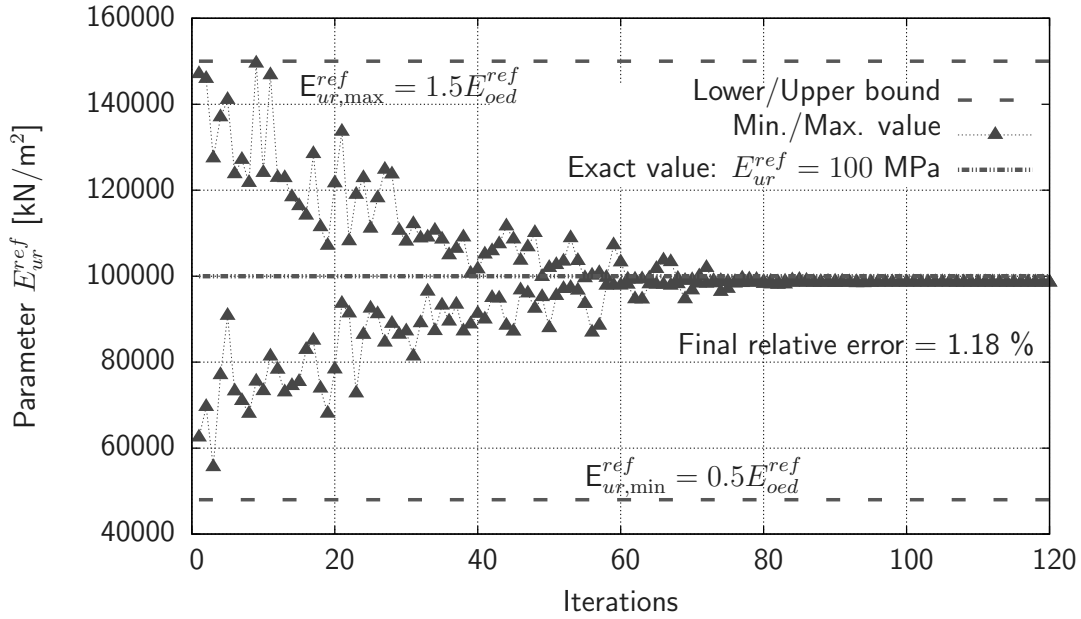
Figure 4.53.: Identification of the soil modulus for unloading/reloading E_{ur}^{ref} in identification variant (1).

In column (2) there are used observation points O_{12} and M_{12} during the excavation, i.e. totally $N = 2 \times 13 = 26$ measurements. In column (3) and (4) there are used observation points O_{12} and M_{12} during the excavation up to the observation cross-section (i.e. 0 m before it), and 3.0 m before it, i.e. totally $N = 2 \times 4 = 8$, respectively $N = 2 \times 3 = 6$ measurements. Further, in column (5) there are used observation points O_{12}, K_{12}, L_{12} and M_{12} during the excavation, i.e. totally $N = 4 \times 13 = 52$ measurements. In the next column (6) there are used the same number of observations like in (5), but to these measurements it is added 20 % statistical noise according to Equation 4.42. Finally, in columns (7) and (8) there are used points O_{12}, K_{12}, L_{12} and M_{12} during the excavation up to the observation cross-section (i.e. 0 m before it), and 3.0 m before it, i.e. totally $N = 4 \times 4 = 16$, respectively $N = 4 \times 3 = 12$ measurements.

From the presented results in Table 4.6 it can be concluded that by increasing the number of the observation points in the observation cross-section, the relative error is decreasing, i.e. the accuracy of the identified parameters is increased – column (5) compared with (1) and (2). Further, it is shown from the comparison of column (5) and (6) that the statistical noise has relatively small influence on the identification of the two parameters φ and E_{ur}^{ref} which have the highest sensitivity, while the influence on E_{oed}^{ref} is significant. Finally, by comparison column (3) and (4) with (2), respectively column (7) and (8) with (5) it is shown that the parameters can not be identified with a high reliability when the
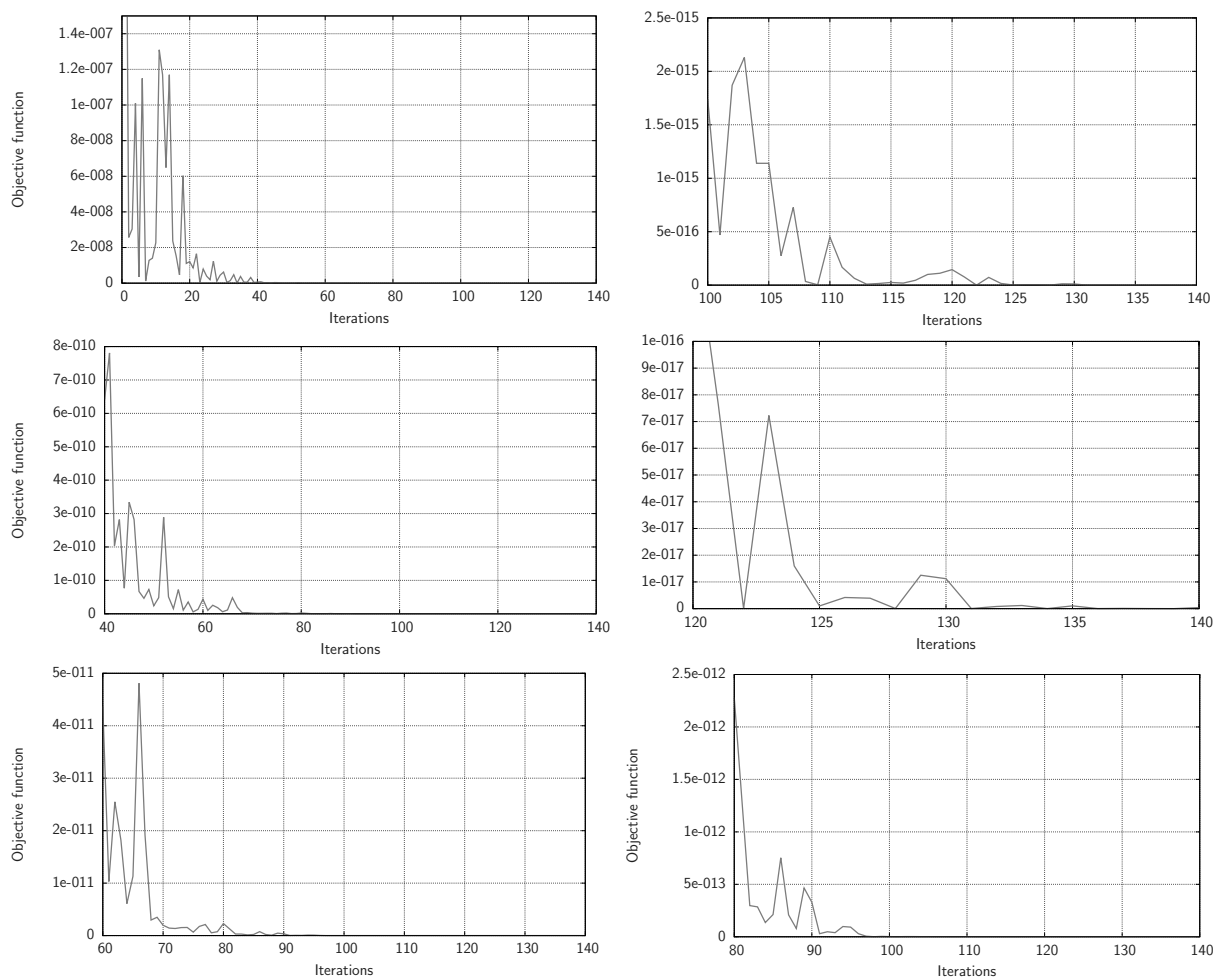
Figure 4.54.: Minimum value of the objective function in each iteration (zoomed); identification variant (1) of the synthetic back analysis of the shallow tunnel.

TBM is still before the observation cross-section, i.e. when not enough records during the tunnelling are made.

4.2.2.3. Application to Design of Experiment in Mechanized Tunneling Projects

In order to investigate the variation of the parameters subject to identification – i.e. to validate their sensitivity calculated before in Section 4.1.2.2, or to evaluate their "confidence", the probability distribution of the residual values (PDF) is calculated. This is done for each of the eight identification variants, whilst the PSO is ran 4 times each time with different initial random swarms.

Table 4.6.: Relative error for the identified parameters φ, E_{ur}^{ref}, E_{oed}^{ref} (started with the same initial random population) for different variants regarding the used information from the observations – number and place of the observation points (see also Fig. 4.36), and number of observations from each single point.

Para-meter	Exact value	Relative error from the exact value, in %					
		O, S	O, M	O, M 0.0 m	O, M 3.0 m	O, K, L, M	O, K, L, M + 20% noise
		(1)	(2)	(3)	(4)	(5)	(6)
φ	35.0°	0.91	1.75	7.69	32.23	0.77	1.77
E_{oed}^{ref}	35 000 kN/m²	1.48	3.56	28.07	24.48	0.26	20.13
E_{ur}^{ref}	100 000 kN/m²	1.18	2.48	14.82	14.10	1.24	0.83

Para-meter	Exact value	Relative error from the exact value, in %	
		O, K, L, M 0.0 m	O, K, L, M 3.0 m
		(7)	(8)
φ	35.0°	4.12	11.89
E_{oed}^{ref}	35 000 kN/m²	18.76	38.33
E_{ur}^{ref}	100 000 kN/m²	7.64	20.43

4.2.2.3.1. Influence of the Number & Location of the Observations

Here it is demonstrated that by increasing the number of the observation points in the observation cross-section, the variation of the three most sensitive input parameters – φ, E_{oed}^{ref}, and E_{ur}^{ref} – is decreasing (shown in Fig. 4.55–4.57 comparing identification variants (1), (2), and (5)), i.e. the accuracy of these identified parameters is increased. In Figure 4.57 it is shown that these three most sensitive parameters have a 95 % probability staying in the range of ±5 %.

4.2.2.3.2. Influence of the Excavation Distance to the Observation Cross-Section

There are investigated again several identification variants with different number and location of the observation points, but now the excavation of the tunnel is up to:

- the observation cross-section 12 (identification variant (3) and (7)), or

- 3 m before the observation cross-section 12 (identification variant (4) and (8)),

The results are presented in Figures 4.58–4.61. Now there are less observations available during the tunnelling. The results show decreased accuracy of the identified parameters with decreasing the records during the tunnelling, i.e. with decreasing the excavation length before the observation cross-section.

4.2.2.3.3. Effect of Noise in the Measurements

It is added a 20 % statistical noise to the (synthetic) measurements. The results show negative influence of the parameters which have low, or moderate sensitivity like E_{oed}^{ref} (see Figure 4.62). The parameters with the highest sensitivity – φ and E_{ur}^{ref} – are relatively not significantly influenced, and they have a 95 % probability staying in the range of ± 5 %.

Figure 4.55.: Identification variant (1). "Confidence" – totally $N = 2 \times 13 = 26$ measurements in observation points O_{12} and S_{12}. I.e. recorded are the displacements from excavation stage 6 to 30 each 3rd meter (i.e. each 2nd excavation stage) and used in the objective function (Eq. 4.33).
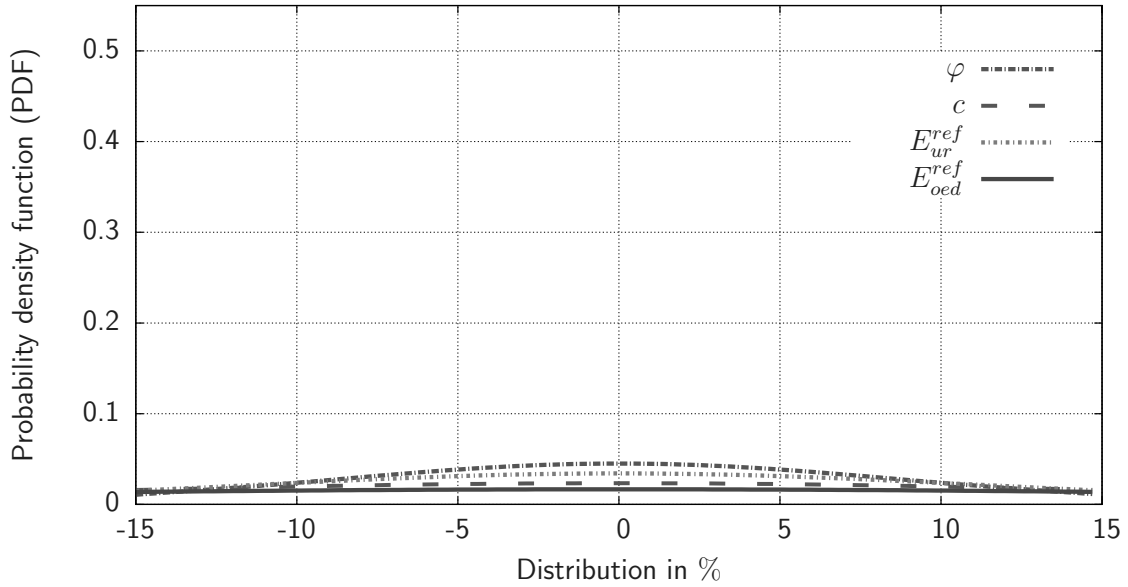
Figure 4.56.: Identification variant (2). "Confidence" – totally $N = 2 \times 13 = 26$ measurements in observation points O_{12} and M_{12}. I.e. recorded are the displacements from excavation stage 6 to 30 each 3rd meter (i.e. each 2nd excavation stage) and used in the objective function (Eq. 4.33).
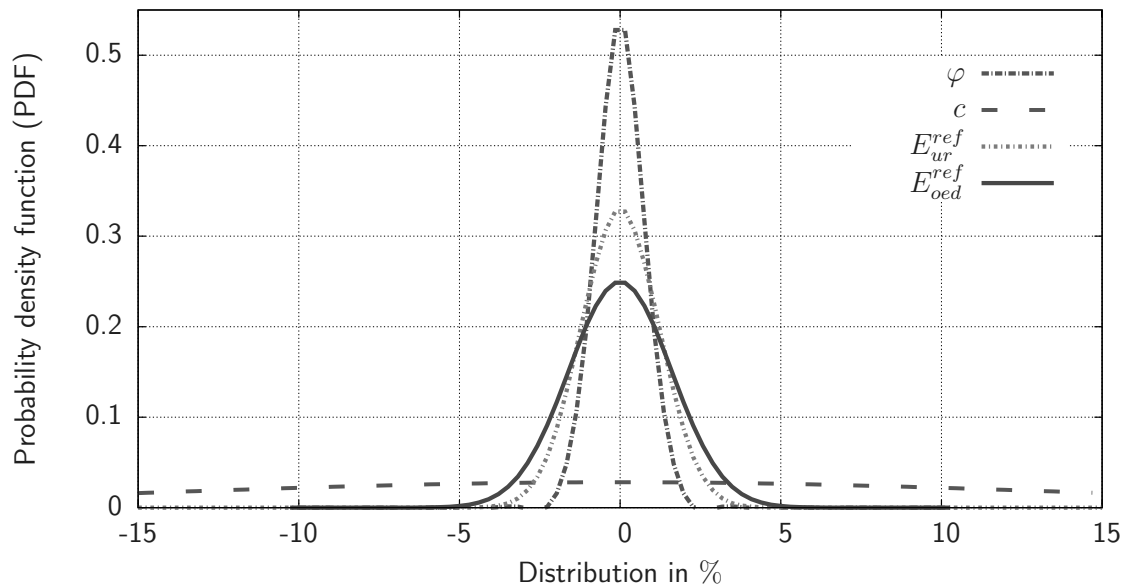
Figure 4.57.: Identification variant (5). "Confidence" – totally $N = 4 \times 13 = 52$ measurements in observation points O_{12}, K_{12}, L_{12}, and M_{12}. I.e. recorded are the displacements from excavation stage 6 to 30 each 3rd meter (i.e. each 2nd excavation stage) and used in the objective function (Eq. 4.33).
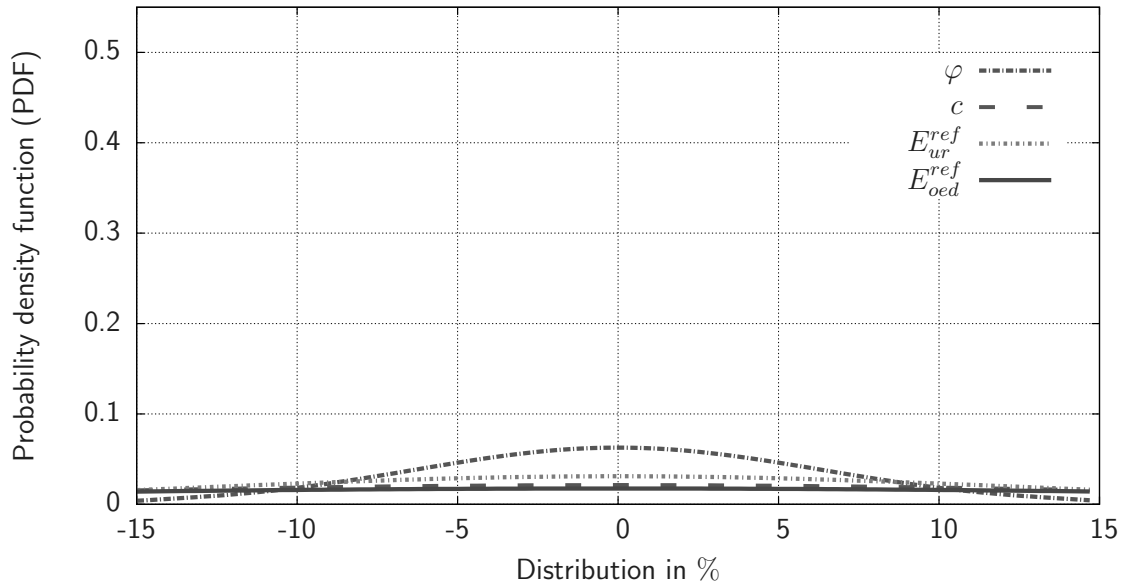
Figure 4.58.: Identification variant (3). "Confidence" by excavation up to the observation cross-section – totally $N = 2 \times 4 = 8$ measurements in observation points O_{12} and M_{12}. I.e. recorded are the displacements from excavation stage 6 to 12 each 3rd meter (i.e. each 2nd excavation stage) and used in the objective function (Eq. 4.33).
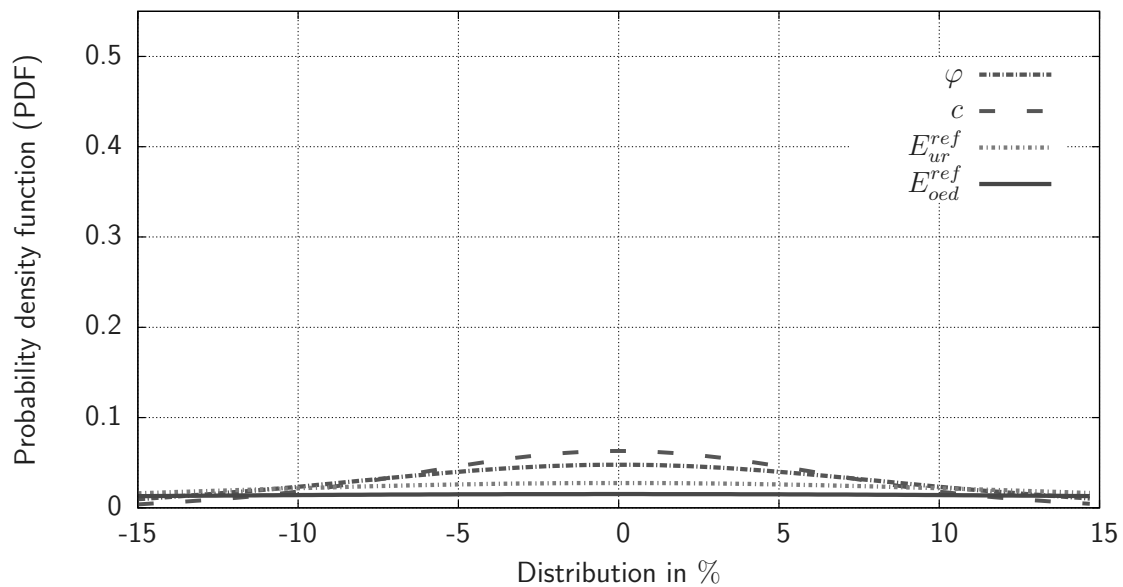
Figure 4.59.: Identification variant (4). "Confidence" by excavation 3.0 m before the observation cross-section – totally $N = 2 \times 3 = 6$ measurements in observation points O_{12} and M_{12}. I.e. recorded are the displacements from excavation stage 6 to 10 each 3rd meter (i.e. each 2nd excavation stage) and used in the objective function (Eq. 4.33).
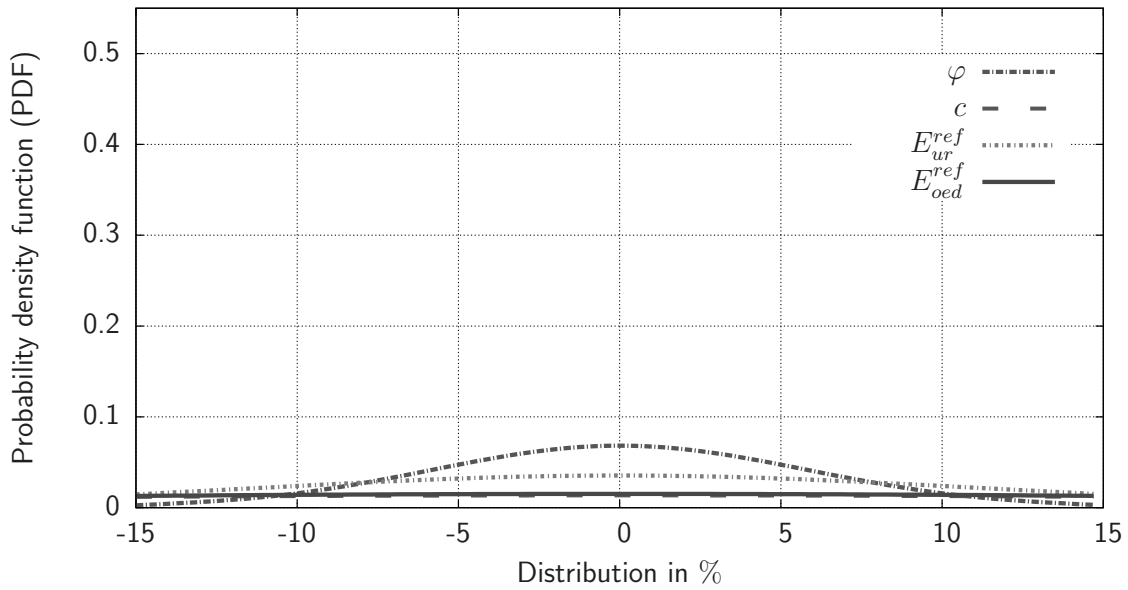
Figure 4.60.: Identification variant (7). "Confidence" by excavation up to the observation cross-section – totally $N = 4 \times 4 = 16$ measurements in observation points O_{12}, K_{12}, L_{12}, and M_{12}. I.e. recorded are the displacements from excavation stage 6 to 12 each 3rd meter (i.e. each 2nd excavation stage) and used in the objective function (Eq. 4.33).
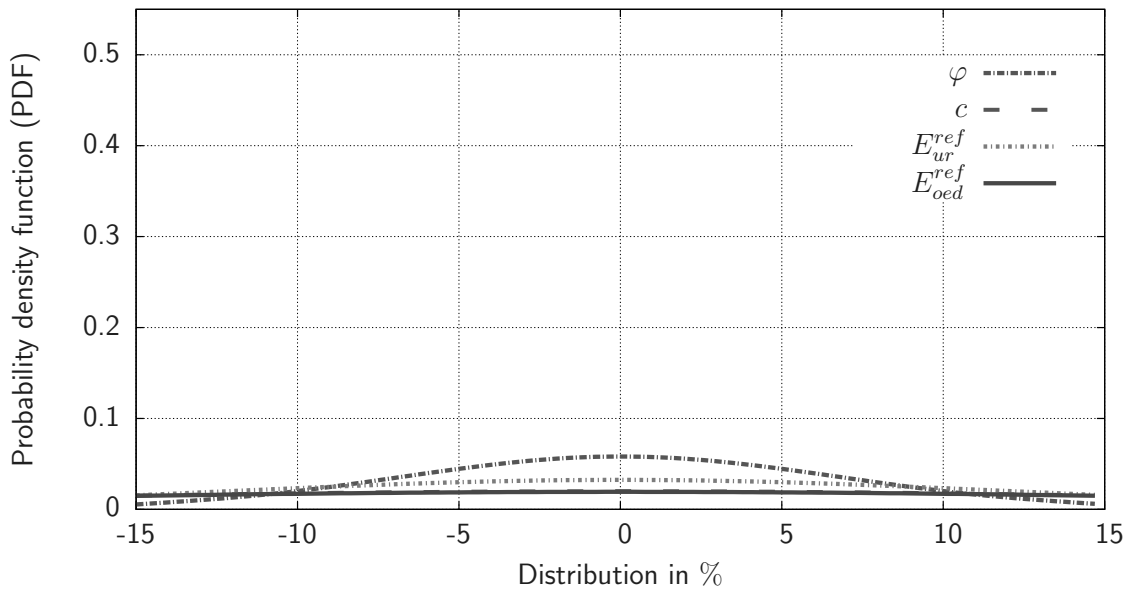
Figure 4.61.: Identification variant (8). "Confidence" by excavation 3.0 m before the observation cross-section – totally $N = 4 \times 3 = 12$ measurements in observation points O_{12}, K_{12}, L_{12}, M_{12}. Recorded are the displacements from excavation stage 6 to 10 each 3rd meter (i.e. each 2nd excavation stage) and used in the objective function (Eq. 4.33).
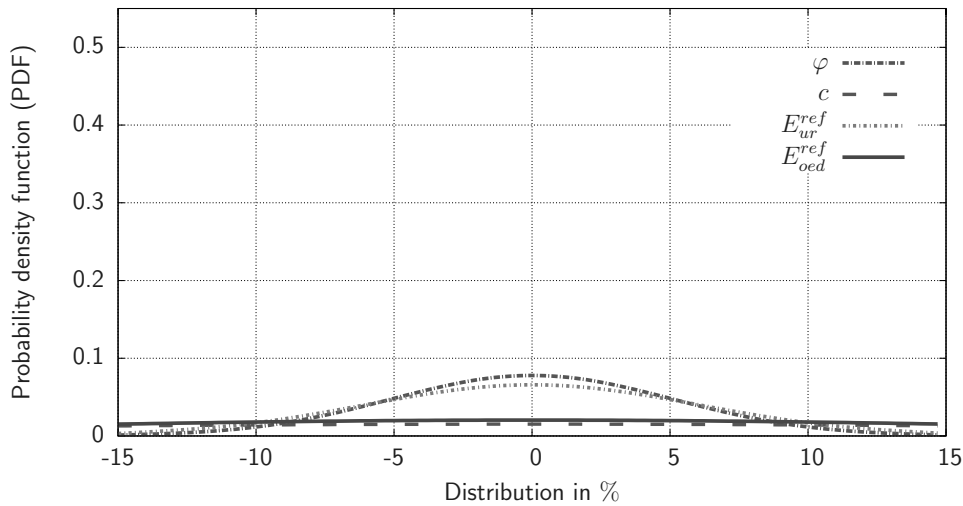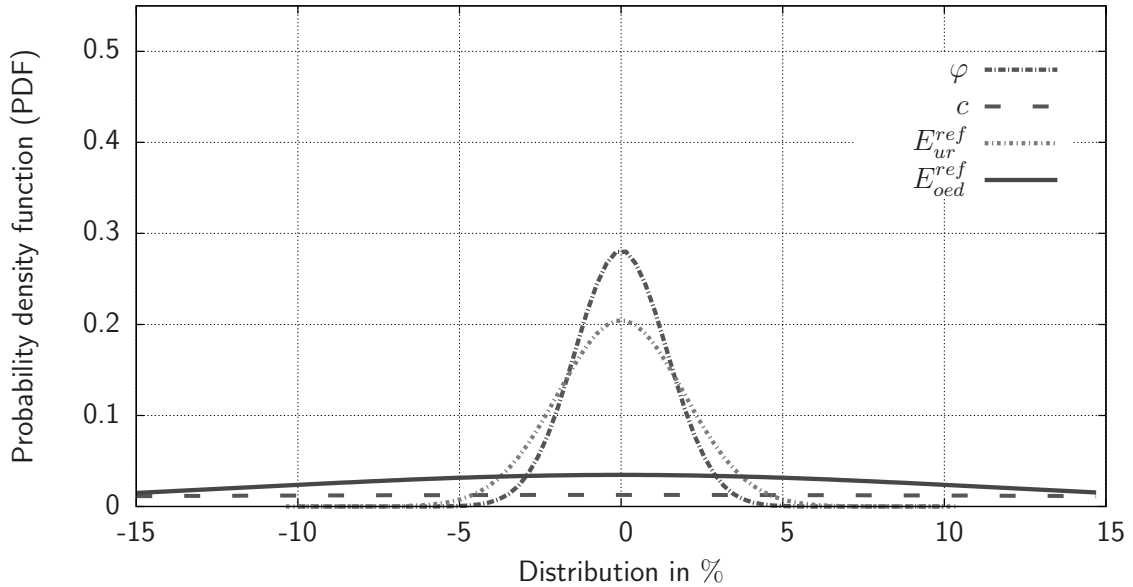
Figure 4.62.: Identification variant (6). "Confidence" – totally $N = 4 \times 13 = 52$ measurements in observation points O_{12}, K_{12}, L_{12}, and M_{12} with 20% statistical noise. I.e. recorded are the displacements from excavation stage 6 to 30 each 3rd meter (i.e. each 2nd excavation stage) and used in the objective function (Eq. 4.33).

4.2.3. Summary and Conclusions

A sensitivity analysis regarding the investigated soil constitutive input parameters of the adopted advanced elastoplastic model was carried out in order to asses the FE-model performance and to increase the understanding about the identified parameters.

The results provided by the performed local SA, by the PDF distribution, and by the global SA performed in Miro *et al.* (2012a) show identical ranging (sensitivity, CSS_j) of the investigated input parameters of the HS model:

$$CSS(\varphi) > CSS(E_{ur}^{ref}) > CSS(E_{oed}^{ref}) \gg CSS(c).$$

The most important (i.e. sensitive) parameters are $x_2 = \varphi$ and $x_3 = E_{ur}^{ref}$, $x_4 = E_{oed}^{ref}$ has moderate sensitivity, while the least sensitive parameter is $x_1 = c$ which may be excluded from the identification procedure.

Most tunnels in urban areas are long, linear structures, and values for model parameters can be obtained by performing field measurements or from laboratory tests. However, in tunnelling it is often technically difficult to collect sufficient data needed for reliable numerical simulation. The back calculated soil constitutive parameters help to make the

numerical predictions more reliable. Such predictions can then be used for the revision and improvement of the tunnel design, e.g. excavation procedure, support pressures and improvement of the properties (chemical, mechanical) of the support materials – bentonite and grout (see e.g. Kavvadas 2003) in order to minimize risks such as possible damage to existing buildings at the ground surface. The number, the place, and the type of the measurements, are strongly dependent on the complexity of the investigated geotechnical problem. In the present study for the identification of the soil constitutive input parameters a direct back analysis was successfully carried out using the PSO for minimizing the disagreements between the measurements and the numerical simulation of the mechanized tunnelling. For performing the direct back analysis the 3D FE-code Plaxis has been coupled with the software MATLAB in which the adopted PSO (PSO with inertia, Shi & Eberhart 1998a) was implemented. Further, in the back analysis it was demonstrated that using maximum number of 4 observation points during the excavation – identification variant (5) – the identification has been significantly improved. The uncertainty in the measurements (20 % noise) – identification variant (6) – has relatively small influence on $x_2 = \varphi$ and $x_3 = E_{ur}^{ref}$ which have the highest sensitivity, but $x_4 = E_{oed}^{ref}$ is negatively influenced, because its sensitivity is much lower.

One current shortage of the adopted parameters identification procedure via direct back analysis results from the iterative computation time used for repeated solution of the forward problem. By using a suitable PSO parameters like number of particles, number of maximum iterations, etc., it is possible to reduce the number of calls of the forward model improving the performance of the PSO algorithm. In addition, proper sub-modelling can be used to reduce the calculation time required to solve the forward problem.

Interesting comparison can be made with the back analysis performed in Nguyen & Nestorovic (2013) where it is used the same simulation of the mechanized excavation of the shallow tunnel and the Hardening Soil (HS) model. The parameters subject of the identification and the relations between then are the same. In Figure 4.63 there are presented the results obtained with two measurement points (like in identification variant (1)) using as optimization algorithm the Extended Kalman filter (EKF) or the Unscented Kalman filter (UKF). The EKF and the UKF can utilize prior information to identify the parameters of the nonlinear HS model arbitrarily fast. Although the EKF requires less number of forward calculation of the numerical model ($j + 1$ for the EKF and $2j + 1$ for the UKF, where $j = 4$ is the number of model parameters, in each iteration), the UKF is favored in that it drives low sensitive parameter (the cohesion, c) to convergence more easily than the EKF does. One more attractive property of the UKF is that it does
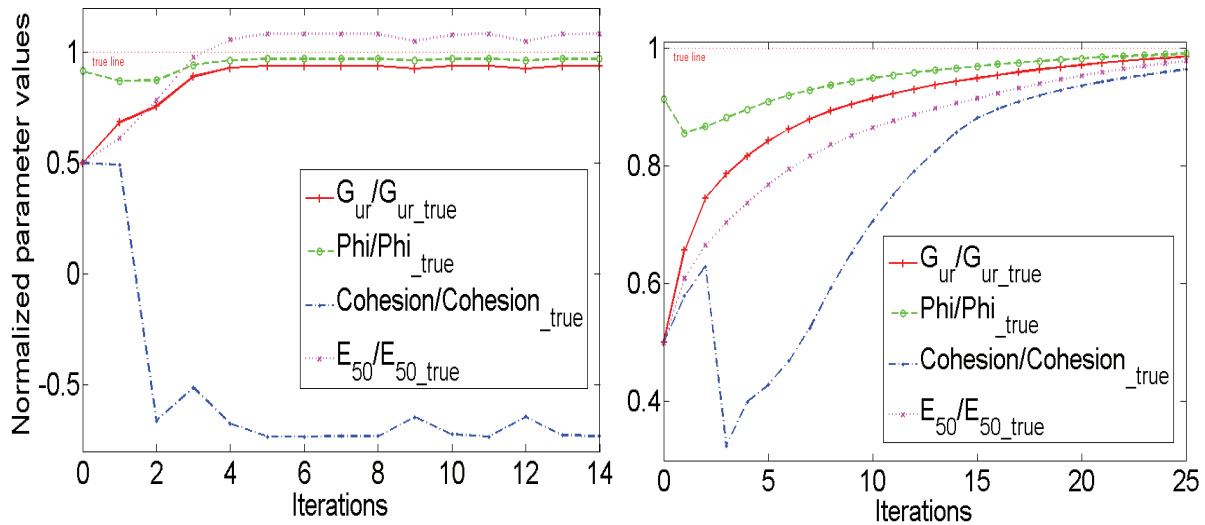
Figure 4.63.: Parameters identification of the HS model performed with the EKF (left) and with the UKF (right) in Nguyen & Nestorovic (2013).

not require calculation of the derivatives of the observables with respect to the identifying parameters. Comparing these results (Fig. 4.63) with these presented in Figures 4.50–4.53 obtained with the PSO, it can be seen that the Kalman filters are at least 4 times faster (less number of iterations up to convergence) than the PSO in the identification of the soil constitutive parameters. Reason for this could be that by the EKF and UKF the direction and the length to move from one iteration step to the next is well calculated so that only a small number of iterations compared to the PSO are required to obtain convergence. However, main disadvantage of the EKF is that calculation of derivatives is needed and the method may fail for highly non-linear, non-smooth objective functions with several optima.

5. Case Study – Slurry Shield Driven Tunnel Project

5.1. The Westerschelde Tunnel in the Netherlands

5.1.1. Description of the Project

The Westerschelde Tunnel is a shallow twin bore road tunnel under the estuary of the Schelde in the Netherlands (Fig. 5.1 and 5.2). First it is bored the east line and it is the one which is investigated in the current part of the thesis.

The tunnels each have a length of approximately 6.6 km and a bored diameter of 11.33 m. The thickness of the prefabricated concrete tubings is 0.45 m and their width (i.e. length in excavation direction) is 2.00 m. The total length of the TBM is the length of the shield which is 10.95 m plus some additional length of few decimeters because of the cutterhead at front (e.g. see (1) in Fig. 3.1 for an imagination). By the construction maximum settlements of almost 14 cm on the ground surface above the tunnel are measured, which is much higher value than by the most urban tunnels constructed via TBM in the last two-three decades. However, the Westerschelde Tunnel is not an urban tunnel, i.e. there were no any buildings on the ground surface. Therefore, (due to economical reasons) the support pressures of the TBM – especially the grouting pressure within the annular gap – are being not so high and therefore this larger ground deformations have occurred.

The geology along the tunnels is made up of different sand and clay formations. Figure 5.3 shows the geology and a longitudinal section of the tunnel. Also in the same figure in the aloft left corner in the red box it is marked the investigated south part of the east tunnel line. The uppermost 20 to 30 m consist mostly of medium to fine grained sands (Z1). In the area of the investigated tunnel length – the south beginning of the tunnel – there are available thin clay layers (K1) above the sand layers (Z1), and above the ground level before the tunnel excavation there was built an artificial earth dam (Dike) against sea
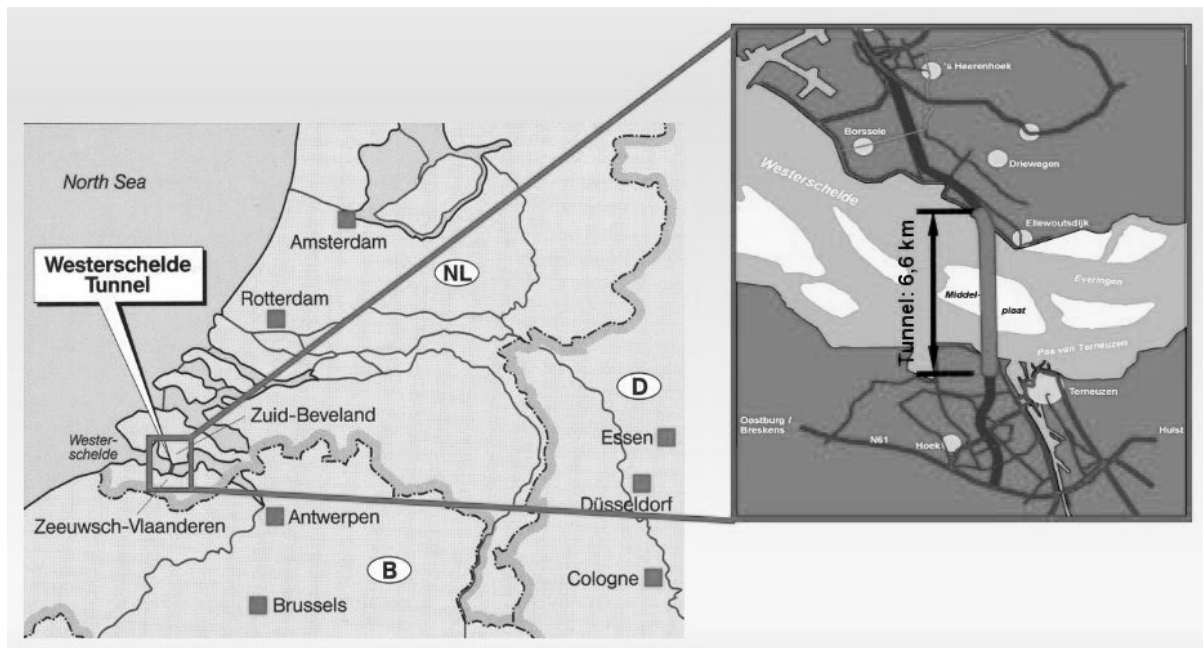
Figure 5.1.: Layout of the Westerschelde Tunnel (Grimm 2002).
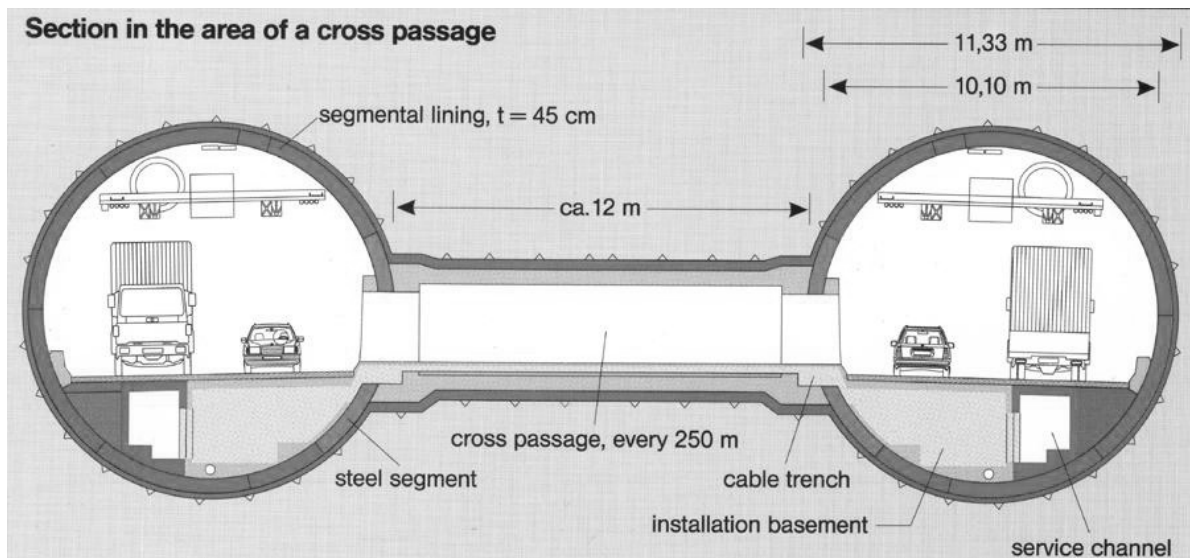
Figure 5.2.: Cross-section of both tunnels with cross-passage (Grimm 2002).

flooding – see in Figure 5.4. "Boomse clays" (BK1 & BK2), overconsolidated stiff to firm tertiary clays are situated beneath the sands. These layers have a thickness of between 10 to 30 m – at the area of the investigated tunnel length about 15 m thickness (Fig. 5.4). The "Boomse clays" are located at a greater depth in the north than in the south. According to their clay content and their mechanical properties the "Boomse clays" can be divided into two layers: The "upper Boomse clays" (BK1) with an average clay fraction of about
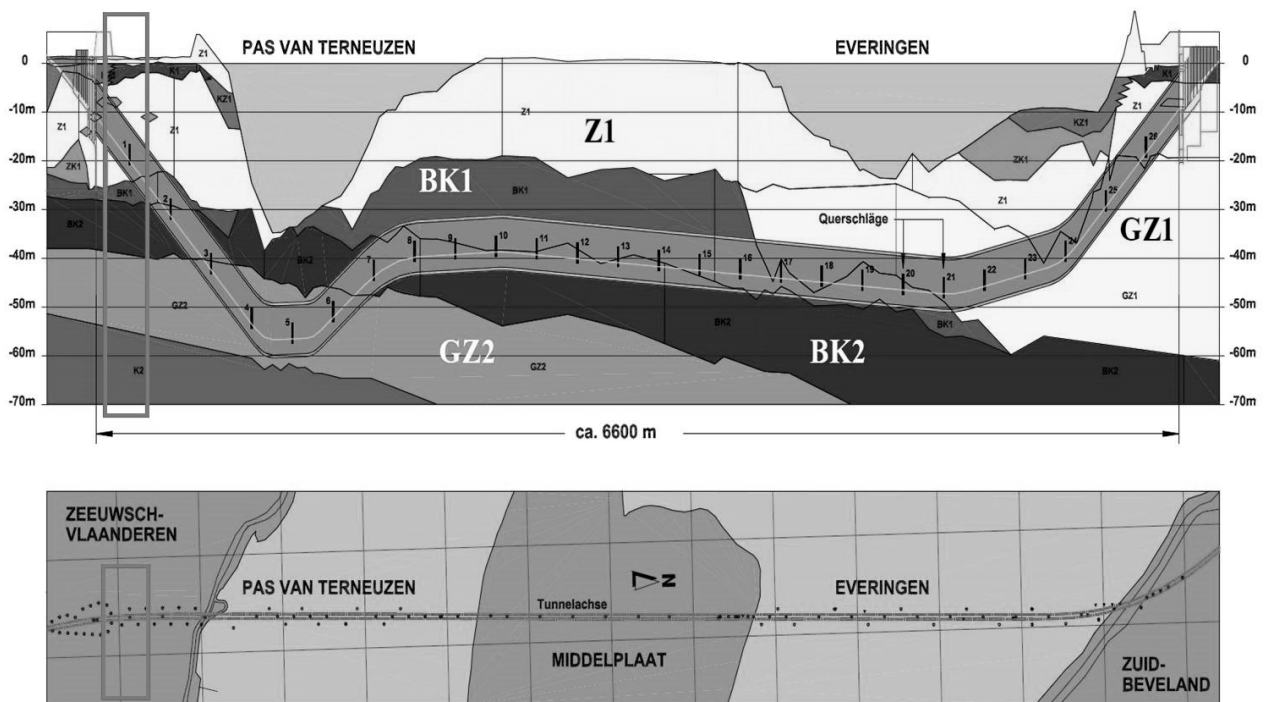
Figure 5.3.: Longitudinal section of the Westerschelde Tunnel (Grimm 2002).
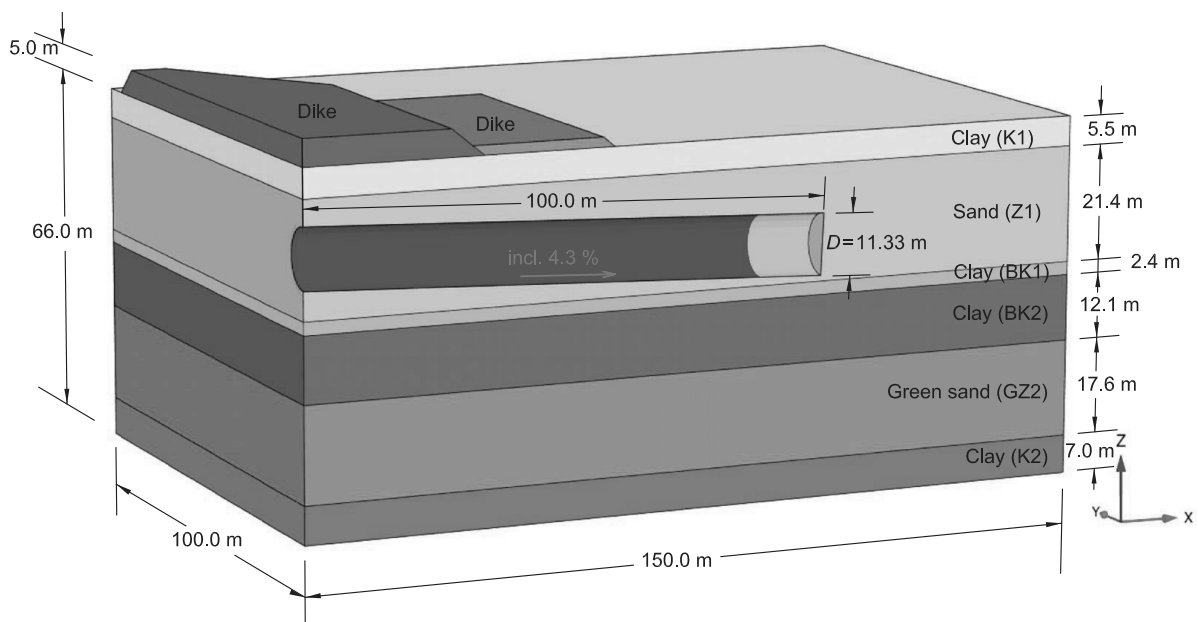
Figure 5.4.: Geometry of the investigated part of the Westerschelde Tunnel. The ground water level is 1.50 m below the ground surface, i.e. in the upper clay layer K1.

60 % and the "lower Boomse clays" (BK2) with a clay fraction of roughly 40 %. Tertiary, glauconitic sands (GZ1 & GZ2) are found beneath the "Boomse clays". These glauconitic sands especially behaves extreme stiffly, and this is partly the result of the cementatious

character of the material (van der Vliet *et al.* 2009). The mechanical properties of the soil layers at the investigated tunnel area were summarized in Brodeßer (2012).

At the investigated area, the tunnel line descent from the south side with a slope of 4.5 % towards the deepest point of the trasse (see Fig. 5.3 and 5.4). The groundwater levels are influenced mainly from the North Sea and there are close to the ground surface. For the numerical simulation it is assumed a constant water level 1.50 m below the ground surface.

5.1.2. Numerical Simulation and Parameter Identification Procedure

First: It was created a 3D FE-model (Plaxis 3D, version 2012) of the investigated tunnel length. Next, there were selected an appropriate set of input soil parameters for the adopted HSsmall model (see Table 5.1) for a first run of the numerical simulation.

Second: It was performed a local sensitivity analysis in order to understand which HSsmall model parameters are most influencing the predicted results, i.e. the settlement profiles which are subject of the subsequent back calculation.

Third: The most relevant HSsmall model parameters were manually tuned (iteratively varied) till it was achieved a better match of the measurements. The best tuned parameters set is then summarized in Table 5.3 (marked in red).

Fourth: Because of the very long calculation time the 3D model (Fig. 5.6) is reduced to a 2D forward model simulating a cross-section which coincide with the measured transverse settlement profile (points 1,2,..., 8 in Fig. 5.6). The response in the transverse settlements profile obtained in the both – 3D and 2D simulations is compared and it is shown that the 2D model is an acceptable approximation of the 3D behaviour in that case. Thereafter, this 2D model is used for the subsequent iterative optimization because of its short calculation time.

Fifth: With the 2D forward FE-model it is performed a direct back analysis using the PSO for minimizing the disagreements between the measurements and the calculations. The best optimized parameters set of the adopted soil constitutive model – the HSsmall model for the two soil layers K1 and Z1 – is then used as an input in the 3D numerical model.

Table 5.1.: Parameters of the used HSsmall model used for the first calculation – Numerical prediction 1.

Soil Constitutive Parameters for the HSsmall Model							
	Dike	K1	Z1	BK1	BK2	GZ2	K2	
φ	20	18	30	28	28	34	40	[°]
ψ	0	0	0	0	0	4	0	[°]
c	5	5	6.4	20	20	11. 4	40	[kN/m^2]
E_{50}^{ref}	14 000	10 000	17 000	25 000	30 000	30 000	50 000	[kN/m^2]
E_{oed}^{ref}	11 000	7000	17 000	25 000	30 000	30 000	50 000	[kN/m^2]
E_{ur}^{ref}	30 000	27 000	60 000	60 000	100 000	90 000	180 000	[kN/m^2]
G_0^{ref}	40 000	40 000	45 000	65 000	100 000	110 000	150 000	[kN/m^2]
$\gamma_{0.7}$	0.0002	0.0002	0.0002	0.0002	0.0002	0.0002	0.00015	[-]
p^{ref}	100	100	100	100	100	100	100	[kN/m^2]
m	0.7	0.7	0.5	0.7	0.7	0.5	0.7	[-]
R_f	0.90	0.90	0.90	0.90	0.90	0.90	0.90	[-]
ν_{ur}	0.20	0.20	0.20	0.20	0.20	0.20	0.20	[-]
γ_{unsat}	19	18	18	18	17	17	17	[kN/m^3]
γ_{sat}	20	20	19	21	19.3	20.2	20	[kN/m^3]
K_0^{nc}	0.52	0.54	0.44	0.53	0.53	0.40	0.36	[-]
OCR	1.0	1.0	1.0	2.7	2.8	2.5	3.0	[-]

5.1.2.1. Description of the 3D Numerical Simulation

Because the geometry (cylindrical shape of the tunnel), the soil layers and their material properties, initial and excavation conditions all are assumed to be symmetric about a vertical plane of symmetry that is parallel to the tunnel axis (i.e. the X-axis), only one-half of the model need to be analyzed. In Figure 5.4 there are given the main dimensions of the created FE-model. The whole model is 150 m long (in the X-axis direction), 100
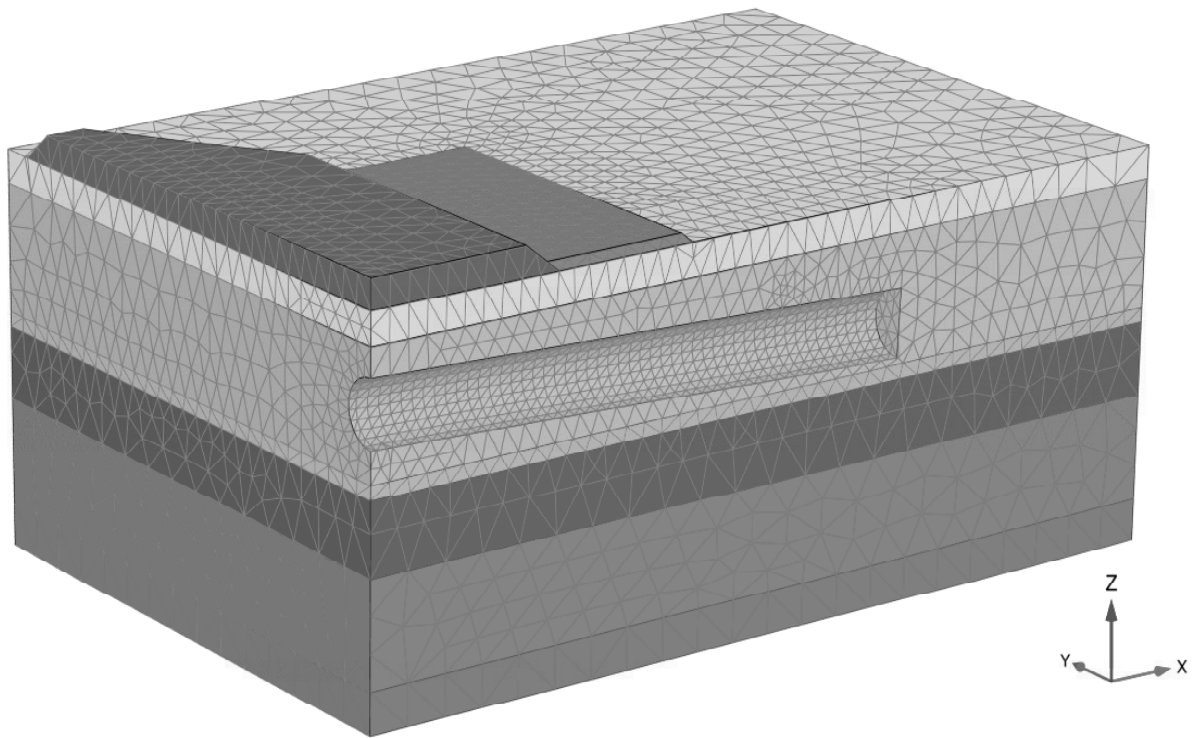
Figure 5.5.: Discretization of the FE-model.

m wide (in the Y-axis direction) and with a maximum depth of 71 m (in the Z-axis direction). The TBM is modeled to be 12.00 m long, i.e. 6×2.00 m (where 2.00 m is also the width of one tubing ring), simulated with cylindrical plate elements, and an area with a total length of 100 m (50 excavation stages each 2.00 advance) in the X-direction with an inclination of 4.3 % has been investigated. The tunnel diameter is D=11.33 m. The chosen finite element discretization (mesh) adopted for the simulation is shown in Figure 5.5. The space occupied by the soil material is discretized using 10-node tetrahedral elements. The number of these soil elements is about 70000 elements. The lining and the TBM are modeled as a linear elastic plate elements with properties listed in Table 5.2.

The support pressure needed to prevent active failure at the tunnel face is simulated as a non-uniformly distributed pressure: 137 kN/m^2 at the tunnel crown up to 250 kN/m^2 at the tunnel invert. The grouting pressure acting at the place of the annular gap was not considered.

The contact between the shield skin (plate elements in the model) with the surrounding ground (soil elements), and between the tunnel lining (plate elements in our model) and the ground is simulated via interface elements with an linear elastic material behaviour: $E = 20\,000$ kN/m^2 and $\nu = 0.30$.

Table 5.2.: Parameters of the employed linear elastic model for the structural elements.

Parameter	Lining	TBM	Unit
d	0.45	0.35	[m]
E	22 000	210 000	[MPa]
γ	24	38	[kN/m^3]
ν	0.10	0.30	[-]

The applied mechanical boundary conditions are the same as defined in Section 3.2.1.

The excavation process is modeled by means of step-by-step procedure. In the first calculation step, i.e. first calculation phase, the initial conditions (without activating the soil elements of the dike) are applied according to a *K0 procedure* (see Section 3.1.2.2). In the next phase (called: plastic nil-step) the dike elements are activated in order to simulate their construction and the resulting additional stress in the ground under the dike. In the next, first excavation phase only the stress field is taken from the previous plastic nil-step, while, the displacements are reset to zero. All of the next calculation phases (i.e. excavation stages) are meant to simulate an advance of 2.00 m (2.00 m is the tubing width; see in Fig. 3.5 for imagination) and are performed as a drained analysis using the elastoplastic HSsmall model for all of the soil layers. The steps which are modeled in a single excavation stage are the following:

- excavation of the soil in front of tunnel (deactivation of the finite elements at that place with 2.00 m tunnel advance);

- applying a face support pressure at the tunnel face;

- activation of the TBM shield, i.e. of the plate element (the next 2.00 m);

- installing (activation) a new concrete lining ring with width of 2.00 m;

- applying contractions of the plates of the TBM and the first 4 m of the lining in order to simulate the volume losses due to overcutting and conicity during the excavation; they are applied linearly decreased – from 0.4 % at the TBM face to 2.096 % at the 16th m behind the tunnel face. This corresponds to 2.5 % volume losses.

In each calculation phase the input for the staged construction is identical, except for its location, which has been shifted by 2.00 m each phase.
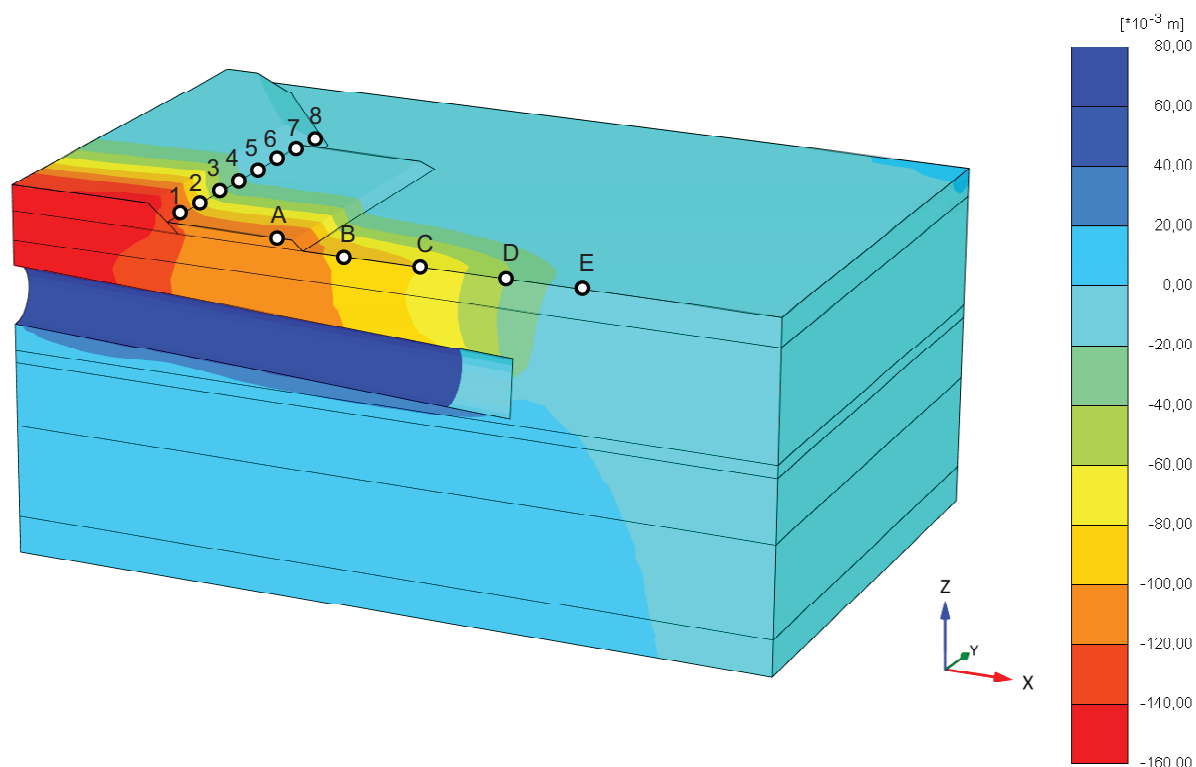
Figure 5.6.: Calculated vertical displacements u_z in Z-direction with parameters set from Table 5.1 (Numerical prediction 1). Shown are the observation (measurement) points in longitudinal (points A, B, C, D, and E) and in transversal direction (points: 1, 2,..., 8).

5.1.2.2. Sensitivity Analysis

Based on the geotechnical investigations (summarized in Brodeßer 2012) there is selected an appropriate set of input soil parameters for the adopted HSsmall model (see Table 5.1) for an initial run of the numerical simulation. In Figure 5.6 there are shown the calculated vertical displacements in the Z-direction u_z, and the observation (measurement) points in longitudinal (A, B, C, D, and E) and in transversal direction (1, 2,..., 8).

In Figures 5.9 and 5.10 there are presented the calculated transversal and longitudinal settlement profiles in the observed cross-sections – the dashed dark-green curves. The calculated profiles are wider than the measured. In order to improve further the numerical predictions, it is performed a local sensitivity analysis (LSA) with the soil constitutive parameters of the Dike, K1, and Z1 layers. For calculating the sensitivity derivatives it is used a forward finite difference scheme (i.e. Eq. 4.24) with step size $\Delta x = 10$ % for each input parameter. The goal is to understand which parameters influence mostly the size of the both settlement profiles.
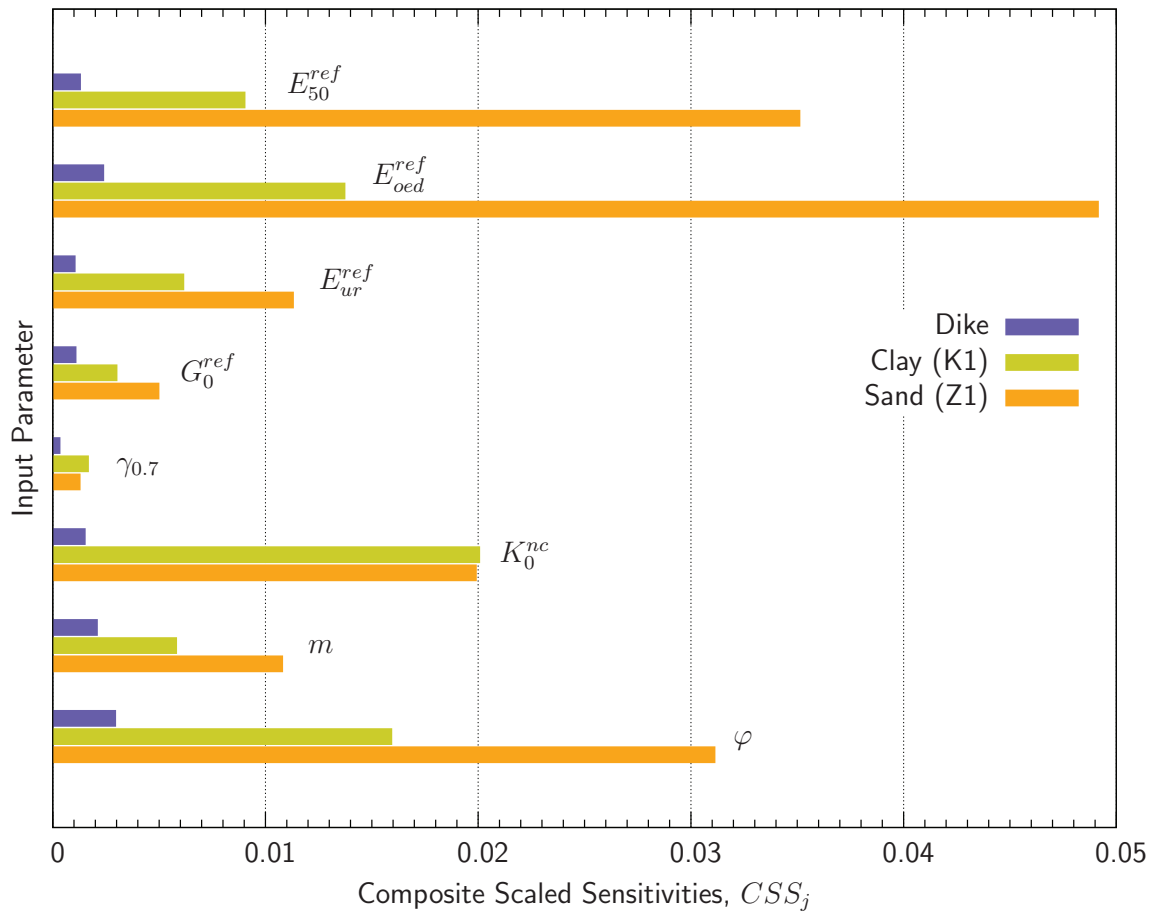
Figure 5.7.: Overall sensitivities regarding the vertical displacements u_z in observation points 1, 2, 3, A, B, C, and D.

In Figure 5.7 there are presented the calculated overall sensitivities using as observations the vertical displacements u_z in points 1, 2, 3, A, B, C, and D at time moment when the TBM is at the 44th excavation stage, i.e. 88 m from the tunnel beginning. This is done in order to understand which parameters of the HSsmall model and in which order of magnitude these influence the depth of the both settlement profiles. The results demonstrate that the largest influence is coming from the sand layer Z1 in which the tunnel is excavated, while the smallest influence has the dike which is situated on the ground surface. The largest influence have the two stiffnesses for primary loading E_{oed}^{ref} and E_{50}^{ref}, the angle of internal friction φ, followed by the value of K_0^{nc}.

In Figure 5.8 there are presented the calculated overall sensitivities using as observations the horizontal displacements u_y in points 1 and 3 at time moment when the TBM is at the 44th excavation stage, i.e. 88 m from the tunnel beginning. This is done in order to understand which parameters of the HSsmall model and in which order of magnitude these
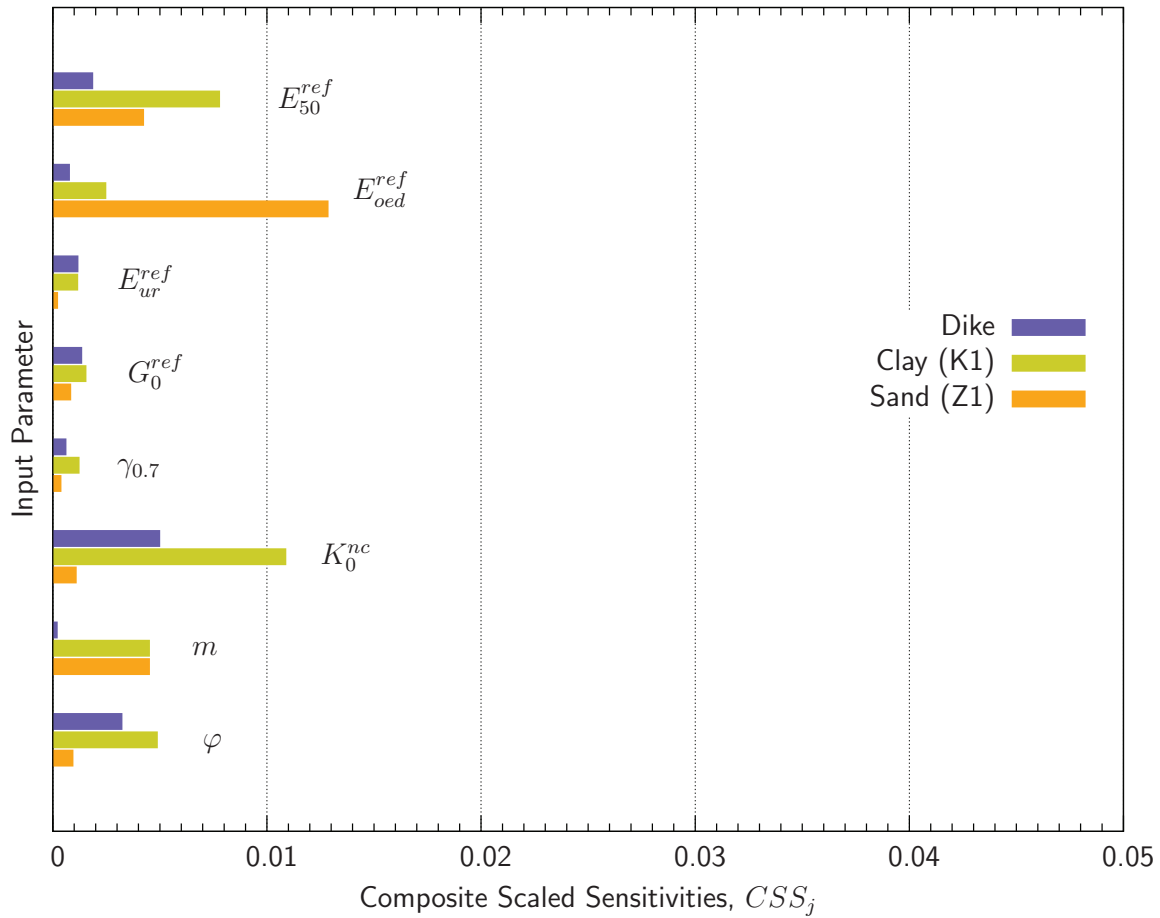
Figure 5.8.: Overall sensitivities regarding the horizontal displacements u_y in observation points 2 and 3.

influence the width of the transverse settlement profile. Points 2 and 3 are chosen because at that places there are the largest disagreements between the numerical predictions and the measurements.

It was very interesting to see that the two small-strain stiffness parameters G_0^{ref} and $\gamma_{0.7}$ have relatively low sensitivity compared to the rest of the investigated input parameters of the HSsmall model.

In order to minimize further the discrepancy between the numerical predictions and the measurements it was decided to perform manually iterations by changing the parameters of the HSsmall model starting with the most important of these. During the iterations there were changed also the contractions of the plate elements, and the magnitude of the face support.
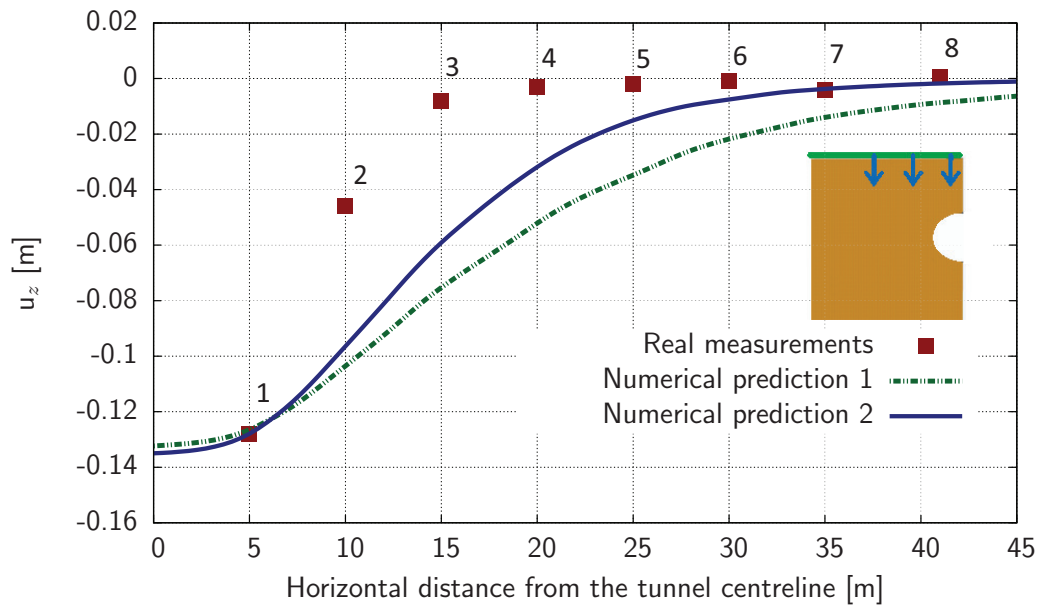
Figure 5.9.: Transverse settlements on the ground surface in the observation cross-section (see Fig. 5.6) when the TBM is at the 44th excavation stage, i.e. 88 m from the tunnel beginning.
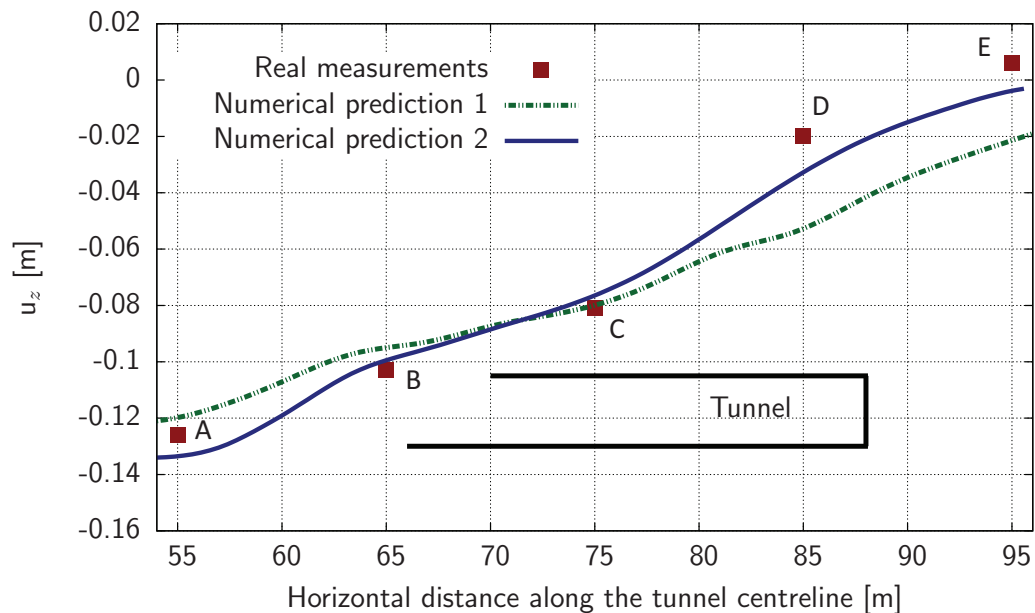
Figure 5.10.: Longitudinal surface settlements on the ground surface in the observation section (see Fig. 5.6) when the TBM is at the 44th excavation stage, i.e. 88 m from the tunnel beginning.

Table 5.3.: Optimized parameters of the used HSsmall model – Numerical prediction 2.

	Dike	K1	Z1	BK1	BK2	GZ2	K2	
Soil Constitutive Parameters for the HSsmall Model								
φ	28	22	34	28	28	34	40	[°]
ψ	0	0	0	0	0	4	0	[°]
c	5	5	6.4	20	20	11. 4	40	[kN/m^2]
E_{50}^{ref}	30 000	24 000	35 000	25 000	30 000	30 000	50 000	[kN/m^2]
E_{oed}^{ref}	30 000	20 000	37 000	25 000	30 000	30 000	50 000	[kN/m^2]
E_{ur}^{ref}	90 000	60 000	80 000	60 000	100 000	90 000	180 000	[kN/m^2]
G_0^{ref}	160 000	150 000	140 000	65 000	100 000	110 000	150 000	[kN/m^2]
$\gamma_{0.7}$	0.0002	0.0002	0.0002	0.0002	0.0002	0.0002	0.00015	[-]
p^{ref}	100	100	100	100	100	100	100	[kN/m^2]
m	0.7	1.0	0.5	0.7	0.7	0.5	0.7	[-]
R_f	0.90	0.90	0.90	0.90	0.90	0.90	0.90	[-]
ν_{ur}	0.20	0.20	0.20	0.20	0.20	0.20	0.20	[-]
γ_{unsat}	19	18	18	18	17	17	17	[kN/m^3]
γ_{sat}	20	20	19	21	19.3	20.2	20	[kN/m^3]
K_0^{nc}	0.53	0.69	0.41	0.53	0.53	0.40	0.36	[-]
OCR	1.0	1.0	1.0	2.7	2.8	2.5	3.0	[-]

Finally, the stiffness and the strength of the three layers Dike, K1, and Z1 was increased. The used HSsmall parameters are summarized in Table 5.3. The contractions of the plates of the TBM and the first 4 m of the lining were also increased, i.e. the volume losses were increased; In the final calculation there are from 1.4 % at the TBM face to 3.8 % at the 16th m behind the tunnel face, which corresponds to 5.2 % volume losses. The E-modulus of the interfaces was reduced 10 times to $E = 2000$ kN/m^2. Reason for this was the numerical stability of the simulation, because of the increased gap displacements normal to the interfaces around the TBM. The face support was also increased. Up to

excavation stage 41 the values are 159 kN/m^2 at the tunnel crown up to 262 kN/m^2 at the tunnel invert, in excavation stage 42 there are 172 kN/m^2 up to 285 kN/m^2, and in excavation stages 43-44 there are 187 kN/m^2 up to 300 kN/m^2.

So, the improved results (called here: Numerical prediction 2) are presented in Figures 5.9 and 5.10 – the dark-blue continuous curve. It is shown, that the calculated longitudinal settlements profile is now matched well. The calculated transverse settlements profile was improved, but, it is still wider than the measured one. There is a place for further improvements of the simulation. This will be done in the next Section 5.1.2.3 applying a direct back analysis.

5.1.2.3. 2D Numerical Forward Model and Back Analysis

Because of the very long computational time the 3D model (Fig. 5.6) is reduced to a 2D forward model (Plaxis 2D, version 2010) simulating a cross-section which coincide with the measured transverse settlement profile measured in points 1, 2,..., 8 (see Fig. 5.6). The model is created as a plane strain model. The geometry and the applied mechanical boundary conditions to the mesh are presented in Figure 5.11. The space occupied by the soil material is discretized using 15-node FE. The number of these elements in the model is 809.

First, the initial conditions (without activating the soil elements of the dike) are applied according to a *K0 procedure* ($\sigma'_v = \sigma'_y = \gamma_{soil} \; z - p_{steady}$, $\sigma'_h = \sigma'_x = \sigma'_v \; K_0$, with $z-$depth, above the groundwater level $\gamma_{soil} = \gamma_{unsat}$ and $p_{steady} = 0$, below $\gamma_{soil} = \gamma_{sat}$ and $p_{steady} = \gamma_{water} \; z$). In the next phase (called: plastic nil-step) the dike elements are activated in order to consider the additional stress in the subsoil due to the weight of the dike. The excavation is then modeled in one single excavation stage where the soil elements inside the tunnel are deactivated and the water is also removed. In the same phase the tunnel lining and the interface between the lining and the soil is activated; the interface play the role of an impermeable screen in order to model the tunnel lining as impermeable. To the lining the final surface contraction of 3.8 % is applied.

As in the 3D model for the 2D model the HSsmall model is applied for all of the soil layers. Using the tuned input parameters given in Table 5.3, i.e. Numerical prediction 2, the calculated transverse settlements are compared in Figure 5.12. The results obtained with the both models are similar in that case, however, the 2D approximation gives slightly larger settlements (about 1 cm) above the tunnel centreline. This difference may be due
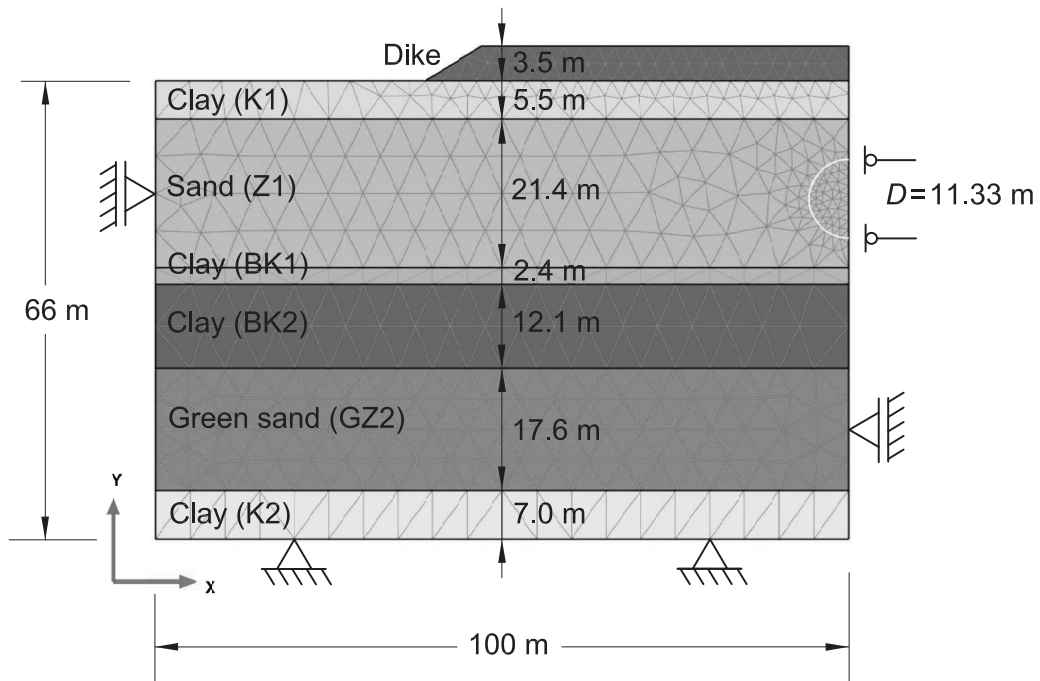
Figure 5.11.: Geometry, mechanical boundary conditions, and discretization of the 2D forward model of the Westerschelde Tunnel.
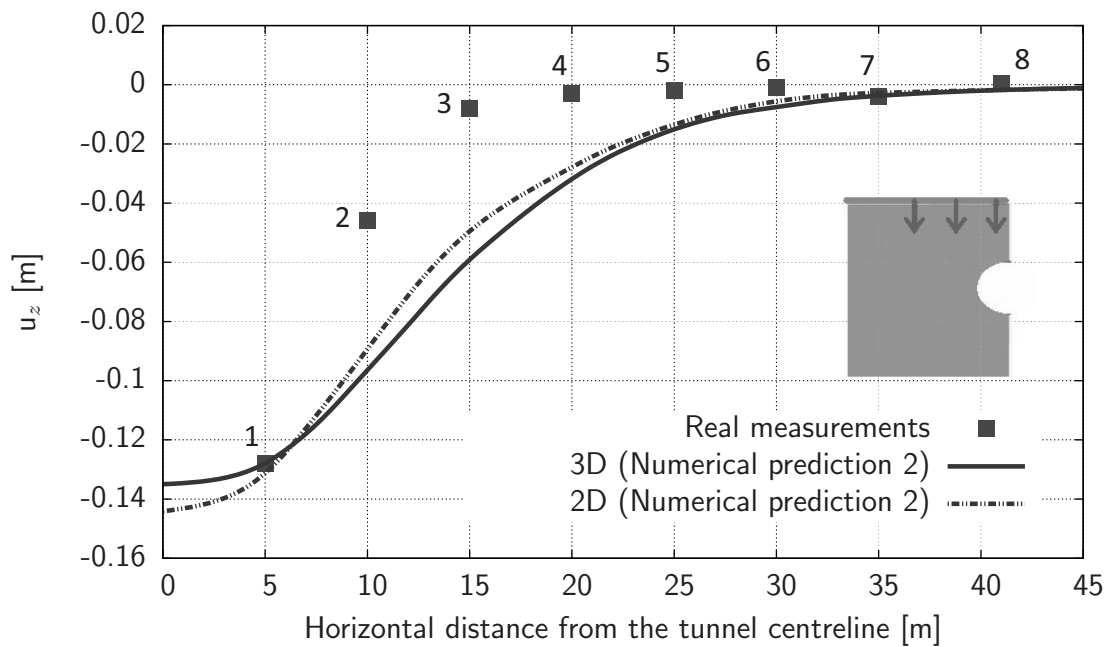
Figure 5.12.: 2D versus 3D numerical prediction. Comparison of the transverse settlement profile (input values of the HSsmall model acc. to Tab. 5.3).

Table 5.4.: Search space of the chosen parameters of the HSsmall model subject of optimization.

	Soil layer	**Parameter**	**Lower bound**	**Upper bound**	
1	clay K1	φ	17	30	[°]
2	sand Z1	φ	30	40	[°]
3	clay K1	E_{oed}^{ref}	15 000	28 000	[kN/m^2]
4	sand Z1	E_{oed}^{ref}	28 000	50 000	[kN/m^2]
5	clay K1	E_{ur}^{ref}	40 000	85 000	[kN/m^2]
6	sand Z1	E_{ur}^{ref}	70 000	150 000	[kN/m^2]

Table 5.5.: PSO parameters used in the back calculation of the Westerschelde Tunnel.

PSO parameters	Value [-]
K_p	15
ω_{max}	0.9
ω_{min}	0.4
c_1	0.5
c_2	1.2
T_{max}	200
Stop	$f(X_k) < 1 \times 10^{-4}$

to the neglecting of the 3D arching effect at the tunnel face which is missing in the present 2D model.

Next, the direct back analysis is applied to the upper two soil layers – the sand (Z1) and the clay (K1) – using the 2D forward model. Based on the results from the sensitivity analysis, the input parameters of the HSsmall model which have been chosen to be optimized are φ, E_{oed}^{ref}, and E_{ur}^{ref}, i.e. totally 6 parameters for the both soil layers. The search space of each of these parameters is presented in Table 5.4. For the dilatancy angle it is used the relation according to Equation 4.30. The empirical relation between the two primary loading E-module according to Equation 4.31 is applied, together with the inequality given with

Equation 4.32. The used input parameters of the PSO are listed in Table 5.5. The two adopted stopping criteria are the chosen minimum value of the objective function $f(X_k)$ and the allowed maximum number of iterations $T_{\max}$, as shown in the same Table 5.5.

Two variants of the back analysis – called PSO-1 and PSO-2 – regarding the definition of the objective function are calculated. In both variants the vertical displacements in points 1, 2, and 3 of the last calculation phase of the 2D model are used (see Fig. 5.12).

- PSO-1: The objective function according to Equation 4.33 is used. No additional weighting factors to the measurements in points 1, 2, and 3 are applied;

- PSO-2: In the objective function – see Equation 5.1 – there are added weighting factors to the three observations, i.e. $w_1 = 1.0$, $w_2 = 0.5$, and $w_3 = 0.4$, respectively for point 1, 2, and 3.

$$f(X) = \frac{1}{N} \sum_{i=1}^{N} \left[w_i \left(y_i^{calc}(X) - y_i^{meas} \right)^2 \right] \tag{5.1}$$

5.1.2.4. Results and Discussion

In Table 5.6 there are summarized the final best values of the performed two identification variants – PSO-1 and PSO-2. In Figure 5.13 there are given the back calculated transverse settlement profile in the 2D simulation of the Westerschelde Tunnel. It is demonstrated that by adding weighting factors in order to make the measurements in point 1 more important the results become better. In Figures 5.14–5.19 it is presented the performance of the identification using variant PSO-2. At the 142th iteration the iterations are stop according to the stop criterion, i.e. reaching the predefined minimum value of the objective function.

Next, the optimized HSsmall model parameters with variant PSO-2 are used back as an input in the 3D model. The results are presented in Figures 5.20 and 5.21. It is shown, that the calculated longitudinal settlements profile is matched well. The calculated transverse settlements profile was improved, however, the width of the settled area is still larger than the measured one. There is a place for further improvements of the simulation. Such an improvement may comes from the change/improvement of the used soil constitutive model for the two upper soil layers K1, and Z1 (e.g. if the anisotropy and destructuration effects plays any role; additional geotechnical survey is needed to clear this question). A major limitation also of the used HSsmall model is the fact that it doesn't reproduce the strain-softening behaviour of the soil with ongoing straining. Additionally, the accuracy of the back analysis may be improved if extra measurements of the ground deformations during

Table 5.6.: Optimized parameters of the HSsmall model after the applied direct back analysis.

Soil Constitutive Parameters for the HSsmall Model						
Before optimization (Numerical prediction 2)		PSO-1 (no weighting)		PSO-2 (with weighting)		
K1	Z1	K1	Z1	K1	Z1	
φ	22	34	17.65	39.96	17.57	38.03	[°]
ψ	0	0	0	9.96	0	8.03	[°]
c	5	6.4	5	6.4	5	6.4	[kN/m^2]
E_{oed}^{ref}	20 000	37 000	16 106.9	33 498.4	25 894.6	34 855.2	[kN/m^2]
E_{50}^{ref}	24 000	35 000	16 106.9	33 498.4	25 894.6	34 855.2	[kN/m^2]
E_{ur}^{ref}	60 000	80 000	78 459.3	74 925.4	78 608.4	80 653.2	[kN/m^2]
G_0^{ref}	150 000	140 000	150 000	140 000	150 000	140 000	[kN/m^2]
$\gamma_{0.7}$	0.0002	0.0002	0.0002	0.0002	0.0002	0.0002	[-]
p^{ref}	100	100	100	100	100	100	[kN/m^2]
m	1.0	0.5	1.0	0.5	1.0	0.5	[-]
R_f	0.90	0.90	0.90	0.90	0.90	0.90	[-]
ν_{ur}	0.20	0.20	0.20	0.20	0.20	0.20	[-]
γ_{unsat}	18	18	18	18	18	18	[kN/m^3]
γ_{sat}	20	19	20	19	20	19	[kN/m^3]
K_0^{nc}	0.69	0.41	0.69	0.41	0.69	0.41	[-]
OCR	1.0	1.0	1.0	1.0	1.0	1.0	[-]

the tunnelling were collected, such as e.g. extensometer and inclinometer measurements of the ground deformations around (above and sidewards) the tunnel circumference (see Section 4.2.1.3.3).
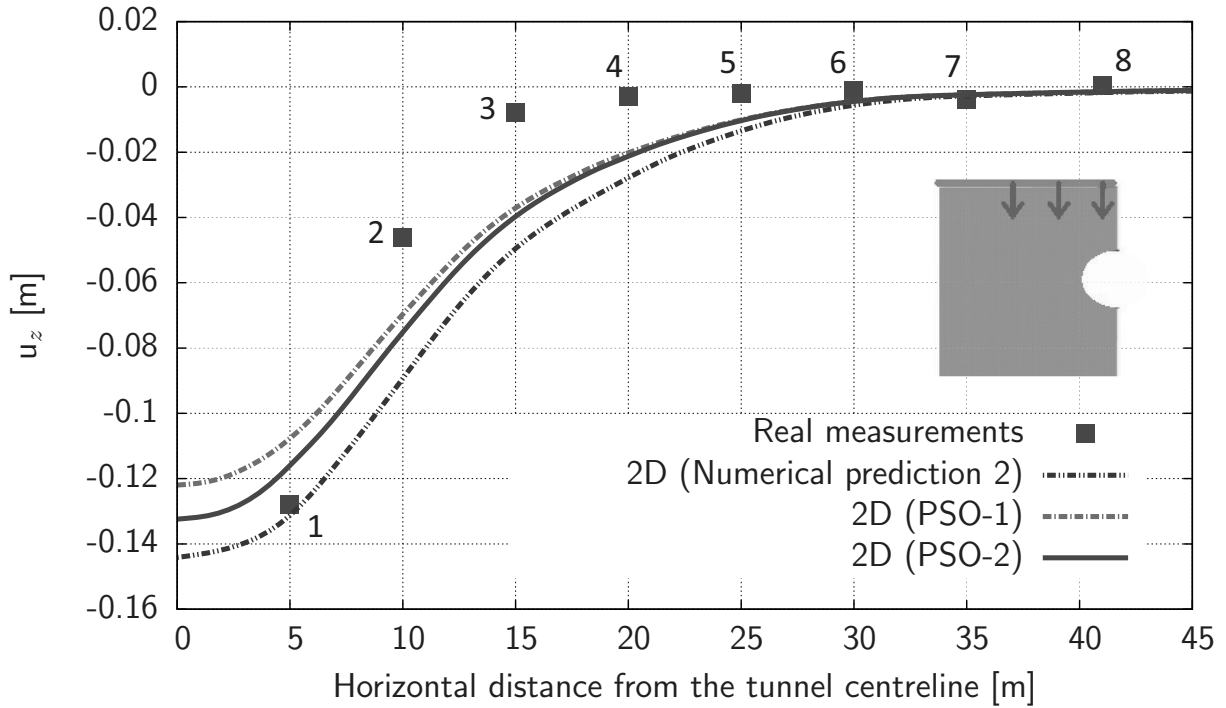
Figure 5.13.: Back calculated transverse settlement profile using the 2D numerical model of the Westerschelde Tunnel.
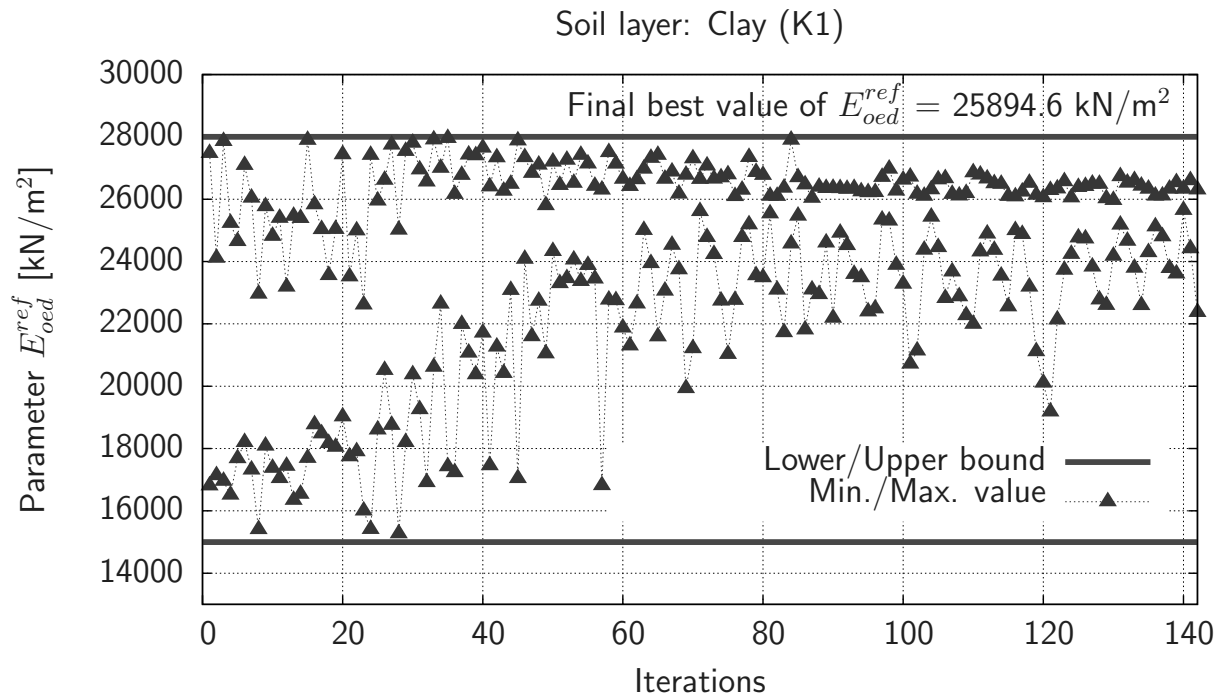
Figure 5.14.: Identification of the soil stiffness for primary loading E_{oed}^{ref} in the clay layer K1 using identification variant PSO-2.
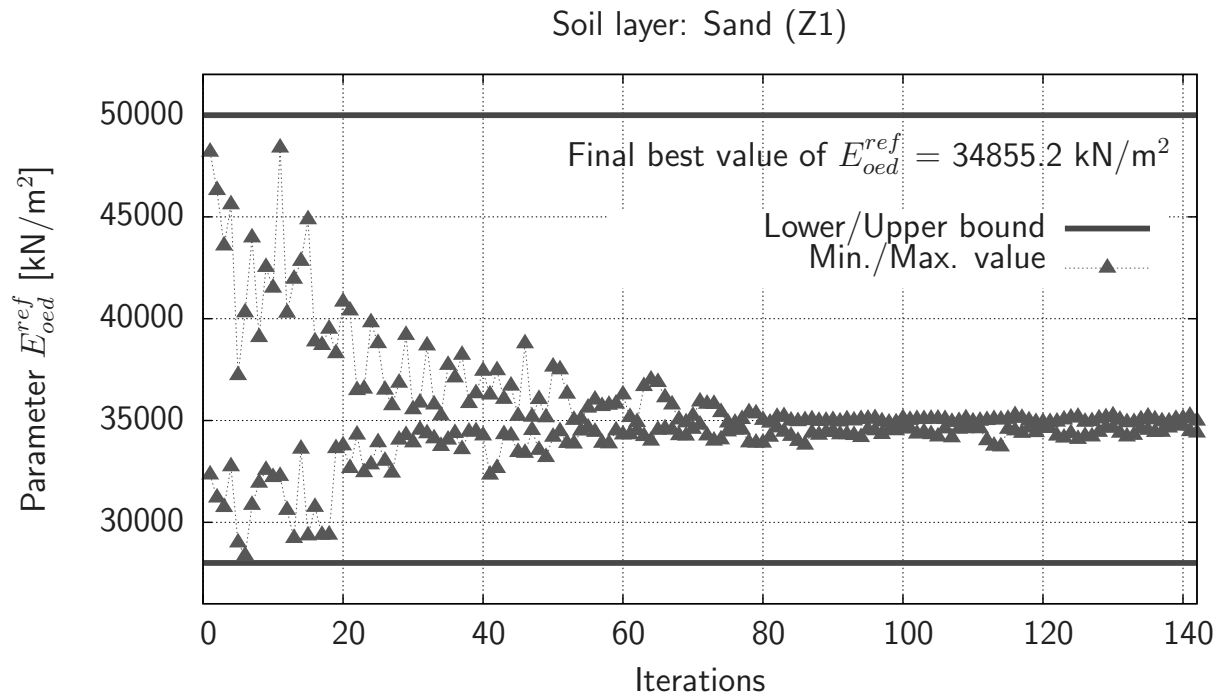
Figure 5.15.: Identification of the soil stiffness for primary loading E_{oed}^{ref} in the sand layer Z1 using identification variant PSO-2.
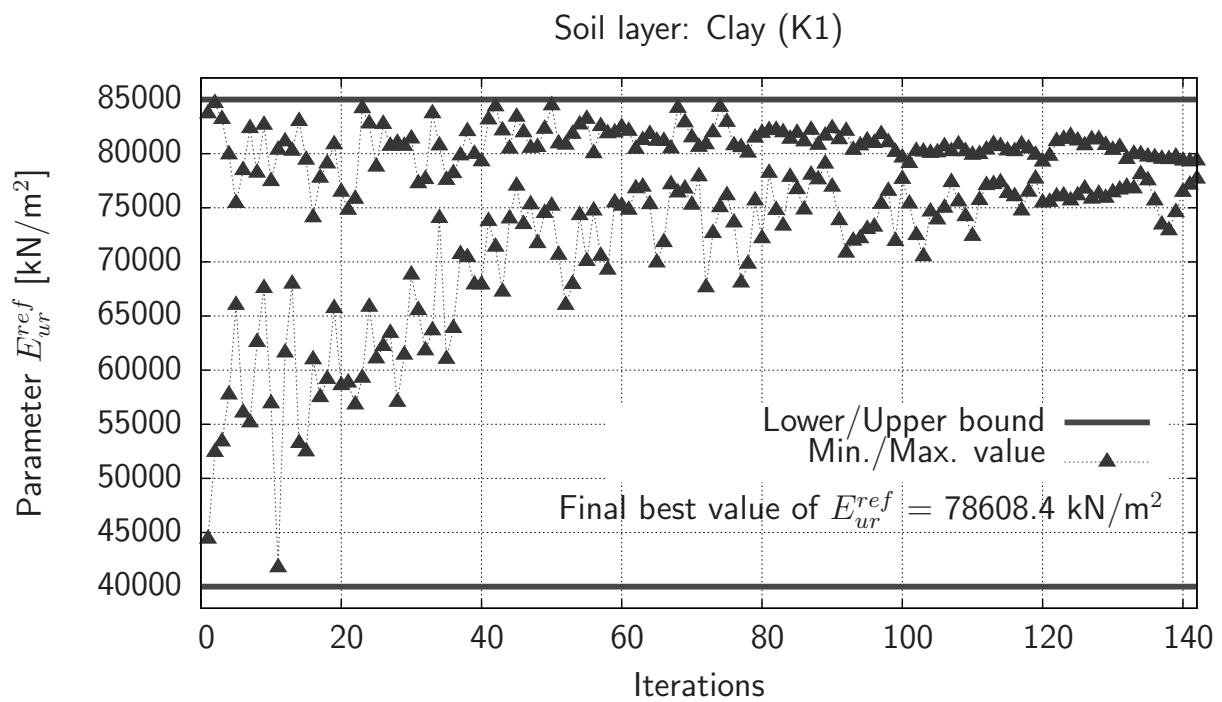
Figure 5.16.: Identification of the soil stiffness for unloading/reloading E_{ur}^{ref} in the clay layer K1 using identification variant PSO-2.

Soil layer: Sand (Z1)
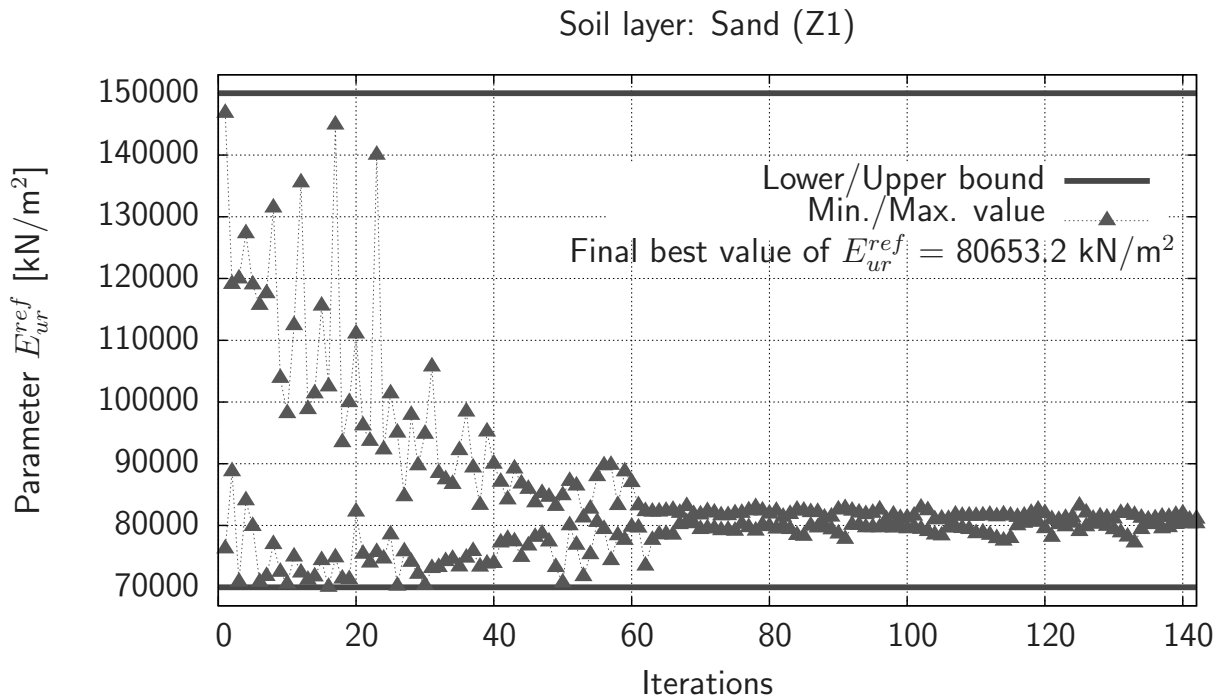
Figure 5.17.: Identification of the soil stiffness for unloading/reloading E_{ur}^{ref} in the sand layer Z1 using identification variant PSO-2.

Soil layer: Clay (K1)
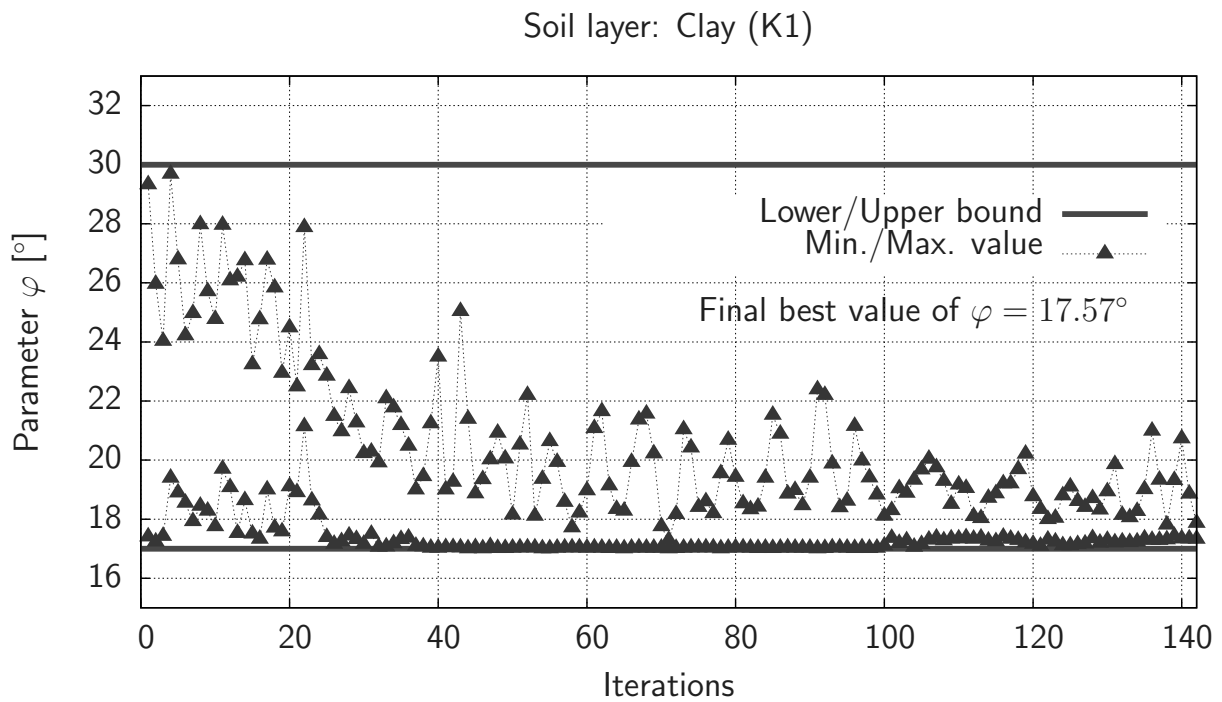
Figure 5.18.: Identification of the soil angle of internal friction φ in the clay layer K1 using identification variant PSO-2.
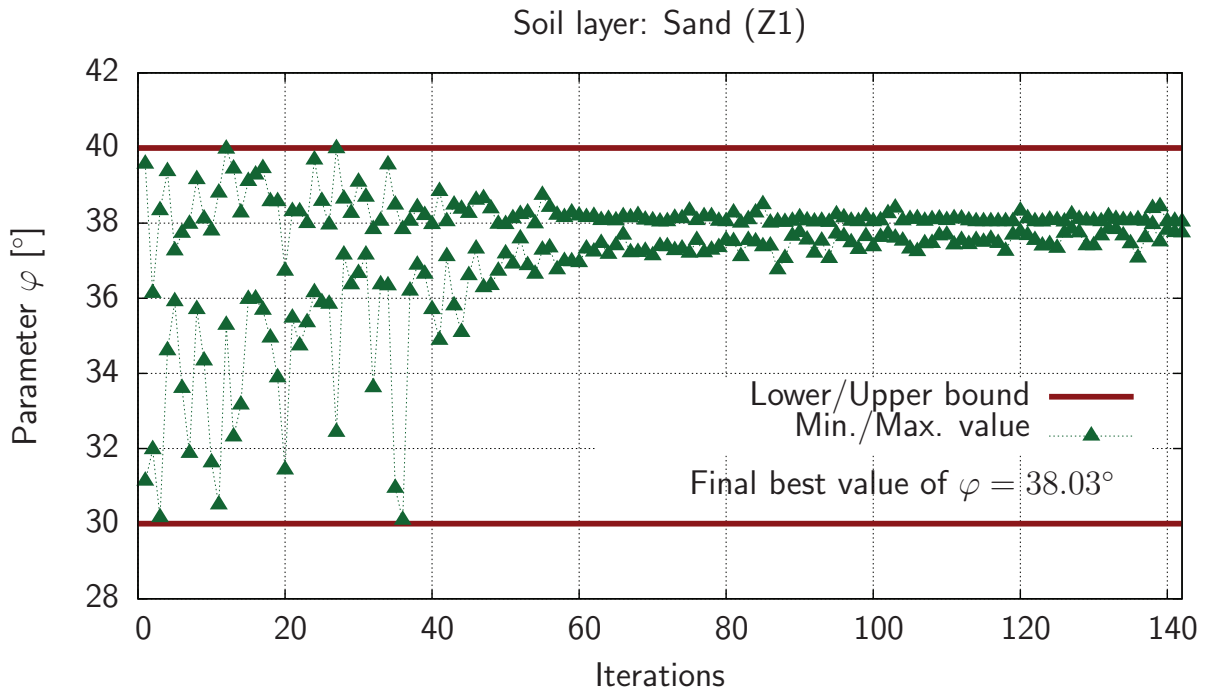
Figure 5.19.: Identification of the soil angle of internal friction φ in the sand layer Z1 using identification variant PSO-2.
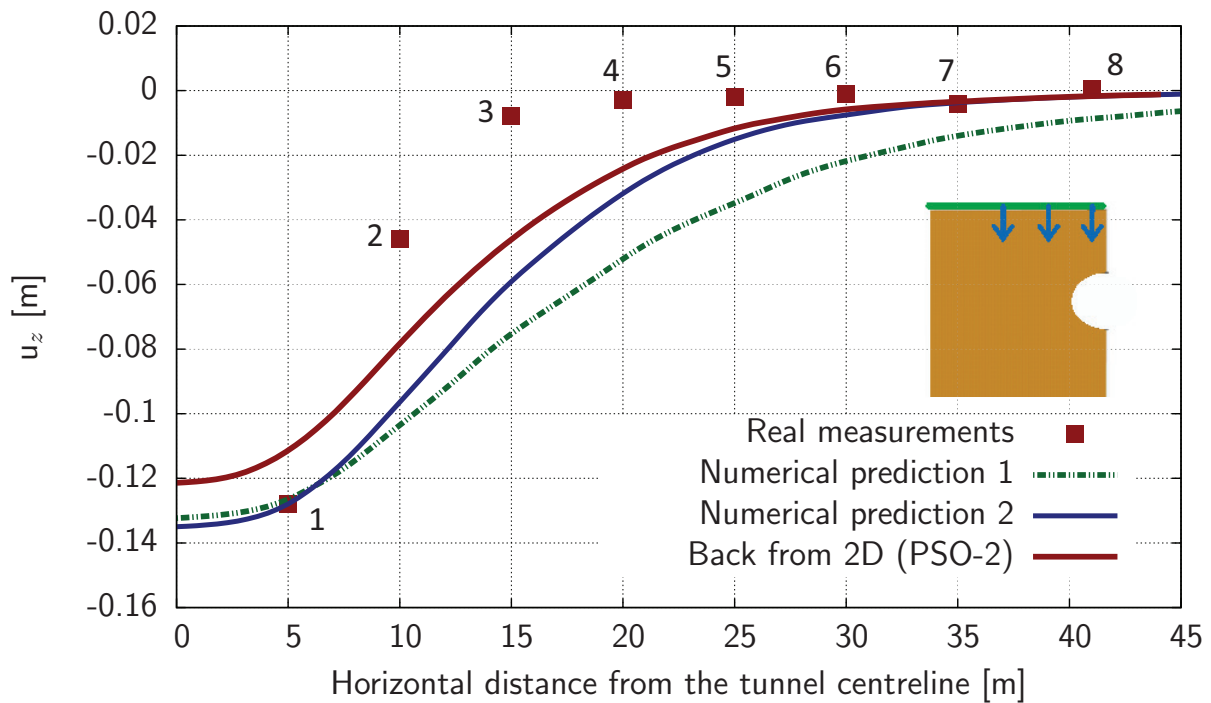
Figure 5.20.: Back calculated transverse settlements on the ground surface in the observation cross-section (see Fig. 5.6) when the TBM is at the 44th excavation stage, i.e. 88 m from the tunnel beginning (3D model).
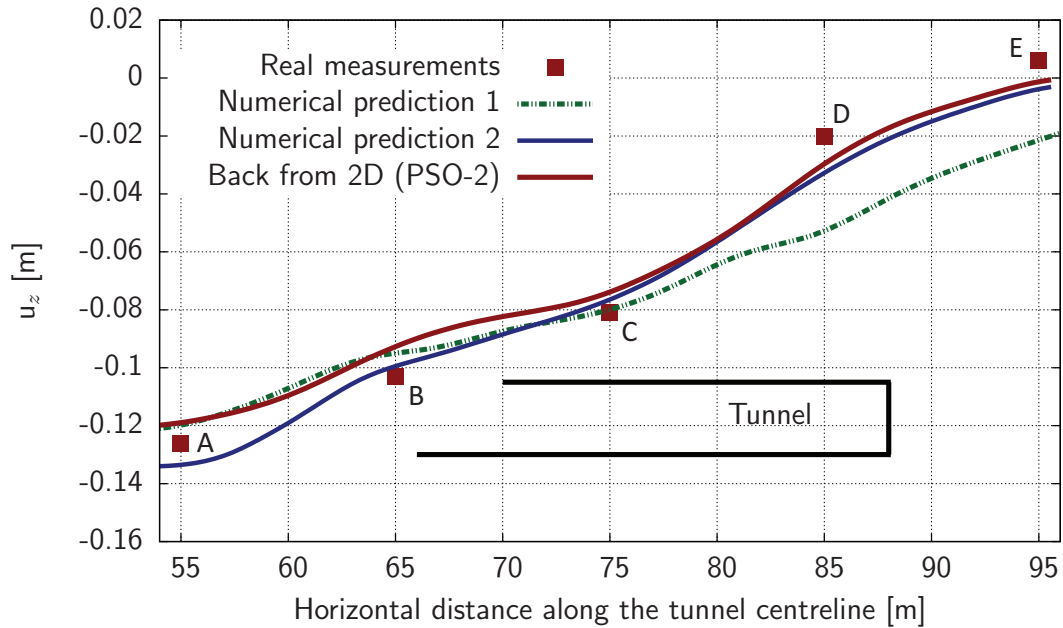
Figure 5.21.: Back calculated longitudinal surface settlements on the ground surface in the observation section (see Fig. 5.6) when the TBM is at the 44th excavation stage, i.e. 88 m from the tunnel beginning (3D model).

The simplest way to check the quality of the fit is the visual control of the disagreements between the real measurements and the numerical predictions (e.g. as it is shown in Fig. 5.20 and 5.21). However, a more detailed quantification of the back calculated results can be done. For doing this the residual plots, or also called $Q - Q$ plots ($''Q''$ stands for quantile), between measurement normalized data $y_i^{meas,norm}$ and numerical simulation normalized data $y_i^{calc,norm}$ are used to assess the goodness of fit of the numerical model. The normalization of the measurements y_i^{meas} and numerical predictions y_i^{calc} is done in the following way:

$$y_i^{meas,norm} = \frac{y_i^{meas}}{\max_i \left(\max \left(y_i^{meas}, y_i^{calc}\right)\right)} \tag{5.2}$$

and

$$y_i^{calc,norm} = \frac{y_i^{calc}}{\max_i \left(\max \left(y_i^{meas}, y_i^{calc}\right)\right)} \tag{5.3}$$

Additionally, the coefficient of determination R^2 is a commonly used estimate on how well the goodness of fit is. This statistical value is defined as:

$$R^2 = 1 - \frac{\sum_{i=1}^{N}(y_i^{meas} - y_i^{calc})^2}{\sum_{i=1}^{N}(y_i^{meas} - \bar{y})^2} \tag{5.4}$$

where

$$\bar{y} = \frac{1}{N} \sum_{i=1}^{N} y_i^{meas}. \tag{5.5}$$

In regression, the R^2 coefficient of determination is a statistical measure of how well the regression line approximates e.g. the real measurement points. Values of R^2 close to unity indicates very little discrepancy between measured and simulated data, i.e. the regression line perfectly fits the real measurement data. Actually, the measure R^2 is derived for linear problems but it is often applied to non-linear problems as well (see e.g. Zadeh 2008).

In Figure 5.22 there are presented the residual plots with respect to the transverse and longitudinal settlements profiles. In the same Figure 5.22, left, it is shown that the transverse settlements profile is not fit perfectly. The calculated coefficient of determination $R^2 = 0.7548$ denotes that only about 75 % of the measurements are represented by the 3D numerical simulation model of the Westerschelde Tunnel (using as input the results obtained in identification variant PSO-2). However, the fit of the longitudinal settlements profile is exelent (see Fig. 5.22, right) with a high value of $R^2 = 0.9755$.
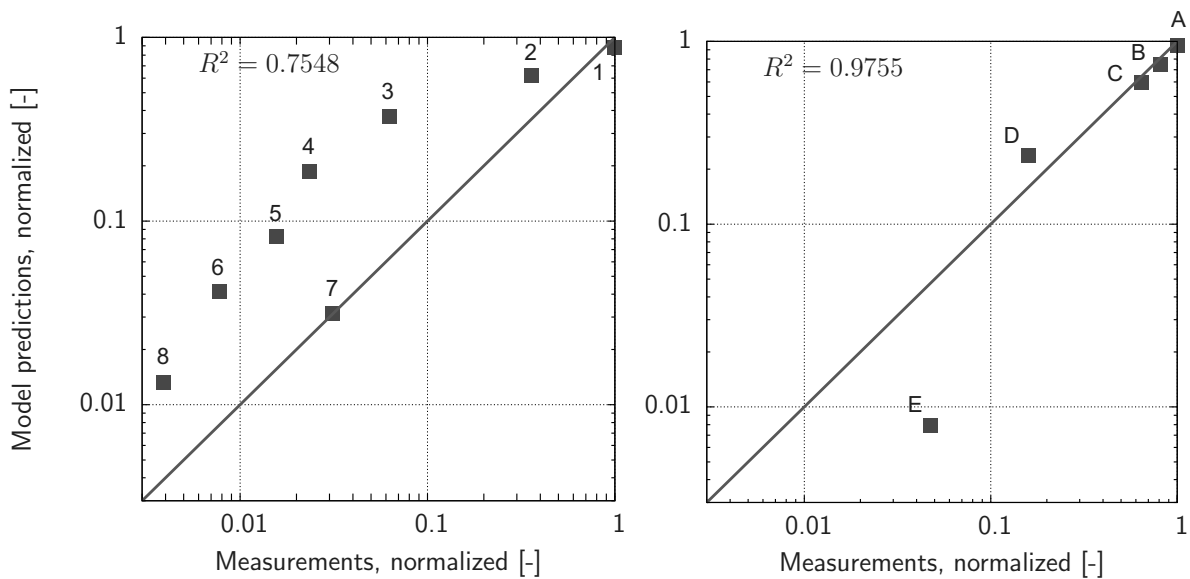
Figure 5.22.: Residual plots: Normalized measurements vs. normalized simulation results (obtained using identification variant PSO-2, see in Fig. 5.20 and 5.21) of the transverse settlements profile (left) and of the longitudinal settlements profile (right).

6. Summary and Conclusions

The primary purpose of the research in the current thesis is to define an adequate numerical model to simulate the tunnel excavation using closed face slurry shield TBM. The created 3D numerical model includes all relevant components of the mechanized tunnelling process like TBM, face support, grouting the annular gap, concrete tunnel lining, sequential advance, soil-tunnel interaction, and have correct mechanical and hydraulic boundary conditions. Next, it is investigated the influence of several of these components on the predicted displacements. Several modelling variants are investigated for the way of modelling the annular gap. It has been shown that the excavation speed in water-saturated ground and the soil hydraulic conductivity have a major influence on the deformations and the settlements on the ground. The higher the excavation speed in a water-saturated ground with enough low hydraulic conductivity, the lower are the surface settlements. Further, a 1D numerical model of the mesoscopic approach elaborated by Schaufler *et al.* (2012b) within the framework of the theory of porous media is used to calculate the soil hydraulic evolution (change) in the ground around the TBM and tunnel due to the support substance. Comparison of the results has shown that there is no meaningful influence coming from considering the hydraulic conductivity evolution.

The defined 3D numerical model is used as a forward model in back calculating the model input parameters of the adopted advanced elastoplastic soil constitutive model. For doing this, first, a derivative based local sensitivity analysis is performed to the main input parameters of the soil model in order to asses the FE model performance. The applicability and accuracy of this type of sensitivity analysis are investigated and discussed. An appropriate step size is selected for calculating the partial derivatives.

Further, for calibration of the input soil constitutive parameters a direct back analysis is carried out using the Particle Swarm Optimizer, minimizing the discrepancy between the numerical predictions and the synthetic measurements. A Design of Experiment is performed, i.e. several scenarios for measurement locations are investigated providing different amount of measurements for the back analysis. It is shown that the amount of measurements is crucial for the accurate and successful model parameter identification.

In the last part of the research the back analysis is applied to a real shallow tunnel project in soft ground – the Westerschelde Tunnel in the Netherlands. Finally, the results are evaluated. The fit of the longitudinal surface settlements profile is excellent, i.e. about 98 % of the measurements are represented by the numerical simulation. However, only about 75 % of the transverse surface settlements profile is represented by the simulation.

7. Outlook

The identification, validation, and adaption of adequate ground models for mechanized tunnel simulation are the objectives of the current thesis. The identification and validation processes have been conducted utilizing back analysis technique. Consequently, a deterministic direct back analysis procedure is performed for identifying the input parameters of the adopted advanced elastoplastic soil constitutive model. In this context, it is also useful probabilistic methods to be applied for the identification process considering the different uncertainties. However, this is done in a parallel by a colleague of the author – Mr. Shorash Miro, who is working on the same project. He has adopted the probabilistic approach in a Bayesian framework (Miro *et al.* (2012b)). In this formulation, the information about ground model parameters, which is obtained from boreholes and field investigations, is represented as a joint Probability Density Function of the parameters. For this purpose, a transformation strategy based on Nataf-Model for transforming the single distributions to a multivariate probability distribution, taking into account the possible correlations between the parameters, has been development (Nataf 1962, Liu 1986). Furthermore, the uncertainty about the field measurements is also modelled by a probability density function. As a result, the combination of the prior knowledge with the likelihood function, which represents the probability of the model for producing the measurements, constitutes the probabilistic solution of the inverse problem. This solution has been successfully sampled and analyzed using Monte Carlo Markov Chain method. The adopted probabilistic approach has been employed for identifying ground model parameters in homogeneous conditions (Miro *et al.* 2012a), as well as for identifying a soil layer change in front of a mechanized tunnel (Miro *et al.* 2013).

Based on the results achieved in the present thesis, new methods for automatic model adaptation can be further developed taking into account on field measurements. This can be done in conjunction with the development of optimal measurement programs. Following methods can be systematically developed to achieve the above-mentioned objectives:

- The validation and adaptation of ground models is carried out by an inverse analysis using results of driving simulations. Normally, the underlying data is involving

207

several uncertainties. Therefore, many runs of the forward FE-model must be performed in order to identify appropriate ground models for mechanized tunnelling. Surrogate models (meta-models) have to be developed by implementing model reduction techniques to minimize the calculation time of the forward model. It is possible to substitute specific parts of the forward computation model in order to construct a hybrid-model. In the hybrid-model the computationally sophisticated parts of the forward model, such as the area around TBM face, are kept without substitution, and the surrounding area will be reduced utilizing a chosen meta-model technique. This hybrid approach is expected to represent a highly accurate meta-model to be used in further studies that require a large number of forward calculations.

- The identification of appropriate ground models is based on using pre-defined ground scenarios. Pattern recognition methods have to be developed to identify specific ground scenarios. Adjusted scenarios can be generated by combining the features of existing or already identified scenarios. In turn, this will be used as a data base for further identification problems. The specification and detection of features and scenarios requires an optimal measurement program.

- The quality of identification and adaptation strongly depends on the available data. For a feature-based detection, the measurement program must be optimized. However, restrictions regarding possible spatial and temporal measurements in mechanized tunnelling need to be considered. Taking into account the uncertainties (constitutive parameters, underground geometry, boundary conditions) innovative concepts should be developed to generate an optimized measurement program. To create an optimal measurement program it has to be investigated which types of data have to be collected during the tunnelling – e.g. displacements (on the ground surface, in the subsoil, of the installed tunnel lining), stresses and pore water pressures in the subsoil, etc. This should be done by taking into account also the cost effectiveness and the technical limitations of such measurements. For each of the pre-defined subsoil scenarios it has to be investigated further:

  - at which fields (i.e. vertical observation cross-sections perpendicular to the tunnel trace) to be situated the observations,

  - at which location in the corresponding cross-section to be placed the observation points, and how many points are optimally needed,

– at which moment to start and finish with the measurement at the points, respectively, whit which frequency (i.e. how often) the data to be recorded, how much is the influence of the noise in the corresponding measurements on the identification accuracy.

At the same hand more precise measurements/calculations (i.e. understanding/ investigations) are needed of the actual support pressures – both face and grout – in the annular and the steering gap, in order to evaluate more accurate how large are the actual volume losses around the tunnel at each moment of time. Only by considering accurately these volume losses it is possible to identify in a reliable way the unknown model parameters.

A. Appendix – Symbols of the Constitutive Parameters in the FE Simulation

γ	Unit wight	[kN/m^3]
γ_{sat}	Unit wight of the fully water saturated soil	[kN/m^3]
γ_{unsat}	Unit wight of the soil with natural humidity	[kN/m^3]
$\gamma_{0.7}$	Level of shear strain at which the secant shear modulus G_s is reduced to about 70 % of G_0 (i.e. $G_s = 0.722G_0$)	[-]
θ	Lode angle (third stress invariant)	[°]
ν	Poisson's ratio	[-]
ν_{ur}	Poisson's ratio for unloading-reloading	[-]
φ	Peak angle of internal friction (effective; for brevity $\varphi = \varphi'$)	[°]
ψ	Angle of dilatancy	[°]
c	Cohesion (effective; for brevity $c = c'$)	[kN/m^2]
d	Thickness of the concrete tunnel lining	[m]
E'	Drained Young's modulus of the soil	[kN/m^2]
E	Young's modulus of the concrete lining and TBM	[kN/m^2]

E_{50}^{ref}	Secant stiffness in standard drained triaxial test	$[kN/m^2]$
E_{oed}^{ref}	Tangent stiffness for primary oedometer loading	$[kN/m^2]$
E_{ur}^{ref}	Unloading / reloading stiffness	$[kN/m^2]$
G_0^{ref}	Shear modulus at very small strains	$[kN/m^2]$
I_1	First stress invariant	$[kN/m^2]$
J_2	Second deviatoric stress invariant	$[(kN/m^2)^2]$
K_0	Coefficient of lateral earth pressure at rest	$[-]$
k_f	Coefficient of permeability (hydraulic conductivity)	$[m/s]$
m	Power for stress-level dependency of stiffness	$[-]$
p^{ref}	Reference stress for stiffnesses	$[kN/m^2]$
p_{active}	Total pore pressures	$[kN/m^2]$
p_{excess}	Excess pore pressures	$[kN/m^2]$
p_{steady}	Steady-state pore pressures	$[kN/m^2]$
q_a	Asymptotic value of the shear strength of the soil	$[kN/m^2]$
q_f	Ultimate deviatoric triaxial stress	$[kN/m^2]$
$R_{\texttt{inter}}$	Strength reduction factor for interfaces in PLAXIS	$[-]$
R_f	Failure ratio q_f/q_a	$[-]$

References

Anagnostou, G., and K. Kovári (1994), *The Face Stability of Slurry-Shield-Driven Tunnels*, Tunnelling & Underground Space Technology, Vol. 9, No. 2, pp. 165-174.

Anagnostou, G., and K. Kovári (1996a), *Face Stability Conditions with Earth Pressured Balanced Shields*, Tunnelling & Underground Space Technology, Vol. 11, No. 2, pp. 165-173.

Anagnostou, G., and K. Kovári (1996b), *Face Stability in Slurry and EPB Shield Tunneling*, Proc. of the International Simosium Geotechnical Aspects of Underground Construction in Soft Ground, pp. 453-458, London, 15-17 April.

Anagnostou G. (2007), *The One-Step Solution of the Advancing Tunnel Heading Problem*, EURO:TUN 2007, 1st International Conference on Computational Methods in Tunnelling, Vienna, 27-29 August.

Anagnostou, G. (2008), *The Effect of Tunnel Advance Rate on the Surface Settlements*, 12th International Conference of International Association for Computer Methods and Advances in Geomechanics, Goa, India, pp. 892-899, 1-6 October.

Atkinson, J.H., and G. Sallfors (1991), *Experimental Determination of Soil Properties*, Proc. of the 10th EC on SMFE, Vol. 3, pp. 915-956, Florence, Italy.

Babendererde, S. (1999), *Grouting the Shield Tail Gap*, Tunnel & Tunnelling International, No. 11, pp. 48-49.

Bakker, K.J., E.A.H. Teunissen, P. van den Berg, and M.Th.J.H. Smith (2003), *K100, Research at the Second Heinenoord Tunnel*, Proc. of the ITA Conference – Reclaiming Underground Space, Amsterdam, The Netherlands.

Beer, G. (editor) (2003), *Numerical Simulation in Tunnelling*, Springer, 477 p. ISBN: 3-211-00515-3

Benz, T. (2007), *Small-Strain Stiffness of Soils and its Numerical Consequences*, PhD Thesis, Universität Stuttgart, Germany.

Benz, T., R. Schwab, and P. Vermeer (2009), *Small-strain stiffness in geotechnical analyses*, Bautechnik Special issue 2009 – Geotechnical Engineering, Vol. 86, pp. 16-27. DOI: 10.1002/bate.200910038

Benz, T., M. Wehnert, and P.A. Vermeer (2008), *A Lode Angle Dependent Formulation of the Hardening Soil Model*, Proc. of the 12th International Conference of International Association for Computer Methods and Advances in Geomechanics (IACMAG), Goa, India, October.

Bezuijen, A. (2013), *Modelling of Foam-Sand-TBM Interaction*, Proc. of the EURO:TUN 2013: 3rd International Conference on Computational Methods in Tunnelling and Subsurface Engineering, Ruhr University Bochum, Germany, pp. 675-686, 17-19 April.

Bezuijen A. (2009), *The Influence of Grout and Bentonite Slurry on the Process of TBM Tunnelling*, Geomechanics and Tunnelling, Vol. 2, No. 3, pp. 294-303.

Bezuijen A. (2007), *Bentonite and Grout Flow Around a TBM*, Proc. ITA 2007, Prague.

Bezuijen A., and W.H. van der Zon (2007), *Volume Changes in Grout Used to Fill up the Tail Void*, Proc. ITA 2007, Prague.

Bezuijen A., J.F.W. Joustra, A.M. Talmon, and B. Grote (2005), *Pressure Gradients and Muck Properties at the EPB Face*, Tunnels & Tunnelling International, No. 12, pp. 14-17.

Bezuijen A., and A.M. Talmon (2006), *Grout Pressure Around a Tunnel Lining, Influence of Grout Consolidation and Loading on Lining*, Tunnelling. A Decade of Progress. GeoDelft 1995-2005 (edited by H. van Lottum and A. Bezuijen), pp. 109-114, Taylor & Francis. DOI: 10.1201/9781439834268.ch16

Bezuijen A., and A.M. Talmon (2003), *Grout, the Foundation of a Bored Tunnel*, Proc. of the Internal Conference on Foundations "Innovations, Observations, Design & Practise" (ICOF Dundee), Thomas Telford, London.

Bezuijen A. (2002), *Consolidation of Grout. Elements Tests*, GeoDelft Report 403050/3, 10 p.

Biot M.A. (1941), *General Theory of Three-Dimensional Consolidation*, Journal of Applied Physics, Vol. 12, No. 2, pp. 155-164.

Biot M.A. (1956), *General Solutions of the Equations of Elasticity and Consolidation for a Porous Material*, Journal of Applied Mechanics, 23 (2), pp. 91-96.

Blom, C.B.M., E.J. van der Horst, and P.S. Jovanovic (1999), *Three-dimensional Structural Analyses of the Shield-Driven "Green Heart" Tunnel of the High-Speed Line South*, Tunnelling and Underground Space Technology, Vol. 1, No. 2, pp. 217-224.

Blom, C.B.M. (2002), *Design Philosophy of Concrete Linings in Soft Soils*, PhD Thesis, Delft University, The Netherlands. ISBN 90-407-2366-4

de Boer, R. (2000), *Theory of Porous Media: Highlights in Historical Development and Current State*, Springer, 634 p. ISBN-13: 9783642640629

Bolton, M.D. (1986), *The Strength and Dilatancy of Sands*, Geotechnique, Vol. 36, No. 1, pp. 65-78.

Bosshard, M., H.-R. Müller, K. Kovari, and J. Bolliger (2001), *Zimmerberg Base Tunnel: Findings with the Hydro-Shield Drive in Greatly Varying Subsoil*, Proc. of the STUVA Conference 2001, Munich, pp. 45-51. ISBN: 3-980-3390-7-6.

Boubou, R., F. Emeriault, and R. Kastner (2008), *Correlation Between TBM Parameters and Ground Surface Settlements, Neural Network Method*, ISSMGE TC 28, Budapest, Hungary: presentation slides, 12-13 September. Source: `http://issmge-tc28-hungary. net/download/Presentations/II_2_Richard_Kastner_presentation.pdf`

Brassinga, H.E., and A. Bezuijen (2005), *Modelling the Grouting Process Around a Tunnel Lining in a Geotechnical Centrifuge*, In A. Bezuijen & H. van Lottum (eds.): Tunnelling – A Decade of Progress (GeoDelft 1995-2005), pp. 71-75, Taylor & Francis, London, UK. DOI: 10.1201/9781439834268.ch11

Brinkgreve, R.B.J. (2005), *Selection of Soil Models and Parameters for Geotechnical Engineering Application*, In Goetechnical special publication, No. 128, J.A. Yamamuro & V.N. Kaliakin (Eds.), Soil Constitutive Models – Evaluation, Selection, and Calibration, ASCE, pp. 69-98, Austin, Texas.

Brinkgreve, R.B.J., E. Engin, and W.M. Swolfs (2011a), *PLAXIS 3D Version 2011, Material Models Manual*, Plaxis bv, Delft, The Netherlands.

Brinkgreve, R.B.J., E. Engin, and W.M. Swolfs (2011b), *PLAXIS 3D Version 2011, Reference Manual*, Plaxis bv, Delft, The Netherlands.

Brinkgreve, R.B.J., E. Engin, and W.M. Swolfs (2011c), *PLAXIS 3D Version 2011, Scientific Manual*, in Point 2. Deformation Theory, Plaxis bv, Delft, The Netherlands.

Brinkgreve, R.B.J., K.J. Bakker, and P.G. Bonnier (2006), *The Relevance of Small-Strain Soil Stiffness in Numerical Simulation of Excavation and Tunnelling Projects,*

In H.F. Schweiger (ed.): Numerical Methods in Geotechnical Engineering; Sixth European Conference on Numerical Methods in Geotechnical Engineering (Graz, Austria, 6-8 September 2006), pp. 133-139, London, UK, Taylor & Francis. DOI: 10.1201/9781439833766.ch19

Brinkgreve, R.B.J., and E. Engin (2013), *Validation of Geotechnical Finite Element Analysis* , Proceedings of the 18-th International Conference on Soil Mechanics and Geotechnical Engineering (18th ICSMGE), pp. 677-682, 2-7 September, Paris, France.

Brodeßer, M. (2012), *Adäquates Simulationsmodell zur numerischen Analyse maschineller Tunnelvortriebe am Beispiel des Westerscheldetunnels*, bachelor thesis, Chair for Foundation Engineering, Soil and Rock Mechanics, Ruhr-Universität Bochum, Germany.

Bui, H.G., J. Stascheit, and G. Meschke (2013), *A Parallel Block Preconditioner for Coupled Simulations of Partially Saturated Soils in Finite Element Analyses*, In: P. Ivanyi, and B. H. V. Topping (eds.), Proc. of the Third International Conference on Parallel, Distributed, Grid and Cloud Computing for Engineering, Civil-Comp Ltd., paper 24, Hungary, 25-27 March. DOI: 10.4203/ccp.101.24

Burland, J.B. (1989), *Ninth Laurits Bjerrum Memorial Lecture: "Small is Beautiful" – the Stiffness of Soils at Small Strains*, Canadian Geotechnical Journal, Vol. 26, No. 4, pp. 499-516.

Buljak, V. (2010), *Proper Orthogonal Decomposition and Radial Basis Functions Algorithm for Diagnostic Procedure Based on Inverse Analysis*, publ. by Faculty of Mechanical Engineering FME Transactions, University of Belgrade, Serbia, Vol. 38, No. 3, pp. 129-136.

Buljak, V. (2012), *Inverse Analysis with Model Reduction: Proper Orthogonal Decomposition in Structural Mechanics*, Springer, 204 p. ISBN: 978-3-642-22702-8, DOI: 10.1007/978-3-642-22703-5.

Clayton, C.R.I. (2011), *Stiffness at Small Strain: Research and Practice*, Geotechnique, Vol. 61, No. 1, pp. 5-37. DOI: 10.1680/geot.2011.61.1.5.

Clerc, M., and J. Kennedy (2002), *The Particle Swarm-Explosion, Stability, and Convergence in a Multidimensional Complex Space*, IEEE Transactions on Evolutionary Computation, Vol. 6, No. 1, pp. 58-73.

Cividini, A., L. Jurina, and G. Gioda (1981), *Some Aspects of 'Characterization' Problems in Geomechanics*, International Journal of Rock Mechanics and Mining Sciences &

Geomechanics Abstracts, Vol. 18, No. 6, pp. 487-503. DOI: 10.1016/0148-9062(81)90513-1.

Campolongo, F., J. Cariboni, and A. Saltelli (2007), *An Effective Screening Design for Sensitivity Analysis of Large Models*, Environmental Modelling and Software, Vol. 22, pp. 1509-1518.

Cao, T.B., K. Chmelina, J. Stascheit, and G. Meschke (2013), *Enhanced Monitoring and Simulation Assisted Tunnelling (EMSAT)*, Proc. of the EURO:TUN 2013: 3rd International Conference on Computational Methods in Tunnelling and Subsurface Engineering, Ruhr University Bochum, Germany, pp. 41-50, 17-19 April.

Curtis, A.R., and J.K. Ried (1974), *The Choice of Step Lengths When Using Differences to Approximate Jacobian Matrices*, J. Inst. Maths. Applics., Vol. 13, pp. 121-126.

Dadvand P., R. Rossi, and E. Oñate (2008), *A Framework for Developing Finite Element Codes for Multi-disciplinary Applications*, Proc. of the 8th World Congress on Computational Mechanics (WCCM8), Venice, Italy, June 30 - July 5.

Dias, D., R. Kastner, and M. Maghazi (2000), *Three Dimensional Simulation of Slurry Shield Tunnelling*, In: O. Kusakabe, K. Fujita, Y. Miyazaki (Eds.), Geotechnical Aspects of Underground Construction in Soft Ground, pp. 351-356, Balkema, Rotterdam.

Dimov, I., and R. Georgieva (2010), *Monte Carlo Algorithms for Evaluating Sobol' Sensitivity Indices*, Mathematics and Computers in Simulation, Vol. 81, No. 3, pp. 506-514. DOI: 10.1016/j.matcom.2009.09.005

Do, N.A., D. Dias, P. Oreste, and I. Djeran-Maigre (2013), *3D Modelling for Mechanized Tunnelling in Soft Ground – Influence of the Constitutive Model*, American Journal of Applied Sciences, Vol. 10, No. 8, pp. 863-875. DOI: 10.3844/ajassp.2013.863.875

Duncan, J.M., and C-Y. Chang (1970), *Nonlinear Analysis of Stress and Strain in Soils*, Journal of the Soil Mechanics and Foundations Division, Proc. of the ASCE, Vol. 96 (SM 5), pp. 1629-1653, September.

Duncan, J.M., P. Byrne, K.S. Wong, and P. Mabry (1980), *Strength, Stress-Strain and Bulk Modulus Parameters for Finite Element Analysis of Stresses and Movements in Soil Masses*, Report No. UCB/GT/80-01, College of Engineering, Office of Research Services, University of California, Berkeley, August.

Eberhart, R.C., and J. Kennedy (1995), *A New Optimizer Using Particle Swarm Theory*, Proc. of the 6th International Symposium on Micro Machine and Human Science, Nagoya, Japan, pp. 39-43, October 4-6.

Eberhart, R.C., P.K. Simpson, and R.W. Dobbins (1996), *Computational Intelligence PC Tools*, 1st edition Boston, MA: Academic Press Professional, 464 p.

Eberhart, R.C., and Y. Shi (1998), *Comparison Between Genetic Algorithms and Particle Swarm Optimization*, Evolutionary Programming VII: Proc. of the Seventh Annual Conference on Evolutionary Programming, San Diego, CA, pp. 611-616.

Ehlers W., and J. Bluhm (2002), *Porous Media: Theory, Experiments and Numerical Applications* Springer, 459 p. ISBN-10: 3540437630; ISBN-13: 978-3540437635

Fieldsend, J.E., and S. Singh (2002), *A Multi-Objective Algorithm based upon Particle Swarm Optimisation, an Efficient Data Structure and Turbulence*, Proc. of the 2002 U.K. Workshop on Computational Intelligence, Birmingham, UK., pp. 37-44.

Fourie, P.C., and A.A. Groenwold (2002), *The Particle Swarm Optimization Algorithm in Size and Shape Optimization*, Structural and Multidisciplinary Optimization, Vol. 23, No. 4, pp. 259-267, May.

Franzius, J.N. (2003), *Behaviour of Buildings due to Tunnel Induced Subsidence*, Doctoral thesis, Department of Civil and Environmental Engineering, Imperial College London, UK.

Galvan, A., and F. Pena (2013), *Structural Behaviour of Segmented Tunnels taking into Account the Interaction between Rings*, Proc. of the EURO:TUN 2013: 3rd International Conference on Computational Methods in Tunnelling and Subsurface Engineering, Ruhr University Bochum, Germany, pp. 183-190, 17-19 April.

Gill, E.P., W. Murray, and M.H. Wright (1989), *Practical Optimization*, 8th Edition, Academic Press, Inc.

Gill, E.P., W. Murray, M.A. Saunders, and M.H. Wright (1983), *Computing Forward-Difference Intervals for Numerical Optimization*, SIAM J. Sci. and Stat. Comp., Vol. 4, No. 2, pp. 310-321.

Gioda, G., and G. Swoboda (1999), *Developments and Applications of the Numerical Analysis of Tunnels in Continuous Media*, International Journal for Numerical and Analytical Methods in Geomechanics, Vol. 23, No. 13, pp. 1393-1405.

Graham, J., and G.T. Houlsby (1983), *Anisotropic Elasticity of Natural Clay*, Geotechnique, Vol. 32, No. 2, pp. 165-180.

Grimm, K. (2002), *Tunneling and Compressed Air - New Innovations. The Westerschelde Tunnel: Saturation Diving*, British Tunneling Society, Proc. of the 2nd International

Conference on Engineering and Health in Compressed Air Work, pp. 125-136, Oxford, 25-27 September.

Haftka, R.T., and Z. Gardal (1992), *Elements of Structural Optimization*, in Chapter 7: Sensitivity of Discrete Systems, 3rd Edition, Kluwer Publishers.

Hardin, B.O., and V.P. Drnevich (1972), *Shear Modulus and Damping in Soils: Measurement and Parameter Effects*, Proc. of ASCE: Journal of the Soil Mechanics and Foundation Division, Vol. 98, No. SM7, pp. 667-692.

He, S., Q.H. Wu, J.Y. Wen, J.R. Saunders, and R.C. Paton (2004), *A Particle Swarm Optimizer With Passive Congregation*, BioSystems, Vol. 78, No. 1-3, pp. 135-147.

Hejazi, Y., D. Dias, and R. Kastner (2008a), *Impact of Constitutive Models on the Numerical Analysis of Underground Constructions*, Acta Geotechnica, Vol. 3, pp. 251-258. DOI 10.1007/s11440-008-0056-1

Hejazi, Y., D. Dias, and R. Kastner (2008b) *Elastoplastic Soil Models for Numerical Analysis of Underground Constructions*, Proc. of the 12th International Conference of the International Association for Computer Methods and Advances in Geomechanics (IACMAG), Goa, India, 1-6 October.

Hill, M.C., and C. R. Tiedeman (2007), *Effective Groundwater Model Calibration: With Analysis of Data, Sensitivities, Predictions, and Uncertainty*, ISBN-13: 978-0-471-77636-9, John Wiley & Sons, Hoboken, N.J., 464 p.

Hill, M.C. (1998), *Methods and Guidelines for Effective Model Calibration*, U.S. Geological Survey Water-Resources Investigations Report 98-4005. US Geological Survey, Denver, Colorado.

Homma, T., and A. Saltelli (1996), *Importance Measures in Global Sensitivity Analysis of Model Output*, Reliability Engineering and System Safety, Vol. 52, pp. 1-17.

Houlsby, G.T., and C.P. Wroth (1991), *The Variation of the Shear Modulus of a Clay with Pressure and Overconsolidation Ratio*, Soils and Foundations, Vol. 31, No. 3, pp. 138-143.

Iott, J., R.T. Haftka, and H.M. Adelman (1985), *Selecting Step Size in Sensitivity Analysis by Finite Differences*, NASA TM-86382.

Itasca Consulting Group, Inc. (2009), *FLAC – Fast Lagrangian Analysis of Continua*, Version 4.0, User's Manual, Minneapolis, USA.

Jaky, J. (1948), *Earth Pressure in Silos*, Proc. of the Second International Conference on Soil Mechanics and Foundation Engineering - ICSMFE, London, Vol.1, pp. 103-107.

Janbu, N. (1963), *Soil Compressibility as Determined by Oedometer and Triaxial Tests*, Proc. of the 3rd European Conference on Soil Mechanics and Foundation Engineering, Vol. 1, (ECSMFE), Wiesbaden, pp. 19-25.

Jardine, R.J., D.M. Potts, A.B. Fourie, and J.B. Burland (1986), *Studies of the Influence of Non-Linear Stress-Strain Characteristics in Soil-Structure Interaction*, Geotechnique, Vol. 36, No. 3, pp. 377-396.

Javadi, A.A., R. Farmani, and T.P. Tan (2005), *A Hybrid Intelligent Genetic Algorithm*, Advanced Engineering Informatics, Vol. 19, No. 4, pp. 255-262.

Javadi, A.A., T.P. Tan, and M. Zhang (2003), *Neural Network for Constitutive Modelling in Finite Element Analysis*, Computer assisted Mechanics and Engineering Sciences, Vol. 10, pp. 523-529.

Javadi, A.A., M. Zhang, and T.P. Tan (2002), *Neural Network for Constitutive Modelling of Material in Finite Element Analysis*, Proc. of the 3rd International Workshop/Euroconference on Trefftz Method, University Of Exeter, UK, 16-18 September.

Kappen, J.M.J., G. Giardina, M.A.N. Hendriks, and J.G. Rots (2013), *3D Numerical Analysis of Tunnelling Induced Damage: the Influence of the Alignment of a Masonry Building with the Tunnel Axis*, Proc. of the EURO:TUN 2013: 3rd International Conference on Computational Methods in Tunnelling and Subsurface Engineering, Ruhr University Bochum, Germany, pp. 467-474, 17-19 April.

Kasper, T. (2004), *Finite Elemente Simulation maschineller Tunnelvortriebe in wassergesättigtem Lockergestein*, (in German), PhD Thesis, Chair for Static and Dynamic, Ruhr-Universität Bochum, Germany.

Kasper, T., and G. Meschke (2006a), *A Numerical Study of the Effect of Soil and Grout Material Properties and Cover Depth in Shield Tunnelling*, Computers and Geotechnics, Vol. 33, pp. 234-247.

Kasper, T., and G. Meschke (2006b), *On the Influence of Face Pressure, Grouting Pressure and TBM Design in Soft Ground Tunnelling*, Tunnelling and Underground Space Technology, Vol. 21, pp. 160-171.

Kasper, T., and G. Meschke (2004), *A 3D Finite Element Simulation Model for TBM Tunnelling in Soft Ground*, International Journal for Numerical and Analytical Methods in Geomechanics, Vol. 28, pp. 1441-1460.

Kasper, T., and G. Meschke (2005), *Numerische Untersuchungen zu den Wechselwirkungen bei Schildvortrieben im Lockergestein*, Bauingenieur, Vol. 80, pp. 413-421.

Kavvadas M. (2003), *Monitoring and Modelling Ground Deformations during Tunnelling*, Proc. of the 11th Int. Symposium on Deformation Measurements, Santorini-Greece, pp. 371-390, Published by the Dept. of Civil Engineering, University of Patras, May.

Kennedy, J., and R.C. Eberhart (1995), *Particle Swarm Optimization*, Proc. of IEEE International Conference on Neural Networks, Vol. 4, pp. 1942-1948.

Kennedy, J. (1997), *The Particle Swarm: Social Adaptation of Knowledge*, Proc. of IEEE International Conference on Evolutionary Computation, Indianapolis, pp. 303-308.

Kennedy, J. (2000), *Stereotyping: Improving Particle Swarm Performance With Cluster Analysis*, Proc. of the IEEE Congress on Evolutionary Computation (CEC 2000), Vol. 2, San Diego, CA., pp. 1507-1512.

Khaledi, K. (2012), *Methods of Model Approximation for Mechanized Tunnel Simulation*, Master thesis, Chair for Foundation Engineering, Soil and Rock Mechanics, Ruhr-Universität Bochum.

Khaledi, K., M. Shorash, and T. Schanz (2012), *Application of Metamodeling techniques for Mechanized Tunnel Simulation*, Proc. of the Int. Scient. Conf. on Mechanics (MECH2012), Bulgarian Academy of Sciences, Sofia, Bulgaria.

Koiter, W.T. (1960), *General Theorems for Elastic-Plastic Solids*, In: Progress in Solid Mechanics, Vol. 6, ed. 1, J.N. Sneddon & R. Hill (eds.), Amsterdam: North-Holland Publ.

Komiya, K., K. Soga, H. Akagi, T. Hagiwara, and M.D. Bolton (1999), *Finite Element Modeling of Excavation and Advancement Processes of a Shield Tunnelling Machine*, Soils and Foundations, Vol. 39, No. 3, pp. 37-52.

Komiya, K. (1999), *FE Modelling of Excavation and Operation of a Shield Tunnelling Machine*, Geomechanics and Tunnelling, Vol. 2, No. 3, pp. 199-208.

Kondner, R.L., and J.S. Zelasko (1963), *A Hyperbolic Stress-Strain Formulation for Sands*, Proc. of the 2nd Panamerican Conference of Soil Mechanics and Foundation Engineering (CSMFE), Vol. 1, pp. 289-324, Sao Paolo, Brazil.

Kondner, R.L. (1963), *Hyperbolic Stress-Strain Response: Cohesive Soils*, Journal of Soil Mechanics and Foundation Division, Proc. of the ASCE, Vol. 89, pp. 115-143.

Kuszyk, R., and A. Sieminska-Lewandowska (2013), *Back Analysis of Blow Out in Warsaw Project*, Proc. of the EURO:TUN 2013: 3rd International Conference on Compu-

tational Methods in Tunnelling and Subsurface Engineering, Ruhr University Bochum, Germany, pp. 889-, 17-19 April.

Lo Presti, D.C.F., M. Jamiolkowski, O. Pallara, and A. Cavallaro (1996), *Rate and Creep Effect on the Stiffness of Soils*, Proc. of the ASCE, Geotechnical Engineering Division, "*Measuring and Modelling Time Dependent Soil Behaviour*" (edited by T.C. Sheahan and V.N. Kaliakin), Geotechnical Special Publication No. 61, pp. 166-180.

Li, Z., K. Soga, X. Bian, and P. Wright (2013), *Ovalisation of Cast-iron Bolted Tunnels and their Modelling*, Proc. of the EURO:TUN 2013: 3rd International Conference on Computational Methods in Tunnelling and Subsurface Engineering, Ruhr University Bochum, Germany, pp. 871-878, 17-19 April.

Liu, P.-L., and A. Der Kiureghian (1986), *Multivariate Distribution Models With Prescribed Marginals and Covariances*, Probabilistic Engineering Mechanics, Vol. 1, pp. 105-112.

Løvbjerg, M., T.K. Rasmussen, and T. Krink (2001), *Hybrid Particle Swarm Optimiser with Breeding and Subpopulations*, Proceedings of the Genetic and Evolutionary Computation Conference (GECCO 2001), San Francisco, USA, July.

Lyness, J.N., and C.B. Moler (1967), *Numerical Differentiation of Analytic Functions*, SIAM Journal on Numerical Analysis, Vol. 4, No. 2, pp. 202-210.

Lyness, J.N. (1977), *Has Numerical Differentiation a Future?*, Proc. of the Seventh Minitoba Conference on Numerical Mathematics and Computing, Univ. of Manitoba, Winnipeg, pp. 107-129.

Maidl, B. (2008), *Systemverhalten und Prozessoptimierung beim Erddruckschild*, Geomechanics and Tunnelling, Vol. 1, No. 3, pp. 229-235.

Maidl, B., M. Herrenknecht, and L. Anheuser (2006), *Mechanised Shield Tunneling*, ISBN-10: 3-433-01292-X, ISBN-13: 978-3-433-01292-5, Ernst&Sohn, Berlin, Germany, 428 p.

Mair, R.J. (1993), *Developments in Geotechnical Engineering Research: Applications to Tunnels and Deep Excavations*, Unwin memorial Lecture 1992; Proc. of Institution of Civil Engineers: Civil Engineering, Vol. 93, pp. 27-41.

Mayne, P.W., B.R. Christopher, and J. DeJong (2001), *Manual on Subsurface Investigations. Geotechnical Site Characterization*, National Highway Institute Publication No. FHWA NHI-01-031, Federal Highway Administration, Washington,

DC, USA. Source: `http://geosystems.ce.gatech.edu/Faculty/Mayne/papers/NHI%202002%20Subsurface%20Investigations.pdf`

Meschke, G., A. Alsahly, J. Ninić, and J. Stascheit (2011), *Parallelized Simulations of Advancement Processes and Soil-Structure Interactions in Mechanized Tunneling*, In: H. Mang, J.-Z. Cui, Y.-B. Yang, and M.-W. Yuan, (eds.), Third International Symposium on Computational Mechanics (ISCM III), Second Symposium on Computational Structural Engineering (CSE II), Taipei, Taiwan, ISCM III-CSEII.

Meschke, G., J. Ninić, J. Stascheit, and A. Alsahly (2013), *Parallelized Computational Modeling of Pile-Soil Interactions in Mechanized Tunneling*, Engineering Structures, Vol. 47 pp. 35-44. DOI: 10.10.16/j.engstruct.2012.07.001

Meier, J., M. Datcheva, and T. Schanz (2007), *Identification of Constitutive and Geometrical Parameters of Numerical Models with Application in Tunnelling*, Proc. of ECCOMAS Thematic Conference on Computational Methods in Tunneling (EURO:TUN 2007), Vienna, Austria, 27-29 August.

Meier, J. (2008), *Parameterbestimmung mittels inverser Verfahren für geotechnische Problemstellungen*, in German, PhD thesis, Bauhaus-Universität Weimar.

Meier, J., M. Datcheva, and T. Schanz (2009a), *Identification of Obstacles ahead of Tunnel Face Applying Inverse Approach*, Proc. of ECCOMAS Thematic Conference on Computational Methods in Tunneling (EURO:TUN 2009), Ruhr University Bochum, pp. 673-680, 9-11 September.

Meier, J., S. Rudolph, and T. Schanz (2009b), *Effective Algorithm for Parameter Back Calculation – Geotechnical Applications*, Bautechnik, Vol. 86, Issue S1, pp. 86-97.

Meissner, M., M. Schmuker, and G. Schneider (2006), *Optimized Particle Swarm Optimization (OPSO) and its Application to Artificial Neural Network Training*, BMC Bioinformatics, **7**:125. DOI: 10.1186/1471-2105-7-125.

Melis, M., L. Medina, J.M. Rodriguez (2002), *Prediction and Analysis of Subsidence Induced by Shield Tunnelling in the Madrid Metro Extension*, Canadian Geotechnical Journal, Vol. 39, No. 6, pp. 1273-1287. DOI: 10.1139/t02-073.

Mihalowski, R.L. (2005), *Coefficient of Earth Pressure at Rest*, Journal of Geotechnical and Geoenvironmental Engineering - ASCE, Vol. 131, No. 11, pp. 1429-1433.

Miro, S., D. Hartmann, T. Schanz, and V. Zarev (2012a), *System Identification Methods for Ground Models in Mechanized Tunneling*, K. Gürlebeck, F. Werner, T. Lahmer (Editors): 19th International Conference on the Applications of Computer Science and

Mathematics in Architecture and Civil Engineering, ISSN 1611-4086, Weimar, Germany, 4-6 July.

Miro, S., D. Hartmann, T. Schanz, and V. Zarev (2012b), *Scenario-Driven System Identification for Specification of Ground Models in Mechanized Tunneling*, Proc. of the 14th International Conference on Computing in Civil and Building Engineering 2012, Moscow, Russia.

Miro, S., D. Hartmann, and T. Schanz (2013), *Identification of a Layer Change in Front of a Mechanized Tunnel Face Considering Uncertainties*, Proc. of the 14th International Conference on Civil, Structural and Environmental Engineering Computing, Cagliari, Sardinia, Italy, Paper 183, 3-6 September. DOI:10.4203/ccp.102.183

Mohr, C.O. (1900), *Welche Umstände bedingen die Elastizitätsgrenze und den Bruch eines Materials?*, in German, Journal "Vereins Deutscher Ingenieure", Vol. 24, pp. 1524-1530, 1572-1577, Germany.

Morris, M.D. (1991), *Factorial Sampling Plans for Preliminary Computational Experiments*, Technometrics, Vol. 33, pp. 161-174.

Möller, S. (2006), *Tunnel Induced Settlements and Structural Forces in Linings*, PhD Thesis, Universität Stuttgart.

Möller, S., and P.A. Vermeer (2008), *On Numerical Simulation of Tunnel Installation*, Tunnelling and Underground Space Technology, Vol. 23, pp. 461-475.

Murray, B., J. Waggoner, S. Swartz, and H. Lum (2008), *Utilization of Strain Measurements on Shielded Tunnel Boring Machines*, Proc. of the North American Tunneling Conference, San Francisco, USA, pp. 91-100. ISBN-13: 978-0-87335-263-5.

Nagel, F. (2009), *Numerical Modeling of Partially Saturated Soil and Simulation of Shield Supported Tunnel Advance*, PhD Thesis, Chair for Static and Dynamic, Ruhr-Universität Bochum, Germany, 191 p.

Nagel, F., J. Stascheit, and G. Meschke (2010), *Process-Oriented Numerical Simulation of Shield-Supported Tunneling in Soft Soils*, Geomechanics and Tunneling, Vol. 3, pp. 268-282.

Nagel, F., I. Spohr, and L. Speier (2012), *Observation Method in Geotechnics – Interlinking Measurements and Simulation*, Tunnel, Vol. 3, pp. 40-47. ISSN: 0722-6241

Nataf, A. (1962), *Determination des distributions de probabilites dont les marges sont donnees*, Comptes Rendus de l'Academie des Sciences, Vol. 225, pp. 42-43.

Naterop, D. (2001), *Instrumentation and Data Management for the Zurich Zimmerberg Railway Tunnel Construction*, Geotechnical Instrumentation for Field Measurements at GeoDelft, 3-5 April. Source: `http://www.solexperts.com/index.php?option=com_content&view=article&id=246&Itemid=48&lang=de`

Nguyen, L.T, and T. Nestorovic (2013), *The Extended Kalman Filter and the Unscented Kalman Filter for Material Parameter Identification with Application in Tunneling*, Proc. in Applied Mathematics and Mechanics (PAMM), Vol. 13, No. 1 (special Issue: 84th Annual Meeting of the International Association of Applied Mathematics and Mechanics (GAMM); Editors: L. Cvetkovic, T. Atanackovic and V. Kostic), pp. 393-394, Novi Sad.

Ninić, J., J. Stascheit, and G. Meschke (2011a) *Numerical Simulation of Interactions Between TBM-Driven Tunnel Construction and Pile Foundations*, In: N. Khalili, and M. Oeser (eds.), Proc. of Computer Methods for Geomechanics: Frontiers and New Applications, IACMAG 2011, pp. 213-218, Melbourne, Australia, 9-11 May.

Ninić, J., J. Stascheit, and G. Meschke (2011b), *Prediction of Tunnelling Induced Settlements using Simulation-Based Artificial Neural Networks*, In: Y. Tsompanakis, and B.H.V. Topping, (eds.), Proc. of the Second International Conference on Soft Computing Technology in Civil, Structural and Environmental Engineering, Chania, Crete, Greece, paper 26, September.

Ohde, J. (1951), *Grundbaumechanik*, Hütte.

Pedersen, M.E.H. (2010), *Tuning & Simplifying Heuristical Optimization*, PhD thesis, University of Southampton, School of Engineering Sciences, Computational Engineering and Design Group.

Pedersen, M.E.H., and A.J. Chipperfield (2009), *Simplifying Particle Swarm Optimization*, Applied Soft Computing, Vol. 10, No. 2, pp. 618-628. DOI: 10.1016/j.asoc.2009.08.029.

Perez, R., and K. Behdinan (2007), *Swarm Intelligence: Focus on Ant and Particle Swarm Optimization*, Chapter 21 *Particle Swarm Optimization in Structural Design*, pp. 373-394, International Journal of Advanced Robotic Systems, first edition, September. ISBN 978-3-902613-09-7.

Potts, D.M. (2012), *Using Numerical Analysis in Geotechnical Engineering Practice*, First Leonardo Zeevaert Lecture, Sociedad Mexicana de Ingenieria Geotecnica A.C., Cancun, Mexico, pp. 1-31.

Potts, D.M. (2003), *Numerical Analysis: A Virtual Dream or Practical Reality?*, Geotechnique, Vol. 53, No. 6, pp. 535-573 (42-th Rankine Lecture).

Potts D.M., and L. Zdravkovic (2001), *Finite Element Analysis in Geotechnical Engineering: Application*, Pub. Thomas Telford Ltd, London, 500 p. ISBN:9780727727831

Potts D.M., and L. Zdravkovic (1999), *Finite Element Analysis in Geotechnical Engineering: Theory*, Pub. Thomas Telford Ltd, London, 440 p.

Putke, T., M.A. Ahrens, and P. Mark (2013), *Towards Topology and Shape Optimised Concrete Linings for Shear Load Transfer in Ring Joints*, Proc. of the EURO:TUN 2013: 3rd International Conference on Computational Methods in Tunnelling and Subsurface Engineering, Ruhr University Bochum, Germany, pp. 147-155, 17-19 April.

Rowe, P.W. (1962), *The Stress-Dilatancy Relation for Static Equilibrium of an Assembly of Particles in Contact*, Proc. of the Royal Society of London, Series A, Mathematical and Physical Sciences, Vol. 269, No. 1339, pp. 500-527.

Rowe, P.W. (1971), *Theoretical Meaning and Observed Values of Deformation Parameters for Soil*, In: Stress-Strain Behaviour of Soils, Proc. of Roscoe Memorial Symposium, Cambridge University (Henley-on-Thames: G.T. Foulis & Co.), (ed. R.H.G. Parry), pp. 143-194.

Sakurai, S. (1997), *Lessons Learned from Field Measurements in Tunnelling*, Tunnelling and Underground Space Technology, Vol. 12, No. 4, pp. 453-460.

Saltelli, A., M. Ratto, T. Andres, F. Campolongo, J. Cariboni, D. Gatelli, M. Saisana, and S. Tarantola (2008), *Global Sensitivity Analysis. The Primer*, John Wiley & Sons, 304 p. ISBN-10: 0470059974; ISBN-13: 978-0470059975

Saltelli, A., M. Ratto, S. Tarantola, and F. Campolongo (2006), *Sensitivity Analysis Practices: Strategies for Model-based Inference*, Reliability Engineering & System Safety, Vol. 91, No. 10-11, pp. 1109-1125, Oktober. DOI: 10.1016/j.ress.2005.11.014

Santos, J.A., and A. Gomes Correia (2001), *Reference Threshold Shear Strain of Soil. Its Application to Obtain an Unique Strain-Dependent Shear Modulus Curve for Soil*, Proc. of the 15th International Conference on Soil Mechanics and Geotechnical Engineering, Vol. 1, pp. 267-270, Istanbul, Turkey.

Schanz, T., V. Zarev, and T. Barciaga (2012), *Adäquate Modellbildung für die numerische Analyse maschineller Tunnelvortriebe*, in German, Proc. of the 3. RuhrGeo Tag 2012: Innerstädtischer Tunnel- und Spezialtiefbau, Bergische Universität Wuppertal,

Fachbereich D, Abteilung Bauingenieurwesen, Berichte des Lehr- und Forschungsgebietes Geotechnik, M. Pulsfort (editor), Nr. 32, pp. 131-146, March.

Schanz, T., P.A. Vermeer, and P.G. Bonnier (1999), *The Hardening Soil Model: Formulation and Verification*, Beyond 2000 in Computational Geotechnics - 10 Years of PLAXIS.

Schanz, T., and P.A. Vermeer (1998), *On the Stiffness of Sands*, Geotechnique, Vol. 48, pp. 383-387.

Schanz, T. (1998), *Zur Modellierung des mechanischen Verhaltens von Reibungsmaterialien*, in German, Habilitation Dissertation, University of Stuttgart, Germany.

Schanz, T., and P.A. Vermeer (1996), *Angles of Friction and Dilatancy of Sand*, Geotechnique, Vol. 46, No. 1, pp. 145-151.

Schaufler, A., C. Becker, H. Steeb, and A. Scheuermann (2013), *Simulation of the Backfilling Process with Annular Gap Grouting Mortar*, Proc. of the EURO:TUN 2013: 3rd International Conference on Computational Methods in Tunnelling and Subsurface Engineering, Ruhr University Bochum, Germany, pp. 587-597, 17-19 April.

Schaufler, A., C. Becker, H. Steeb, and A. Scheuermann (2012a), *A Continuum Model for Infiltration Problems* Proc. of the 6th International Conference on Scour and Erosion – ICSE6 Paris, pp. 663-670, Paris, 27-31 August, 2012a.

Schaufler, A., C. Becker, and H. Steeb (2012b), *Infiltration Processes in Cohesionless Soils*, ZAMM – Journal of Applied Mathematics and Mechanics, Vol. 93, No. 2-3, pp. 138-146, 2012b.

Schindler, S., and P. Mark (2013), *Evaluation of Building Stiffness in the Risk-assessment of Structures Affected by Settlements*, Proc. of the EURO:TUN 2013: 3rd International Conference on Computational Methods in Tunnelling and Subsurface Engineering, Ruhr University Bochum, Germany, pp. 477-486, 17-19 April.

Schmitt, J., M. Fritsch, J. Gattermann, and J. Stahlmann (2005), *Numerical Investigations to the Influence of Rearrangement of Ground Pressure for Shield Tunneling*, Proc. of the 9th International Conference on Structural Safety And Reliability, ICOSSAR'05, pp. 1317-1323, Rom, Italy. ISBN 90-5966-040-4

Schmitt, J., J. Stahlmann, U. Rehm, and M. Herrenknecht (2008), *Untersuchungen zur Porenwasserdruckentwicklung im Bereich der Ortsbrust bei maschinellen Tunnelvortrieben*, Bautechnik, Vol. 85, No. 1, pp. 64-75.

Schweiger, H.F. (2008), *The Role of Advanced Constitutive Models in Geotechnical Engineering*, Geomechanics and Tunnelling, Vol. 1, No. 5, pp. 336-344.

Shi, Y., and Eberhart, R.C. (1998a), *A Modified Particle Swarm Optimizer*, Proc. of the IEEE Congress on Evolutionary Computation (CEC 1998), Piscataway, NJ. pp. 69-73.

Shi, Y., and Eberhart, R.C. (1998b), *Parameter Selection in Particle Swarm Optimization*, Evolutionary Programming VII: Proc. of the Seventh Annual Conference on Evolutionary Programming, New York. pp. 591-600.

Shi, Y., and Eberhart, R.C. (2001), *Particle Swarm Optimization With Fuzzy Adaptive Inertia Weight*, Proc. of the Workshop on Particle Swarm Optimization 2001, Indianapolis, IN: Purdue School of Engineering and Technology.

Sobol, I.M. (1993), *Sensitivity Estimates for Nonlinear Mathematical Models*, Matematicheskoe Modelirovanie, Vol. 2, No. 1, pp. 112-118, 1990 (in Russian), English translation in: Mathematical Modeling and Computational Experiment, Vol. 1, No. 4, pp. 407-414.

Song, E.X. (1990), *Elasto-plastic Consolidation under Steady and Cyclic Loads*, Doctoral thesis, Delft University of Technology, The Netherlands.

von Soos, P. (1990), *Properties of Soil and Rock*, in German, in: Grundbautaschenbuch, Part 4, Edition 4, Ernst&Sohn, Berlin, Germany.

Stascheit, J., M. Eitzen, and G. Meschke (2011), *Parallel Simulation of Shield Tunnelling on Distributed Memory and GPGPU Systems*, In: P. Ivanyi, and B. H. V. Topping (eds.), Proc. of the Second International Conference on Parallel, Distributed, Grid and Cloud Computing for Engineering 2011, paper 28, Ajaccio, Corsica, France, 12-15 April. DOI: 10.4203/ccp.95.28

Steeb, H. (2008), *Non-Equilibrium Processes in Porous Media*, Habilitation, Universität des Saarlands, Saarbrücken.

Sugimoto, M., A. Sramoon, and H. Iwasaki (2006), *Influence of Grout Material in Shield Tail on Shield Tunnelling Performance*, Geotechnical Aspects of Underground Construction in Soft Ground. Proc. of the 5th International Symposium TC28, The Netherlands, 15-17 June 2005, edited by K.J. Bakker, A. Bezuijen, W. Broere, and E.A. Kwast, pp. 313-318. ISBN: 978-0-415-39124-5; DOI: 10.1201/NOE0415391245.ch41

Tatsuoka, F., S. Shibuya, and R. Kuwano (2001), *Advanced Laboratory Stress-Strain Testing of Geomaterials*, Swets & Zeitlinger, 340 p. ISBN-13: 978-90-265-1843-0

Terzaghi, K. (1936), *The Shear Resistance of Saturated Soils*, Proc. of the 1st International Conference on Soil Mechanics and Foundation Engineering, Harvard University Press: Cambridge, Massachusetts, USA, Vol. 1, pp. 54-56.

Terzaghi, K. (1943), *Theoretical Soil Mechanics*, New York, John Wiley & Sons, 528 p. ISBN 0-471-85305-4; DOI: 10.1002/9780470172766.

Thurlow, P., and H. Knitsch (2011), *Supporting Measures for Urban Tunnelling*, 8th International Symposium on Field Measurements in GeoMechanics Berlin, Publication GT 11-28 E, pp. 1-10, September 12-16.

Thut, A., U. Raz, D. Naterop, and H.-J. Becker (2002), *Monitoring during Construction in Urban Areas*, Proc. of the 2nd Int. Conference on Soil Structure Interaction in Urban Civil Engineering, Swiss Federal Institute of Technology ETH Zurich, Zurich, Switzerland, pp. 489-496, March.

Vermeer, P.A., Möller, S., and N. Ruse (2003), *On the Application of Numerical Analysis in Tunnelling*, Proc. of the 12th Asian Regional Conference on Soil Mechanics and Geotechnical Engineering (12 ARC), Singapore, Vol. 2, pp. 1539-1544, 4-8 August.

Vermeer, P.A., and H. van Langen (1989), *Soil Collapse Computations With Finite Elements*, Ingenieur-Archiv 59, pp. 221-236.

Viggiani, G., and J.H. Atkinson (1995), *Stiffness of Fine-Grained Soil at Very Small Strains*, Geotechnique, Vol. 45, No. 2, pp. 249-265.

van der Vliet, C., F. Bijlaard, G. Kooijman, and M. Naaktgeboren (2009), *Shield Tail Deformations: Experience, Mechanics ans Lessons*, ITA - AITES World Tunnel Congress 2009 & the 35th ITA - AITES General Assembly, Budapest, Hungary, 23-28 May.

Will, J. (2006), *The Calibration of Measurement and Simulation as Optimization Problem*, lecture presented at the NAFEMS Conference, Wiesbaden, Germany, 10-11 May. Source: `http://www.dynardo.de/fileadmin/Material_Dynardo/bibliothek/Optimierung_Sensitivitaet/NAFEMS_will_2006_engl.pdf`

Yu, Hai-Sui (2006), *Plasticity and Geotechnics*, Springer, Advances in Mechanics and Mathematics, Vol. 13, 524 p. ISBN-10: 0387335978; ISBN-13: 978-0387335971

Yu, Hai-Sui (1998), *CASM: A Unified State Parameter Model for Clay and Sands*, International Journal for Numerical and Analytical Methods in Geomechanics, Vol. 22, pp. 621-653.

Zadeh, K.S. (2008), *Parameter Estimation in Flow through Partially Saturated Porous Materials*, Journal of Computational Physics, Vol. 227, No. 24, pp. 10243-10262.

Zarev, V., M. Datcheva, T. Schanz, and I. Dimov (2013), *Soil-Model Parameter Identification via Back Analysis for Numerical Simulation of Shield Tunneling*, Proc. of the EURO:TUN 2013: 3rd International Conference on Computational Methods in Tunnelling and Subsurface Engineering, Ruhr University Bochum, Germany, pp. 345-356, 17-19 April.

Zarev, V., T. Schanz, and M. Datcheva (2011a), *Three-Dimensional Numerical Simulation of Mechanized Tunneling*, Proc. of the 11th International Scientific Conference VSU' 2011, Higher School of Civil Engineering (VSU) "Lyuben Karavelov", Sofia, Bulgaria, VI, pp. 19-25 June.

Zarev, V., T. Schanz, and M. Datcheva (2011b), *Three-Dimensional Finite-Element Analysis of Mechanized Tunneling in Urban Areas*, In: Y. Tsompanakis, and B.H.V. Topping, (eds.), Proc. of the CC2011: The Thirteenth International Conference on Civil, Structural and Environmental Engineering Computing, Chania, Crete, Greece, paper 223, September.

Zdravkovic, L., and D.M. Potts (2010), *Application of Numerical Analysis in Geotechnical Engineering Practice*, Proc. of GeoFlorida 2010: Advances in Analysis, Modeling & Design, pp. 69-88. DOI: 10.1061/41095(365)4

Zhang, Z.F., A.L. Ward, and G.W. Gee (2003), *Estimating Soil Hydraulic Parameters of a Field Drainage Experiment Using Inverse Techniques*, Vadose Zone Journal 2, pp. 201-211.

Schriftenreihe des Lehrstuhls für Grundbau, Boden- und Felsmechanik der Ruhr-Universität Bochum

Herausgeber: H.L. Jessberger

1 (1979) **Hans Ludwig Jessberger**

Grundbau und Bodenmechanik an der Ruhr-Universität Bochum

2 (1978) **Joachim Klein**

Nichtlineares Kriechen von künstlich gefrorenem Emschermergel

3 (1979) **Heinz-Joachim Gödecke**

Die Dynamische Intensivverdichtung wenig wasserdurchlässiger Böden

4 (1979) **Poul V. Lade**

Three Dimensional Stress-Strain Behaviour and Modeling of Soils

5 (1979) **Roland Pusch**

Creep of soils

6 (1979) **Norbert Diekmann**

Zeitabhängiges, nichtlineares Spannungs-Verformungsverhalten von gefrorenem Schluff

unter triaxialer Belastung

7 (1979) **Rudolf Dörr**

Zeitabhängiges Setzungsverhalten von Gründungen in Schnee, Firn und Eis

der Antarktis am Beispiel der deutschen Georg-von-Neumayer- und Filchner-Station

8 (1984) **Ulrich Güttler**

Beurteilung des Steifigkeits- und Nachverdichtungsverhaltens von

ungebundenen Mineralstoffen

9 (1986) **Peter Jordan**

Einfluss der Belastungsfrequenz und der partiellen Entwässerungs-

möglichkeiten auf die Verflüssigung von Feinsand

10 (1986) **Eugen Makowski**

Modellierung der künstlichen Bodenvereisung im grundwasserdurchströmten

Untergrund mit der Methode der finiten Elemente

22 (1994) **Diethard König**

Beanspruchung von Tunnel- und Schachtausbauten in kohäsionslosem Lockergestein

unter Berücksichtigung der Verformung im Boden

23 (1995) **Thomas Neteler**

Bewertungsmodell für die nutzungsbezogene Auswahl von Verfahren zur Altlastensanierung

24 (1995) **Ralph Kockel**

Scherfestigkeit von Mischabfall im Hinblick auf die Standsicherheit von Deponien

25 (1996) **Jan Laue**

Zur Setzung von Flachfundamenten auf Sand unter wiederholten Lastereignissen

26 (1996) **Gunnar Heibrock**

Zur Rissbildung durch Austrocknung in mineralischen Abdichtungsschichten

an der Basis von Deponien

27 (1996) **Thomas Siemer**

Zentrifugen-Modellversuche zur dynamischen Wechselwirkung zwischen Bauwerken

und Baugrund infolge stoßartiger Belastung

28 (1996) **Viswanadham V. S. Bhamidipati**

Geosynthetic Reinforced Mineral Sealing Layers of Landfills

29 (1997) **Frank Trappmann**

Abschätzung von technischem Risiko und Energiebedarf bei Sanierungsmaßnahmen

für Altlasten

30 (1997) **André Schürmann**

Zum Erddruck auf unverankerte flexible Verbauwände

31 (1997) **Jessberger, H. L. (Herausgeber)**

Environment Geotechnics, Report of ISSMGE Technical Committee TC 5

on Environmental Geotechnics

Herausgeber: Th. Triantafyllidis

32 (2000) **Triantafyllidis, Th. (Herausgeber)**

Boden unter fast zyklischer Belastung: Erfahrung und Forschungsergebnisse (Workshop)

33 (2002) **Christof Gehle**

Bruch- und Scherverhalten von Gesteinstrennflächen mit dazwischenliegenden Materialbrücken

34 (2003) **Andrzej Niemunis**

Extended hypoplastic models for soils

35 (2004) **Christiane Hof**

Über das Verpressankertragverhalten unter kalklösendem Kohlensäureangriff

36 (2004) **René Schäfer**

Einfluss der Herstellungsmethode auf das Verformungsverhalten von Schlitzwänden in weichen bindigen Böden

37 (2005) **Henning Wolf**

Zur Scherfugenbänderung granularer Materialien unter Extensionsbeanspruchung

38 (2005) **Torsten Wichtmann**

Explicit accumulation model for non-cohesive soils under cyclic loading

39 (2008) **Christoph M. Loreck**

Die Entwicklung des Frischbetondruckes bei der Herstellung von Schlitzwänden

40 (2008) **Igor Arsic**

Über die Bettung von Rohrleitungen in Flüssigböden

41 (2009) **Anna Arwanitaki**

Über das Kontaktverhalten zwischen einer Zweiphasenschlitzwand und nichtbindigen Böden

54   (2014)   **Qasim Abdulkarem Jassim Al-Obaidi**

                    Hydro-Mechanical Behaviour of Collapsible Soils

55   (2015)   **Veselin Zarev**

                    Model Identification for the Adaption of Numerical Simulation Models — Application

                    to Mechanized Shield Tunneling

Curriculum Vitae

Personal information

Name	Veselin Zarev
Born	31.01.1983, Kyustendil, Bulgaria

Education

2011–2014	Ruhr-Universität Bochum, Germany
	Chair of Foundation Engineering, Soil and Rock Mechanics
	Doctoral study in Computational Geomechanics
2002–2008	Vienna University of Technology, Austria
	Department of Civil Engineering
	Graduation to Diplom-Ingenieur (equivalent to M.Sc.)

Professional positions

2014–present	KHP König und Heunisch Planungsgesellschaft mbH & Co KG
	Frankfurt am Main, Germany
	Project engineer, designing and consulting
2011–2014	Ruhr-Universität Bochum, Germany
	Chair of Foundation Engineering, Soil and Rock Mechanics
	Research associate in Computational Geomechanics
2010–2010	Horner und Ingenieure
	Berlin, Germany
	Project engineer, designing
2008–2010	Risk Engineering, Ltd
	Sofia, Bulgaria
	Project engineer, consulting